

A study of Raman spectroscopy for the early detection and characterization of prostate cancer using blood plasma and prostate tissue biopsy.



Submitted by

Bassey Essien Ndiyo

To the University of Exeter
as a thesis for the degree of
Doctor of Philosophy in Physics
In October 2022

This thesis is available for Library use on the understanding that it is copyright material and that no quotation from the thesis may be published without proper acknowledgement.

I certify that all material in this thesis which is not my own work has been identified and that no material has previously been submitted and approved for the award of a degree by this or any other University.

Signature: B.Ndiyo

Abstract:

Prostate cancer (PC) is the most common cancer in men after non-melanoma skin cancer in the United Kingdom (Cancer Research UK, 2019). Current diagnostic methods (PSA, DRE, MRI & prostate biopsy) have limitations as these are unable to distinguish between low-risk cancers that do not need active treatment from cancers which are more likely to progress. In addition, prostate biopsy is invasive with potential side effects. There is an urgent need to identify new biomarkers for early diagnosis and prognostication in PC.

Raman spectroscopy (RS) is an optical technique that utilises molecular-specific, inelastic scattering of light photons to interrogate biological samples. When laser light is incident on a biological sample, the photons from the laser light can interact with the intramolecular bonds present within the sample. The Raman spectrum is a direct function of the molecular composition of the tissue, providing a molecular fingerprint of the phenotypic expression of the cells and tissues, which can give good objective information regarding the pathological state of the biological sample under interrogation.

We applied a technique of drop coating deposition Raman (DCDR) spectroscopy using both blood plasma and sera to see if a more accurate prediction of the presence and progression of prostate cancer could be achieved than PSA which would allow for blood sample triage of patients into at risk groups. 100 participants were recruited for this study (100 blood plasma and 100 serum samples). Secondly, 79 prostate tissue samples (from the same cohort) were interrogated with the aid of Raman micro-spectroscopy to ascertain if Raman spectroscopy can provide molecular fingerprint that can be utilised for real time *in vivo* analysis. Multivariate analysis of support vector machine (SVM) learning and linear discriminant analysis (LDA) were utilised differently to test the performance accuracy of the discriminant model for distinguishing between benign and malignant mean plasma spectra. SVM gave a better performance accuracy than LDA with sensitivity and specificity of 96% and 97% respectively and an area under the curve (AUC) of 0.98 as opposed to sensitivity and specificity of 51% and 80% respectively with AUC of 0.74 using LDA. Slightly lower performance accuracy was also observed when blood serum mean spectra analysis was compared with blood plasma mean spectra analysis for both machine learning algorithms (SVM & LDA).

Tissue spectral analysis on the other hand recorded an overall accuracy of 80.8% and AUC of 0.82 with the SVM algorithm compared to performance accuracy of 75% and AUC of 0.77 with LDA algorithm (better performance noted with the SVM algorithm). The small sample size of 79 prostate biopsy tissues

was responsible for the low sensitivity and specificity. Therefore, the tissues were insufficient to describe all the variances in each group as well as the variability of the gold standard technique.

Conclusion: Raman spectroscopy could be a potentially useful technique in the management of Prostate Cancer in areas such as tissue diagnosis, assessment of surgical margin after radical prostatectomy, detection of metastasis, Prostate Cancer screening as well as monitoring and prognosticating patients with Prostate Cancer. However, more needs to be done to validate the approaches outlined in this thesis using prospective collection of new samples to test the classification models independently with sufficient statistical power. At this stage only the fluid-based models are likely to be large enough for this validation process.

Acknowledgement

My sincere gratitude goes to the Almighty God, who made this dream come true, I am eternally grateful for His wisdom, knowledge and understanding all through this process. His guidance has actually helped me navigate through this project with ease. I know that sometimes I felt like giving up especially when things were not working as expected but I drew strength in the fact that He who began a good work in me was faithful to complete it, that kept me going . Thank you, Lord for the destiny helpers that you connected me with, I could not have made it without Him.

This work was funded by the Department of Urology, Darent Valley Hospital, and the University of Exeter. A lot of people at different sites (University of Exeter, Dartford and Gravesham NHS Trust and Maidstone & Tunbridge Wells NHS Trust) have contributed to this research project during the past five years.

My sincere thanks goes to my supervisors, Prof Nick Stone and Prof Sanjeev Madaan for their precious time and efforts to support me in this academic work. Both Prof Stone and Prof Madaan have done a remarkable job at supporting me all through this project. Prof Stone's depth of knowledge and experience in clinical research has always been pivotal in ensuring that this project is completed. There were times when nothing had crystalised with regards this project and I thought, we may as well pack it up and do something else, but his strong resilience and passion had kept me going during those difficult times. I remain eternally grateful to Prof Madaan, whose depth of clinical knowledge and experience had been crucial in ensuring that the right clinical team was assembled to offer the right level of support during this project. Those period of discussions that we had in his office had refocussed my thought process on the direction that this project should go. Both Prof Madaan and Prof Stone are well known and respected for their love and enthusiasm when it comes to research projects.

My gratitude also goes to Dr Michael Brand (Senior Governance Manager) and Mrs Bridget Fuller (Research and Development Manager) at Dartford and Gravesham NHS Trust. Both Michael and Bridgett were very supportive during the application for ethical approval. Both worked tirelessly to ensure that my research proposal was suitable for local research and ethics committee as well as the national ethics committee approvals.

The team at Poplar unit of the Urology department deserve my special thanks as they were amazing all through the course of the study, all the nurses were very helpful, and I am very sure without you the

project would not have been complete. Dr Hussein deserve a special thanks for helping in obtaining all the biopsy samples utilized for this project, I am indeed grateful to him for his diligence and professionalism. All the administrative staff supported in the booking of patients and ensuring orderliness in the scheduling of participants for the study. The team at the Pathology department (Darent Valley Hospital) and Maidstone and Tunbridge Wells NHS Trust were absolutely a delight to work with and I am also grateful for their support in helping with the storage of the research samples, arranging courier to and from different sites under dry ice as well as preparing samples on slides for histological analyses.

Special recognition to Miss Julie Knowles (Research Governance Officer) and Mr Paul Denham (Histology Lead) at the Maidstone and Tunbridge Wells NHS trust who worked extremely hard to ensure that the Trust (Maidstone & Tunbridge Wells) ethics approval was given for this project, I am really grateful for your hard work.

Dr Amit Goel (Consultant Histopathology, Maidstone & Tunbridge Wells) deserves a special credit for his professional time in providing histopathological report (assessment) for all the research tissue samples for this study, I am very grateful.

The Biospectroscopy team were a unique set of individuals who took special interest in this project and gave me all the needed support to ensure that I was successful. Special thanks Dr Ben Gardner, Dr Alex Dudgeon, Dr Jayakrupakar Nallala and Dr Adrian Ghita for their kind support.

Special thanks to my darling wife Dr (Mrs) U Ndiyo for your understanding and support all through this project especially during the period of writing up this thesis. I know you had to make a lot of adjustments to enable me to have the time to focus on this piece of work and to complete this thesis, thank you so much for the love and support. My children, Aviva, Joshua and Emmanuel, you guys have been amazing, and I want to say a big thank you to all of you for your love, patience, and encouragement. You guys were always checking my word count to see if I am anywhere close to the target, well, you will be pleased to know that I have reached the target now.

My friends and family especially, my siblings and uncles and aunties, sorry about the neglect you suffered during this period, this was not intentional, but it was to enable me focus on the research project so that I could give my very best to the study.

Thank you to Bishop Paul and Pastor Joyce Fadeyi for all their spiritual support and encouragement, your care for my successful completion can never go unnoticed, I am very grateful. Elder Dr & Mrs J Obasohan have been so supportive of my academic advancement and I am eternally grateful for their kind support all through the period of my studies.

Lastly, I am grateful to my dad and mum (Mr and Mrs Essien Ndiyo Eyo) of blessed memory who brought me into this world and nurtured me to be who I am today, those teachings and discipline have paid off and your value for education had been my inspiration all through the period of my study. I know you would have love to see this day, but I know that you are in a better place right now, but I just want to say that you are highly appreciated.

Table of Contents

Chapter 1 -Introduction.....	18
Chapter 2 – Background	22
2.1. Anatomy, Physiology and Histology	23
2.2. Prostate Cancer:	25
2.3. Pre- Cancers:.....	25
2.3.1. High grade Prostatic Intraepithelial Neoplasia (High grade PIN)	25
2.3.2. Proliferative Inflammatory Atrophy (PIA).....	26
2.3.3. Atypical Small Acinar Proliferation (ASAP).....	27
2.4. Gleason grading system.....	27
2.5. Current Diagnostic pathways.....	28
2.5.1. Gold standard Techniques for detection & diagnosis.....	28
2.5.2. Prostate Specific Antigen.....	30
2.6. Ultrasound	31
2.6.1. Ultrasound in Diagnosis of Prostate cancer.....	33
2.7. Computerized Tomography	34
2.8. Digital Rectal Examination	34
2.9. Magnetic Resonance Imaging.....	36
2.9.1. The role of mpMRI in biopsy naïve patients.....	39
2.9.2. The role of positive mpMRI in previous patient (Active surveillance)	40
2.10. Histopathology of prostate cancer	40
2.10.1. Histopathological features consistent with carcinoma	40
2.11. Staining	41
Chapter 3: Novel Optical Diagnostic Techniques.....	43
3.1. Raman spectroscopy.....	43
3.1.1. Raman spectroscopy and Historical perspective	44
3.1.2. Underpinning Principles of Raman Spectroscopy.....	44
3.1.2. Raman microscopy:	45
3.2. What is a laser?.....	46
3.2.1. What are the characteristics of the light that is emitted?	46
3.2.2. Why is it different to light from other sources...?.....	46
3.2.3. Light source	47
3.3. Interaction of light and biological samples.....	47
3.3.1. Light interaction with tissue samples:	49
3.3.2. Scattering of Light:.....	50
3.4 – Blood.....	51

3.4.1. Plasma.....	51
3.4.2. Serum.....	53
3.4.3. Collection, handling and storage of plasma and serum.....	53
3.5. Biomarker in biological fluids	55
3.5.1. Why blood plasma and serum	56
3.5.2. Drop Coating Deposition Raman Spectroscopy	56
3.5.3. Underpinning principles of Droplet evaporation.....	58
3.5.4. Proteomic Profiling	58
3.5.5. Metabolites and other chemical species screening.....	58
3.5.6. Metabolites in Cancer diagnostics	60
3.5.7. Glycolysis:	60
3.6. Raman spectroscopy of blood constituents and cancer diagnostics	60
3.7. Establishing the biochemical basis of urological disease measured with Raman Spectroscopy.	61
3.8. Clinical utilisation of Raman spectroscopy	62
3.9. Raman Spectroscopy in prostate cancer	64
3.9.1. Tissue diagnosis and prediction of cancer grade:.....	64
3.9.2. Assessment of surgical margin following radical prostatectomy:	65
3.9.3. Detection of metastasis:	67
3.9.4. Assessment of castration resistant prostate cancer:.....	68
3.9.5. Monitoring treatment effectiveness:	68
Chapter 4 – Methodology.....	71
4.1– Basic Raman Instrumentation for measuring biological samples	71
4.2. Alignment and calibration	72
4.3. Sampling stage.....	72
4.4. Sample preparation and presentation.....	73
4.5. Experimental set up.....	74
4.6. Data Analysis Techniques	77
4.7.2. Normalization:	80
4.7.3. Smoothing:	80
4.7.4. Removal of Outliers	80
4.7.7. Cross Validation	81
4.7.8. Receiver Operating Characteristic Curve	81
4.8. Histological Analysis:	82
4.9. Raman Spectroscopy Data analysis	84
4.9.1. Analysis of prostate tissue spectra	84
4.9.2. Data pre-processing:.....	84

Chapter 5 – Result	86
5.1. Tissue samples:.....	86
5.1.1. Two Pathology Group Training model:.....	88
5.1.2. SVM learning model with a two-pathology group training model	91
5.1.3: Two Group classification model	96
5.1.4: Four group classification model (Gleason grade scoring system)	98
5.1.5: Two Group classification model (Low grade versus high grade tumour)	99
5.1.6: Three Group classification Model.....	102
5.1.7: Four Group classification Model (Gleason grade group scoring system)	104
5.1.8: Three Group classification Model (Gleason grade group scores).....	105
.....	106
5.1.9: Four-group classification (Gleason grade group 1, 3, 4 & 5)	110
5.1.10: Five group classification model (Gleason grade group scores).....	111
5.1.11: Comparison between two sets of two-group classification models:.....	112
5.1.12: Partial least square analysis:.....	114
5.2: Serum Spectral analysis:.....	115
5.2.1: Two group pathology training classification model.....	116
5.2.2: Four Group training model:.....	117
5.2.3: Two Pathology Group training classification model: Low versus high grade tumours.....	119
5.2.4: Three Group training classification model.....	120
5.2.5: The two-group pathology classification (after training)	121
5.2.6: Three group classification model.....	134
11.3 Blood Plasma analysis:.....	143
5.3.1: Two Class discrimination Models:	144
5.2.2: Two Group classification model with Low grade versus high grade tumours	150
5.3.3: Three Group Classification model.....	155
.....	163
Chapter 6– Discussion	170
6.0: Contribution to knowledge:.....	170
6:1: Performance of the classification models:	170
6.2: Tissue Samples analysis:	170
6.3: Classification performance for the Liquid biopsy spectra	174
6.4: Plasma Spectral features:	180
6.5: Serum spectral features:	184
6.6: Translation of vibrational Spectroscopy of blood plasma, serum and tissues into clinical practice.....	186
6.7: Conditions for translation into clinical application	187

6.8: Limitations of Raman spectroscopy in clinical applications.....	189
6.9: Clinical Validity:	190
6.10: Clinical utility	191
Chapter 7 – Conclusion.....	192
References	194
Appendices:	206
Appendix A : Ethical approval.....	206
Appendix B: Research Ethics Committee favourable Opinion.....	208
Appendix C : Confirmation of capacity and capability.....	211
Appendix D: Guidance for sponsors and investigators after ethical review.....	213
Appendix E - CONSENT FORM	218
Appendix F: Participant Information Sheet	220
Appendix G -Curriculum Vitae	227
Appendix H: University’s Letter of sponsorship	2
Appendix I: Material Transfer Agreement.....	4

Lists of Figures:

Fig. 1.1: Estimated number of new cancer cases (worldwide) in 2020 for all ages in males (Globocan, 2020).	19
Fig. 1.2: Males related Cancer incidence and mortality patterns in Europe: Estimates for 40 countries and 25 major cancers in 2018 (Ferlay <i>et al.</i> , 2018).....	20
Fig. 2.1 Prostate anatomy. The transverse slice with the highest diameter and therefore, most extensive surface (green line) lies close to the middle cross-sectional plane (blue line) but is shifted towards the prostate base. [image copyright: www.paradoja7.com].....	23
Fig. 2.2. Gleason grade score and Grade group score (Chen N Zhou Q, 2016).....	28
Fig. 2.3: Schematic diagram showing the use of HIFU in tumour therapy (Izadifar Z et al 2020).....	32
Fig. 3.1. Schematic presentation of How Raman spectroscopy signal are generated and the subsequent spectrum acquisition. Plot reprinted with permission from {J. Phys. Chem. C, 2011, 115 (46) pp 22761 - 22769}. Copyright {2011} American Chemical Society)	45
Fig. 3.2: Schematic diagram showing Light beam absorption and scattering by a tissue. A. Both absorption and scattering occur here. Common with the NIR light source interactions. B. Mostly absorption occur here. Often seen with UV or MIR/FIR interactions. C. scattering is the main attenuation process occurring here. Common with NIR interactions (Ibid, 2015).....	50

Fig. 3.3: The separation of blood plasma from blood cells (https://en.wikipedia.org/wiki/Blood-spinning)	52
Fig. 4.1: InVia Raman Microscope.....	74
https://www.renishaw.com/en/invia-confocal-raman-microscope--6260	74
Fig. 4.2: Prostate biopsy tissues measured by Raman at 5 distinct position.....	75
Fig. 4.3: Dried blood serum with measurement taken from the circular ring on the periphery of the dried sample.	76
Fig 5.1. Flow chart showing the number of tissue samples collected and subsequently used for Raman measurement and histology analysis.....	87
Fig. 5.2: Comparison of the raw data with data corrected with EMSC	88
Fig. 5.3: Plot of Linear discriminant function scores for each spectrum, colour coded according to pathology opinion for the training model for benign (Green) vs cancer (Red). ...	89
Fig. 5.4: Receiver Operating Characteristic curve for a 2 group (benign vs cancer) mean spectral Linear Discriminant model showing an area under the curve of 0.7 and an overall accuracy of 72.6%.	90
Note: class 2 is the positive group which is the cancer group.	90
Fig. 5.5: Confusion matrix for a two group LDA classification model for benign vs malignant (cancer).....	91
Fig. 5.6: Receiver Operating Characteristic curve for a 2 group (benign versus cancer) mean spectral Quadratic SVM model showing an area under the curve of 0.69. the positive class here is the cancer group (class 2).	92
Fig.5.7: Model 3.2 showing the confusion matrix of a Quadratic Support Vector Machine Learning Model for a two-group classification (benign vs cancer).....	92
Fig. 5.8: Difference between benign and malignant tissue spectra measured	93
Fig 5.9: Mean spectra after background subtraction and smooth post Raman assessment (benign versus malignant).	93
Fig. 5.10a: First 12 principal components.....	95
Fig. 5.10b: the next 12 principal components.	95
Fig. 5.11: Receiver Operating Characteristics curve for a two-group classification showing the Area Under the Curve of 0.77 in a LDA model.	96
Fig. 5.12: The confusion matrix of the two-group classification model using a linear discriminant analysis.....	96
Fig. 5.13: Medium Gaussian SVM showing the AUC of 0.82 and the prediction accuracy of 80.....	97

Fig. 5.14: Confusion matrix of a two-group classification model using a Medium Gaussian SVM.....	98
Fig. 5.15: Three-Dimensional Plot of the linear discriminant function of the scores for each class spectrum, colour coded according to the histopathology report following normalization to area under the curve (Benign, GS<7, GS=7, GS>7).	99
Fig. 5.16: Bar chart showing the Raman spectroscopy prediction power of a two group (benign & GS<7 vs GS 7 & >7) with the aid of PC-LDA model with normalisation of the raw data to the area under the curve. The green bars represented the low-grade tumour -class 1 (GS = benign & <7), Red bars represent the high-grade tumour – class 2 (GS = ≥7).....	100
Fig. 5.17: Two group classification LDA (benign & GS<7 vs GS 7 & >7) with the aid of PC-LDA model with normalisation of the raw data to the area under the curve and a 5-fold cross validation model showing the AUC of 0.65 and overall accuracy of 61.9%.....	101
Fig. 5.18: A confusion matrix for a two-group classification model (benign & GS<7 vs GS 7 & >7) with the aid of PC-LDA model with normalisation of the raw data to the area under the curve.	102
Fig. 5.19: Plot of the linear discriminant function of the scores for a three-group classification model using LDA for the Gleason risk stratification groups (benign + <7, 7 & >7). Each class spectrum were colour coded according to the histopathology report.	103
Fig. 5.20: Plot of the linear discriminant function of the scores for a four-group classification model using LDA for the Gleason grade group scores. Each class spectrum were colour coded according to the histopathology report.	104
Fig. 5.21: Plot of the linear discriminant function of the scores for a three-group classification model using LDA for the Gleason grade group scores with spectra from Gleason grade group 4 merged with 5.	106
Fig. 5.22: Three group classification LDA and a 5-fold cross validation model showing the AUC of 0.73 and overall accuracy of 52.5% (Gleason 7, <7 & >7).....	107
Fig. 5.23: A confusion matrix of a three-group classification LDA and a 5-fold cross validation model showing the AUC of 0.73 and overall accuracy of 52.5% (Gleason 7, <7 & >7)	108
Fig. 5.24: Three group classification Quadratic SVM and a 5-fold cross validation model showing the AUC of 0.79 and overall accuracy of 64.6% (Gleason 7, <7 & >7).	109
Fig. 5.25: Confusion matrix of a three-group classification using Quadratic SVM and a 5-fold cross validation model (Gleason 7, <7 & >7).....	109
Fig. 5.26: Plot of the linear discriminant function of the scores for a four-group classification model using LDA for GG1, GG3, GG4 & GG5.	110

Fig. 5.27: Plot of the linear discriminant function of the scores for a five-group classification model using LDA for the Gleason grade group scores (GG1, GG2, GG3, GG4 & GG5) spectra.111

Fig. 5.28: Bar chart showing the Raman spectroscopy prediction power of a two group (benign vs cancer) with the aid of PC-LDA model with normalisation of the raw data to the area under the curve.....112

Fig. 5.29: Bar chart showing the Raman spectroscopy prediction power of a two group (benign & GS<7 vs GS 7 & >7) with the aid of PC-LDA model with normalisation of the raw data to the area under the curve.....113

Fig. 5.30: Partial Least squares regression of the PSA showing a RMSEP of 7.3840114

Fig. 5.31: Spectral differences between benign and cancer from the raw data after histology assessment was carried out.116

Fig. 5.32: Bar chart showing the training classification model for two pathology groups (benign vs cancer) with the aid of PC-LDA model.116

Fig. 5.33: Training classification model showing a 3-Dimensional (3D) Plot of the linear discriminant function of the scores for each class spectrum (Benign, GS<7, GS=7, GS>7). 118

Fig. 5.34: Bar chart showing the Raman spectroscopy prediction power of a two group (low risk vs intermediate and high-risk tumours) with the aid of PC-LDA model.....119

Fig. 5.35: Plot of the linear discriminant function of the scores for a three-group training classification model using LDA for the Gleason risk stratification groups (benign + Gleason <7, 7 & >7).120

Fig. 5.36: Two group classification LDA and a 5-fold cross validation model showing the AUC of 0.78.....121

Fig. 5.37: Confusion matrix used to evaluate the performance of the LDA model as classification model of the group (Low-grade tumours versus intermediate and high-grade tumours).....122

Fig. 5.38 The confusion matrix of a two-class prediction model showing the true positive and false negative rates low grade versus intermediate & high-grade tumours.123

Fig. 5.39: The confusion matrix of a two-class (low grade versus intermediate & high-grade tumours) prediction model showing the positive predictive value and false discovery rates. 124

Fig. 5.40: Receiver Operating Characteristic curve with a five-fold leave one out cross validation for a 2 group mean spectral (low grade versus intermediate and high-grade tumours) cubic SVM model showing an area under the curve of 0.97 with an overall accuracy of 94%.....125

Fig. 5.41: Confusion matrix for a 2 group SVM classification model (Benign / GS = <7 VS GS7 / GS = >7).	126
Fig. 5.42: Confusion matrix for a 2 group SVM classification model (Benign / GS = <7 VS GS7 / GS = >7).	127
Fig. 5.43: Confusion matrix for a 2 group SVM classification model (Benign / GS = <7 VS GS7 / GS = >7).	127
Fig. 5.44: Two group classification LDA and a 5-fold cross validation model showing the AUC of 0.81 (Gleason grade group score of (1, 2, 3) vs (4 &5)).	128
Fig. 5.45: Confusion matrix for a 2 group LDA classification model (Gleason grade group score of (1, 2, 3) vs (4 &5)).	129
Fig. 5.46: Confusion matrix for a 2 group LDA classification model.	129
Fig. 5.47: Confusion matrix for a 2 group LDA classification model showing positive predictive values and false discovery rates for class 1 and 2.	130
Fig. 5.48: Two group classification (Low grade vs high grade tumours) Support vector machine and a 5-fold cross validation model showing the AUC of 0.98 with overall accuracy of 94.6%.	131
Fig. 5.49: Confusion matrix for a 2 group SVM classification model	132
Fig. 5.50: Confusion matrix for a 2 group SVM classification model showing True positive and false negative rates.	132
Confusion matrix for multiple classes calculations and interpretation:	133
Fig. 5.51: Three group classification (Low grade vs high grade tumours) LDA and a 5-fold cross validation model showing the AUC of 0.80 with overall accuracy of 64.6%.	134
Fig. 5.52: Confusion matrix with absolute values for a three-group discrimination with the aid of LDA model.	135
Fig. 5.53: Confusion matrix for a three-group discrimination with the aid of LDA model showing True positive rates and False negative Rates.	136
Fig. 5.54: Confusion matrix for a three-group discrimination with the aid of LDA model showing positive predictive values and False discovery rates.	137
Fig. 5.55: Three group classification (benign vs Low grade vs high grade tumours) Support vector machine and a 5-fold cross validation model showing the AUC of 0.98 with overall accuracy of 93.2%.	138
Fig. 5.56: Confusion matrix for a 3 group SVM classification model	139
Fig. 5.57: Confusion matrix for a 3 group SVM classification model	140
Fig. 5.58: Confusion matrix for a 3 group SVM classification model	141

Fig. 5.59: The spectral features used for discrimination.	142
Fig. 5.60: Spectra difference between benign and cancer serum samples with peak assignment.	142
Fig. 5.61: Spectral differences between the low Gleason score (mean) and high Gleason score (mean).	143
Fig. 5.62: Showing the separation between the mean spectra of the benign and the malignant samples.	144
Fig. 5.63: Two class discrimination using PC-LDA with an AUC of 0.74 (threshold 0.49, 0.80). Low grade versus high grade tumour spectra.	145
Fig. 5.64: Confusion matrix of the LDA classification model showing class 1 (benign & Gleason <7) and class 2 (Gleason 7 & >7).	145
Fig. 5.65: Showing the Positive predictive values and False discovery rates for the two classes (Low grade vs high grade).	146
Fig. 5.66: Showing the True positive rates (sensitivity) and False Negative rates for two classes (low grade vs high grade).	147
Fig. 5.67: Support Vector machine learning algorithm for a two class (benign + Gleason <7 versus Gleason 7 & >7) discrimination model showing an AUC of 0.98.	148
Fig. 5.68: The confusion matrix for a two class SVM model demonstrating the true positive and negative (green) and false positive and negative (pink) respectively.	149
Fig. 5.69: The confusion matrix for a two class (Benign + < Gleason 7 vs Gleason ≥7) SVM model demonstrating the true positive rates and false negative rates (red) respectively.	149
Fig. 5.70: The confusion matrix for a two class SVM model showing positive predictive values and false discovery rates respectively.	150
Fig. 5.71: Receiver operating characteristic curve showing an AUC of 0.69 in a two-group classification LDA model for low grade versus high grade tumours (Gleason grade group scores).	151
Fig. 5.72: Confusion matrix showing the true positive and false positives as well as the true and false negatives for Gleason 1,2 & versus Gleason 4 & 5 using LDA classification model.	152
Fig. 5.73: Confusion matrix showing the true positive and false positives rates for Gleason 1,2 & 3 versus Gleason 4 & 5 using LDA classification model.	152
Fig. 5.74: Receiver operating characteristic curve showing an AUC of 0.98 in a two-group classification SVM model for low grade versus high grade tumours (Gleason grade group scores 1, 2, & 3 vs 4 & 5).	153

Fig. 5.75: Confusion matrix with correct prediction in green while false prediction in pink for Gleason 1,2 &3 versus Gleason 4 & 5 using SVM classification model.	154
Fig. 5.76: Confusion matrix showing the true positive and false positives rates for Gleason 1,2 & 3 versus Gleason 4 & 5 using SVM classification model.	154
Fig. 5.77: Receiver operating characteristic curve showing an AUC of 0.68 in a three-group LDA classification model for benign, low grade & high-grade tumours.	155
Fig. 5.78: Confusion matrix showing correct (green) and false (pink) predictions for benign, low-grade, and high-grade tumours using LDA classification model.	156
Fig. 5.79: Confusion matrix showing the true positive rates and false negative rates for discrimination into benign, low-grade, and high-grade tumour classes using LDA classification model.	157
Fig. 5.80: Confusion matrix showing the positive predictive values and the false discovery rates for the three group LDA classification model.	158
Fig. 5.81: Receiver operating characteristic curve showing an AUC of 0.98 in a three-group SVM learning classification model for benign, low grade & high-grade tumours.	159
Fig. 5.82: Confusion matrix for a three-group pathology showing the true positive and false positives SVM classification model.	160
Fig. 5.83: Confusion matrix for a three-group pathology showing the true positive and false negative rates with the aid of SVM classification model.	161
Fig. 5.84: Confusion matrix showing the positive predictive values and the false discovery rates for the three group SVM learning classification model.	162
Fig. 5.85: Linear discriminant functions of the spectral features used for discrimination.	163
Fig. 5.86: Mean spectral differences between benign and cancer samples (Plasma).	163
Fig. 5.87: Spectral difference between the low- and high-grade tumours (plasma).	164
Fig. 6.1: Spectral assignment for benign minus cancer plasma data.	181
Fig. 6.2: Spectral assignment after subtraction of mean spectral intensity of high Gleason scores from the low Gleason scores.	182
Fig. 6.3: Mean plasma spectra for benign and cancer groups.	183
Fig. 6.4: Mean plasma spectral differences between low Gleason scores and high Gleason scores.	183
Fig. 6.5: Mean serum spectral difference between benign and cancer.	184
Fig. 6.7: Mean serum spectra of low Gleason scores and high Gleason scores.	185

Lists of Tables:

Table 4.1: Prostate biopsy Processing Schedule	83
Table 5.1a. Table showing the training classification performance for benign vs Cancer	89
Table 5.2a: Training classification in a three-group PC-LDA model with Gleason <7, 7 & >7 with histology versus Raman predictions.....	104
Table 5.2b: Showing the training classification performance in a three-group PC-LDA model with Gleason <7, 7 & >7.	104
Table 5.3a: Showing the training classification performance for Raman versus histology in a four-group PC-LDA model with Gleason grade group 1, 3, 4 & 5.....	105
Table 5.3b: Showing the training classification performance in a four-group PC-LDA model with Gleason grade group 1, 3, 4 & 5.	105
Table 5.4a: Raman prediction accuracy against histology in a three-group PC-LDA model with Gleason grade group 1, 3 & 4+5.....	106
Table 5.4b: Showing the training classification performance in a three-group PC-LDA model with Gleason grade group 1, 3 & 4+5.	106
Table 5.5a: Raman prediction against histology prediction in a 4-group model	110
Training Classification Performance	110
Table 5.5b: Showing the training classification performance in a four-group PC-LDA model with Gleason Grade Group score 1, 3, 4 & 5.....	110
Table 5.6a: Raman prediction accuracy against histology predictions for a 5-group training model.	111
Table 5.6b: Showing the training classification performance in a five-group PC-LDA model with Gleason grade group score 1-5.....	111
Table 5.7a: Raman prediction accuracy against histology in a 2-group training model.....	113
Table 5.7b: Showing the training classification performance in a two-group PC-LDA model with benign versus malignant tumours.	113
Table 5.8a: Raman prediction accuracy against histology in a two-group model (low grade versus high grade tumours.	114
Table 5.9a: Raman prediction accuracy against histology in a two training PC-LDA model in blood serum samples.....	117
Table 5.9b: Showing the training classification performance in a two-group PC-LDA model with benign versus malignant tumours.	117

Table 5.10a & b: Showing the training classification performance in a four-group PC-LDA model with Benign, GS <7, GS =7, GS >7.....	118
Table 5.11a & b: Showing the training classification performance in a two-group PC-LDA model with low-risk vs intermediate / high risk tumours.....	119
Table 5.12a: Showing the training classification performance in a three-group PC-LDA model with Gleason Risk stratification scores using blood serum samples.	120
Table 5.12b: Showing the training classification performance in a three-group PC-LDA model with Gleason Risk stratification scores using blood serum samples.	121
Table 5.13: Two Group classification: Benign vs Malignant (Tissues)	164
Table 5.14: Two Group classification: Low-grade tumour vs High-grade tumour (Tissues) ..	165
Table 5.15: Three-Group classification: Predominant 3g (Tissues).....	165
Table 5.16: Two-group Classification model: Low-grade versus high-grade tumours.....	166
Table 5.17: Predominant 2 groups: Low-grade versus high-grade tumours.....	166
Table 5.18: 3-group classification model: Benign, low-grade versus high-grade tumours	167
Table 5.19: 2-group classification mode: Benign + low-grade versus high-grade tumours ...	167
Table 5.20: Low-grade versus high-grade (2 Group classification model).	168
Table 5.21: 3-group classification model (benign versus low-grade versus high grade tumours).....	168
Table 5.22 : Calculation of sensitivity, specificity, positive and negative predictive values ...	169

Chapter 1 -Introduction

Prostate cancer is one of the most frequently diagnosed cancers globally. It accounts for 7.1% of all cancers affecting men globally. In the United States of America and the United Kingdom (UK), for instance,

it is the second most commonly diagnosed cancer after melanoma skin cancer. In the UK, 47,500 men are diagnosed annually with this disease condition. Therefore, suggesting that 129 men are diagnosed with this condition daily throughout the UK. One in every eight men in the UK is diagnosed with prostate cancer. It is also the third leading cause of cancer death globally. The mortality rate of this disease has increased, with at least one man recorded to die from prostate cancer every 45 minutes in the UK. There are about 11.500 deaths In the UK yearly due to prostate cancer. A worldwide assessment of new cancer cases was conducted in 2020, and prostate cancer contributed to about 14.1% of the population of all new cases of male-related cancers for all ages. As demonstrated in figure 1.1 below.

Estimated number of new cases in 2020, worldwide, males, all ages

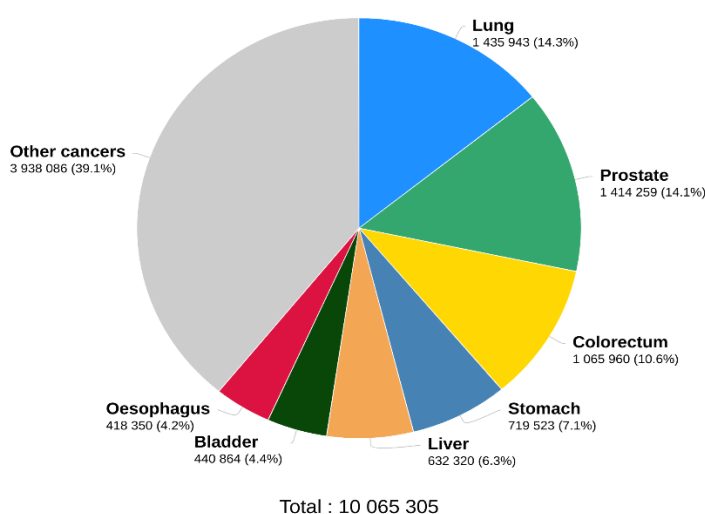


Fig. 1.1: Estimated number of new cancer cases (worldwide) in 2020 for all ages in males (Globocan, 2020).

When prostate cancer incidence was analyzed based on age standardization rate from country to country, France and Guadeloupe had the highest figures with 189.1 per 100,000 people. Bhutan recorded the lowest incidence of 1.0 per 100,000 people (Ferlay et al., 2019).

The incidence and mortality rates of prostate cancer are closely related to increasing age, with men below 40 having recorded very low incidence and mortality rates. The mean age at the time of diagnosis

of prostate cancer is around 66 years globally. Globally, the incidence of men with prostate cancer is 1 in every 350 men under the age of 50 years (Ibid, 2019). However, the rate of incidence has been shown to increase quite significantly after the age of 50. Between 50 and 59, this disease is about 1 in every 52 men, with a higher incidence for men over 65.

Globally, prostate cancer accounts for 21.8% of all cancer incidences in men. Nevertheless, the mortality rate is only 10%, meaning that most men can live with prostate cancer for the rest of their lives if the tumor is indolent.

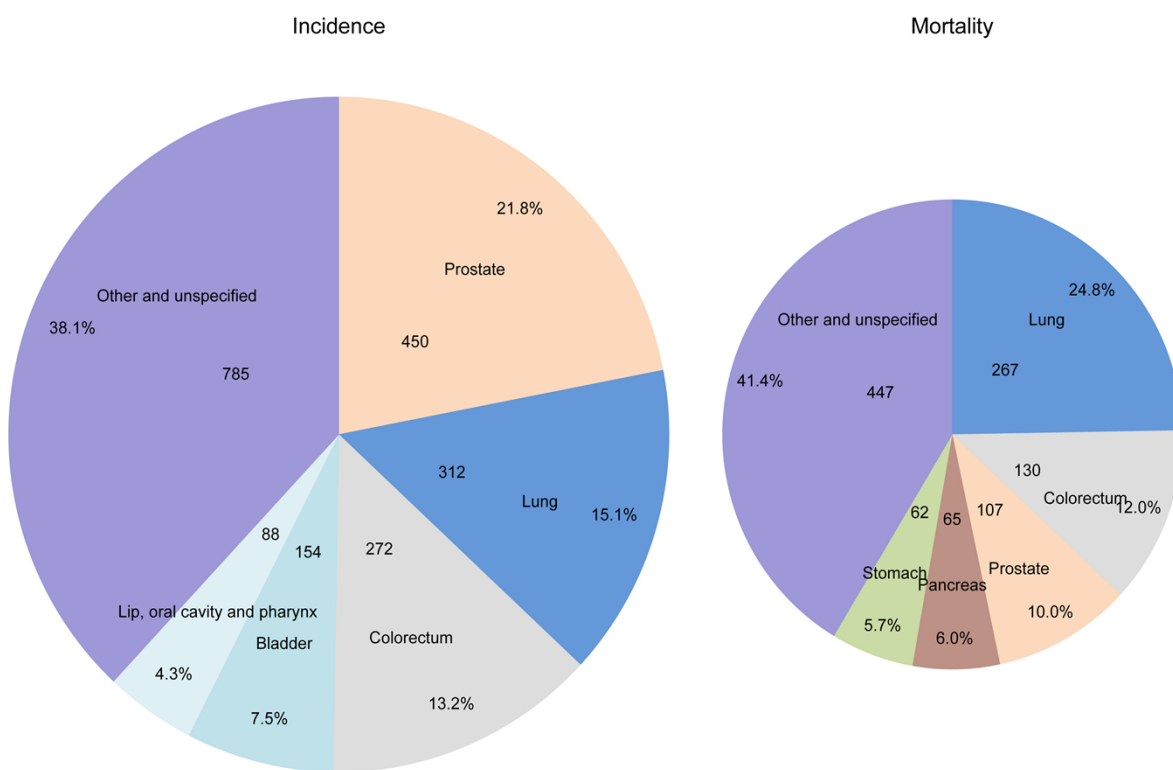


Fig. 1.2: Males related Cancer incidence and mortality patterns in Europe: Estimates for 40 countries and 25 major cancers in 2018 (Ferlay et al., 2018).

With the available statistics, one can safely infer that this disease condition has recently become a public health concern worldwide. Therefore, there is a need to investigate and explore better diagnostic tools to assist in early diagnosis and risk stratification of prostate cancer. A correlation of molecular biomarkers with the Gleason Scoring system is necessary for classifying biopsies and blood samples from patients on surveillance (Prostate Cancer UK, 2013).

The primary aim of this study was to measure blood plasma with Raman spectroscopy from individuals referred to a prostate biopsy clinic for suspected prostate cancer. Biomarkers measured in the Raman spectra correlated with the PSA and the stage and grade of disease found.

Secondly, it was also necessary to ascertain the usefulness of Raman Spectroscopy as a minimally invasive diagnostic tool in assessing real-time, molecular-specific fingerprints of prostate diseases.

The objective was to provide a more accurate prediction of prostate cancer's presence and progression than PSA, enabling blood sample triage of patients into at-risk groups for further investigation.

The lack of reliable assays to identify tumours destined to remain indolent has contributed to overtreatment and permanent side effects of treatment for those slow-growing or self-limiting tumours that would not cause problems for the patient during their lifetime (Kelloff G.J et al., 2009).

The practice of watchful waiting (which involves no treatment or specific program of monitoring with the plan that palliative treatment would be used if a progressive disease condition develops) and active surveillance are alternatives to the overtreatment of indolent tumours with potential side effects.

The main benefit of watchful waiting and active surveillance is that it minimizes the severe side effects of urinary incontinence and impotence associated with surgery and radiation therapy. However, the disadvantage of active surveillance is that it may miss the window of opportunity for early intervention when tumours that seem indolent turn out to be aggressive.

Prostate Specific antigen is present in small quantities of blood serum of men with a healthy prostate. However, it is often elevated in the presence of prostate cancer or other prostate disease conditions. The reliability of this screening tool has been called to question in recent times due to its low sensitivity. Many countries, such as the United Kingdom, have not adopted PSA as a widespread screening tool for the early detection of prostate cancer. Since there is no other reliable assay for the early detection of prostate cancer and disease progression, it remains the first line of an assay for prostate cancer detection.

This thesis will seek to address some of the problems encountered during prostate cancer screening and diagnosis to suggest a more accurate diagnostic tool that can be utilized as an addition to existing ones in managing prostate cancer. Therefore our research questions will be:

Firstly, can Raman spectroscopy provide a more accurate prediction of the presence and progression of prostate cancer than PSA and allow blood sample triage of patients into at-risk groups?

Secondly, can Raman spectroscopy of prostate tissue provide molecular signatures that may be used for real-time in vivo analysis?

Chapter 2 – Background

Prostate cancer has been shown in the previous chapter as one of the leading causes of cancer death among men, with an increased mortality rate and incidence among those advanced in the age above 50 years. The lack of reliability of the available screening and diagnostic tools has therefore brought about the need to investigate new approaches that will assist in the early detection and characterization of this disease condition. In this chapter, we will endeavour to examine prostate anatomy, physiology, and histology. After that, prostate cancer and some pre-cancerous conditions related to the prostate gland will be discussed. The Gleason grading system and the current diagnostic pathways, including the gold standard technique for diagnosis of prostate cancer and prostate-specific antigen, will follow subsequently.

2.1. Anatomy, Physiology and Histology

The prostate gland is a firm, elastic gland with the shape of an inverted pyramid located at the base of the urinary bladder and is the size of a walnut (Amis, 1994). Five prostatic ducts derived from the urogenital sinus are found within the prostate gland, which helps divide the prostate into five distinct lobes (the anterior, middle, posterior, left, and right lateral lobes) (Ibid, 1994).

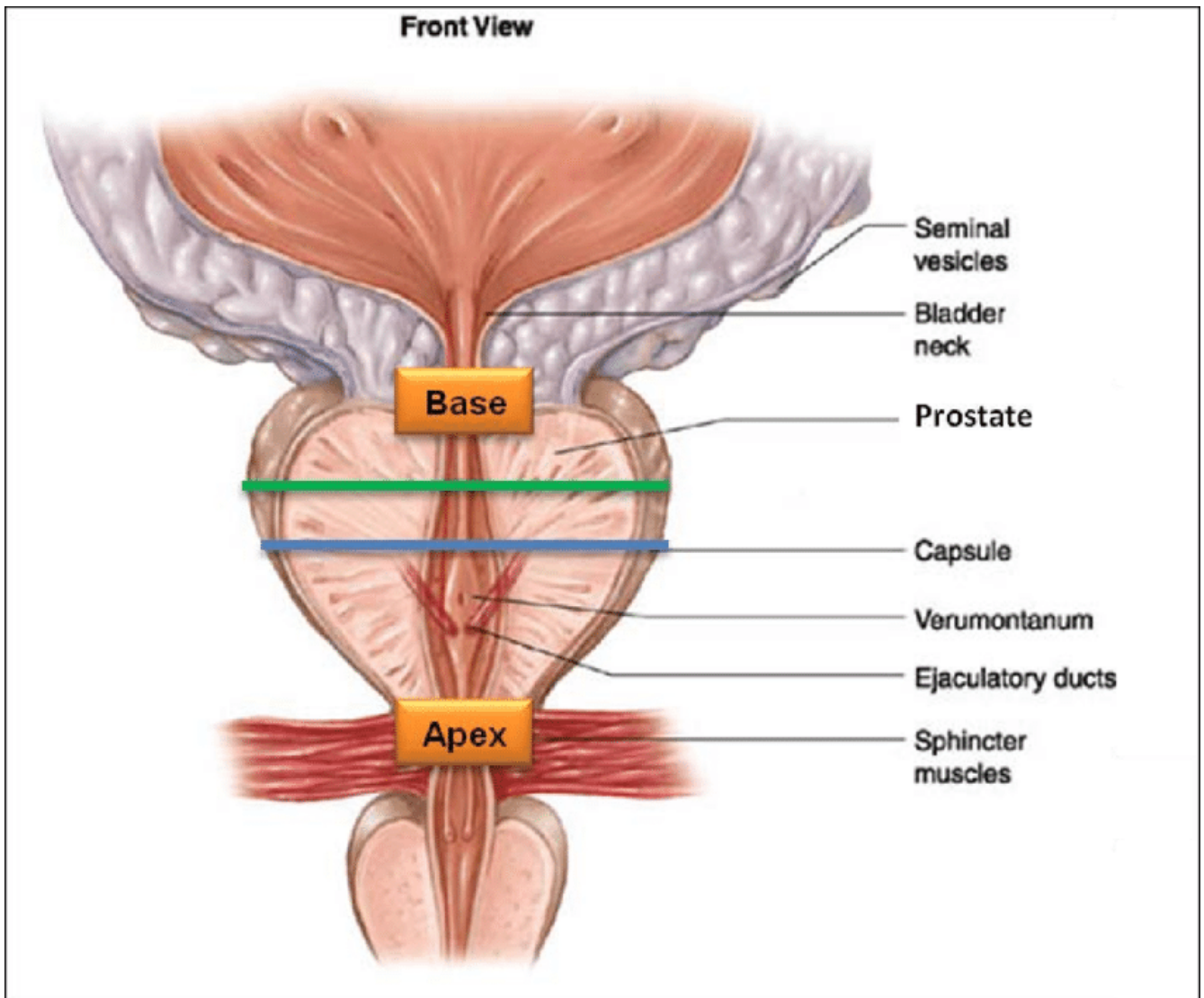


Fig. 2.1 Prostate anatomy. The transverse slice with the highest diameter and therefore, most extensive surface (green line) lies close to the middle cross-sectional plane (blue line) but is shifted towards the prostate base. [image copyright: www.paradoja7.com]

The prostate base is attached urinary bladder neck, and the prostatic urethra passes through the middle of it, as shown in figure 2.1 above. The apex is the lower and narrow part of the prostate, which is covered by the anterior fibromuscular stroma. The apex contacts the superior fascia of the urogenital diaphragm and the medial surface of the levator ani muscle. The posterior surface of the prostate is triangular and flat and is in contact with the anterior wall of the rectum. The inferior-lateral surface meets the anterior surface as it rests on the levator ani fascia superior to the urogenital diaphragm. A thin filmy connective tissue known as Devillier's fascia demarcates the prostate and seminal vesicles from the rectum (Aaron LT et al., 2016).

John McNeal divided the prostate into three main areas based on histological and anatomical composition. This non-glandular fibromuscular stroma engulfs the gland and the two glandular zones, the peripheral and central zones (McNeal, 1981).

The peripheral zone comprises about 70% of the glandular tissue. It engulfs the distal urethra and spans from the apex to the base found in the posterior surface of the gland. Ductal and acinar elements and very few interwoven smooth muscles are located in the peripheral zone. Hence, the T2 Weighted MRI sequence is often observed as having a high signal intensity. Cancer, chronic prostatitis, and post-inflammatory atrophy are usually seen in this zone compared to other zones.

The central zone is a cone-shaped structure made up of 25% of the glandular tissue and situated between the peripheral and transition zone. It engulfs the ejaculatory ducts and narrows to an apex at the verumontanum. The verumontanum is a rounded eminence of the urethral crest within the posterior wall of the mid-prostatic urethra, where the ejaculatory ducts enter the urethra. Urologists utilize it as a surgical landmark during TURP to locate the urethral sphincter (McNeal, 1981).

The transition zone is made up of 5% of the glandular tissue. Essentially, two small glandular lobules of tissue engulf the proximal prostatic urethra immediately above the verumontanum. BPH often occurs within the transition zone (Ibid, 1981).

The transition zone is often seen as nodular areas of different signal intensities depending on the relative proportion of the glandular and stromal enlargement (Ibid, 1981). Because there are more ductal and acinar components and secretions within the epithelial hyperplasia, it is often seen on the T2 Weighted MRI sequence as an area of high signal intensity. Since there are more fibrous and muscular components within the stromal hyperplasia, lower signal intensity is often observed in the regions with stromal hyperplasia on T2 Weighted MR imaging.

2.2. Prostate Cancer:

Tumours in the prostate gland start with a mutation in the normal glandular cells, especially in the peripheral basal cells. About 75% of all prostate cancers are found within the peripheral zone, which could be palpable by physicians during Digital Rectal Examination (DRE). It is common to see growth and multiplication and the spread of the cancerous cells within the prostate gland. These cells could

sometimes grow such that the prostatic capsule is broken, resulting in extracapsular extension of the tumour. Some tumours in the prostate are organ-confined, while some could spread to the surrounding tissues, such as lymph nodes, or other distant organs, such as the liver and bones. Several features could easily demonstrate the presence of cancerous cells within the prostate tissue.

The infiltrative glandular growth pattern of abnormally enlarged cell nuclei with prominent nucleoli and the presence of high-grade Prostatic Intraepithelial Neoplasia could also indicate that some cancerous tissue may be present within the prostatic gland (Ibid, 2003). The extracapsular extension has shown a minimal correlation with disease aggression (Ibid, 2003). Absent basal cell membrane alongside increased mitotic figure, intraluminal crystalloids, and amphophilic cytoplasm are some of the possible malignant features (Ibid, 2013)

2.3. Pre- Cancers:

2.3.1. High grade Prostatic Intraepithelial Neoplasia (High grade PIN)

PIN refers to the proliferation of glandular epithelium that shows critical structural abnormality with the prostatic ducts and acini (Zhou M, 2018). A PIN is not often detectable by DRE, and it does not result in an elevated PSA level either. Cells of high-grade PIN often present with prominent nucleoli with severe pleomorphism. Some researchers have shown a 25% chance of detecting prostate cancer in patients during a repeat biopsy following a previous diagnosis of high-grade PIN at an initial biopsy (Ibid, 2018). It has been well-established as pre-cancerous growth and is often seen in 5% of prostate biopsies and some radical prostatectomy specimens (Ibid, 2018). Greater prevalence is observed among the black population as compared to Caucasians. When High-grade PIN is seen in more than one core biopsy, it is recommended that a re-biopsy is carried out within six months with increased sampling of the affected site and adjacent area. However, if only one core biopsy is found with High-grade PIN, the decision for re-biopsy is often based on the potential risk using clinical, radiological, and laboratory findings. It is suggested that no treatment is needed for high-grade PIN whose diagnosis has been established only by biopsy alone (Zhou M, 2018).

2.3.2. Proliferative Inflammatory Atrophy (PIA)

Proliferative inflammatory atrophy (PIA) is a lesion in the prostate gland of glandular atrophy, chronic inflammation, and epithelial hyperplasia (Angelo M et al., 1999). Prostatic atrophy is often seen as a decline in the volume of the already existing glands and stroma. Diffused and focal atrophy are the two main types of atrophy (De Marzo AM et al., 1999). In contrast, a diffused atrophy involves a uniform

decrease in the circulating androgens and the entire prostate. Focal atrophy, on the contrary, is not related to circulating androgens. It often occurs as patches of atrophic epithelium within the background of surrounding normal-appearing non-atrophic epithelium (Ibid, 1999). Focal atrophies are usually seen within the peripheral zone of the prostate gland and increase in frequency with advancing age. Some researchers believe that PIA occurs following a process of infection; toxins or some other factors could cause the epithelial tissues in the prostate to become small or inflamed.

Furthermore, the cell in the affected area begins to multiply at a faster rate than the normal cells. Although PIA is a benign condition, it sometimes tends to undergo malignant transformation. Therefore it is sometimes referred to as a pre-cancerous lesion (Celma A et al., 2014). Due to its genetic instability, it can sometimes degenerate into either PIN or carcinoma. The imbalance between proliferation and apoptosis and subsequent molecular-biological abnormalities relevant to oxidative stress or malignancy could be responsible for this assertion. Cancer development entails a recurrent impairment of tissue and resurgence amid highly reactive oxygen and nitrogen species. These reactive molecules, such as H₂O₂ and nitric oxide (NO), are often released from the inflammatory cells and can interact with DNA in the proliferating epithelium to produce permanent genomic changes such as mutations, deletion, and rearrangement (De Marzo AM et al., 1999).

Although some authors believe there is no association between PIA and PIN, inflammation is often connected with atrophic epithelia, resulting in increased proliferation and reduced apoptosis compared to normal epithelium. PIA is often seen associated with less aggressive and clinically insignificant tumours.

2.3.3. Atypical Small Acinar Proliferation (ASAP)

Atypical small acinar proliferation focuses on small acinar structures formed by atypical epithelial cells (Montironi R et al., 2006) having some features of cancer but not all (Koca O et al., 2011). About 5% of needle biopsies have been demonstrated to present with ASAP, according to the histopathological report (Montironi R et al., 2006). ASAP is used to define glands suspicious of adenocarcinoma, which lacks enough evidence of features consistent with the diagnosis of carcinoma (Ibid, 2006). Therefore, this term consists of benign lesions that look like cancerous glandular proliferations and tiny malignancy foci that contain some but not all features consistent with malignancy. Although some researchers have argued that the use of the term ASAP is inappropriate because some urologists still believe that ASAP

is synonymous with high-grade prostatic intraepithelial neoplasia, whereas these are two distinct entities. Secondly, not all ASAP possess small acinar because there are others with large diameter acinar (Ibid, 2006).

Although ASAP is regarded as a high-risk precursor for prostate cancer, the clinical relevance of these lesions is somewhat questionable. There is a 40-50% chance of finding overt prostate cancer on repeat biopsy. Therefore the current European Association of Urology guidelines recommends prostate re-biopsy in all patients with ASAP.

In a consensus meeting in 2004, sponsored by the World Health Organization, the committee members recommended that there was a need to specify if the ASAP is either suspicious or highly suspicious of cancer by the pathologist at the point of making their diagnosis (Koca O et al., 2011). The cancer detection rates at repeat biopsies have been known to vary between 21% and 51%. Targeting the repeat biopsy to the area where ASAP was detected in the previous biopsy had been advised (Koca O et al., 2011).

2.4. Gleason grading system

The Gleason grading system has been utilized extensively to determine the degree of aggressiveness of the tumour. A handy tool (to a large extent) in predicting the prognosis of the disease. It has been well established that the higher the Gleason score, the higher the propensity for the tumour to grow and metastasize. Gleason's score ranges from 1 to 5, which informs us of how much the cancer cells differ from the normal cells, as demonstrated in figure 2.2 below. More often than not, two grades are assigned per patient. While the first score is given to the most common cell morphologically, the second score is usually given to the next dominant cell. It is also possible to have three patterns in which the first score is regarded as the primary pattern while the second is taken as the pattern with the highest grade. For example, if the primary pattern is two and the second grade is three, there is a tumour pattern of 4. Then the Gleason score would be $2+3=5$. The combined Gleason score ranges between 2 and 10, with the higher numbers indicating a high chance of mortality and a poor outcome for the patient. A Gleason score of 2 is regarded as a well-differentiated tumour, while those with a score closer to 10 are generally regarded as poorly differentiated tumours. Well-differentiated tumours are often low-grade tumours. Intermediate-grade tumours are moderately differentiated, while high-grade tumours are often referred to as poorly differentiated tumours.

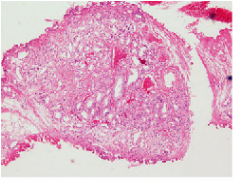
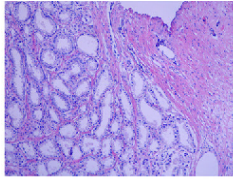
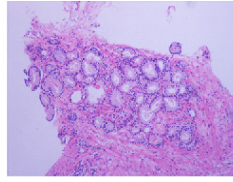
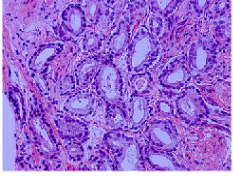
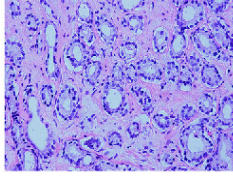
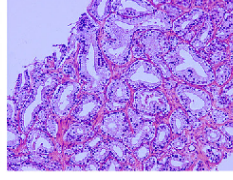
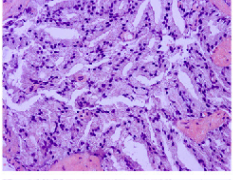
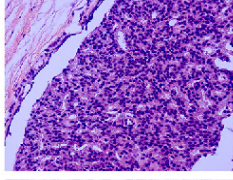
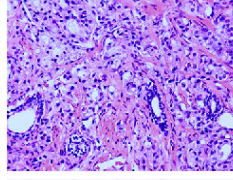
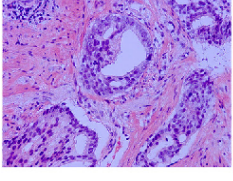
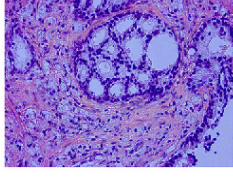
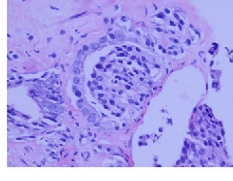
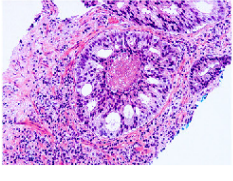
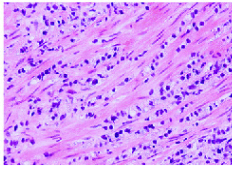
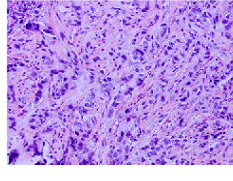
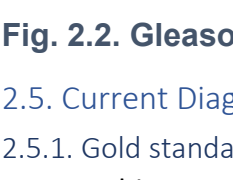
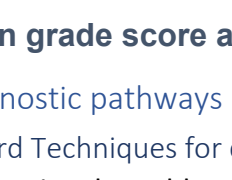
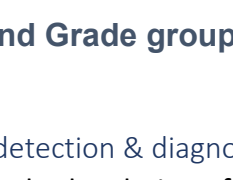
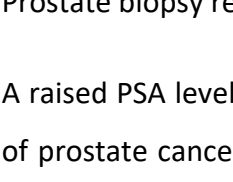
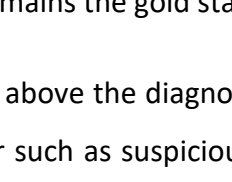
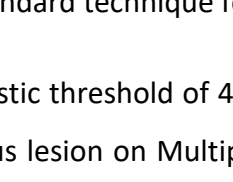
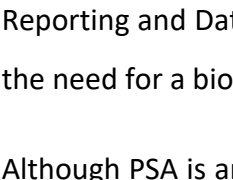
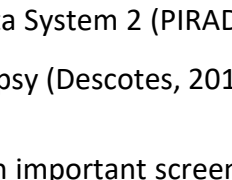
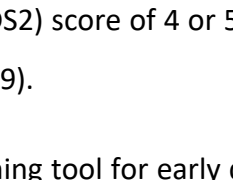
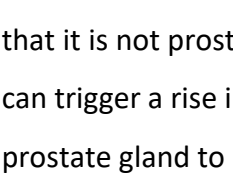
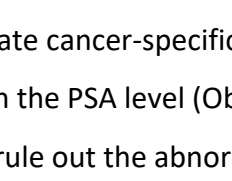
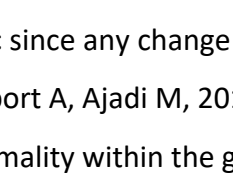
			Gleason patterns 1–3 distinct, discrete, individual glands	Gleason score ≤ 6	Grade group I
					
			Gleason pattern 4 fused, cribriform, or poorly-formed glands, or glomerularion	Gleason score 3+4=7	Grade group II
					
			Gleason pattern 4 fused, cribriform, or poorly-formed glands, or glomerularion	Gleason score 4+4=8 3+5=8 5+3=8	Grade group III
					
					
			Gleason pattern 5 comedo necrosis, cords, sheets, solid nests, single cells	Gleason score 4+5=9 5+4=9 5+5=10	Grade group IV
					

Fig. 2.2. Gleason grade score and Grade group score (Chen N Zhou Q, 2016).

2.5. Current Diagnostic pathways

2.5.1. Gold standard Techniques for detection & diagnosis

Prostate biopsy remains the gold standard technique for the detection of prostate cancer.

A raised PSA level above the diagnostic threshold of 4 ng/mL, abnormal DRE, or any clinical suspicion of prostate cancer such as suspicious lesion on Multiparametric MRI (mpMRI) with Prostate Imaging Reporting and Data System 2 (PIRADS2) score of 4 or 5 or family history of prostate cancer will trigger the need for a biopsy (Descotes, 2019).

Although PSA is an important screening tool for early detection of prostate cancer, it has been shown that it is not prostate cancer-specific since any change in the morphology or biochemistry of the gland can trigger a rise in the PSA level (Obort A, Ajadi M, 2013). Clinicians widely utilize DRE in assessing the prostate gland to rule out the abnormality within the gland.

DRE has high interobserver variability and a poor positive predictive value (PPV) for detecting cancer (5-30%). Therefore, it cannot be utilized as a stand-alone screening tool to assess the presence or absence of prostate carcinoma.

Since the screening assays have not been very precise in the early detection of a tumour within the gland, there is a need for precision and objectivity in the clinical workup of the disease condition.

Due to the multifocal nature of this disease condition, imaging techniques have been instrumental in carrying out a total assessment of what goes on within the gland. The advent of the PIRADS2 scoring system (Schaudinn et al., 2019) alongside multiparametric MRI has ensured that both structural and functional assessment of the gland is carried out during imaging sessions. However, the disadvantage of MR imaging concerning prostate cancer diagnosis is that sometimes non-clinically significant tumours are detected during routine imaging (Siddiqui MM et al., 2015). Patients with indolent tumours can survive for the rest of their lives without any disease-specific mortality.

50-76% of all radical retropubic prostatectomy specimens have more than one focus (multifocal).

About three hundred and eight participants who underwent radical prostatectomy were recruited for the study. Two hundred and six participants were recorded to have multifocal prostate cancer, which accounted for 66.9%, which means that about two third of the population had lesions found in more than one location. On the other hand, one hundred and two participants had tumour focus in one area, which accounted for a third of the total population. Furthermore, when the multifocal lesions were assessed closely, 63% had lesions in two locations, while 37% had lesions in three or more areas (Djavan B et al., 1999).

Since these lesions are often multifocal, the process of a random sampling of tissues during a biopsy for histological assessment could mean that many of the lesions are not picked up during the biopsy. However, when tissue samples are harvested, the tissue must be adequately interrogated histologically to determine the disease's grade and the clinical outcome based on the character of the tissue.

2.5.2. Prostate Specific Antigen

Prostate Specific Antigen (PSA) is a screening tool, like a mammogram (breast cancer), targeted at early detection of prostate cancer which could allow for therapeutic interventions with curative intention. Although, there is conflicting information about its benefits in prostate cancer diagnosis. Stamley et al. (1987) showed that PSA was elevated for newly diagnosed prostate cancer and those with advancing

tumour stage. Their group also demonstrated that the PSA level could go undetectable for patients undergoing surgery or radiation therapy. 86% of men with BPH have been shown to have a rising PSA level which shows unequivocally that elevated PSA is not only related to prostate cancer, but some benign conditions could offer a raised PSA level (Stamey TA et al., 1987). Oesterling JE et al. assessed about 101 participants booked for cystoscopy, biopsy, and TURP. Sixty-nine participants were for cystoscopy, and thirty-two were for TURP and prostate biopsy.

Interestingly, there was no significant difference between those participants for flexible, rigid cystoscopy or the control. However, prostate biopsy instantly elevated serum PSA concentration with a median increase of 7.9 ng/mL ($P < 0.0001$). TURP also demonstrated an instant elevation in the serum PSA concentration with a median change of 5.9 ng/mL ($P < 0.001$) (Oesterling JE et al., 1993). The average time necessary for the PSA concentration to return to a stable level post-biopsy was recorded at 15 days for prostate cancer patients. However, for those without prostate cancer, it took about 17 days for the PSA to return to a stable baseline value.

On the other hand, an average of 18 days for patients who underwent TURP was recorded for the PSA level to return to the stable baseline level (Ibid, 1993). A critical assessment of these findings demonstrated almost unequivocally that there was no variation in the PSA level due to either flexible or rigid cystoscopy. However, TURP and prostate biopsy demonstrated an instant elevation in the PSA concentration, which often goes back to a stable state after about three weeks. Nevertheless, in some cases, the PSA level can be seen to remain elevated even up to 4 weeks post prostate biopsy or TURP. Therefore, it is recommended that about six weeks should be allowed after either a prostate biopsy or TURP before another PSA level is obtained to ensure the accuracy of the result (Ibid, 1993).

Men below 40 have been advised not to have the test done unless there are prevailing clinical concerns, such as a previous family history of prostate cancer because this population was seen as a low-risk group. The Prostate Cancer Prevention Trial had shown that men with a PSA value of 4 ng/ml with a normal DRE have a 30-35% risk of having cancer (Thompson IM et al., 2004). There is a significant risk among the population of men with a PSA level of less than four ng/ml as well (Ibid, 2004). Therefore, the American Urological Association (Thompson IM et al., 2004) suggested that a risk calculator should be adopted following suspicion from the PSA level to guide the decision to proceed with a biopsy.

2.5.2.1. Post-treatment Monitoring and PSA Timing

The process whereby a PSA attains an undetectable level following a radical treatment such as radical prostatectomy, radiation therapy, or androgen deprivation therapy is often known as PSA nadir (Fady B. Geara et al., 2017). PSA levels are often utilized to monitor the treatment of prostate cancer patients, especially those with intermediate or high-risk tumours confined to the prostate gland. Baseline PSA is often established before the treatment is commenced. After the treatment, a gradual decline in the PSA levels is usually observed, which often signifies an excellent response to the treatment. After several weeks depending on the therapy (about 4 weeks for surgery), the PSA level reaches its lowest point (Skove SL et al., 2017). However, about a third of prostate cancer patients undergo biochemical recurrence within ten years after surgical intervention. Time to nadir could differ for different therapeutic procedures (Ibid, 2017). A short time to nadir following radiation therapy could mean an increased chance of biochemical recurrence and metastasis (Ibid, 2017).

Nevertheless, following surgery, a long time to nadir could signify the presence of distant metastasis. A commonly accepted definition of biochemical recurrence is a rise in PSA level following curative treatment. For example, a PSA level greater than 0.2 ng/mL after surgical intervention often indicates biochemical recurrence (Ibid, 2017). However, PSA may continue to decrease after radiation therapy for several years before reaching the PSA nadir. Any rise in PSA by 2.0 ng/mL above nadir is often regarded as a biochemical recurrence following radiation therapy (Fady B. Geara et al., 2017). A combination of androgen deprivation therapy and external beam radiation therapy has significantly improved biochemical recurrence, distant disease spread, and mortality rate (Skove SL et al., 2017).

2.6. Ultrasound

Ultrasound uses high-frequency sound waves to create images of the body's internal structures. The transducer delivers the vibrations with a frequency higher than the upper limit of human audible hearing. The ultrasound waves deposit energy as they traverse the tissue. For imaging purposes, the deposited energy is insignificant and does not result in tissue damage. However, during therapeutic procedures such as High-Intensity Focus Ultrasound (HIFU), a large amount of energy is deposited with increased intensity waves, resulting in tissue destruction (Jang HJ et al., 2010). During therapeutic procedures, thermal and cavitation methods are the two methods causing tissue damage (Ibid, 2010). Absorption of ultrasound energy by the tissue converted into heat causes a thermal effect (Ibid, 2010). The temperature in the sonicated tissues rises to a level that causes irreversible tissue damage. Rapid temperature increase can be achieved up to 100°C within a few seconds with each pulse (Ibid, 2010). The cavitation occurs due to the interaction of the ultrasound with the micro-bubbles in the sonicated

tissue. The exchange could cause an oscillation of the micro-bubbles collapse and dispersion of energy which aids the process of tissue ablation. It is important to note that both approaches result in cell damage due to coagulative necrosis, as demonstrated in figure 2.3 below.

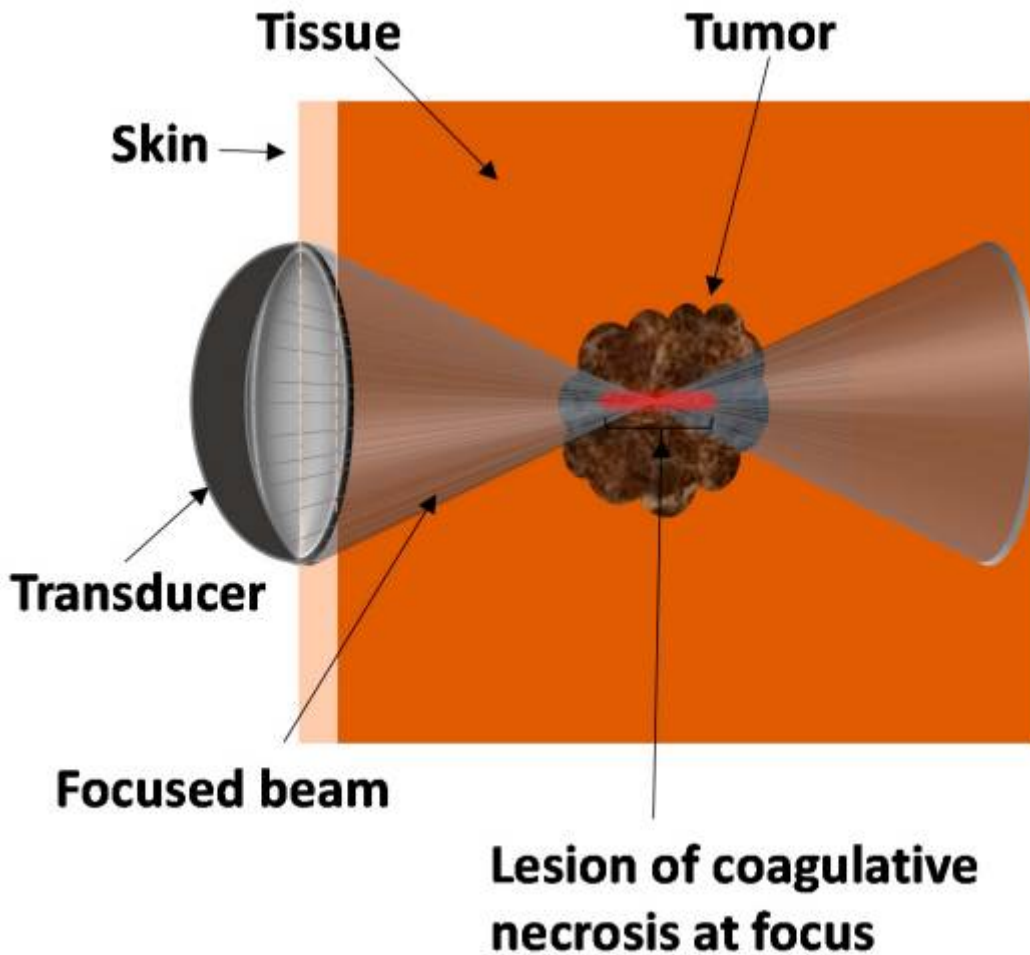


Fig. 2.3: Schematic diagram showing the use of HIFU in tumour therapy (Izadifar Z et al 2020).

HIFU can focus the ultrasound beam and its energy onto a millimeter-size target for treatment purposes (Izadifar Z et al., 2020). Careful utilization of this technique is a non-invasive technique for the treatment of several solid tumours, including prostate, kidney, bones, breast as well as uterine fibroids (Ibid, 2020). Recent advancements in physics, imaging, and biology have improved the precision of focusing the ultrasound beam on deeply seated targets in the body. The ultrasound beam has been shown to focus the beam's intensity at a focal point within a small volume of about 1 mm in diameter and about 10 mm in length (Zhou Y, 2011), which reduces the potential tissue damage away from the focal area.

Thermal tissue damage due to high temperature is linearly related to the length of the exposure but exponentially to the increase in the temperature (Haar G et al., 1991).

2.6.1. Ultrasound in Diagnosis of Prostate cancer

The primary limitation of ultrasound is that about 40% of prostate carcinomas have the same echo texture as the surrounding structures (Pallwein L et al., 2008). Therefore, it is slightly difficult to differentiate this lesion from the surrounding tissues. As a result, cancerous lesions could easily be missed. About 66% of prostate tumours are hypoechoic in texture, and only a third of these hypoechogenic lesions are cancerous. It is, therefore, challenging to rely on the echo texture of the lesion to characterize these lesions, as not all cancerous lesions have the same echotexture. Therefore, the positive diagnostic value of ultrasound as a diagnostic tool is as low as 30-40%. Contrast-enhanced colour Doppler and elastography (Pallwein L et al., 2008) have improved ultrasound sensitivity and specificity in prostate cancer diagnosis. Contrast-enhanced colour Doppler ultrasound aids in assessing prostate blood flow to investigate an area of suspected focal neoplastic proliferation (Ibid, 2008), highlighting that angiogenesis is often observed within the vicinity of cancerous growth. Comparison between systematic and contrast-enhanced targeted biopsies have demonstrated that the targeted approach can depict more cancers, especially those with high Gleason scores (clinically significant cancers). Therefore, reducing the number of core biopsies taken.

Ultrasound elastography can map the tissue stiffness of the prostate gland. Prostate cancer tissue is harder in texture than normal tissues (Correas JM et al., 2013). It helps improve the sensitivity of ultrasound as a diagnostic tool for prostate cancer by measuring the tissue elasticity during TRUS. Tissues with cancerous cells have been shown to tend to have a higher cell density and therefore are stiffer than the normal tissues (Correas JM et al., 2013).

Some sonographic features could indicate the infiltration of cancerous tissues into the prostate capsule. These features include blurring the image, tearing off its integrity, and lifting the capsule. These features could be an indication of extracapsular extension. Neurovascular bundle invasion could be seen as a thickening of the bundle and a poor or not visible flow. At the same time, the seminal vesicle invasion could also be seen as an asymmetry, an enlargement of the anteroposterior dimension over 1.5 cm of their solid structure. The blurring of the angles between the vesicles and the prostate base and the displacement of the seminal vesicles to the front such that the distance from the rectal wall is greater than 1 cm (Pallwein L et al., 2008).

2.7. Computerized Tomography

One of the primary roles of Computed tomography (CT) is the assessment of the involvement of lymph nodes in prostate cancer spread and the presence of extracapsular extension. Lymph node metastasis has been established as an indication for assessment of biochemical recurrence (BCR) free survival. However, this modality lacks sensitivity for early disease detection. Some recent studies have shown a sensitivity of about 35% (De Visschere P et al., 2010). CT has minimal use in detecting tumours confined within the prostate gland except for high-risk patients with clinically apparent advanced disease. Therefore, if the primary goal of the clinician is to identify early disease occurrence, then this may not be the most suitable imaging modality. Alternative imaging could be considered (Ibid, 2010). Disease spread from the primary site of origin (prostate) to distant organs could come under the remit of this modality (Ibid, 2010).

2.8. Digital Rectal Examination

Digital rectal examination is one screening tool used by clinicians to rule out the presence of abnormalities in the prostate gland. Nodularity, significant asymmetry, induration, or loss of anatomical landmarks, as determined by the examiner, are some of the positive findings of DRE that could raise suspicion of abnormality within the prostate gland.

Svetec D et al. and colleagues (1998) put forward that before a test can be deemed as fit in clinical practice as a screening tool. Apart from the cost-effectiveness of this potential test, it is essential to ascertain that the disease condition must be considered a public health concern. Recently, prostate cancer has been shown as one of the leading most diagnosed cancers among men, with increasing mortality rates. The following essential criteria for acceptance of a test as a screening tool is that the test must be able to identify the disease condition at an early stage of the disease, preferably during an asymptomatic phase of the disease, when the lesion is still confined to the primary organ of origin (Svetec D et al., 1998). Both DRE and PSA can detect this disease condition at an early phase. Therefore, judging from the above criteria, DRE has qualified to be utilized as a screening tool. However, there are a few issues concerning the suitability of DRE as a screening tool for prostate cancer. The potential screening tool must have sufficient sensitivity and specificity and positive and negative predictive values. Secondly, the curative ability to cure the disease must be more remarkable for the cohort of patients detected by the screening test. Finally, there must be enough evidence showing improved outcomes associated with the screening test. No clear indications show if DRE can meet all the criteria highlighted for acceptance as a screening tool for prostate cancer.

Nevertheless, autopsy reports have also shown that about 30% of men aged 20 to 40 have been diagnosed with prostate carcinoma (Ibid, 1998). The figures have further demonstrated that the percentage of men with prostate neoplasm has increased by more than 50% in men above the age of 50 years (Svetec D et al., 1998). These were all unsuspected carcinomas during the lifetime of the patients under interrogation. Further indicates that sometimes men could have prostate cancer, be asymptomatic, and live with the disease for the rest of their lives (Naji L et al., 2018). Also, it explains why only a 3.64% lifetime risk of dying from prostate cancer has been estimated (this figure may be related to organ-confined tumours) (Ibid, 2018). However, with local spread to the lymph node, there is an increasing risk of disease-specific death up to about 70% (Svetec D et al., 1998). A significant increase in mortality rate can impact the patient's life quite severely with poor outcomes. About 50% of this cohort are expected to die within two years, which means poor outcomes are associated with disease spread (Svetec D et al., 1998). Hence it is essential to detect this disease condition quite early, especially while the disease is still asymptomatic and organ confined.

The difficulties resulting from either biopsies or therapeutics include incontinence, impotence, and urinary dysfunction, and patients could also be subjected to undue anxiety. Radiation therapy has also been shown to have complications related to bowel and rectal symptoms, such as acute or chronic radiation enteritis, which can cause pain, bloating, nausea, faecal urgency, and diarrhea as rectal bleeding (Ibid, 2011).

Erectile dysfunction, incontinence, and perioperative mortality rates are common complications of prostatectomy.

A study conducted in the UK by Downing and colleagues tagged life after prostate cancer diagnosis (LAPCD), assessing the patient-reported outcomes of over 3,000 prostate cancer survivors at 18-42 months following diagnosis. About 81% of patients documented that their overall sexual function was poor or very poor in some cases. The prevalence of poor or very poor sexual function among men aged 60 and above is usually 33% (Downing et al., 2019), which shows a decline in the sexual functions of men who have undergone some form of radical therapy.

Therefore, until the effectiveness of the screening tool to decrease disease-specific mortality is established, a screening tool should not be adopted as a nationwide scheme. However, this can be adopted based on the risk calculation on an individual basis.

When Catalona W J (2017) compared the impact of DRE and PSA in early prostate cancer detection in a multicentre study of about 6,630 participants, PSA detected clinically significant tumours in about 82% of the population while DRE showed a detection rate of 55%. Of the 160 participants who underwent radical prostatectomy and pathological staging, 114 (71%) were organ-confined cancers. PSA detected 85 (75%) while 64 (56% $p=0.003$) were detected by DRE. Demonstrating that PSA was superior at detecting organ-confined tumours when compared to DRE. The cancer detection rate was 3.2% for DRE and 4.6% for PSA. However, a combination of the two screening tools depicted an increase in the detection rate of organ-confined cancer (5.8%). Although findings from DRE do not present a strong indication for a biopsy, it could be considered an additional test to PSA to further strengthen the premise for prostate biopsy (Catalona WJ et al., 2017). Halpern J A et al. suggested that DRE may be used for follow-up and adjunct testing with elevated PSA levels (Halpern JA et al., 2018).

2.9. Magnetic Resonance Imaging

Magnetic Resonance Imaging is a non-invasive imaging modality that utilizes the interactions between a strong magnetic field, radio frequency pulses, and body tissues to acquire images of planes within the body (Schaudinn et al., 2019). This imaging technique exploits the magnetic field to polarize protons within tissues. Pulse energy is often directed into the tissues, which knocks some protons out of alignment. When the pulse is turned off, the radio waves can be detected as the proton moves back into its aligned position (Ibid, 2019).

A few concerns limited the inclusion of Magnetic Resonance Imaging (MRI) into the prostate cancer diagnostic pathway a few years ago. One of such limitations was that MR imaging was often carried out following prostate biopsy. Post-biopsy MR images were often seen with haemorrhage and inflammation, which causes artefacts on the images, resulting in false positive or negative results or even suboptimal images, which could be of little or no diagnostic value. The second limitation of this imaging modality concerning prostate cancer diagnosis was that attention was most often focused on the peripheral zone of the gland since most prostate cancer is often found in this zone. However, the downside is that tumours within the anterior fibromuscular stroma or the central zone could easily be missed. Furthermore, TRUS biopsies have been shown to lack the ability to adequately sample lesions in the anterior part of the gland due to the greater distance of the biopsy needle from the rectum (Delongchamps NB et al., 2013).

Providing a cost-effective MR imaging approach to increase the detection rates of clinically significant tumours while reducing the detection rate of indolent tumours in the prostate gland would be a welcome approach that can add value to the clinical diagnosis of prostate cancer.

The initial utilization of MRI as far as prostate cancer diagnosis was concerned was primarily for local staging, seminal vesicle invasion, and the detection of extracapsular extension. Nevertheless, the advent of Multiparametric MRI (mpMRI) has some promising roles, such as tumour localization, disease diagnosis, staging, and risk stratification of clinically significant prostate carcinomas.

Olson et al. (2019) reported a case study of a patient who had a consistent negative prostate biopsy with a consistent elevation of PSA 5 different times. However, when a different Urologist was contacted, this urologist decided to order a multiparametric MRI. A 3cm mass in the anterior fibromuscular stroma and anterior aspect of the transition zone to the right of the midline was depicted.

A CT-guided biopsy of the mass was obtained, and the sample was sent for histological assessment, further demonstrating a Gleason 5+4 adenocarcinoma of the prostate gland involving more than 95% of the needle core and 15 mm in aggregate length. This patient was treated with radiotherapy with MRI used for treatment planning (Olson DO et al., 2019).

Multiparametric MR imaging is often made up of structural (T2 Weighted Imaging), functional (Dynamic Contrast Enhanced Imaging & Diffusion Weighted Imaging), and spectroscopic imaging techniques (Siddiqui MM et al., 2015). T1 Weighted imaging is often utilized in assessing post-biopsy haemorrhage. However, in recent times most prostate biopsies have been carried out after MR imaging to avoid any biopsy-related artefacts such as haemorrhage. Therefore, T1 Weighted imaging is of limited use as far as prostate cancer imaging is concerned except when post-contrast dynamic scans are required (Abdi H et al., 2015).

T2 Weighted Imaging (T2 WI) is often utilized to assess the morphology of the prostate gland due to its high spatial resolution (Siddiqui MM et al., 2015). The zonal anatomy, seminal vesicle, neurovascular bundle, ejaculatory ducts, and urethra are often well delineated with the aid of T2 WI. The peripheral zone in the prostate gland is made of glandular tissue and is often seen as an area of high signal intensity on a T2 WI due to the higher water content. However, the presence of a malignant lesion is often seen as an area of low signal intensity within the peripheral zone (Schaudinn et al., 2019). Other conditions can present as an area of low signal intensity within the peripheral zone, including scar tissue, fibrosis,

prostatitis, post-irradiation, or post-biopsy haemorrhage. The transition zone comprises two distinct histological tissue types: the glandular and stromal tissues. In the normal transition zone, the glandular tissues are often seen as an area of hyperintensity, while the stromal tissues are often seen as an area of low signal intensity (Abdi H et al., 2015). Hence the signal intensity of the transition zone is often heterogeneous due to the presence of the glandular and stromal tissues. Detecting carcinoma in this zone could be slightly challenging due to high and low signal intensities (Ibid, 2015). The main features (histological) that distinguish the transition carcinoma from the normal tissue are increased cellular density, decreased luminal volume, decreased extracellular space, and the presence of new blood vessels formed (neo-angiogenesis). A focal, homogenous hypointensity against a background of the high signal intensity of the glandular tissue with poorly defined margins is often seen on T2 WI as a feature of transition carcinoma (Stabile A et al., 2018). The lenticular shape, the absence of a capsule, and the invasion of the anterior fibromuscular stroma can also be attributable to cancer in the transition zone (Stabile A et al., 2018).

Restricted diffusion is often a feature of a malignant lesion in the prostate gland on the Diffusion Weighted Imaging (DWI) which often presents as an area of high signal intensity on DW images due to the increased cellular density and membrane permeability (Ibid, 2018). However, on the apparent diffusion coefficient map, in most cases, malignant lesions are presented as areas of low signal intensity within the transition zone (Schaudinn et al., 2019). Sometimes the features depicting restricted diffusion may only be observed in either DWI or ADC map and not often seen on both, especially for tumours with Gleason score 6 and 7 (mainly for 3+4) when the b-value is ≤ 1000 . Nevertheless, when the b-value is ≥ 1600 , restricted diffusion is often observed on both the ADC map and DWI (Stabile A et al., 2018). Due to the new blood vessels formed due to a tumour in the transition zone, there is early and fast contrast enhancement within the area where the lesion is found, and subsequently, contrast washout is observed. It is also important to note that quick contrast enhancement and washout are not essential characteristics of transition zone cancer. However, they may increase the confidence level for a suspicious lesion (Ibid, 2018).

The introduction of the Prostate Imaging – Reporting and Data System (PIRADS) in 2011, published in the European Radiology journal in 2012 (Barentsz JO et al., 2012) brought about the ability to differentiate between a clinically significant and a clinically insignificant lesion within the prostate gland (Ibid, 2012). This structured reporting system comprises T2 WI, DWI, and DCE findings. Any tumour with a Gleason Score ≥ 7 (3+4), tumour volume greater than 0.5 mL, and extracapsular extension are often

clinically significant. PIRADS tends to assign scores from 1 to 5 depending on the degree of probability of being a cancerous lesion, with one being highly unlikely and five being highly likely. This scoring system allows the clinician to determine if a biopsy is necessary or not. In most cases, biopsies are often considered for PIRADS 4 and 5 lesions, while no biopsy is often planned for patients with PIRADS 1 and 2 lesions. Although PIRADS considers anatomical and functional imaging features to determine if the lesion is of any clinical significance, it is also important to note that some dominant sequences are more sensitive on different prostatic zones.

The PROMIS study demonstrated a sensitivity and negative predictive value of mpMRI of 88% and 76% for detecting tumours with a Gleason score $\geq 3+4$ (Faria R et al., 2018). If an initial biopsy proves without cancer, multiparametric MRI is often considered for the diagnosis of clinically significant cancer in the prostate gland. PROMIS was the most extensive accuracy study utilising mpMRI and TRUS biopsy (TRUSB) to diagnose prostate cancer. With the aid of a template mapping as a reference standard, it was discovered that mpMRI had better sensitivity for detecting clinically significant prostate cancer than TRUSB. However, mpMRI had a lower specificity (Ibid, 2018).

2.9.1. The role of mpMRI in biopsy naïve patients

TRUS and MRI-targeted biopsy have been shown to provide the highest detection rate of clinically significant prostate cancer (Abdi H et al., 2015). The combination of these two biopsy strategies compared to the use of the targeted strategy alone did not significantly increase the detection of clinically significant ($p=0.21$) (Ibid, 2015). Higher accuracy in depicting clinically significant prostate carcinoma was demonstrated by MRI- targeted biopsy when compared to TRUS biopsy (Ibid, 2015). It was also easier to avoid indolent cancers with the MRI-targeted biopsy than TRUS biopsy (Ibid, 2015).

2.9.2. The role of positive mpMRI in previous patient (Active surveillance)

Active surveillance is a process of monitoring men diagnosed with localised prostate cancer to avoid or delay unnecessary treatment in men with low volume or risk of prostate carcinoma. Adding MRI-targeted biopsy to the standard of care made it possible for clinicians to depict more clinically significant carcinoma of the prostate gland. Abdi et al. demonstrated that a combination of MRI- targeted biopsy and standard mpMRI could increase prostate cancer progression's detection rate during active surveillance (Abdi H et al., 2015). Furthermore, Siddiqui et al. demonstrated that using mpMRI could reduce repeat biopsies by 68% (Siddiqui MM et al., 2015).

2.10. Histopathology of prostate cancer

Histopathology, as it relates to prostate cancer, involves the microscopic assessment of prostate tissue biopsy and surgical specimens to rule out the presence of prostate cancer. Often carried out after the specimen or samples have been processed, and histological sections have been placed on glass slides.

During a prostate biopsy, the standard routine process involves using an 18-gauge needle to obtain biopsy cores through the transrectal or transperineal route. Radical prostatectomy specimens can also be sent for histopathological interrogation.

2.10.1. Histopathological features consistent with carcinoma

Typical malignancies include extraprostatic spread, perineural invasion, collagen micronodules, and glomeruloid intraglandular projections (Baisden BL et al., 1999). Although part of the prostate gland is found outside the gland, it is often an indication of malignancy within the prostate gland; nevertheless, some cases of ectopic benign prostatic glands are found outside the gland. This prostate tissue has been seen in the testis, the root of the penis, subvesical space, seminal vesicle, penile urethra, peri-colonic fat, epididymis, submucosal and perirectal fat, urachal and spleen (Humphrey PA, 2003)

Perineural invasion is the main feature of malignancy in the prostate gland, one of the most frequently used pathways to spread malignant disease. Therefore, perineural invasion involves a process whereby the cancerous cell infiltrates into, around, or through a nerve. By implication, the malignant cell does not necessarily need to be in the perineural space but may infiltrate anywhere within the nerve. This feature has been found in most cases of prostate cancer (84%-94%) (Byar DP et al., 1972). However, only 25% of the needle biopsy cases have been shown to have perineural invasion (Bismar TA et al., 2002). The fact that there is a prostate gland immediately next to a nerve does not necessarily confirm the diagnosis of malignancy since some benign prostatic glands have been shown to abut or wrap around nerves (Ali TZ et al., 2005). The presence of epithelial cells around a nerve can help distinguish benign from the malignant perineural epithelium.

Lymphovascular space invasion by prostatic epithelial cells can be seen as a specific diagnostic feature for malignancy. Nevertheless, it may not even be seen in needle core biopsy. The lymphovascular invasion has been found in 5% - 53% of radical prostatectomy cases. This invasion is often correlated with higher grade, volume, and stage and is often associated with an increased risk of biochemical recurrence and distant metastases (Fajkovic H et al., 2016).

Collagenous micronodules are microscopic aggregates of hyalinized stroma, an unusual response to invasive prostate adenocarcinoma (McNeal et al., 1991; Baisden et al., 1999). The micronodules are mainly collagen and sparsely distributed, with a few elongated fibroblastic nuclei observed. Nevertheless, about 13% - 22% have been detected through radical prostatectomy (Kaleem et al., 1998; Bostwick et al., 1995). These are often linked with Gleason pattern 3 or 4 adenocarcinomas (Kim et al., 2015).

Glomeruloid structures are renal glomeruloid-like epithelial aggregates within the acini of the prostate adenocarcinoma (Baisden et al., 1999). Although this growth pattern is believed to be consistent with cancer, they have limited use because only 3%-15% have been reported for tissue biopsies for adenocarcinoma. In contrast, 5% have been reported for prostatectomies with cancers (Pacilli et al., 1998; Verma et al., 2012). Round tufts or buds into small to medium-sized malignant glands are often seen as features of glomeruloid bodies on the microscope. Although the glomeruloid structures are often small features of cancer, they represent a high-grade Gleason pattern 4 (Epstein et al., 2016b).

2.11. Staining

Histopathologists tend to depend (to a greater extent) on contrasting stains for assessing tissue samples. Nevertheless, histological stains are often made for microscopic assessment.

Tissue morphology and architectural details could easily be detected from Haematoxylin and Eosin stains; however, it is challenging to determine the gene expression profile of cells from H & E Staining. However, to determine the gene expression profile, image analysis of immunohistochemical (IHC) is often carried out to provide the functional details needed to determine the likelihood of the presence of a disease condition. A typical example is that it can be challenging to ascertain the presence or absence of a basal cell layer on H & E alone. However, IHC could be very useful in assisting the detection process. The ability to obtain information and further assess features such as nuclear density and intensity that could indicate the possibility of a disease condition can be obtained through stained digitized by whole-slide imaging systems at high resolution. A computational model can be built with the aid of the features to assess the spatial distribution of disease on each whole-slide image (WSI).

Immunohistochemical assessment involves the monoclonal or polyclonal antibodies to determine the presence or absence of specific antigens in the tissue sample (Carneiro et al., 2018).

Immunohistochemistry determines the characteristics of the tumour, disease spread, response to treatment, and cellular differentiation. In some other instances, it has also been shown to be relevant in materials secreted by specific cells of interest and identification of structures of organisms (Ibid, 2018).

Inter and intra-observer variability could be minimised in histological analysis through computer-assisted analysis, enhancing patients' outcomes (Ibid, 2018). High-quality image data is needed to ensure the process of digital pathology is effectively delivered.

Prostate tissues are often stained with H&E, although this has been found to give a suboptimal distinction between glandular epithelium and stroma as both stains in shades of red/pink by eosin. There is, therefore, a need to identify another stain with optimal quality differentiation between the glandular epithelium and the stroma so that adequate prostate gland segmentation can be achieved. Litjens and colleagues (2016) were able to manually define cancer regions from H&E-stained prostate tissue with the aid of a convolutional neural network (CNN). A cancer likelihood map from CNN with good agreement with the manual identified cancer region (Litjens G et al., 2016). These researchers could show that it was possible to reduce the workload of pathologists while increasing the objectivity of diagnosis. All prostate cancer slides were automatically detected with the deep machine learning approach. In contrast, 30-40% of the slides with benign and normal were distinguished with any additional immunohistochemical markers or human intervention (Ibid, 2016).

In summary, the lack of precision of the available screening and diagnostic tools in the early detection and risk stratification of prostate cancer has allowed for the search for a novel diagnostic tool with improved precision.

Chapter 3: Novel Optical Diagnostic Techniques

Raman spectroscopy has been shown to possess an innate ability to unravel the biochemical composition of biological samples. In this chapter, we will discuss the potential ability of Raman spectroscopy as a novel optical diagnostic tool that can be utilised to detect early molecular changes within biological samples. We will look at the history of Raman spectroscopy, which will lead us to explore its underpinning principles and the different components of Raman spectroscopy equipment. Light interactions with biological samples will be examined. Blood serum and plasma were used for analysis in our study, followed by the technique and underpinning principles of Drop Coating Deposition Raman Spectroscopy. Proteomic profiling and metabolites in cancer diagnostics will be discussed, followed by glycolysis and Raman spectroscopy of blood constituents. Then establishing the biochemical basis of urological diseases measured by Raman spectroscopy and, finally, the clinical utilisation of Raman spectroscopy will be discussed.

3.1. Raman spectroscopy

Raman spectroscopy is an analytical tool for acquiring chemical data through inelastic light scattering. This technique has been very amenable in detecting early-onset disease conditions such as precancers. It provides the ability to interrogate the biochemical composition and function of cells, tissues, and biofluids in a non-destructive and label-free mode. Biochemical changes occur long before structural changes are evident in many disease conditions. Therefore, better outcomes are often expected in the clinical environment if these disease conditions are detected early. For example, if tumours are detected early, either at the precancerous stage or stage 1 or 2, treatment options with curative intent can be administered in molecular disease conditions such as cancer.

Nevertheless, when these disease conditions are detected through structural imaging modalities or when the patient becomes symptomatic, the disease may have progressed to a stage where palliative treatment is the only option available to the patient and the clinician. Therefore, a diagnostic assay with an innate ability to detect early cellular differentiation, mitosis, and programmed cell death will be helpful in diagnosis, early treatment, and better patient outcomes. Raman spectroscopy has been shown to detect these molecular changes early. It could therefore revolutionise the clinical

3.1.1. Raman spectroscopy and Historical perspective

Adolf Gustav Stephan Smekal was an Austrian theoretical physicist interested in solid-state physics. In 1923, he predicted the inelastic scattering of light, but it was not seen in practice until 1928. C.V Raman and K.S. Krishnan were the first to notice the inelastic scattering of light in organic liquids in 1928.

However, this effect was seen in inorganic crystals by Grigory Landsberg and Leonid Mandelstam. Franco Rasetti discovered the Raman spectra in 1929 in gas.

In 1930, Sir Raman was awarded the Nobel Prize in Physics for discovering Raman scattering. This technique was not extensively used until the 1960s because the necessary equipment, such as lasers, detectors, and spectrographs, were unavailable. The advent of various optical technologies and instrumentations in the late 1960s brought about an ability to assess the biochemical components of different materials and create a database for spectral features of lipids, proteins, and peptides. Assessment of molecular components of biological cells and tissues, as well as biofluids, started in the 1970s with the aid of Raman spectroscopy.

3.1.2. Underpinning Principles of Raman Spectroscopy

When laser light is incident on a biological sample, the photons from the laser light can interact with the intramolecular bonds within the sample. Most commonly, the oscillating electric field of the photon causes the molecule to vibrate with the same frequency as the photon, leading to a rapid emission of a photon with the same energy as the incident one and the molecule to return to the relaxed state it was prior to the interaction with the photon. A change to the energy in the molecule occurs due to the interaction hence photon is emitted. During this process, the photon donates energy to or receives energy from the molecule, producing a change in the molecule's vibrational state. When the photons are emitted from the molecule, the energy becomes altered precisely by the amount of energy donated to or captured from the molecule, thus changing the colour of the light from that of its illumination, often referred to as inelastic scattering or Raman scattering (named after its discoverer CV Raman). This change in the photon's energy is referred to as Raman shift and is measured in wavenumbers (which are proportional to photon energy). This shift is specific to the molecule and its environment. Photons interacting with different biochemical bonds within the tissues or biofluids can result in different Raman shifts leading to the formation of a Raman spectrum when combined. The Raman spectrum is a direct function of the molecular composition of the tissue or biofluid, providing a molecular fingerprint of the phenotypic expression of the biological fluid and tissues, which can give good objective information regarding the pathological state of the biological sample under interrogation.

3.1.2. Raman microscopy:

A combination of a light microscope and Raman Spectroscopy provides a great analytical tool to assess a biological sample's morphological and molecular features. A single spectrum can be acquired from volumes smaller than one μm^3 either by point-by-point scanning or a line-by-line scanning technique, which has been utilised extensively to assess the biochemical components and variations in the biomolecules in cells, tissues, and biofluids. A typical Raman micro-spectrometer includes laser transmissive imaging optics, high contrast rejection filter for Rayleigh scattered light, and a high-resolution spectrometer containing an efficient grating and sensitive charge-coupled device, which can be seen in figure 3.1 below.

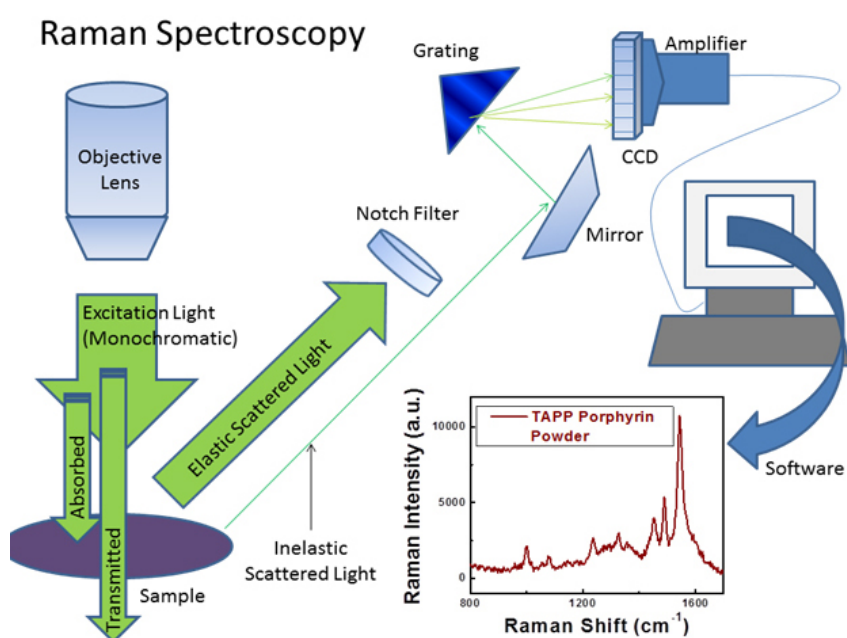


Fig. 3.1. Schematic presentation of How Raman spectroscopy signal are generated and the subsequent spectrum acquisition. Plot reprinted with permission from {J. Phys. Chem. C, 2011, 115 (46) pp 22761 - 22769}. Copyright {2011} American Chemical Society)

The most scattered light is elastically scattered, meaning it has the same wavelength as the excitation source. The elastically scattered light is often removed from the path of the light beam with a notch filter to avoid overwhelming the Raman signals. The Raman scattered light may be dispersed according to wavelength and detected by a CCD. A Raman spectrum for tetra(4-aminophenyl) porphyrin (TAPP) powder is shown in figure 3.1 above (Plot reprinted with permission from {J. Phys. Chem. C, 2011, 115 (46) pp 22761 - 22769}. Copyright {2011} American Chemical Society).

3.2. What is a laser?

A laser is a device that emits light through optical amplification based on stimulated emission or electromagnetic radiation.

Theodore Maiman produced the first laser on the 7th of July, 1960, using ruby as a lasing medium that was stimulated using high-energy flashes of intense light. It is important to note that the term laser is a short form for "light amplification by stimulated emission of radiation." Einstein's quantum theory of radiation underpins the stimulated emission.

3.2.1. What are the characteristics of the light that is emitted?

Monochromatic: laser lights are often monochromatic with a single wavelength or narrow band of wavelengths. Because laser light is monochromatic, it is possible to ensure accurate targeting of the biological sample under investigation while avoiding the surrounding structures.

Coherence: The coherence of laser light is a measure of the precision of the waveform. Therefore, a highly coherent laser beam can accurately focus on the material. The emitted photons tend to vibrate in phase agreement in space.

Directionality: the direction of travel of the laser beam is often in line with the emission of a very narrow beam of light (radiation) which tends to spread slowly. The directionality allows the laser light to be focused on minimal focal spot size.

3.2.2. Why is it different to light from other sources...?

Lasers differ from other light sources because they emit light coherently, allowing a laser to be precisely focused on a tight focal point. Therefore, this property allows laser light to be utilised in laser cutting and lithography. Spatial coherence also allows the laser beam to stay narrow over a long distance which can be exploited to produce laser pointers.

3.2.3. Light source

3.3. Interaction of light and biological samples

Laser light is often utilised for the excitation of biological samples to acquire Raman spectroscopic measurement of the biochemical compositions of the sample under investigation. Due to the relatively weak Raman signal, it is often necessary to give enough power to the sample to produce Raman scattered photons for detection within an acceptable acquisition time for clinical application. Therefore, issues such as maximum permissible exposure (controlled by American National Standards

Institute or similar organization) and temperature elevation (crucial to avoid tissue damage and maintaining patient comfort) should be considered before Raman measurement is carried out. Therefore, a compromise between patient comfort and safety, signal-to-noise ratio, and instrument consideration must be considered when the choice of laser power is considered. Laser stability must also be considered, mainly when the multimode laser is used, since Raman lines are precise and narrow for a particular vibrational mode. Accurate position bandwidth and spatial mode must always be considered if a consistent result is to be achieved at all times.

It is well established that Raman scattering intensity is inversely proportional to the fourth power of the illumination wavelength, which means that excitation at a longer wavelength leads to a decline in the Raman signal intensity. Furthermore, it is essential to know that the detection's sensitivity relies on the wavelength range. Therefore, a faster detection rate is often observed in wavelengths above 800 nm, mainly when the quantum efficiency of an uncooled silicon-based CCD (charge couple device) is utilized. Indium gallium arsenide (InGaAs) array devices are often utilised for longer wavelength illumination. However, there is a negative impact of a higher noise level and cost implication, resulting in reduced sensitivity. In Raman spectroscopic imaging, spatial resolution is also an important aspect to consider. It is affected by the illumination wavelength since diffraction-limited laser spot diameter is often influenced by $1.22 (\lambda/4)$, where λ is the wavelength.

The optical properties (such as scattering and total attenuation coefficient) of the biological sample under investigation and intrinsic fluorophores' excitation-emission and yield properties should also be considered when deciding on an excitation laser source. The wavelength of the light photon tends to affect each of these parameters. The ability to deliver and obtain light photons beyond a particular layer of biological samples, which could be tissue or biofluid, is governed by the attenuation coefficient, among other factors. Therefore, when a volume of biological sample has a low attenuation coefficient, the light beam can easily pass through the sample without much attenuation of the light beam, which depends on the wavelength of the light and the sample under investigation.

On the other hand, it is also important to note that the molecules within a biological sample with a remarkable ability to absorb light could lead to excess heat deposition, damaging the biological sample with a high irradiance laser beam. Furthermore, robust fluorophores could produce a fluorescence signal, which could overpower the relatively weak Raman signal or peaks. NIR excitation sources are often selected for high-absorbing molecules (such as melanin, water, oxy- and deoxyhaemoglobin)

because of the reduction in their attenuation coefficient linked with these high-absorbing molecules. This decision is often made to avoid a spectrum in which high fluorescence is very likely to occur. Therefore, NIR wavelength often results in a low fluorescence background and makes it easy to identify Raman bands in contrast to UV or visible excitation. Highly autofluorescence tissue samples such as kidneys would probably need a longer excitation wavelength to acquire any significant Raman signal. However, even with different wavelengths, Raman spectra can easily be acquired from tissues with low autofluorescence properties, such as breast tissues.

In the past, argon ion lasers were utilised for visible excitation within the Raman systems. In contrast, neodymium-doped yttrium aluminium garnet (Nd: YAG) was utilised for Fourier transform- Raman applications, and NIR excitations utilised titanium: Sapphire (Ti-Sapph). Near diffraction-limited optical performance could be achieved for all the light sources if high output powers are utilised alongside longitudinal and single spatial modes of operation and Gaussian beam profiles. Nevertheless, for the light sources to be helpful in clinical practice, their cooling must function at an optimum capacity, and the size of the laser and its accompanying electronics must be compact enough for clinical utility. These requirements may be challenging with some of the existing systems. The continuous improvement in the field of diode laser technology has revolutionised the landscape in Raman optical imaging systems. The light emission given by electro-optical components known as diodes is often based on the applied current and the operating temperature. The size of diodes and the need for great precision in controlling electronics are crucial to secure a stable output for Raman excitation. Laser diodes could be subjected to thermal-elastic effects within the laser cavity length, and output power fluctuations could occur if there are no stable thermal and current controls. Elliptical beam output and unequal beam divergence from each dimension of the rectangular facet are often seen with laser diodes making free beam coupling somewhat challenging, often resulting in beam shaping of the optics for practical application. Some laser diodes are built with a pigtail option which enables the coupling of the fibre to the laser diode to reduce the loss caused by the elliptical nature of the beam and astigmatism.

The advent of external cavity diode lasers (ECDL) has brought about a cost-effective and robust light source for Raman excitations. The small thermo-elastic effect is often reduced by the inherent extended length of the resonant cavity of the laser diode by extending the distance between the diode's longitudinal modes. The ECDL has various advantages, which include reduction of mode hops, wavelength tunability permission, reduction in temperature-dependent frequency response, and reduction of the spectral bandwidth of the output light. Where measurement repeatability and high

spectral resolution are essential such as in clinical practice, ECDL provides laser linewidth of less than 0.001 nm (at 785 nm) with mode-locking. Tuneable Littman-Metchaf and Littrow configurations are the ECDL configurations available for routine use. With powers in the region of 300 mW, there are mode stabilizers and diode lasers available for use as single or multimode configurations designed for Raman spectroscopy applications.

3.3.1. Light interaction with tissue samples:

Biological tissue is a dielectric medium with an average refractive index higher than air (Tuchin VV, 2015). When a light beam comes in contact with the surface of biological tissue, a partial reflection occurs at the interface between the air and the tissue since some light access the tissue. Refraction of light is a process whereby there is a change in the direction of the ray of light as it moves from one medium to another obliquely. The speed of light is different as it moves from one medium to another. Refraction obeys Snell's law which states that the ratio of sines of the angles of incidence and refraction is equivalent to the ratio of phase velocities in the two media or equivalent to the reciprocal of the ratio of the indices of refraction (Tuchin VV, 2015). The relative refractive index of these two media can be represented by n_1 and n_2 , where n_2 is greater than n_1 . The refractive index in the tissue's visible / Near-infrared range (wavelength) and its composition varies from a value higher than that of water due to the influence of some organic components (Ibid, 2015). Biological tissues interacting with light are often not homogenous and sometimes multi-layered with rough surfaces and from bulk tissues such as prostatectomy specimens. Therefore, the incident light will undergo reflection, transmission, and another form of attenuation as it traverses the medium of interaction. As the incident light traverses the medium, scattering and absorption occur, as demonstrated in figure 3.2 below.

Most light scattering occurs in the backward projection, whereby the light particles are forced to deviate from the straight trajectory by localized non-uniformities in the medium through which they pass (Tuchin VV, 2015). The way and manner by which light transfers its energy from one point to another are often dependent on the absorption and scattering abilities of the components of the tissue, such as the fibres, cells, and cell organelles. The shape, size, density of the structures, their refractive indices, and the polarization state of the incident light governs the character of light propagation on tissues (Tuchin VV, 2015).

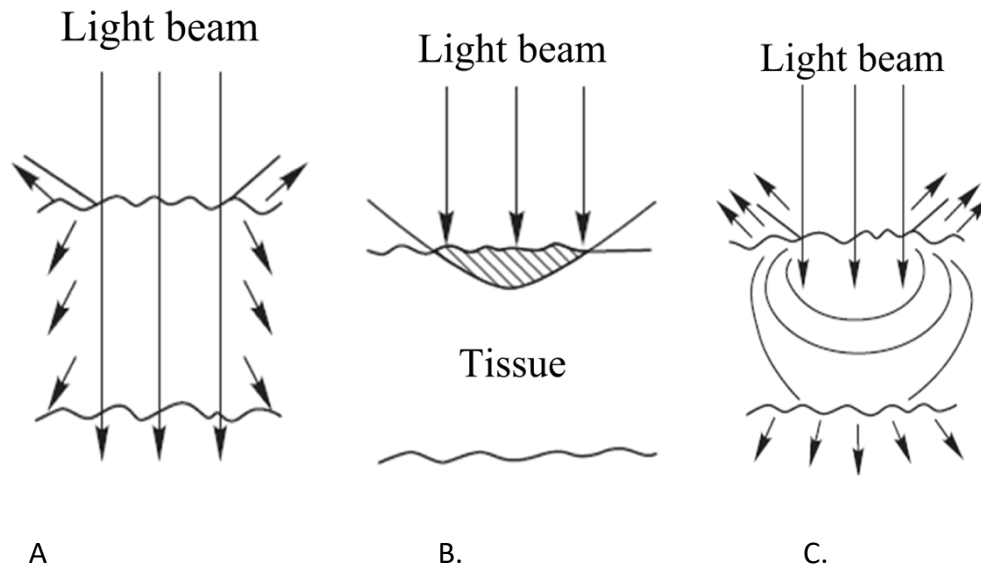


Fig. 3.2: Schematic diagram showing Light beam absorption and scattering by a tissue. A. Both absorption and scattering occur here. Common with the NIR light source interactions. B. Mostly absorption occur here. Often seen with UV or MIR/FIR interactions. C. scattering is the main attenuation process occurring here. Common with NIR interactions (Ibid, 2015).

3.3.2. Scattering of Light:

When light photon in the infrared region interacts with the molecules in a medium, it induces a momentary transition to a virtual energy level. Therefore, the molecules become excited, but since they cannot stay in the virtual energy state for long, it relaxes back to the initial ground state by emitting a photon with the same energy as the incident photon. Since there is no change in the frequency or energy of the emitted light because there was no transfer of energy to the molecule, this process is referred to as Rayleigh scattering. However, suppose the molecule releases a different amount of energy than the incident light photon, known as Raman scattering, since there is a transfer of energy to or from the molecule.

3.4 – Blood

Blood is a mildly alkaline aqueous fluid with a pH value between 7.35 and 7.45, in which several types of free-floating red cells are suspended. Blood helps transport oxygen from the lungs to different body parts and helps move waste products to excretory organs for onward excretion. Nutrients are also conveyed to relevant body parts through the human blood. The concentration of the different levels of nutrients, metabolites, waste products, and oxygen can be measured in the blood. Their results can be

utilised for the clinical assessment of patients for different disease conditions. Different biochemical changes of blood components can be utilised to characterise disease conditions such as malaria, sickle cell anaemia, or diabetes.

3.4.1. Plasma

The plasma is a straw-yellow fluid with a total volume of 2.7 to 3.0 litres (2.8-3.2 quarts) in an average human. About 50% of the total blood volume comprises blood plasma (mildly alkaline). Plasma is primarily made of water (92%) with 8% dissolved proteins (such as globulins, fibrinogen, and albumins), a trace number of clotting factors, and other metabolically relevant compounds such as antibodies, electrolytes, and hormones. Metabolic processes in the human body can be detected through the molecular assessment of blood plasma and serum.

3.4.1.1. Extraction of plasma from whole blood

The extraction of blood plasma from whole blood is often done through centrifugation. The quality of the separation process is often controlled by the purity of the plasma, separation time, the yield of the extracted plasma from the whole blood sample, and the suppression of haemolysis (Mathew J et al., 2020). Since plasma is lighter in weight than the blood cells, it is often seen as the yellowish fluid in the upper part of the blood sample. In contrast, the blood cells are often seen in the bottom part of the sample because they are denser than the plasma (Ibid, 2020), as shown in figure 3.3 below. During the separation, a sharp interface is often observed between the purified plasma and the cell suspension. The interface is often referred to as a shock interface because it represents a sudden discontinuity in the cell suspension. After the separation, a radial stack often consists of a cellular pellet at the bottom and a purified plasma supernatant (Ibid, 2020).

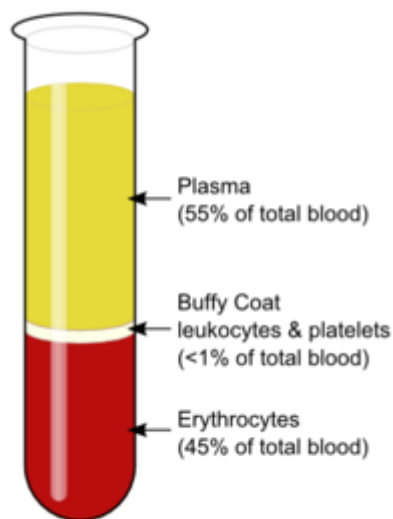


Fig. 3.3: The separation of blood plasma from blood cells (<https://en.wikipedia.org/wiki/Blood-spinning>)

The mass density variation causes the separation of the plasma from the blood cells, often referred to as sedimentation. The sedimentation of the suspended particles in the centrifugal field can be substantially enhanced because the centrifugal net force induced by the particle of the volume at radial position scales with the square of the rotational frequency. Therefore, lighter particles are often seen floating on the top, while denser particles are often seen at the bottom. In order to maintain the integrity of the plasma collected, it is advisable to freeze it within 24 hours of collection. Ensures that the clotting factors and immunoglobulins within the plasma continue functioning to the optimum level. The shelf life of the frozen plasma is estimated at one year, after which it should be discarded as it will not function appropriately anymore.

3.4.1.2. Development of plasma

Plasma is often formed from water and salts absorbed from the digestive tract. Nevertheless, plasma proteins have a more distinct organ that produces them depending on an individual stage of development (Mathew J et al., 2020). The mesenchymal cells are often in charge of producing plasma cells during the early conception stage, and albumin is often the first protein to be synthesized. On the other hand, the reticuloendothelial cells of the liver are responsible for plasma protein synthesis in adults. Bone marrow degenerating blood cells and general body tissue cells, together with the spleen, also contributes to the production of plasma proteins (Ibid, 2020).

3.4.2. Serum

When the clotting factors and fibrinogen are removed from plasma, the liquid left is called serum. Therefore, the serum is obtained by collecting plasma without any anticoagulant. The removal of a large portion of the fibrinogen content of plasma in the form of fibrin clot results in serum with a lower protein concentration.

Over 20,000 different proteins are known components of blood serum that flow through the body's different organs. Peptidome, a Low Molecular Weight fraction serum composition of blood, contains much information that can be exploited for diagnostic purposes.

3.4.3. Collection, handling and storage of plasma and serum

The collection, handling, and storage of plasma and serum are crucial in the practical analysis of biofluids since the reproducibility, sensitivity, and selectivity are often dependent on these parameters. Furthermore, overnight fasting, speed and time of centrifugation, and storage conditions such as temperature (Issaq H et al., 2007) could also impact the analysis and subsequent plasma and serum proteome results.

Silicones are often utilised to coat the internal surface of the collection tubes, and polymers such as polyvinylpyrrolidone or polyethylene glycols can be added. A few recent studies have demonstrated the presence of polymeric compounds in clinical samples, which could further compromise the integrity of the spectral information due to unwanted peaks from the polymeric components. Different studies have observed a significant difference between collection tubes, primarily when a red-top tube (without preservatives or anticoagulant) is utilised compared with tiger-top tubes (serum separator tubes). Fasting and the time the sample was collected from the patients were also demonstrated to impact the proteomic profiling (Ibid, 2007) significantly.

Variations in sample-related factors and patient-related factors could significantly impact the data acquisition and analysis of data, which inadvertently affect the validity of the result obtained during vibrational spectroscopy of biological fluids. Sample-related factors such as the presence or absence of anticoagulant (Li-Heparin or EDTA) in the collection tubes of blood plasma has been shown to have some confounding peaks, which could interfere with the spectral peaks of the biological sample under investigation. Some authors have suggested that when the interfering peaks from the anticoagulants are filtered out from the spectra, an accurate representation of the biological samples under study can

be seen. In order to prevent this interference, since the serum is essentially plasma without the presence of fibrinogen, some authors have suggested that it is probably better to employ serum when analysis of biochemical components of blood samples is considered (Baker M et al., 2015). Secondly, the freezing process can affect the fibrinogen, making it coagulate irregularly.

Patient-related factors that could inadvertently affect the result of most spectroscopy (Ibid, 2015) studies include an improper choice of participants in the study group and control group. Recruitment into the study and control groups must be matched appropriately for sex, age, and other conditions, such as pathologies other than the disease of interest, so bias can be excluded from the study. Crucial because the observed differences in spectra could be attributable to the confounding factors instead of what goes on between the two groups under interrogation.

Specific technical features could essentially affect the validity of the analysis of the biological composition of the samples under investigation. Close attention should be paid to the interaction of the biological samples with light to maintain the result's reproducibility, robustness, and accuracy. Esmonde-White K et al. (2014) attempted to assess the impact of the substrate surface and fluid concentration on the dried outer ring's visual appearance and chemical heterogeneity. Light microscopy and Raman spectroscopy were exploited to interrogate the morphology as well as the chemical composition of the droplets.

Raman spectra were acquired over the surface of the outer ring in order to measure the chemical heterogeneity. Information on the chemical characteristics and the outer ring's geometry were acquired from the dried droplets in the form of Raman spectra and microscopic images. While the final deposition pattern was influenced by the substrate's lack of affinity for water (hydrophobicity), as demonstrated by the microscopic images. Subtle variations in the bands consistent with hydrogen bonding of aromatic amino acid were seen on the Raman data when fluids were diluted. Spatial heterogeneity of protein distribution was observed on the Raman maps in the outer rings, possibly due to the starting concentration of the biological fluid.

Nevertheless, the majority of the heterogeneity was seen in the undiluted droplets. Lavergne and colleagues demonstrated that the best reproducibility and absorbance intensity that was ideal for spectral analysis was observed with 3-fold dilution, and poor signal-to-noise ratio was observed for more than 3-fold dilution, which did not include the analysis of molecules at a low concentration in the

serum (Lovergne L et al., 2015). Therefore, heterogeneous deposition of the macromolecules should be considered when carrying out point-by-point spectroscopic analysis. Averaging of the spectra taken at three different points on the outer rings was utilised to combat our study's shortfall inhomogeneity of the outer ring spectra. In order to maintain a rigorous protocol for the experimental parameters, an automated sampling approach may be necessary to ensure reproducibility and consistency in data analysis and results. Translation of vibrational spectroscopy into clinical practice can be achieved if inter-instrument transferability can be ensured alongside other requirements, which is crucial as clinicians would want to see the same results from spectra obtained from the different optical equipment manufacturers (Esmonde-White K et al., 2014).

3.5. Biomarker in biological fluids

A biomarker is often defined as a characteristic objectively measured and evaluated as an indicator of normal biological processes, pathological processes, or pharmacological responses to a therapeutic intervention (World Health Organization definition). For instance, an antibody could indicate the presence of infection in the body, and cholesterol values are indicators and biomarkers for coronary and vascular disease conditions. It can be measured in the body through blood or tissue samples. Biomarkers are crucial in screening patients at risk and determining early disease stages, the prognosis of disease conditions, therapeutic response, and monitoring disease progression. Helpful in clinical practice since it helps guide clinical decision-making, especially when other morphological indicators are indeterminate. In oncology, it is well established that tumour cells are highly vascularised, and markers are shed into the bloodstream. A careful study of the blood samples could indicate the presence or absence of biological markers under investigation. There is compelling evidence that there is a high possibility of ascertaining the presence of some potential infectious organism within human beings via assessment of the individual, even at the asymptomatic phase. As a result, exploring such fingerprints in the person's biological fluid before becoming symptomatic is a welcoming development since treatment can commence. In most cases, treatment with curative intent can be administered safely.

Apart from blood, other biological fluids are relevant in the clinical environment and can be exploited for diagnostic purposes as well as monitoring therapeutic outcomes. Urine, sputum, pancreatic juice, bile, ascitic, pleural, and cerebrospinal fluids are close to the body's different organs that may be

diseased. Therefore, the biomarkers or biosignatures released from those organs or tissues are directly shed into the respective fluid. Because they are in close contact with the diseased structures, the biomarkers in those fluids are often in large quantities compared to those in blood samples. Other biofluids require an invasive procedure before the samples can be obtained. For example, cerebrospinal fluid does require lumbar puncture before the fluid can be obtained.

3.5.1. Why blood plasma and serum

Blood plasma and serum have been frequently employed for blood testing because they are made up of biomarkers convenient for disease diagnostics. The results obtained from these tests could indicate what goes on within the cellular and extracellular microenvironment, especially for disease conditions such as cancer.

Secondly, blood samples are easily obtainable with very minimal invasiveness. Blood samples are obtained from the vessels by trained medical personnel by inserting a needle into the vessel, and the blood can be withdrawn by suction through the needle into a collection tube. Because of the availability of blood samples, multi-centre studies can be carried out efficiently.

Thirdly, it is possible to repeat the blood test as often as possible to monitor disease progression and response to therapy, especially in oncology, where close patient monitoring is crucial.

3.5.2. Drop Coating Deposition Raman Spectroscopy

Drop Coating Deposition Raman (DCDR) spectroscopy involves the deposition of a drop of a solution of interest on a substrate. Followed by solvent evaporation, a coffee ring effect is allowed to form. Furthermore, the acquisition of Raman spectra from the analyte deposit occurs. This technique is mainly governed by the fact that components in the solution tend to precipitate in different regions on the DCDR substrate. It is always a good practice to ensure that the measurement positions represent the whole sample droplet. Often, DCDR is mainly performed by pipetting a small quantity of the solution around the region of 1-10 μL in volume to produce a protein spot of about 0.5-5 mm diameter on the substrate. After deposition of the solution on the substrate, time should be for the solvent to pre-concentrate to allow for evaporation. About ten minutes per millilitre deposition or one minute per nanolitre is ideal for evaporation. Using a smaller quantity of the deposited solution often results in faster drying of the deposited solution, thereby enhancing throughput. The ability to reproduce the

measurement is crucial in DCDR, and factors such as temperature and humidity tend to affect reproducibility.

Since Raman spectroscopy is essentially a scattering process instead of absorption, it can be performed on optically transparent or opaque samples and substrates. There is no need for optical tagging or another chemical pre-processing. Resonance Raman (RR) and Surface-Enhanced Raman Scattering (SERS) could potentially assist in increasing the Raman scattering cross-section of various compounds, including biological samples (Zhang D et al., 2003). RR only enhances Raman features firmly attached to the chromophores and could potentially omit other important structural information (Ibid, 2003).

Dongmao Zhang and colleagues published the first work on (DCDR) Spectroscopy in 2003. Measurement of Raman spectra of analytes acquired from low-concentration solutions could be possible through DCDR. It can also effectively separate proteins, lipids, and other vital components of biological fluids from fluorescent impurities and buffers (Zhang D et al., 2003). There are different contributing factors responsible for this separation. A 'coffee ring' effect occurs after solvent evaporation due to convective streaming, which occurs as a result of the evaporation of the liquid from the substrate. This effect is possibly responsible for the predisposition of proteins and other metabolites to assemble in a ring around the outer edge of the DCDR deposits (Ibid, 2003). Thermodynamics is another factor responsible for proteomic analyte segregation since pure solids generally possess lower free energy than solid solutions except for very different structures co-crystallized as the solid solution (Zhang D et al., 2004). Segregation may also be influenced by the differential solubility of different solution components (Ibid, 2004). For instance, since proteins are insoluble (relatively), they tend to precipitate early in evaporation. However, highly soluble compounds such as buffers or other compounds at low initial concentrations tend to remain dissolved in an evaporating drop for an extended time. They tend to deposit inside the region encircled by the outer ring (coffee ring) (Ibid, 2004).

Raman spectroscopy of the whole droplet can be time-consuming in a standard laboratory technique. DCDR can overcome fluorescence and buffer interferences to produce high-quality Raman spectra of solid analytes. Carey et al. utilised a Raman system with enhanced collection efficiency to obtain Raman spectra from protein solutions with a concentration in the 10^{-4} M range. Dongmao Zhang et al. (2004) demonstrated that it was possible to utilise the DCDR to acquire high-quality typical Raman spectra of

proteins acquired from concentrations as low as 1 μ M with approximately 1fmol of protein probed, using a 12 mW, 633 nm, HeNe laser (Zhang D et al., 2004).

3.5.3. Underpinning principles of Droplet evaporation

A contact line is often formed when a liquid droplet is deposited on a flat horizontal surface, the interface between liquid and solid, and that of liquid and vapour. The triple phase line is where the liquid, solid, and vapour meet, while the contact angle is the angle between the contact line and the surface of the solid, which Thomas Young first described in 1805 (Yuan Y., 2013).

Wettability is another core principle of droplet evaporation; it defines the ability of the fluid to be attached to a particular solid surface, which essentially is the measurement of the contact angle (Ibid, 2013). When the liquid spreads quickly on the surface of the solid, complete wetting is said to have occurred, and the contact angle is, therefore, zero. When the contact angle is less than 90 $^{\circ}$, the wettability is favourable, and the liquid spreads over a wider area. Therefore, this is described as hydrophilic. Hydrophobic surfaces are, therefore, surfaces with a contact angle greater than 90 $^{\circ}$ (Yuan Y., 2013).

3.5.4. Proteomic Profiling

Techniques that measure the compositions in biological samples can provide diagnostic fingerprints that could act as therapeutic and diagnostic indicators of a particular disease condition, particularly in the field of oncology, where the presence of malignancies has been known to show up as variations in the proteomic content of the blood (Issaq H et al., 2007). A large number of proteins depicted in a particular patient's blood at a particular time instead of just one particular biomarker could be utilised as a sensitive diagnostic tool for assessing the presence of a disease condition (Ibid, 2007). Therefore, it can be utilised as a basis to detect specific disease conditions that are asymptomatic before the first clinical symptoms become evident. Also, this could be utilised to monitor disease progression and determine treatment efficacy.

3.5.5. Metabolites and other chemical species screening

Raman bands in plasma were found to be related to carotenoids. About ten years later (488 nm excitation), the assignment was confirmed with a larger cohort of patients diagnosed with a wide range of cancers (Ozaki Y et al., 1996). In 1996, Ozaki et al. attempted to address the problem of the fluorescence background from plasma by utilising the chromatic aberration of the lens (514.5 nm excitation) to collect anti-stokes Raman spectra. The approach produced the same strong carotenoid

bands. After adding glucose artificially to both plasma and serum, the researchers exploited the intensity of a band at 1135 cm^{-1} to estimate glucose concentrations (Ozaki Y et al., 1996).

A protein native to blood plasma called C - reactive protein (CRP) is often utilised in a clinical environment as a biomarker for bacterial infection and tissue damage. With an inflammatory process, an elevated CRP concentration is bound to circulate in the blood. The reference concentration of CRP in a healthy adult is $<10\text{ mg/L}$. CRP has been shown to increase with age, possibly due to subclinical conditions such as asymptomatic carriers of a microbe. CRP concentration has been known to rise to 1000 times in the presence of inflammation. The liver synthesizes CRP in response to factors released by macrophages and adipocytes. However, there could also be some seasonal variation in the CRP concentrations. This concentration is not sensitive to a viral infection, making it easy to rule out the need for antibiotics. Interferon alpha prevents the production of CRP from the liver cells, which explains the relatively low level of CRP during viral infection compared to bacterial infection. Increased levels of blood CRP have been found in patients with avian flu H7N9 compared with H1N1 influenza. Elevated levels of CRP were documented in Wuhan, China, in 2020 as one of the clinical features of coronavirus (COVID-19) infection. C-reactive proteins have also been linked with the risk of developing certain cancerous conditions such as colon carcinoma. Nevertheless, there is no correlation between the genetic polymorphisms influencing the circulating level of CRP and carcinogenesis (Ibid, 1996).

In 2009, Researchers (Bergholt MS et al., 2009) from the University of Southern Denmark proposed that there could be a different method of measuring the CRP level from blood samples with the aid of vibrational Raman spectroscopy and multivariate analysis. This proof-of-concept study was based on the fact that Raman spectroscopy can be utilised to interrogate the vibrational frequencies of molecules. It is, therefore, possible to infer that the Raman spectrum of a particular molecule is, in principle, unique, and the Raman bands are narrow and highly resolved; therefore, Raman spectra are specific as a result. The basic principle governing this technique is a linear relationship between the Raman signal of CRP and CRP concentration (Ibid, 2009).

The authors obtained 1 mg of human plasma CRP in a buffered aqueous solution containing Tris aminomethane, sodium chloride, calcium chloride, and sodium azide. With the aid of a 785 nm excitation laser, Raman spectra of CRP in the blood plasma from 40 donors (Bergholt MS, 2009) were acquired. The blood samples were taken from healthy individuals and those with a bacterial infections. In order to avoid thermal effects such as burning, the laser power was maintained at 14 mW. All the

necessary data pre-processing and post-processing techniques were applied. With this proof-of-concept study, the researchers demonstrated that Raman spectroscopy and multivariate analysis could be utilised to predict the concentration of CRP in the presence of patient-to-patient variations. Improved laboratory productivity and point of care system could be achieved through this method when compared to the current biochemical techniques (Ibid, 2009).

3.5.6. Metabolites in Cancer diagnostics

Metabolic activities are often seen altered in the presence of cancer cells, especially compared to normal cells. The alterations ensure that the oncogenic characteristics are maintained (Phan LM et al., 2014). Metabolic reprogramming is the traditional metabolic pathway whose activities are either enhanced or subdued in tumour cells compared to benign due to carcinogenic mutation and other factors (Ibid, 2014). On the other hand, oncometabolite often indicates metabolites found in large quantities in the presence of cancer cells. Oncometabolites are often referred to when there is a distinct mechanism linking a particular mutation in the tumour to the large concentration of the metabolites. Also, there should be an indication of the metabolite's association with the carcinogen's tumour (Ibid, 2014).

Reprogrammed metabolic pathways are often referred to as the Warburg effect or aerobic glycolysis because Dr Otto Warburg observed for the first time in the 1920s that there was an altered metabolism of cancer cells.

3.5.7. Glycolysis:

Glycolysis is, therefore, a physiological reaction to lack of oxygen (hypoxia) in normal tissues; however, in the 1920s, Dr Otto Warburg discovered that tumour slices and ascitic cancer cells constantly absorb glucose and, in return, give out lactate irrespective of the presence or absence of oxygen.

3.6. Raman spectroscopy of blood constituents and cancer diagnostics

In 2013, Murali Krishna et al. obtained serum from 40 patients with tongue cancers and compared it with 16 healthy control samples. They observed differences in bands associated with nucleic acids (the differences suggested an increased cell-free DNA) and a decrease in the concentration of β -carotene for patients in the cancer group (Sahu A et al., 2013). When the study was repeated in 2015 with a larger population group (328 donors, 785 nm excitation) and additional dimension of precancer

chemical conditions, the result was consistent with the previous study in 2013 (Sahu AK et al., 2015) with the feasibility of precancerous and specific cancer detection. Sensitivity and specificity of 64% and 80% were recorded to distinguish between normal and abnormal models. These rates are comparable to standard oral cancer screening approaches (Ibid, 2015). Another study from the same group was carried out in 2015 with the focus on discriminating between serum from patients suffering from malignant tumours who had endured a recurrence of their cancer post-surgery and serum from a patient suffering from malignant tumours who had not (Sahu A et al., 2015). While the spectra reported negligible pre-surgery differences between serum from recurrence and non-recurrence patients, the post-surgery spectra revealed quantifiable differences. These changes were possible due to the groups' DNA and variable protein content (Sahu AK et, 2015).

Researchers from Guangdong, China, conducted a similar Raman spectroscopy study regarding cancer detection with blood plasma. They utilised the drop-coated deposition technique on plasma from patients with colorectal cancer (15 patients) and normal healthy controls (21 volunteers). The Raman data (785nm excitation) suggested an increased level of cell-free DNA and a decreased level of β -carotene in the cancer group, similar to the study reported above. Two mechanisms have been proposed to be responsible for the increased nucleic acid level in the blood plasma of participants with cancer (apoptosis/ necrosis or release of intact cells in the bloodstream and their subsequent lysis). At the same time, a reduction in the β -carotene was also observed. This result was consistent with previous reports (Li P et al., 2015), which were in keeping with a deficiency of anti-oxidant species as an essential risk factor for advancing precancer cancer.

3.7. Establishing the biochemical basis of urological disease measured with Raman Spectroscopy.

The biochemical basis of urological pathologies such as prostate and bladder diseases has recently been studied with Raman Spectroscopy. The biochemical changes that occur in tumour-related disease conditions are believed to be a gradual process that goes from normal to malignant (Stone N et al., 2007b) disease condition. As a result, detecting precancers within the tissues will involve detecting the biochemical changes associated with the disease advancement before they become malignant (Ibid, 2007). Useful in clinical practice because if disease conditions are depicted at early asymptomatic stages but can potentially progress to malignant conditions, therapeutic options can be adopted to ensure that the situation is arrested without causing many problems for the patient. The result of the study by

Stone et al. depicted that the relative DNA content increased as the tissue advanced from normal to malignancy within the bladder and prostate gland tissues.

In contrast, in the bladder, the collagen content decreased. This result was anticipated because the nuclear to cytoplasm (actin) ratio increases from normal to malignant tissue. In malignant conditions, DNA is often found in a large nucleus concentration (Ibid, 2007). Secondly, the cells increase in number, and as a result, the extracellular matrix, which is rich in collagen, is reduced until the tumour becomes prominent. Then more collagen is therefore expected (Ibid, 2007).

As a potential model for necrosis, cholesterol was utilized; as the tumour increased in size, necrotic areas became more prominent within the tumour because it became too big for its blood supply. This study demonstrated an increase in cholesterol as the tumour progressed from benign to malignant disease and increased severity (although the bladder showed a relatively lower concentration than the prostate). Choline levels were also shown to increase with disease progression in the bladder and prostate gland, although still in low concentrations. It is expected for the choline level to increase with membrane synthesis for cell proliferation. Choline has been utilised as a marker for breast cancer in the past as well (Ibid, 2007).

3.8. Clinical utilisation of Raman spectroscopy

The development of a disease condition results in cells becoming dysfunctional, leading to disease-specific changes in the expression of molecular components. One abnormal molecular component can lead to other components becoming abnormal as well. For instance, when the proteins that maintain the stability of the genome fail to function appropriately, DNA aberration occurs, leading to more abnormal protein expression and DNA aberration.

Cancer is a disease of uncorrected DNA mutations which translate into abnormal protein expression and eventually change in other molecular components. As a result, the cell's chemistry can be impacted significantly. These chemical changes can take the form of new or unique signals associated with these changes in the molecular components that arise from the disease. Raman spectroscopy (RS) can be utilised to characterise the biochemical properties of cells. Since the cell structure changes as the tumour become differentiated, the Raman technique can characterise different stages in the progression of a cell, from normal to cancerous.

RS can differentiate between benign and malignant tumours and pre-malignant steps such as dysplasia, which is often difficult for pathologists to distinguish reliably. A wide range of tissues has been shown, including the brain (Desroches J et al., 2019). Jermyn and colleagues have developed a Raman system with a handheld probe for intraoperative use during brain tumour resection. Spectra were obtained from 17 patients with 0.2 seconds acquisition time. Only patients with grade 2 to 4 glioma were included. Normal brain tissues were differentiated from dense cancer, and the normal brain was invaded by cancer cells. A sensitivity of 93% and specificity of 91% were reported for this study by the group (Jermyn M et al., 2015). Their findings were consistent with other studies in this field, with cancer tissues showing an increased nucleic acid concentration than normal brain tissues. However, a population size of 17 seems relatively small to depict all the variances within the spectra. One would have expected a larger population size to depict what goes on within the tissue samples.

Vibration spectroscopy has previously explored skin cancer (Zhang et al., 2018). In 2008, Zhao and colleagues utilised a single-fibre Raman probe to assess nine different skin cancers, including basal and squamous cell carcinoma. A sensitivity of 91% and specificity of 75% were achieved in differentiating between malignant and benign lesions (Zhao J et al., 2008).

Breast cancer has also attracted many researchers' interest in oncology and photonics (Lyng FM et al., 2019); Saha et al. utilised a multi-fibre Raman probe to assess microcalcifications in the breast of patients. A positive predictive value of 97% for detecting microcalcification was recorded (Saha A et al., 2012).

Widjaja and colleagues assessed 105 colon samples with an in-house built Raman probe. A classification model was built to differentiate the samples into different groups. The samples were differentiated into different groups with a diagnostic accuracy of 98% (Widjaja E et al., 2008).

Cervical cancer was assessed by Mahadevan-Jansen et al. in 1998. Kanter and colleagues could utilise a handheld portable Raman Spectroscopy probe to differentiate between low and high-grade squamous intraepithelial lesions and normal tissue. Accuracy for classification was 88%, with a sensitivity of 86% and specificity of 97% (Kanter EM et al., 2009).

Tumours in other locations in the body, such as Larynx (Stone N et al., 2000), lymph nodes (Rau JV et al., 2019), and oesophagus (Stone N et al., 2004), were characterised and are currently being investigated by researchers. Stone et al. (Ibid, 2004) introduced the concepts of RS for various epithelial

cancers and suggested methods of translation of the approaches and interpretation of the data for clinical decision-making. The above studies have demonstrated the potential of Raman spectroscopy in clinical practice. Nevertheless, it is also important to note that these were all proof-of-concept studies, and as such, they are yet to make their way into the clinical environment.

3.9. Raman Spectroscopy in prostate cancer

3.9.1. Tissue diagnosis and prediction of cancer grade:

Crow et al. (2005) demonstrated that it was possible to utilise RS in differentiating between different prostatic adenocarcinoma cell lines in the prostate. Raman spectra were measured from two well-differentiated androgen-sensitive cell lines (LNCaP and Pca2b) and poorly differentiated androgen-insensitive cell lines (DU145 and PC3). Molecular differences between the cell lines were determined with the help of Principal Component Analysis and linear discriminant analysis applied to 200 spectra to construct a diagnostic algorithm capable of differentiating between the different cell lines. The overall sensitivity of 98% and specificity of 99% were recorded, respectively.

The result of the findings of the study conducted by these researchers (Ibid, 2005) demonstrated that a lower concentration of glycogen was associated with poorly differentiated cell lines (DU145 and PC3) when compared to well-differentiated cell lines (LNCaP and Pca2b). Raman spectroscopy has also demonstrated that glycogen (Crow P et al., 2003) is a significant marker for benign tissues. It has been shown with RS to be increased in cells that can tolerate radiation therapy (i.e., radiosensitive cells).

In 2003, Crow et al. conducted an RS study to identify and grade prostatic adenocarcinoma. Following informed consent, one extra biopsy sample was obtained from all the recruited patients undergoing routine biopsy procedures as part of their standard routine care. Those biopsies were snap-frozen with liquid nitrogen to reproduce in vivo conditions as closely as possible and transferred to a -80°C freezer for storage. The frozen biopsies were sectioned onto UV-grade calcium fluoride (Crystal). They were thawed in preparation for Raman measurement using a Raman system (Renishaw 1000) optimised for tissue measurement at an 830 nm laser line. The findings of this study indicated a reduced glycogen content and increased nucleic acid content in malignant prostate tissue samples compared to benign prostate tissue samples. These findings are consistent with the findings of previous studies of the larynx (Stone N et al., 2004), colon (Feld MS et al., 1999), oesophagus (Mahadevan-Jansen A, 1996), and cervix (Mahadevan-Jansen A et al., 1998).

The Raman spectra provide a global tissue fingerprint in biomolecules such as amino acids, proteins, lipids, carbohydrates, RNA, and DNA. This information was utilised to distinguish between prostatic and extra-prostatic tissue and detect prostatic tissues with different cancer grades. Peaks predominant in malignant tissue were made up of DNA/RNA, keeping with the increased proliferation rate associated with cancer cells. Classification accuracy for benign and malignant tissues was achieved at 86% with a sensitivity of 87%, specificity of 86%, and Area Under the Curve (AUC) = 0.93. Dominant peaks for low Gleason Grade Group (GG1) comprised proteins and lipids such as amide 1. On the other hand, the dominant peaks for higher cancer grade (GG5) were related to the presence of DNA/RNA, consistent with higher nucleic acid content in keeping with higher tumour grade.

The clinical need for precision in prostate cancer diagnosis and possibly improving surgical resection during radical prostatectomy led to a proof-of-concept study conducted to assess the efficacy of Raman spectroscopy as an appropriate tool for diagnosis and possible grading of prostate cancer. Aubertin et al. recruited about 32 participants who underwent prostate biopsies with more than two cores having prostate cancer at a biopsy involving >10% of each positive core. With the aid of a custom handheld contact, a Raman spectroscopy probe made up of seven 300 μm core detection fibres surrounding a 272 μm core excitation fibre by which a wavelength stabilized 785 nm laser light was passed. Supervised machine learning neural network methods and leave one out cross-validation were utilised to classify the spectra. The distinction between benign and malignant tissue samples was achieved with the aid of the whole spectrum (500-1700 cm^{-1}) with a sensitivity of 87% and specificity of 86% (Aubertin K et al., 2018).

3.9.2. Assessment of surgical margin following radical prostatectomy:

Positive surgical margins are often associated with tumour at the inked surface of the surgically excised section of the prostate gland. It can result from an incision through the capsule across the tumour that is an extracapsular or unplanned incision into the prostatic capsule in the tumour localised within the prostate (Shuford M D et al., 2004).

The most accurate determination of margin status is often based on the histopathologic evaluation of the removed prostate specimen instead of examining small remnants of in vivo tissue (Cookson MS, 2010).

Ten-year progression-free survival rates of men with organ-confined tumours in the prostate gland have been recorded as 85%. Nevertheless, that rate drops to 55% in men with positive surgical margins and extracapsular extension. The prognosis worsens with positive surgical margins and extracapsular extension. Cookson and colleagues have shown that positive margins range from 4-40% (Ibid, 2010).

RS possesses a high potential for quick intraoperative margin assessment and diagnosis. Since sample preparation is unnecessary, tissue damage does not usually occur if appropriate wavelength and laser power levels are applied. With the advent of fibre optic Raman probes, surgical robots can potentially be coupled to intelligent Raman probes to perform in vivo targeting of surgical margins.

Haka and colleagues examined frozen breast cancer tissue samples both as an in vivo and ex vivo study using RS following partial mastectomy (Haka A et al., 2009), which was achieved with the aid of a fibre optic Raman probe. Both the ex vivo and in vivo Raman spectra data were in good agreement, and the feasibility of RS for intraoperative margin assessment, thereby inferring that the re-excision surgeries from positive margins determined by Raman signal can be reduced in partial mastectomy breast.

Crow et al. studied to ascertain if a fibre-optic Raman system could be utilised to differentiate between the benign and malignant bladder and prostate tumours through in vitro means. In contrast, the bladder algorithm could differentiate benign samples from transitional cell carcinoma samples with an overall accuracy of 84%. The prostate algorithm could differentiate between benign and malignant diseases with an accuracy of 86%. However, the group failed to identify accurately the biochemical constituents that allowed for differentiation among the various pathologic findings (Harder SJ et al., 2015).

After radical prostatectomy, assessing the resected prostate tissues is common practice to rule out the presence of cancer cells within the surgical and anatomical margin. This routine practice is critical because if cancer cells are left behind in the tumour margin, it could increase the risk of biochemical recurrence. Therefore, a positive surgical margin is an evidence that some cancer cells have been left behind at the tissue surface when surgical intervention. During surgery, the surgeon has to decide whether to preserve the neurovascular bundle or not. This decision-making process always has a trade-off, and careful risk analysis and calculation should always be considered. A nerve-sparing approach during prostatectomy prevents unfortunate side effects such as impaired sexual functions. Although surgery is often planned after the result of the biopsy or other diagnostic examination, the decision on

whether to preserve the neurovascular bundles or not is often decided at the time of surgery. About 20% of radical prostatectomies often have positive surgical margins (Auner GW et al., 2018), which ultimately increases the chances of biochemical recurrence of patients with positive margins. Therefore, to mitigate against this unfortunate recurrence, frozen section analysis is often carried out, whereby microscopic analysis of the tissue specimen is carried out after the surgery. The downside of this technique is that histological assessment of the surgical margin possesses a low sensitivity in detecting the presence of cancer cells left behind during surgery (Ibid, 2018). Therefore, there is a need to develop a more accurate diagnostic technique to evaluate the surgical margins for the presence or absence of tumour cells within an acceptable surgical window (time frame). Tactile resonance sensor technology has been demonstrated to have the ability to distinguish between stiff and soft tissue in medical applications. This capability can be helpful in oncology since this can be exploited to differentiate between cancerous and normal epithelial tissues.

Moreover, stroma and prostatic stones (benign conditions) often have higher tissue stiffness, which could be challenging to distinguish from prostate cancer tissue. Based on this premise, if precision in differentiating between benign and malignant lesions is to be achieved, there is a need for a complementary diagnostic tool with a high level of accuracy in diagnosis. Raman spectroscopy and tactile resonance sensor coupled together could increase the sensitivity and specificity when assessing tumour margins to rule out the presence of positive margins following radical prostatectomy. In 2015, Nyberg M et al. developed a dual-modality probe with a tactile resonance sensor (stiffness modality) and Raman spectroscopy. A fibre optic probe was inserted into a hollow stiffness sensor and connected to a 785 nm laser Raman spectroscope (Kaiser Optical). The operator could switch between the two modalities without moving the probe. A total of 36 measurements were acquired ex vivo on four prostatectomy tissues. Stiffness, autofluorescence, and Raman peak found at 2881 cm^{-1} were utilised as discriminatory parameters. Nevertheless, strong fluorescence leads to lower detectability (77% sensitivity and 65% specificity). Moreover, with the combination of stiffness and autofluorescence, a sensitivity of 100% and specificity of 91% was achieved, which is quite impressive (Nyberg M et al., 2015).

3.9.3. Detection of metastasis:

Lymph node metastasis predicts local disease recurrence and lower survival rates for breast cancer patients. Examining the sentinel nodes is an excellent method to detect if the tumour has spread

beyond the breast to the lymphatic system (lymphatic spread) (Day JC et al., 2013). RS has been utilised to interrogate axillary lymph nodes intraoperatively during breast cancer surgery, demonstrating a sensitivity of 91% and specificity of 93% for distinguishing between positive and negative nodes in newly diagnosed breast cancer patients. Mean spectra assessment from the positive and negative groups suggested that positive nodes have increased DNA and tyrosine contributions and reduced levels of collagen contributions when compared to the negative nodes (Shipp DW et al., 2018). Similar technology can be applied to detect the involvement of pelvic lymph nodes in prostate cancer.

3.9.4. Assessment of castration resistant prostate cancer:

Wang L et al. (2013) evaluated the feasibility of using RS as a diagnostic and prognostic tool in assessing castration-resistant prostate cancer. Raman spectra were detected from prostate cancer cell lines (LNCaP and C4-2) using a LabRAM HR 800 Raman Spectrometer. The prediction was achieved with the aid of Principal Component Analysis (PCA) and Support Vector Machine (SVM). A leave-one-out cross-validation was used to train and test the SVM. Castration-Resistant Prostate Cancer tissues were diagnosed effectively with a sensitivity of 88.2% and specificity of 87.9%. Androgen Dependent Prostate Cancers were also diagnosed and differentiated from Castration-Resistant Prostate Cancer with a sensitivity of 85.7% and Specificity of 88.9% (Wang J et al., 2013). Tissue classification in the above studies was based on overall patient diagnosis and not on local histological analysis matched with the Raman optical measurements.

Most cancer-related deaths in men with prostate cancer occur due to metastatic prostate cancer (Corsetti S et al., 2017), resistant to hormonal therapy (Androgen Deprivation therapy). With a high chemical specificity of RS, subtle molecular variations at the cellular level can be detected and quantified for diagnostic purposes. Corsetti et al. (2017) demonstrated in their study the presence of a higher concentration of phenylalanine, tyrosine, DNA, and amide 111 in androgen-resistant prostate cancer cells in contrast to normal cell (PNT2) with a higher concentration of L-arginine. They had a B configuration of DNA (Ibid, 2017).

3.9.5. Monitoring treatment effectiveness:

The work of T. R. Ashworth in discovering tumour cells in the blood of patients with metastatic cancer over a century ago has made it easier to understand and target the cause of metastasis in many malignant conditions (Ashworth TR, 1869). Circulating tumour cells (CTC) are shed by primary tumours and are found in the peripheral blood of patients with metastatic cancers (Yu L et al., 2013). Since CTCs are found in the peripheral blood, they can be carried to distant structures to form secondary deposits

(tumours), affecting the disease's severity and prognosis. CTCs have been detected in PC patients (Danila DC et al., 2007) as well as melanoma (O'Brien CM et al., 2011), breast cancer (Meng Set al, 2004), lung cancer (Hou JM et al., 2011), colon cancer (Marrinucci D et al., 2010) and pancreatic cancer (Rizzo FM et al., 2019) patients. However, Allard and colleagues have demonstrated that CTC has never been detected in benign tumours or healthy individuals (Allard WJ et al., 2004). It has been demonstrated that CTC counts have consistently decreased with a decrease in the tumour sizes of patients undergoing treatments (Ross JS, 2009), which can be a handy tool in monitoring treatment effectiveness and establishing drug-resistance and drug-sensitive biomarkers. The progression of an early primary tumour to metastasis has always been an area of keen interest within the clinical environment. Understanding the functional and molecular analyses of CTCs is crucial in managing metastatic cancers. Since CTC counts are closely related to patient prognosis, it is crucial to adopt a sensitive detection approach to precisely detect and count the isolated CTCs. It is also essential to keep the in vivo environment as close as possible to their native environment to accurately characterise the cells to understand their biology.

The genomic profiling of CTCs from castration-resistant metastatic prostate cancer can be analysed using array comparative genomic hybridization (aCGH) (Magbanua MJ et al., 2012). However, relatively low cell numbers often hinder molecular profiling and quantitative analyses of CTC. The multistep separation process also tends to compromise the viability of the CTCs in revealing their molecular and functional nature.

The lack of a reliable universal marker to characterise CTCs arising from different malignant tumours associated with the low purity and low throughput of these strategies has prevented the use of CTCs to guide therapeutic decisions by clinicians.

Using lab-on-a-chip (LOC) to isolate viable CTCs with high efficiency, purity, and throughput for post-processing can bring about a fresh approach to assessing tumour cell biology, signaling, and drug sensitivity (Wang X et al., 2011).

There is currently evolving development in the use of Nanoparticles (NPS) such as quantum dots (QD), metal NPs and liposomes in the practical analysis of rare cells due to their distinct size-dependent optical, electronic, and magnetic properties.

Combining nanotechnologies and miniaturised biomedical systems with cell biology has a powerful influence on biomedical research. The physical dimensions of cells and their native cellular microenvironment are in the order of micrometres, which correspond well with the scales of the microchannels.

Surface-enhanced Raman spectroscopy (SERS), which enhances the signal of molecules near the surface of nanoscale features in noble metals, has been used to measure gold nanoparticle-targeted CTCs in the presence of white blood cells without subsequent separation procedures (Magbanua MJ et al., 2012). Although the CTCs had more intense Raman signals than the blood cells, probably due to their larger sizes.

In summary, we have shown that Raman spectroscopy can probe the biochemical composition and function of biological samples, which can be utilised to assess the presence of early-onset diseases such as precancers. C.V Raman and K.S Krishnan were the first to observe the inelastic scattering in an organic liquid. The interaction of light with the intramolecular bond within the biological samples has been shown to carry with it biochemical information that is unique to the molecules as well as its environment, therefore providing a Raman spectrum which is a direct function of the molecular composition of the biological sample.

Chapter 4 – Methodology

In this chapter, we will first look at the basic Raman instrumentation for measuring biological samples, followed by alignment and calibration of equipment, sampling stage, preparation, and presentation. We will explore the experimental setup, data analysis, multivariate and histological analysis, and Raman spectroscopy data analysis techniques.

4.1– Basic Raman Instrumentation for measuring biological samples

It is well established that Raman spectra of tissues and biofluids can easily be measured using a microscope or fibre. The laser is often coupled into the microscope using a single-mode fibre and irradiated onto the specimen with a microscope objective. Raman spectroscopic-based confocal imaging can be achieved by collecting the backscattered light using a fibre. The single fibre acts as a pinhole and couples the light into a high-throughput spectrometer that disperses it onto a charge-coupled device (CCD) camera. Hyperspectral Raman imaging is a rapidly advancing technology in the vibrational spectroscopy field, which involves the acquisition of Raman spectra at distinct points over the surface or cross-section of the biological sample under investigation, and analysis is carried out to acquire a spectral-based image. Often fast raster scanning is usually carried out with the aid of a motorized or piezoelectric stage. Although Raman signals received from biological samples are often weak, the advent of new developments in the detectors and instrumentation has significantly improved the speed at which Raman spectral acquisition, decreasing the image acquisition time from hours to minutes while providing high-quality images. There are different variations of Raman microscopy system available in practice, and these include Raman microscopy systems (Puppels GJ et al., 1990), light sheet-excited direct Raman microscopy (Oshima Y et al., 2012), and line scan Raman microscopy (de Grauw CJ et al., 1997).

Selecting the correct laser excitation wavelength is crucial in measuring the Raman spectroscopy of biological samples. The Raman signal is known to scale with the fourth power of the excitation frequency. Often, a compromise between decreasing the background autofluorescence and amplifying the Raman signal intensities (both increase as the wavelength decreases) is always considered when deciding on the choice of wavelength to use for the measurement of Raman data.

Optimizing this balance is highly dependent on the sample type and application. Adequate Raman signal and acceptable low autofluorescence under near-infrared (NIR) 785-1048 nm laser excitation are often observed for measuring biological tissues. However, some tissues can have high autofluorescence,

although NIR excitation has been employed. These tissues include kidneys, spleen, liver, heart, and lung (Huang N et al., 2011). However, for samples with low degrees of autofluorescence, such as bone, cartilage, and cell monolayers, it is advisable to utilise shorter excitation wavelengths, such as 532 or 633 nm, which increases the speeds of the acquisition time as a result of the generation of stronger signals (Ibid, 2011).

Different Raman microscopy systems provide slightly different resolutions, although in most cases, it is diffraction-limited and, therefore, greatly relies on the excitation wavelength and the objective choice. For a state-of-the-art confocal Raman system with visible excitation, the lateral resolution can reach as low as 300 nm and the depth resolution can reach less than 500 nm for sufficiently small pinhole settings (Ibid, 2011).

4.2. Alignment and calibration

When the spectrograph and laser focal point are brought into a perfect sequence, it is called alignment. An offset at the sample end may impact the intensity of the Raman scattered light received, which may result in the microscope performing at a suboptimal level. Over the years, it has been observed that the Raman microscope does suffer some alignment issues, such as drifts resulting from temperature fluctuations in the laboratory, normal wear and tear of the components of the instrument, and external interferences. This misalignment must be adjusted periodically by the manufacturer to ensure that the equipment is functioning at an optimal level with adequate Raman signal acquisition and spatial resolution.

Equipment calibration was carried out before any measurement was performed to ensure that the accuracy of Raman measurement was maintained at all times. A neon lamp, photodiode, a small piece of polystyrene, and a broadband white light source were used to calibrate and align the micro-spectrometer. Aligned the optical path from the spectrometer and laser beam was done with photodiodes and polystyrene. Calibration of the excitation laser frequency and multi-point x-axis calibration for satisfactory correction for distortion and allow for spectrograph-to-spectrograph data transfer were also executed using polystyrene.

4.3. Sampling stage

A Raman map was acquired using an array of Raman spectra at predetermined positions in the biological sample. Traditionally, the instrument stages were driven by motorized steppers, while

modern systems are based on the raster scanning principle, providing a faster imaging system. While the traditional instrument utilizes the point-by-point scanning approach whereby one spot of the sample is imaged simultaneously, the contemporary approach allows for continuous scanning without stopping, sometimes referred to as a line-by-line scanning approach. For this study, point-by-point scanning was carried out, and a magnetic linear motor stage was used to move the stage from one point to another.

The charge-coupled device measured signals generated from the vibrations of molecules from the chemical bonds irradiated by Raman spectroscopy. Variation in the concentration of the molecular composition, the nature of the molecules' functional groups, and its conformation was determined by the signal intensities of the scattered light. Therefore, the vibrational spectroscopic bands were governed by the nature of the molecular functional groups and their conformation. The vibrations of specific biological molecules such as phospholipids, proteins, and carbohydrates provide considerable detail regarding the molecules' morphology and concentrations within the biological samples. As a result, after the interaction of light with the biological samples, the emitted photons carry vital information regarding the molecular structure and composition of the sample under investigation. The Boltzmann distribution of the vibrational state has most molecules in the ground vibrational state, often seen at ambient conditions. Therefore, the incident photons have higher energy than the scattered Raman photons from the ground state. Anti-stokes Raman scattering occurs from the vibrationally excited state that is thermally populated and results in the scattered photon that goes back to the ground vibrational state. At ambient conditions, anti-stokes Raman scattering is often weaker than Stokes Raman scattering. Therefore, stokes scattering is often utilised in mapping experiments.

4.4. Sample preparation and presentation

Certain factors must be considered when considering biological samples for vibrational spectroscopy measurements. These considerations include how the samples would be prepared and processed and the vibrational spectroscopy technique suitable for the application. These must be thought of before any acquisitions can be carried out. It is critical in the sense that, as much as Raman spectroscopy can be compatible with water and its vicinity, on the other hand, Fourier transform infrared spectroscopy may not function effectively in an aqueous environment. Therefore, with Raman spectroscopy, acquisitions can be obtained from biological tissue samples placed in saline solution without any adverse effect on the Raman signal expected (Bergholt MS et al., 2016). As a result, with Raman spectroscopy acquisition, there is no need for sample fixation, embedding in

paraffin wax, or dehydration. However, it is essential to analyse biological samples with flat surfaces to ensure that the same focus is adopted for the investigated area.

4.5. Experimental set up

Ethical approval was obtained to take an extra core during the prostate biopsy of participants as part of the standard care of the patients. Additional blood samples were also collected from each participant following informed consent. The biopsy samples were immediately snap-frozen in liquid nitrogen, mounted on cellulose acetate paper, and transferred to a -70°C freezer for storage at Darent Valley Hospital (recruiting NHS Trust) until couriered on dry ice to Exeter for measurement. The frozen biopsy sections were mounted on a calcium fluoride slide and thawed before Raman measurement. With the aid of an optimised Raman India system (Renishaw) (Figure 4.1 below) exploiting a diode laser light producing a 300-mW power of near-infrared light at 830 nm wavelength.



Fig. 4.1: InVia Raman Microscope

<https://www.renishaw.com/en/invia-confocal-raman-microscope--6260>.

The laser was precisely targeted at the tissue sample through an ultralong working distance times 50 microscope objective. A white light camera was mounted on the microscope which permitted the visualisation of dark field within the area of interest. The laser spot were moved to random locations within the tissues samples to allow up to 5 spectra (4 spectra were acquired from some samples) to be recorded from each sample as shown in the figure 4.2 below.

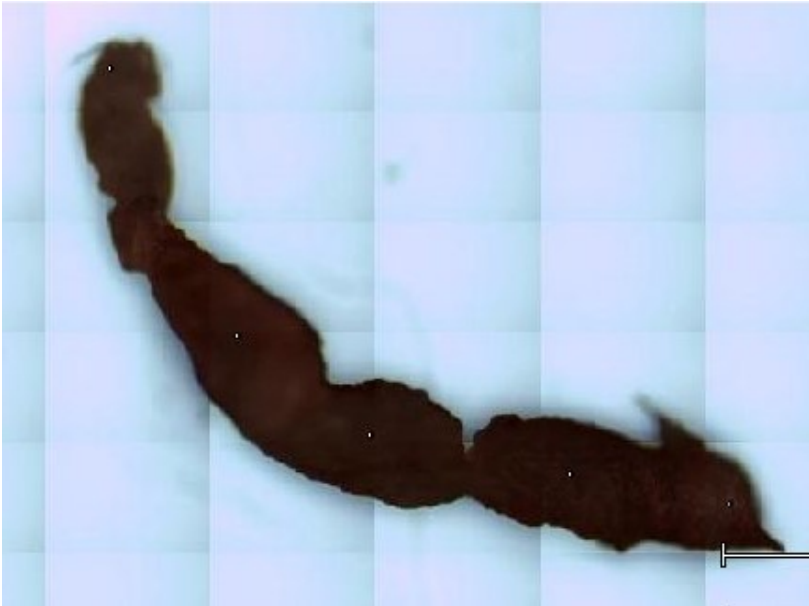


Fig. 4.2: Prostate biopsy tissues measured by Raman at 5 distinct position.

Each Raman spectrum was recorded on the spectrometer using an acquisition time of 20 seconds. Calibration of the system was always done every time the unit was switched on with the aid of the Renishaw silicon calibration source to correct any wavenumber shift.

After Raman measurements, the biopsy samples were transferred to a -80°C freezer for storage until it was time for histological assessment.

The biopsy samples were couriered to Maidstone and Tunbridge Wells NHS Trust for histological analysis. The sections were stained with H&E, and a Consultant Uro-Pathologist performed a histopathological assessment. Spectral data were loaded onto the Matlab platform (MathWorks Inc, Natick, Massachusetts) in conjunction with the PLS Toolbox (eigenvector, Manson, Washington). The Raman spectra were then linked to the histopathology of each participant. The model was tested using a leave-one-out cross-validation.

Following informed consent, blood samples were collected from 100 participants and spun down using a centrifuge. The blood serum and plasma samples were separated and stored in a -70°C freezer. These samples were maintained at -70°C until they were couriered on dry ice to Exeter for Raman spectroscopy measurement. The plasma and serum were defrosted at different times, and 1.5 microlitres were pipetted onto a clean stainless-steel slide. A coffee ring drying pattern with a diameter of approximately 1.7 mm and a width of approximately $100\ \mu\text{m}$ was allowed to pre-concentrate the solution in ambient conditions in the 22°C lab. The coffee ring pattern (Figure 4.3 below) emerged from

a capillary flow in which the attachment of the contact line of the drying drop ensured that solvent evaporating from the drop edge was replenished by liquid from the internal part of the drop. The outward flow of the solvent carried the solute material toward the edge of the drop.

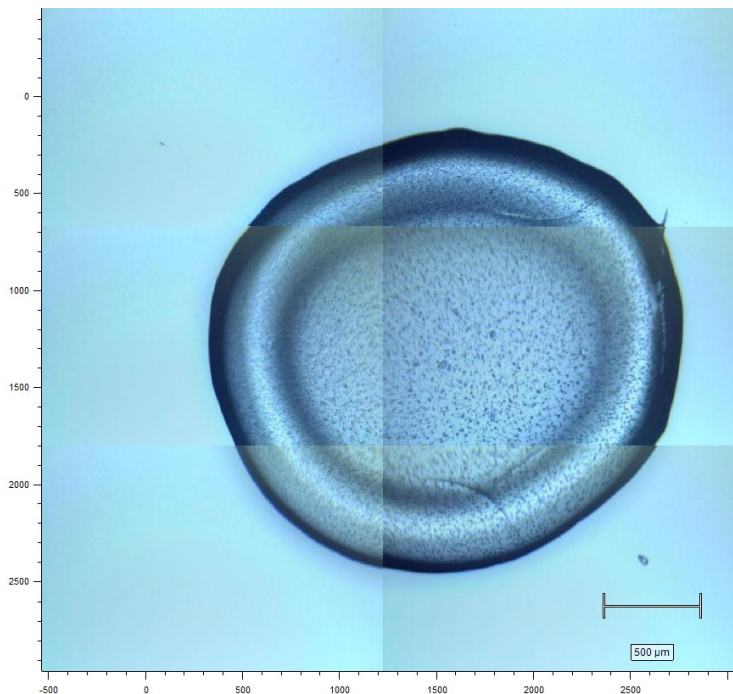


Fig. 4.3: Dried blood serum with measurement taken from the circular ring on the periphery of the dried sample.

After 20 minutes following the deposition of the blood sample on the substrate, Raman spectra were measured at known positions on the sample using a micro-spectrometer by placing a circular ring of Raman map on the periphery of the dried sample to obtain Raman spectra. PSA and prostate pathology status were used to calibrate the machine learning model to evaluate if the drop-coated deposition Raman spectroscopy of blood plasma and serum can predict prostate cancer and cancer stage and grade.

With the aid of the 5X objective (Olympus, Ultra Long Working Distance (ULWD)), a white light montage image of all the drops on the stainless steel was obtained. 50X objective (Olympus, ULWD), Numerical Aperture 0.75 to allow for adequate focus of the laser onto the sample on the stainless steel from the montaged white light image using an 830nm diode laser line with an edge filter to get rid of the unwanted elastically scattered light with a 600 grating with an exposure time of 5 seconds at one accumulation. Approximately 8 minutes were taken to measure a Raman map of one droplet. The backscattered radiation was collected, and spectra were acquired in static mode with the wavelength

centred at 1400 cm^{-1} to ensure that the fingerprint region ($400\text{-}1800\text{ cm}^{-1}$) was included in our acquisition.

4.6. Data Analysis Techniques

Spectroscopy is a method of analysing the properties of matter as a result of its electromagnetic interactions. There are two main goals of spectral analysis: classification and quantification. With classification, we are routinely interested in distinguishing between different types of tissue, cells, or biofluids. In this study, spectral analysis was utilised in differentiating between normal/benign and malignant tissues and biofluids. With quantification, we were interested in measuring the concentration of different molecular components within the prostate tissue, blood plasma, and serum.

Different steps are necessary for a precise spectral analysis of the acquired data. These steps included the following: system calibration, pre-processing of data, empirical peak height, area measurements, and multivariate approaches for classification. Diagnostic algorithms were built to detect subtle changes in spectral features, thereby leading to spectral separation into significant groups. The algorithms were based on empirically identifying diagnostic features such as peak intensity and the number and location of peaks. In order to assist in extracting relevant chemical (clinical) information, online data analysis was performed.

The main aim of the spectral analysis was to classify the spectra into predetermined pathological groups, which allowed for the classification of spectra with pathology analysis. It was helpful because sometimes it can be challenging to find specific bands that can be utilised to discriminate between the different pathology groups. Secondly, it was also imperative to assess the concentration of the molecular components within the biological samples responsible for the discrimination into the different subcategories.

The classification of data into the different groups was conducted, and group membership was predicted by comparison of the spectrum with some reference spectra. Some spectral distance measurements were utilised, and spectra were grouped into those that were very similar. Cluster analysis was carried out to separate the data into different classes. Since there was a high level of collinearity in Raman spectra, Principal Component Analysis (PCA) was utilised. A reference or training set of spectra was utilised to build a multivariate statistical model onto which the measured spectrum was projected, providing a diagnosis for the new spectrum.

Principal component analysis (PCA) was used to analyse the data to reduce the dimensions in the dataset while preserving the information contained in the dataset as much as possible. In order to preserve the variability of the data, new variables were created with linear functions with the original dataset that successively maximized variance and was uncorrelated with each other. The new variables created were known as principal components. Basically, instead of interrogating the entire data set, the first few components containing the majority of the data's variations were examined in greater detail.

With the aid of PCA, the data matrix was broken down into rows (object) and columns (variable) into a structured part (S) and a noise part (E). The objects (m) were the distinct observations (spectra), and the variables (n) were the measurements (wavenumbers) for each object. The variables jointly characterise each of the objects. The n-dimensional coordinate system was made up of orthogonal axes with a common origin for the variables called variable space. PCA's main aim was to convert a coordinate system from n variable space into a Principal Component coordinate space and subsequently eliminate the noise at the same time (Ibid, 2015). The principal components were obtained by calculating the eigenvectors and eigenvalues of the covariance matrix obtained from the data matrix. The first PC (PC1) was the eigenvector with the direction of the most significant variance in the data (highest eigenvalue). PC1 was the direction (axis) that maximizes the longitudinal variance or the axis that minimizes the squared projection distances. The maximum variance in the data was shown by PC1, while PC2 (second principal component) demonstrated the most significant residual variance along a direction orthogonal to PC1. The principal components were independent and unrelated, resulting in a dimension reduction. PCA was performed using customised MATLAB protocols to describe the resulting spectra as a sum of a small orthogonal set (25) of the linear combinations of the original variables. Analysis of variance was utilised to select the most significant principal components.

A supervised input was utilised to cover the range of all normal and pathological spectral variances encountered during normal operation as a pathological or in vivo analysis.

The supervised training methods incorporating information about the sample's origin were applied. The algorithms began from a knowledge base; therefore, they helped address the prediction of new pathway members. Furthermore, because models were built from known biology, they could ignore dataset-specific noise. Prior knowledge from gold standard techniques, such as histopathology in the

case of this study, was used because they assisted us in understanding the essence of the clinical questions that required answering.

Linear discriminant analysis (LDA) has been widely used to extract features from the spectroscopic data set (Fisher R A, 1936). Feature extraction is a crucial step in accurately classifying data into different groups. The primary purpose of LDA here was to identify the "discriminant axes" used to classify the data into two or more classes effectively (Gautam R et al., 2015). PCA and LDA are closely linked because both techniques can uncover the hidden features within the sample or specimen under investigation (Ibid, 2015). LDA is a supervised analytical tool that distinguishes it from PCA, an unsupervised machine learning method. While PCA was used to determine projections to maximize variance, LDA, on the other hand, was utilised to determine the projections that maximize the ratio of between-class to within-class. In other words, it aimed to enhance the separation between groups while minimising the separation within groups. Therefore, LDA was used in this study to assist in classifying spectra into well-defined groups or categories acting as a predictive model for unknown samples.

Data were projected into the new dimensional space with the axes found with LDA. Each observation had fewer variables in the new dimensional space (dimensional reduction). At the same time, observations belonging to the same class formed clusters, and each cluster was differentiated.

The combination of PCA and LDA was a good approach to data analysis since it enhanced classification efficiency and aided in detecting spectral features. PC-LDA model also ensured an easy visualization of the clusters in three-dimensional space using LD scores.

This study used two vital phases of the supervised methods, including the training and prediction phases.

The training phase was a passive phase whereby a training data set was used to find patterns in the data. These model parameters were exploited to learn where vital chemical information was stored for further validation.

The prediction phase was utilised as a testing phase, an active phase whereby data not part of the training set were verified with the model parameters learned in the first phase.

Support vector machine learning algorithm was also utilised as a supervised method to analyze data for classification. It was a great prediction model based on a statistical learning framework. This model

was used to build an algorithm to assign new examples to different classes with the aid of a hyperplane. In this study, the largest separation or margin between the two classes was the hyperplane.

4.7.2. Normalization:

Normalization is the process whereby the inconsistency in the intensity levels is addressed by ensuring that the intensity of a given Raman band of the same material is as close as possible across the spectra recorded under the same experimental parameters. Data were normalized to the area under the curve. These variations could be due to poor alignment of the instrument as well as changes in the laser power levels.

4.7.3. Smoothing:

Smoothing is a technique utilized to eliminate the high-frequency components of the Raman signal (Liu Y et al., 2020). Since the Raman signal is weak, it is easily affected by noise. Although there are different noise sources, the camera and signal (shot noise) are the primary sources of noise as far as the Raman signal is concerned (Ibid, 2020). Therefore, reducing the noise before the data were processed allowed for decent clean data void of obliteration of the chemical information (Ibid, 2020). In order to eliminate the influence of noise, smoothing algorithms are often used (Ibid, 2020). Savitzky-Golay (SG) filter (Ibid, 2020) was utilised for this study, which was applied by fitting each segment of the original Raman spectrum in a separate window to a polynomial function (Gautam R, 2015).

4.7.4. Removal of Outliers

Outliers in data could result in a significant variance introduction with the model, resulting in a distortion of the data.

Some spectra from the same sample can appear different from the rest due to the presence of outliers from equipment artefacts or variations within the sample. Outliers must be removed from the data before multivariate analytical tools are applied. Signal-to-noise ratio (SNR) based on threshold techniques to remove unwanted spectra. A threshold value was set for a specific variable, and any intensity value that exceeds or is below the predetermined threshold was considered an outlier (Ibid, 2009). Principal component analysis was used to determine the presence of outliers within the data in this study.

Spectra that were not within the Region of interest (ROI) were also classified as outliers and were subsequently removed to avoid unnecessary distortion of the data.

4.7.7. Cross Validation

Cross-validation was utilised to assess the predictive ability of our classification model in this study, which was beneficial to determine how the results of this study can be generalised to an independent dataset. Therefore, it estimated how accurately the predictive model would perform in actual practice. After that, a training dataset was presented to the model; unknown data was tested, and the unknown data was called the validation dataset or testing dataset. The main aim was to assess the model's ability to depict new data that was not used in estimating it, helpful in determining the presence of overfitting or selection bias.

4.7.7.1. *Leave one out cross validation*

20% of the data were held back from the training dataset, and the resulting model was evaluated on the left-out observation. This process was repeated for all the observations in the dataset five times (five-fold cross-validation), and the average performance across that iteration was considered the classification mode's performance.

4.7.8. Receiver Operating Characteristic Curve

A receiver operating characteristics (ROC) curve is a graphical representation that depicts the diagnostic ability of a binary classifier system as its discrimination threshold varies (Fawcett, 2006). In our study, receiver operating characteristics curves were created by plotting the True Positive Rate (TPR) against the False Positive Rate (FPR) at various threshold settings. TPR was also regarded as sensitivity or the probability of detection in machine learning, while FPR was the probability of a false alarm. The ROC curve was therefore generated by plotting the cumulative distribution function of the detection probability on the Y-axis versus the false-alarm probability on the X-axis.

The Area Under the Curve is a performance measurement for classification at various threshold settings. ROC is a probability curve, while the AUC represents the degree or measure of separability. It highlights how much a model can differentiate between classes. The higher the AUC, the better the model is at predicting outcomes. Essentially, this was likened to the higher the AUC, the better the model differentiating between different classes or groups in this study.

4.7.8.1. *How to evaluate the performance of a model:*

An excellent model was regarded as one with an AUC closer to 1, meaning it had a good measure of separability. A poor model was regarded as one with an AUC near 0, which means that it had the worst separability measure, effectively predicting 0s as 1s and 1s as 0s in a binary classifier system. However,

when the AUC was 0.5, the model had no class separation capacity whatsoever (Ibid, 2015). For this study, one can see that the SVM learning algorithms for two and 3-group classification models were between 0.97 and 0.98 for the blood plasma and serum spectral analysis. However, for the spectral tissue analysis, the SVM learning algorithm had an AUC of about 0.80 for the two and 3-group classification models, demonstrating that the support vector machine was excellent at discriminating spectra into 2 and 3 groups. Nevertheless, the linear discriminate analysis demonstrated a lower ability to distinguish spectra into different classes for the tissues and blood samples, as shown by the AUC.

4.8. Histological Analysis:

The tissue samples were processed in a laboratory (Maidstone and Tunbridge Wells NHS Trust) accredited to ISO15189 with the United Kingdom Accreditation Service (UKAS).

Prostatic tissue samples were placed in a neutral buffered formal saline solution which was necessary for tissue fixation. Approximately 48 hours after arrival at the laboratory, the tissue samples were removed from the formal solution when the tissues were fully fixed.

The tissue samples were then transferred to tissue cassettes and processed using a standard biopsy processing protocol on the Sakura VIP6 tissue processor (as depicted in table 4.1 below). Processing tissue in this context indicates replacing water within the tissue with paraffin wax. There were a few steps involved in the process since water and wax are not miscible.

Biopsy Processing Schedule		
<u>Solution</u>	<u>Temp (°C)</u>	<u>Time</u>
1) 10% Formalin	40	10 mins
2) 99% Alc	40	10 mins.
3) 99% Alc	40	10 mins.
4) 99% Alc	40	10 mins
5) 99% Alc	40	10 mins
6) 99% Alc	40	10 mins
7) 99% Alc	40	10 mins
8) Xylene	40	10 mins
9) Xylene	40	10 mins
10) Xylene	40	10 mins
11) Wax	63	10 mins
12) Wax	63	10 mins
13) Wax	63	10 mins
14) Wax	63	10 mins

Table 4.1: Prostate biopsy Processing Schedule

NB: Processing required pressure and vacuum to facilitate the impregnation of the tissue with the reagent (otherwise, tissue processing would take several days).

Once the tissues were processed, they were fully impregnated with wax, where there was water within the tissues. The tissues were then transferred to a small metal mould containing molten paraffin wax. The tissue samples were then placed flat and firmly against the base of the mould, and the wax was subsequently allowed to cool and solidify around the tissues by placing the mould on a cold plate. Once cooled, the block shells out of the mould, and we were left with wax-impregnated tissues held within a block of solid wax.

The blocks were safely and efficiently handled at room temperature. Small tissue slices (3 µm) were taken from the block with the aid of a microtome. The tissue sections were collected onto glass slides and stained with the standard histology stain, haematoxylin, and eosin (H&E). An automated process was utilised, and the subsequent cover-slipping of the slide was to protect it from damage.

Once the slides were cover-slipped, they were sent to the Consultant histopathologist for his opinion.

4.9. Raman Spectroscopy Data analysis

4.9.1. Analysis of prostate tissue spectra

Multivariate analysis was utilised to build a linear discriminant classification model for predicting the prostate tissue pathology established upon the measured Raman spectra.

An outline of the technique is given below, followed by a more detailed analysis of each technique in turn.

Spectra with unacceptable SNR or high fluorescence were removed, and the remaining spectra were used to build the training classification model; this was mean-centred.

To ensure that clustering the spectra with the different pathology groups was done to enhance the separation into different groups, weights of the principal components were plotted. Two, three, four, and five class group classifications were utilised at different times to build the diagnostic models to see the best possible classification model. The most diagnostically significant principal components were utilized to conduct linear discriminant analysis. Leave one sample out cross-validation was utilized to assess the prediction accuracy of the different models. The Linear discriminant weights were plotted against each other to assess the separation with the pathology groupings.

4.9.2. Data pre-processing:

Removing unwanted signals from the Raman spectroscopy measurement was crucial in maintaining reproducible data that can be utilised for both quantitative and qualitative analysis. Pre-processing steps such as removal of outliers, denoising, and normalization were applied to the raw data to ensure that data with relevant spectral signals were processed. Although different pre-processing strategies can be applied, care was taken to ensure that appropriate pre-processing techniques were applied to the data.

The following pre-processing steps were applied to the raw data of the prostate tissues using a MATLAB program. Firstly, mean spectra were calculated from the five spectra, and some were four spectra acquired from each tissue sample. Secondly, unwanted background signals were subtracted from the mean spectra. Thirdly, each spectrum was corrected with the spectral response. Fourthly, residual low-frequency components such as autofluorescence were excluded with a sixth-degree polynomial fit. Fifthly, all spectra were normalised using standard normal variate normalization. Finally, wavenumber x-axis calibration was carried out with Tylenol measurement.

In order to authenticate the diagnostic model adopted for analysis of the tissue biopsy samples, it was necessary to validate the data to ensure that the model could be used for in vivo studies.

Deep learning training has uncovered molecular fingerprints of different neoplasia, mainly when large sets of Raman data are involved, which is helpful in tumour margin assessment and the detection of aggressive cancers.

In summary, we have looked at the different components of the Raman instrument, including the laser source and charged-couple device. In order to prevent any form of distortion of the Raman signal, regular equipment calibration was carried out before any measurement was carried out to ensure the accuracy of measurements at all times. Periodic adjustment of the instrument by the manufacturers was carried out to ensure that there was no form of misalignment of the instrument, thereby ensuring optimal instrument functioning.

Chapter 5 – Result

This chapter will demonstrate the degree of prediction accuracy of the different classification models as we attempt to classify the data into different groups, such as 2, 3, 4, and 5 classes. Linear discriminant analysis, and support vector machine learning classification algorithms, were utilised to discriminate the spectra into different classes. The degree of their prediction accuracy was assessed using overall prediction accuracy, positive and negative predictive values, and true and false positive rates. Analysis of Variance was utilised to select the most significant principal components used for scatter plots and inclusion into the multiclass classification model. Scatterplots were used to determine the degree of separability for the different group classifications. Results for tissue samples, serum, and plasma will be presented in this chapter.

5.1. Tissue samples:

One hundred participants were included in this study, with the majority having intermediate or high-grade prostate cancer. Therefore, a small sample for measurement or fluorescence and Raman spectra were obtained from 79 prostate tissue samples after excluding the unwanted specimens due to tissue burning. Nevertheless, the tissue samples were further reduced to 49 (as shown in the flow chart in figure 5.1 below) because some samples were inappropriate for histological assessment. No glandular epithelial tissues were found on the specimens. Therefore histopathologist could not assess only the stromal element of the sample. Therefore about 30 tissue samples were further removed (figure 5.1). Renishaw India spectrometer (Renishaw plc, New Mills, Wotton-under-Edge, Gloucestershire GL12 8JR) was utilized to carry out all the Raman spectroscopy measurements. Raman spectral measurements were conducted over five locations on each tissue sample. A total of 381 Raman spectra were obtained for which histo-pathology analyses were performed, classifying the investigated tissue samples. Gold standard technique assessment against molecular characterization based on the Raman spectra was obtained. Histology analysis led to a characterization of whether the investigated tissues were benign or malignant. Further histological assessment of the participant's standard care biopsy samples (different from the research samples) was carried out to further probe the tissue samples with cancer.

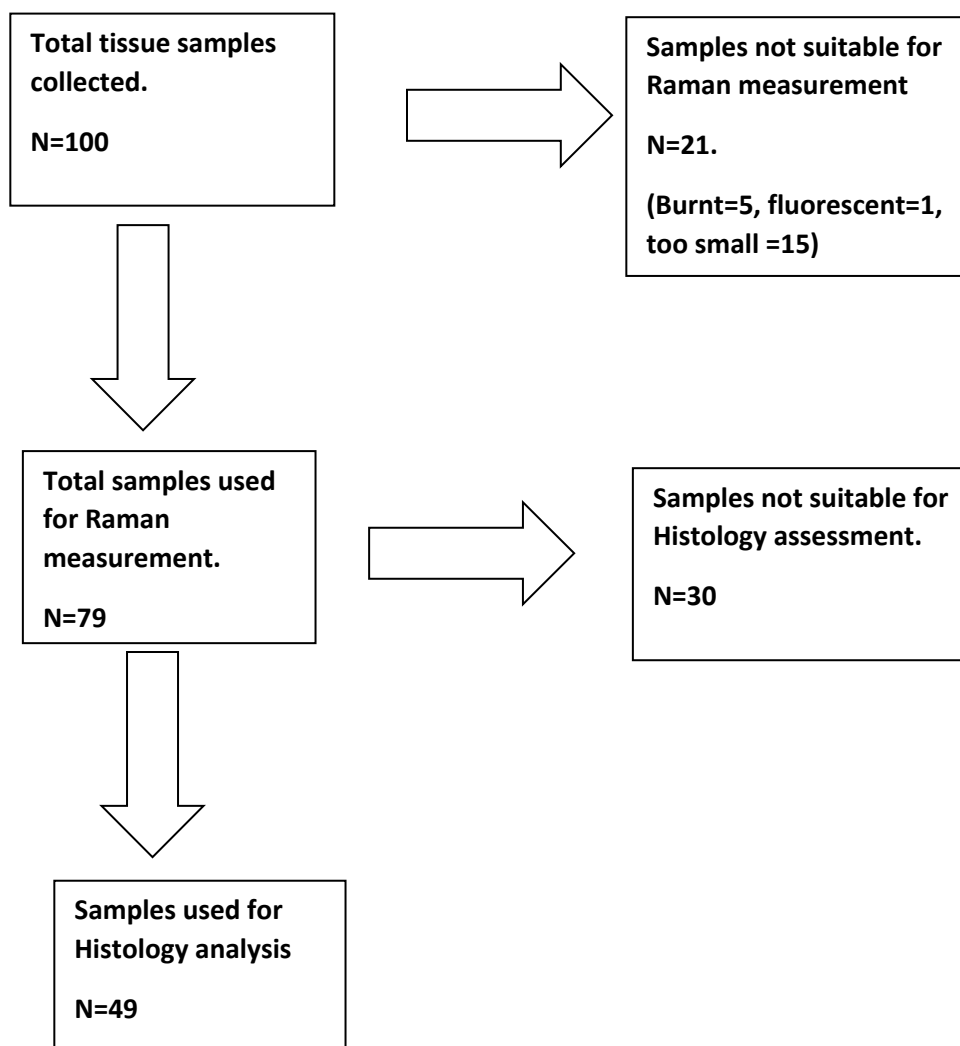


Fig 5.1. Flow chart showing the number of tissue samples collected and subsequently used for Raman measurement and histology analysis.

Extended Multiplicative Signal Correction (EMSC) is often utilized as a pre-processing method to see if the data quality can be improved by removing any unwanted artefact or noise that could obscure the relevant chemical information. The mean spectra of the cancer group were compared with that of the benign group without the EMSC method applied. A good separation between the two groups was easily visualised, as demonstrated in figure 5.2 below. However, when EMSC pre-processing technique was applied, there was a poor separation between the two groups. The possible explanation for this would be that no outliers in the original data needed the inclusion of multiple reference spectra to account for the chemical profiles of the outlier spectra. Therefore, analysis was carried out without EMSC since acceptable quality spectra were achieved with the original data.

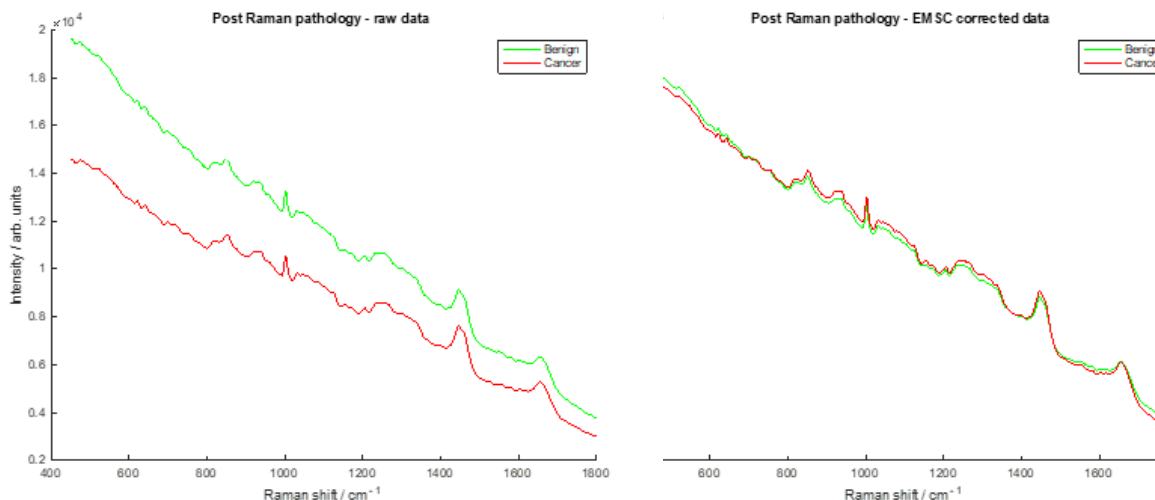


Fig. 5.2: Comparison of the raw data with data corrected with EMSC

One point per wavenumber was used to express the data representation, and energy sensitivity calibration was applied. All spectra were mean-centred to scale the spectra intensities in all the wavenumber channels to zero with unit variance.

Principal component analysis was conducted using singular value decomposition (SVD) of the data matrix (PLS toolbox in MATLAB) since utilizing all the values in the data matrix was unnecessary. Only data with relevant chemical information was utilised for further analysis to represent the entire data.

5.1.1. Two Pathology Group Training model:

A training model was built by combining the spectra into two groups, benign and malignant groups. The groups were assigned such that all prostate tissues with benign and normal features were grouped into one class (class 1), while all tissue samples with malignant features were grouped into another class (class 2). Each principal component was made up of some components of tissues which vary collinearly. Different principal components were initially used to validate the result. Nevertheless, 24 principal components gave the best outcome. Therefore, twenty-four principal orthogonal components (PCs) were used to build the training model, describing 99.9% of the variance of the raw data set. These principal components were therefore utilized as input into a linear discriminant analysis (LDA) model.

The LDA of the PCs utilized to distinguish between the two pathology groups, benign and malignant groups, and minimize the variance within the groups, required two linear discriminant functions for adequate separation between the two groups, as plotted in a bar chart in figure 5.3 below. The first class (Benign) recorded a prediction accuracy of 77.5%, while the second class (malignant) also demonstrated a prediction accuracy of 77.5%. Overall prediction accuracy for this training model was recorded at 77.5%, as seen in table 5.1 below. The percentage of prediction accuracy of the different classes and the overall prediction accuracy can be seen in figure 5.3 below.

Training classification performance	
Class	Percentage of accurate prediction
Class 1	77.5%
Class 2	77.5%
Training performance = 77.5%	

Table 5.1a. Table showing the training classification performance for benign vs Cancer

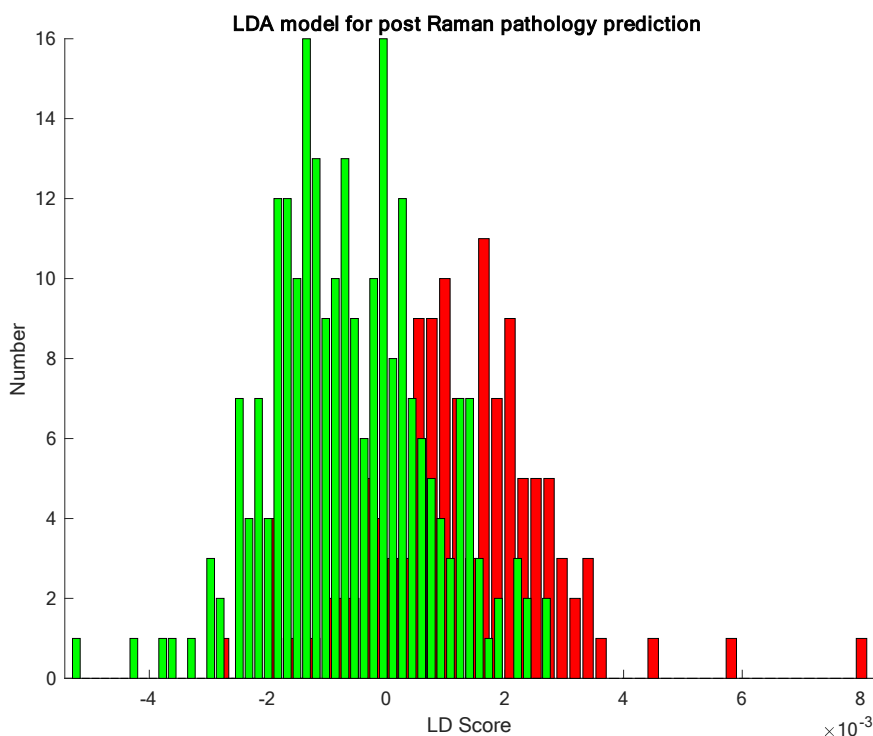


Fig. 5.3: Plot of Linear discriminant function scores for each spectrum, colour coded according to pathology opinion for the training model for benign (Green) vs cancer (Red).

The receiver operating characteristic curve was plotted for the linear discriminant analysis with true positive rates plotted against false positive rates. With the aid of the MATLAB classification app, a 5-fold leave-one-out cross-validation was applied for the two-group mean spectral model (Benign versus cancer). The overall accuracy of 72.6% with an AUC of 0.7 for the two classes can be seen in figure 5.4 below. A negative predictive value was recorded as 86%, which resulted in a false omission rate of 14%. Nevertheless, this model showed a positive predictive value of 46%, resulting in a false discovery rate of 54%. The sensitivity and specificity of this model were measured to determine the proportion of the correctly classified spectra into the respective classes. Therefore, a sensitivity of 76.4% and a specificity of 61% were recorded, respectively.

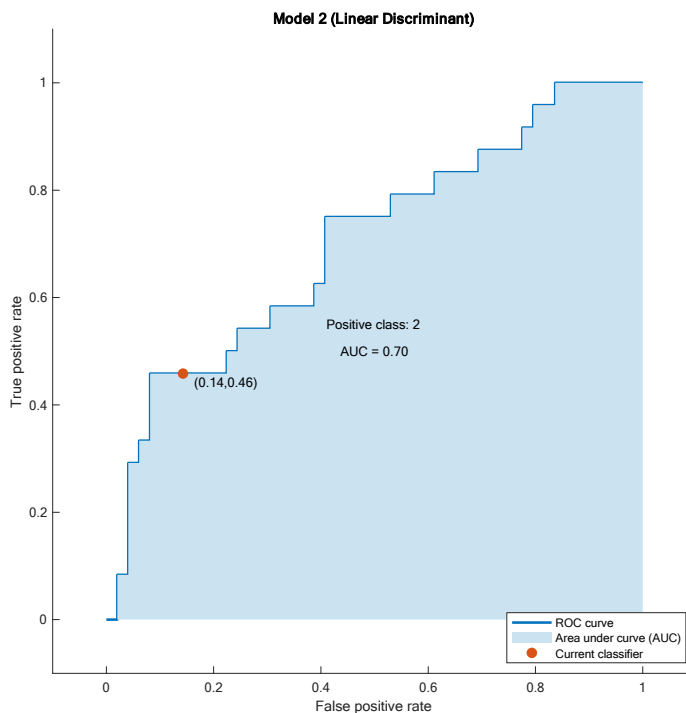


Fig. 5.4: Receiver Operating Characteristic curve for a 2 group (benign vs cancer) mean spectral Linear Discriminant model showing an area under the curve of 0.7 and an overall accuracy of 72.6%.

Note: class 2 is the positive group which is the cancer group.

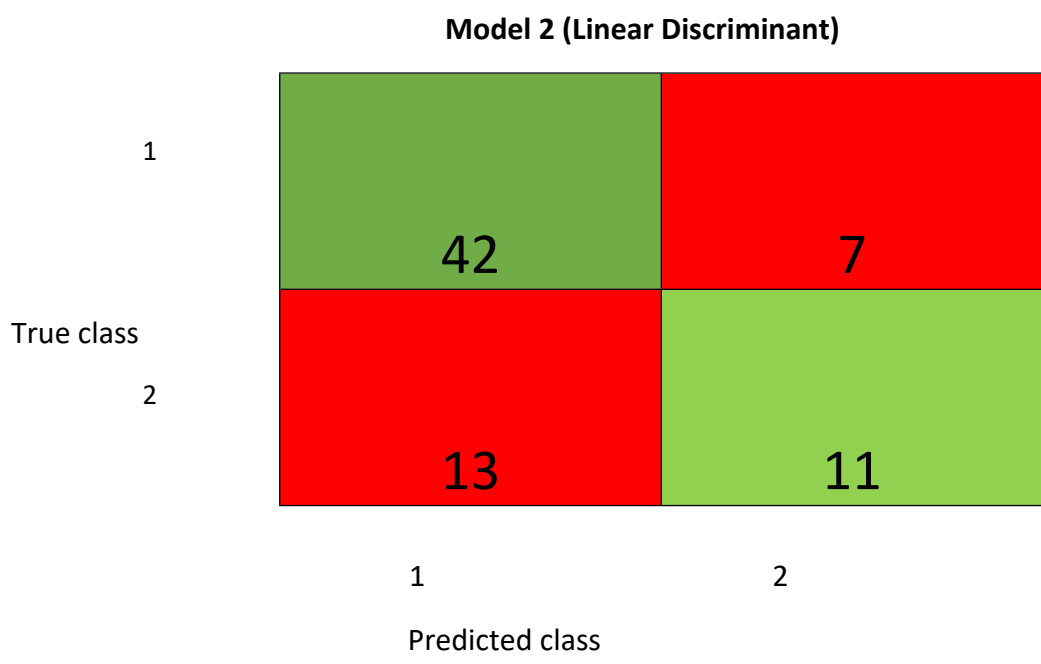


Fig. 5.5: Confusion matrix for a two group LDA classification model for benign vs malignant (cancer).

5.1.2. SVM learning model with a two-pathology group training model
 Quadratic Support Vector Machine (SVM) learning algorithm was also used to classify the spectra into two groups. To compare the performance of LDA model and the Quadratic SVM model, a 5-fold leave one out cross validation was utilized to validate the data with the aid of MATLAB classification app. The AUC was recorded as 0.69 (Figure 5.6) with an overall prediction accuracy of 72.6%. It was observed that this model was worse for cancer prediction but better for benign group classification. The positive predictive value of 38% and a false discovery rate of 62% with a negative predictive value of 90% which resulted in a false omission rate of 10%. The sensitivity and specificity for this model was 64% and 75% respectively.

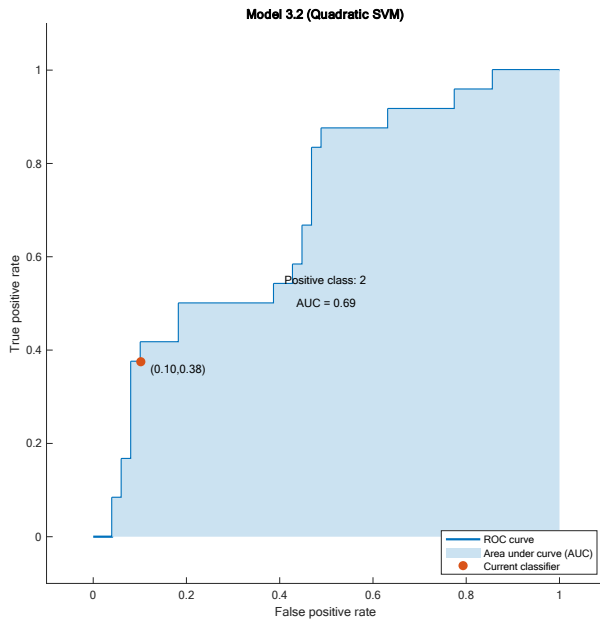


Fig. 5.6: Receiver Operating Characteristic curve for a 2 group (benign versus cancer) mean spectral Quadratic SVM model showing an area under the curve of 0.69. the positive class here is the cancer group (class 2).

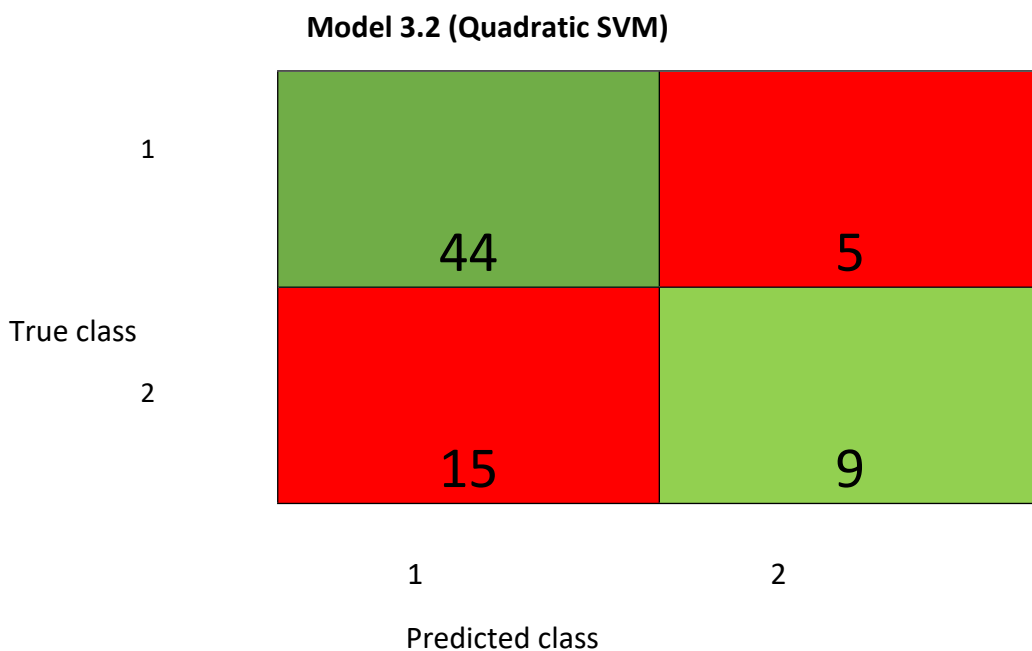


Fig.5.7: Model 3.2 showing the confusion matrix of a Quadratic Support Vector Machine Learning Model for a two-group classification (benign vs cancer).

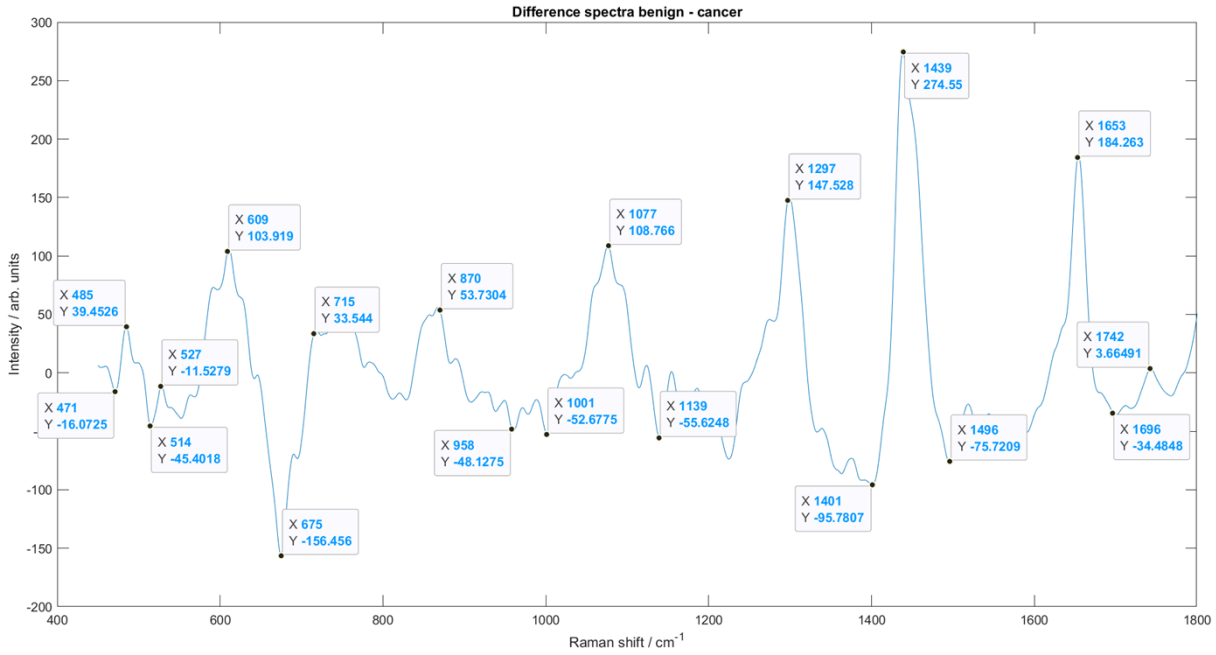


Fig. 5.8: Difference between benign and malignant tissue spectra measured

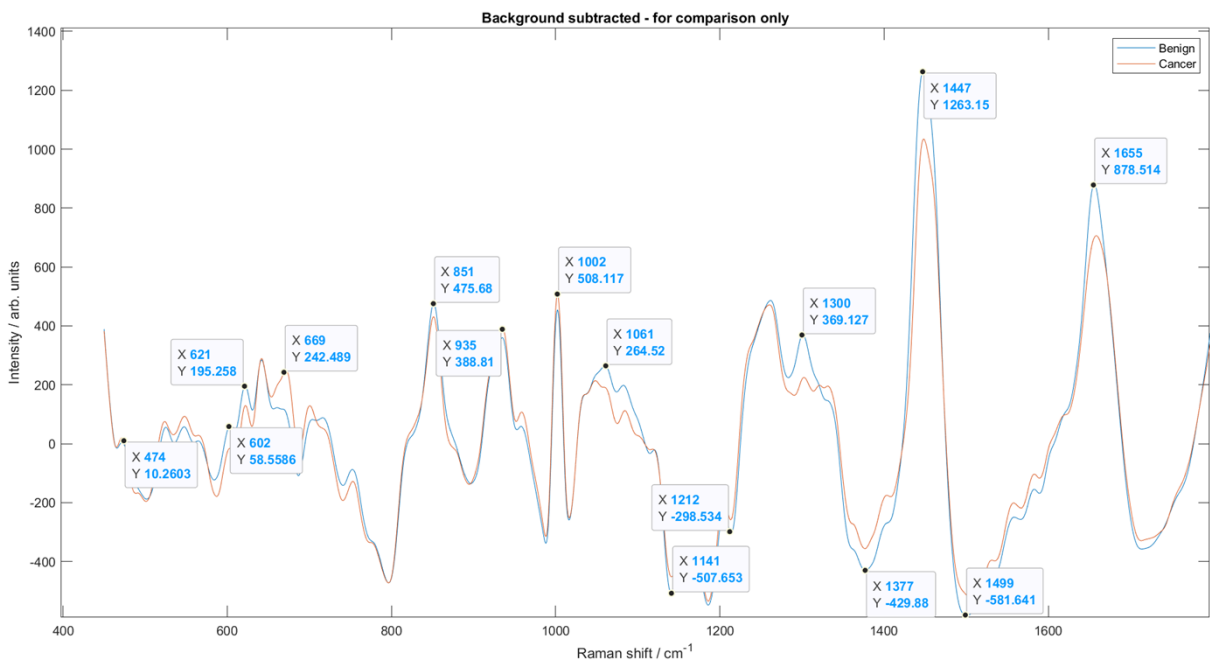


Fig 5.9: Mean spectra after background subtraction and smooth post Raman assessment (benign versus malignant).

The difference spectra were calculated by subtracting the mean spectra of the benign pathology group from the malignant group. This difference in spectra can be useful in understanding the biochemical changes that were responsible for the advancement toward malignancy within the prostate gland. Figure 5.8 above demonstrates the spectral difference between the benign and malignant tissues. The

major positive and negative peaks can be seen above. Positive peaks (above zero) were located at 485, 527, 609, 715, 870, 1077, 1297, 1439, 1653 and 1742 cm^{-1} . Negative peaks were seen at 471, 514, 675, 958, 1001, 1139, 1401, 1495 and 1696 cm^{-1} . The peaks below zero (0) were referred to as negative.

Positive peaks were seen corresponding to glycogen spectrum, which had a peak at 485 cm^{-1} , cholesterol with a peak at 609 cm^{-1} , proline (amino acid) with a peak at 870, triglycerides with a peak at 1077, lipid with a peak at 1297 cm^{-1} & 1742 cm^{-1} , CH_2 deformation due to lipid and protein, amide 1 corresponding to 1653. Negative peaks corresponded to Phenylalanine (amino acid) with a peak at 1001. The relevant pieces of literature were consulted on the nature of these peaks, although the biochemical designations of some peaks were not known (Kendall C, 2002). Higher lipids and unsaturated fats concentrations were seen in benign spectra at positive peak positions 602, 621, 851, 1061, 1300, 1447, and 1655 cm^{-1} . On the other hand, a lower glycogen concentration was seen in the benign spectra than in malignant spectra, which was seen at peak position 1377 cm^{-1} as shown in Figure 5.9 below.

The first twenty-four PCs were plotted in Figures 5.10a & 5.10b below; each PC comprised several collinear tissue compositions. Analysis of variance was used to select the most significant principal components. PC2 was seen to have many distinctive features of prostate tissue peaks, as documented in the literature. PC3 had peaks that were typical of the glycogen spectrum. Peaks from PC4 were typical of nucleic acid with a contribution from glycogen at approximately 480 cm^{-1} . PC5 had peaks linked to amino acids, proteins, and glycogen. PC6 had peaks associated with glycogen, nucleotides, proteins, and lipids. Other peaks shown on the other PCs were not statistically significant.

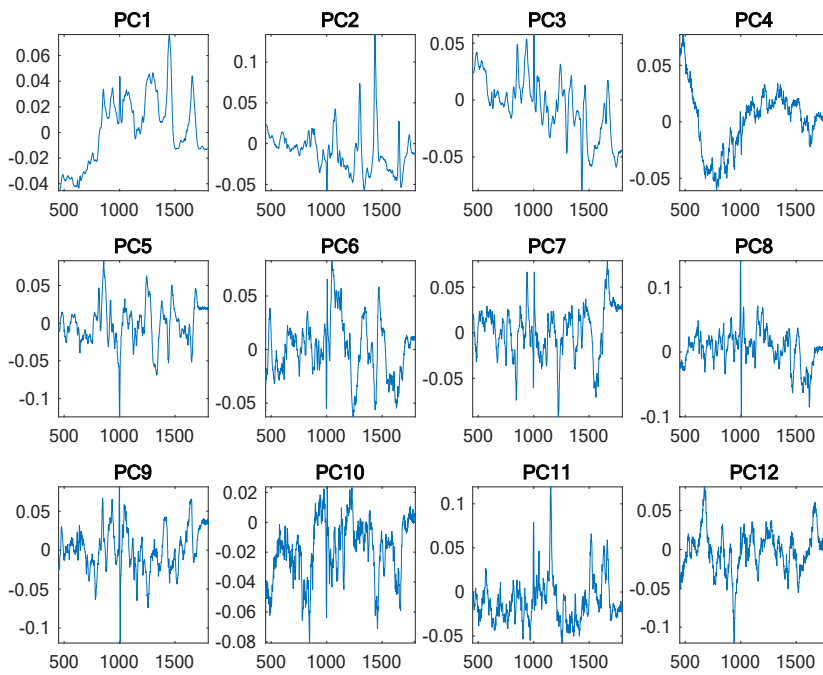


Fig. 5.10a: First 12 principal components

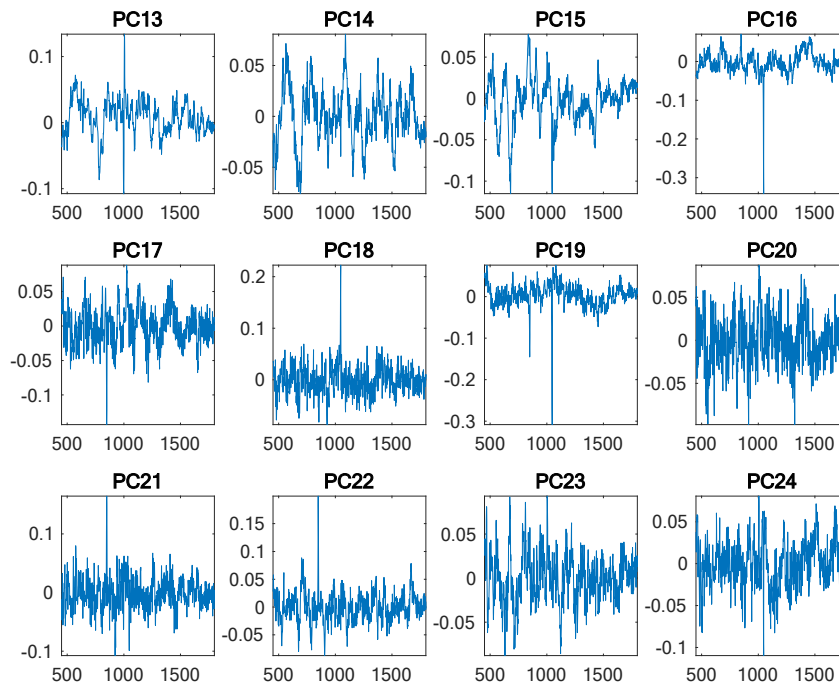


Fig. 5.10b: the next 12 principal components.

5.1.3: Two Group classification model

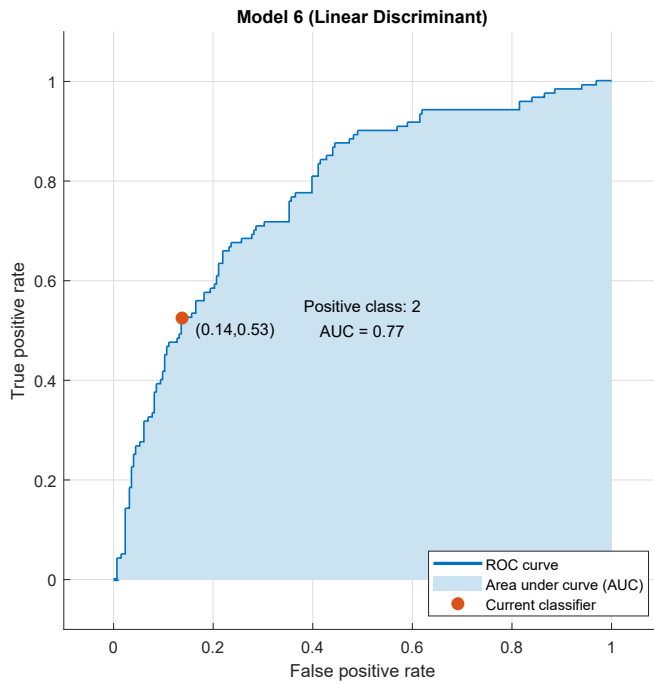


Fig. 5.11: Receiver Operating Characteristics curve for a two-group classification showing the Area Under the Curve of 0.77 in a LDA model.

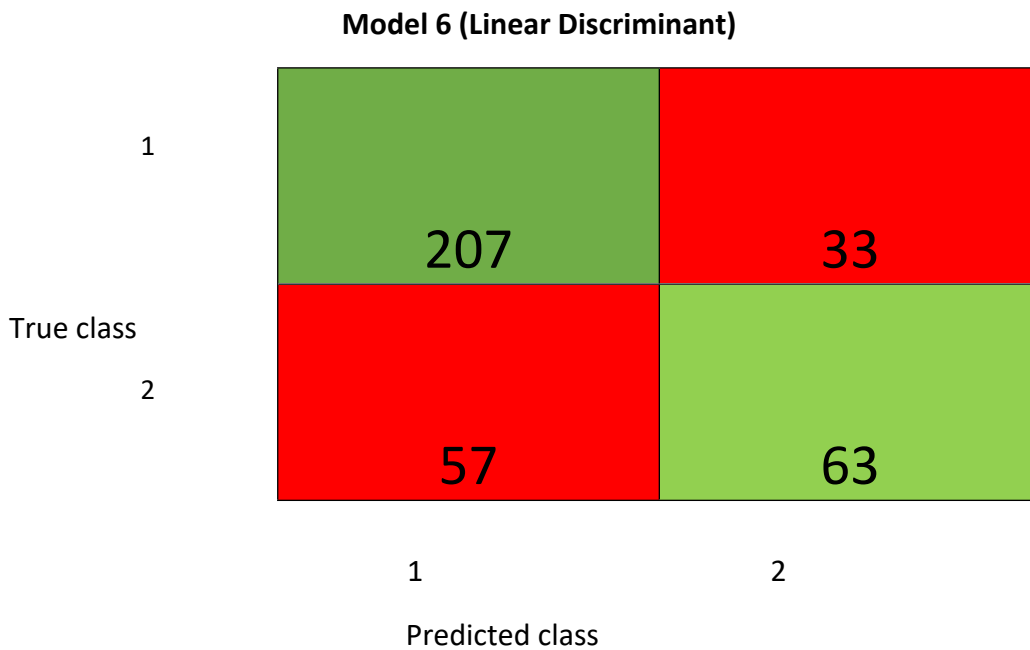


Fig. 5.12: The confusion matrix of the two-group classification model using a linear discriminant analysis

The Area under the curve of 0.77 shows that the above model is a good (acceptable) classification model between different pathological groups, as demonstrated in figures 5.11 & 5.12 above. However, it is by no means a perfect classification model. The sensitivity and specificity for this model were 65.6% and 78.4%, respectively with an overall accuracy of 75%. The positive predictive value was 53% with a corresponding false discovery rate of 47%, while the negative predictive value was 86%, and the corresponding false omission rate was 14%.

However, with the medium Gaussian SVM, the Area under the curve can be seen as 0.82 (as shown in Figures 5.13 & 5.14 below), which was better than the LDA model, although still not a perfect classification (prediction model). The SVM model's overall accuracy of 80.8% was recorded compared to 75% of the LDA model for this two-group classification. The sensitivity and specificity of 87% and 79.4%, respectively, while the positive and negative predictive values of 50% and 96% were recorded, respectively.

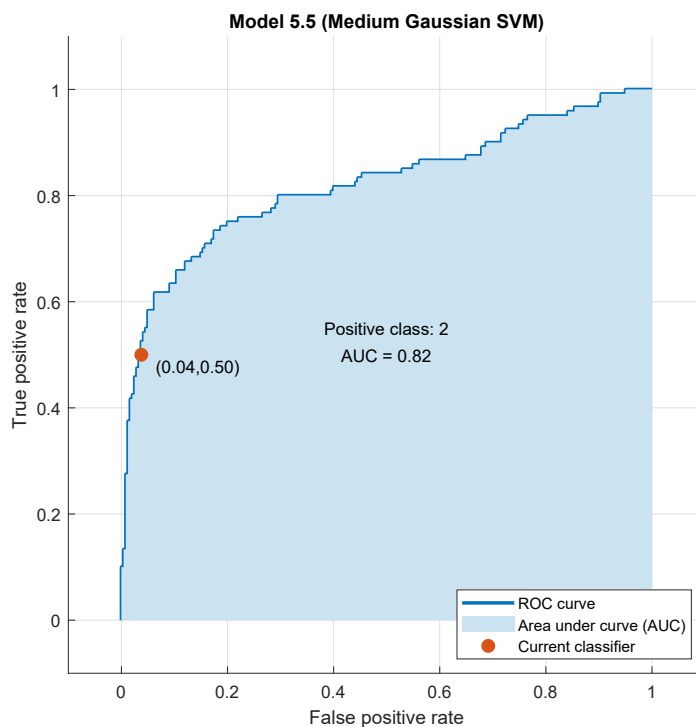


Fig. 5.13: Medium Gaussian SVM showing the AUC of 0.82 and the prediction accuracy of 80.

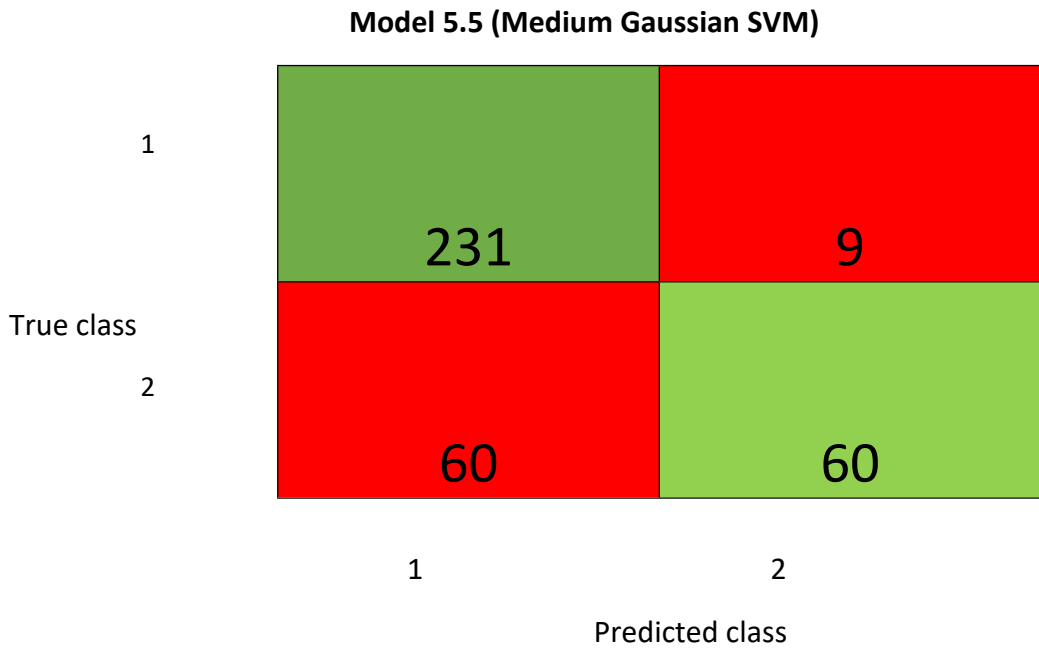


Fig. 5.14: Confusion matrix of a two-group classification model using a Medium Gaussian SVM.

5.1.4: Four group classification model (Gleason grade scoring system)

A three-dimensional (3D) scatter plot was plotted to visualise the level of separation between the four different Gleason risk stratification groups using linear discriminant analysis, as shown in figure 5.15 below. A closer look at the scatter plot shows minimal separation between the four groups.

After the raw data's normalization, the four-group classification model's overall accuracy demonstrated a 50.4% accuracy. The group of tumours with a Gleason score greater than 7 demonstrated the highest prediction accuracy rate of 57.6%. However, all tumours with a Gleason score of 7 showed the lowest prediction accuracy (46.7%).

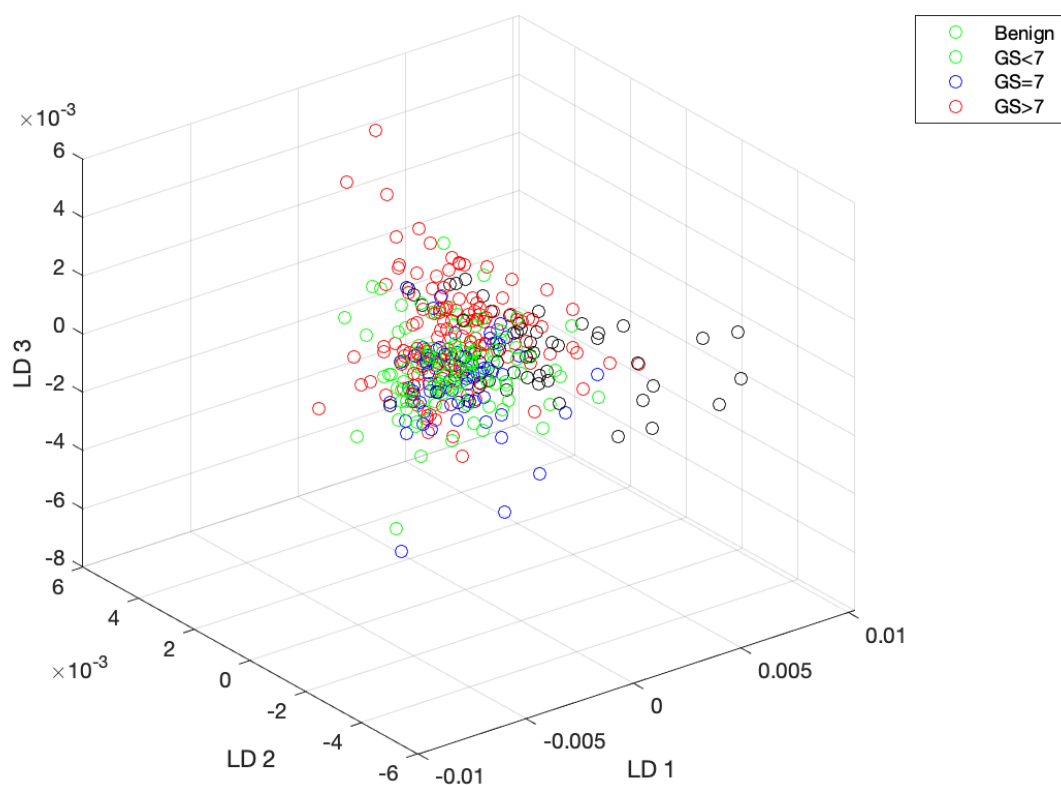


Fig. 5.15: Three-Dimensional Plot of the linear discriminant function of the scores for each class spectrum, colour coded according to the histopathology report following normalization to area under the curve (Benign, GS<7, GS=7, GS>7).

5.1.5: Two Group classification model (Low grade versus high grade tumour)

A two-group classification model depicted an overall prediction accuracy of 68.8% for the PC-LDA model for a low-grade tumour in one group. In contrast, intermediate and high-grade tumours were placed in another group. With this classification, low-grade tumours demonstrated a higher prediction accuracy (70.8%) than high-grade ones (66.8%), as shown in figure 5.16 below.

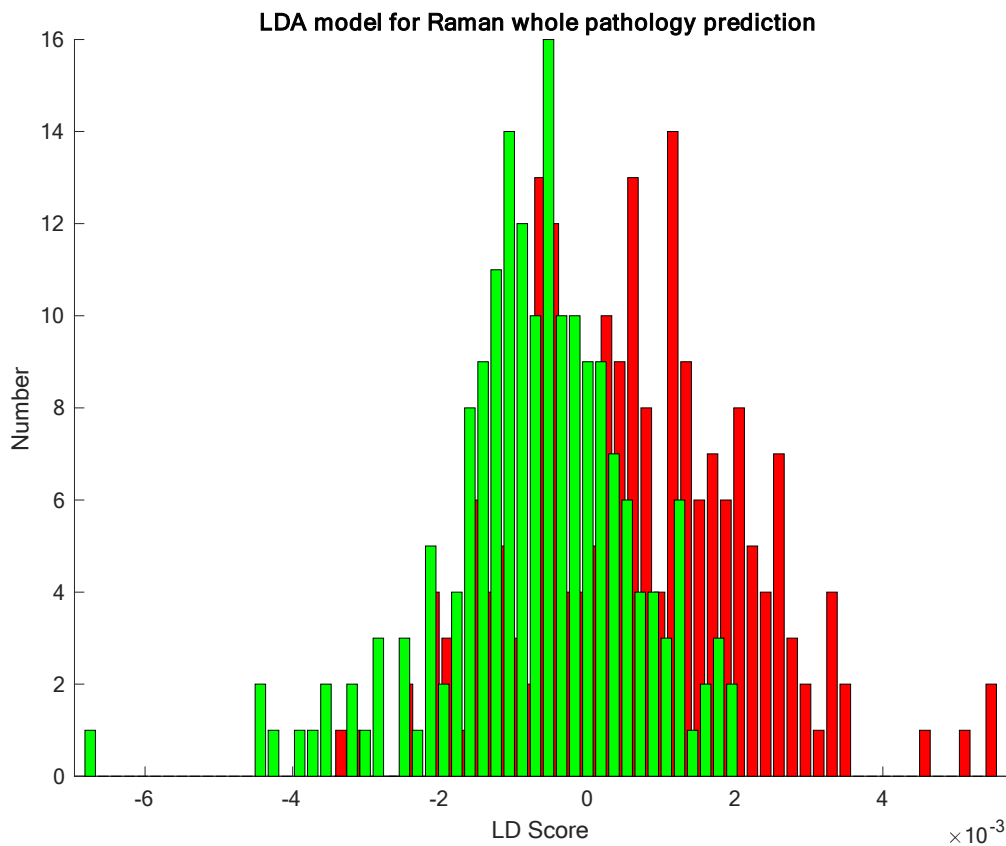


Fig. 5.16: Bar chart showing the Raman spectroscopy prediction power of a two group (benign & GS<7 vs GS 7 & >7) with the aid of PC-LDA model with normalisation of the raw data to the area under the curve. The green bars represented the low-grade tumour -class 1 (GS = benign & <7), Red bars represent the high-grade tumour – class 2 (GS = ≥ 7).

When a confusion matrix was plotted to further scrutinize this model as a classification model, it was discovered that a positive predictive value of 62.7% was recorded. In contrast, a negative predictive value of 61% was documented. Nevertheless, the sensitivity and specificity were recorded as 60%, respectively.

The overall accuracy of 61.9% was recorded with an AUC of 0.65 for the 2-group classification model, as demonstrated in figure 5.17 below. An interpretation of this AUC as it relates to this 2-group classification model of LDA shows that it is a poor model for discriminating between low-grade and high-grade tumours.

However, cubic SVM alongside 5-fold cross-validation on the same two-group classification model demonstrated overall accuracy of 74.8%, and AUC of 0.80, as seen in the figure below. A confusion

matrix depicted a positive predictive value of 73% and a negative predictive value of 76%, respectively. While sensitivity and specificity of 77% and 73% were documented for this classification model, as seen in figure 5.18 below. Demonstrated that the support vector machine learning approach was superior to the linear discriminant analysis with normalisation of the raw data. Although still not a perfect classification model, it is better for discriminating between high-grade and low-grade tumours by normalising the raw data to the Area under the curve.

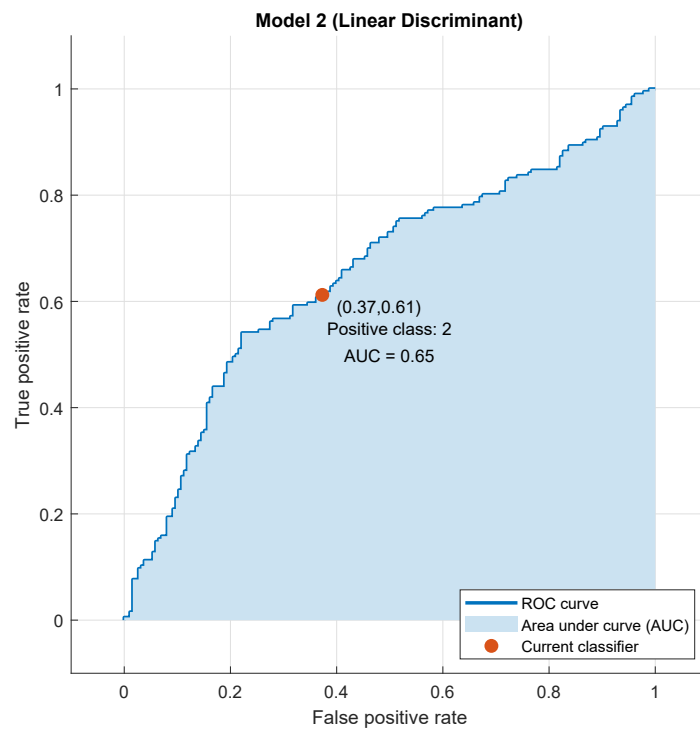


Fig. 5.17: Two group classification LDA (benign & GS<7 vs GS 7 & >7) with the aid of PC-LDA model with normalisation of the raw data to the area under the curve and a 5-fold cross validation model showing the AUC of 0.65 and overall accuracy of 61.9%.

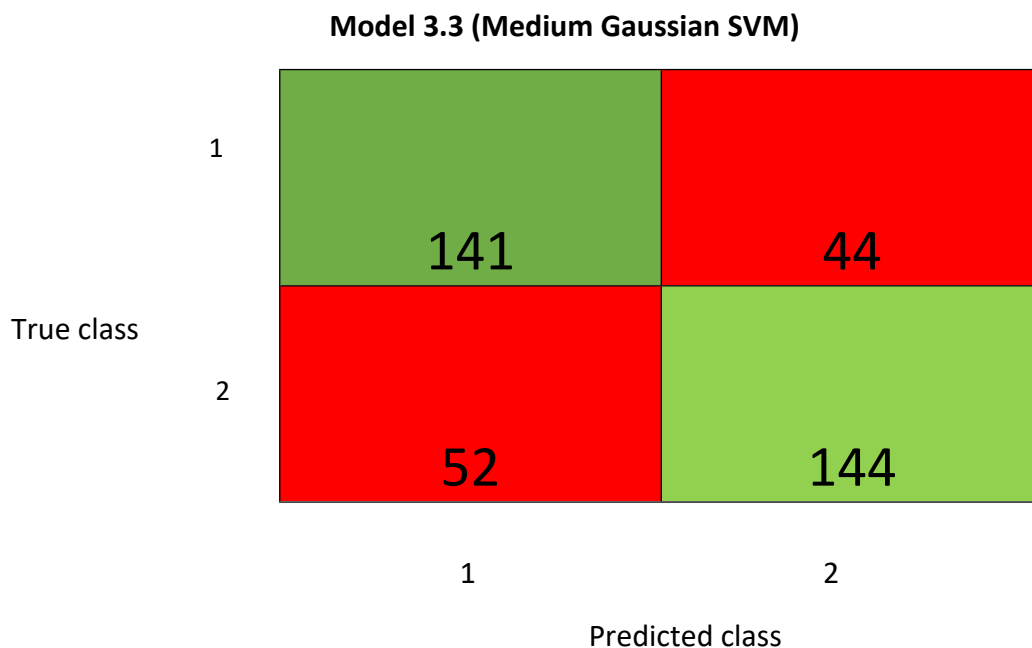


Fig. 5.18: A confusion matrix for a two-group classification model (benign & GS<7 vs GS 7 & >7) with the aid of PC-LDA model with normalisation of the raw data to the area under the curve.

5.1.6: Three Group classification Model

The limitations of the Gleason scoring system from biopsies, such as poor reproducibility and poor correlation with radical prostatectomy grade, were responsible for the introduction of the new Gleason grade group in 2013 by Johns Hopkins Hospital. Gleason 7 tumours which have always been regarded as intermediate-risk cancer, have also been shown to have worse outcomes and biochemical recurrence rates, especially Gleason 4+3. The 5-year biochemical risk-free survival for the Gleason grade group 1 to 5 based on prostatectomy grading was shown to be 96%, 88%, 63%, 48%, and 26%, respectively. This Gleason grade group classification is superior to the Gleason risk stratification (<7, 7 & >7).

Therefore, it was imperative to assess the performance of this diagnostic model against the new Gleason grade group classification and the Gleason risk stratification (the old model). Two linear discriminant functions were utilized to discriminate between the different Gleason grade groups in a four-group LDA classification model. Two linear discriminant functions were used to assess the Gleason risk stratification model in a three-group LDA model. The scores of the two linear discriminant functions for the spectra of the Gleason grade group and the risk stratification model were colour-coded and plotted based on histopathology. These can be seen in the figures below, respectively. Easy visualization of the spectra separation between the different pathology groups can be seen in Figure 5.19 below.

Further analysis was carried out on the Gleason grade group by merging Gleason grade group 4 and 5 spectra and assigning them into one class (class 3). In contrast, Gleason grade group 1 (Gleason 6 or <7) was assigned to class 1, and Gleason grade group 3 (Gleason 4+3) was assigned to class 2.

Measurement of the level of separation between the different classes with different machine learning techniques in a three-group classification model distinguishing the spectra into benign + Gleason <7, Gleason 7, and Gleason >7 using a linear discriminant analysis, the overall accuracy at prediction into these classes was 57.22% as seen in the table 5.2a below. Figure 5.19 below is a scatter plot showing the separation between the three pathological groups. However, there was no significant separation between the groups, as seen in the figure below.

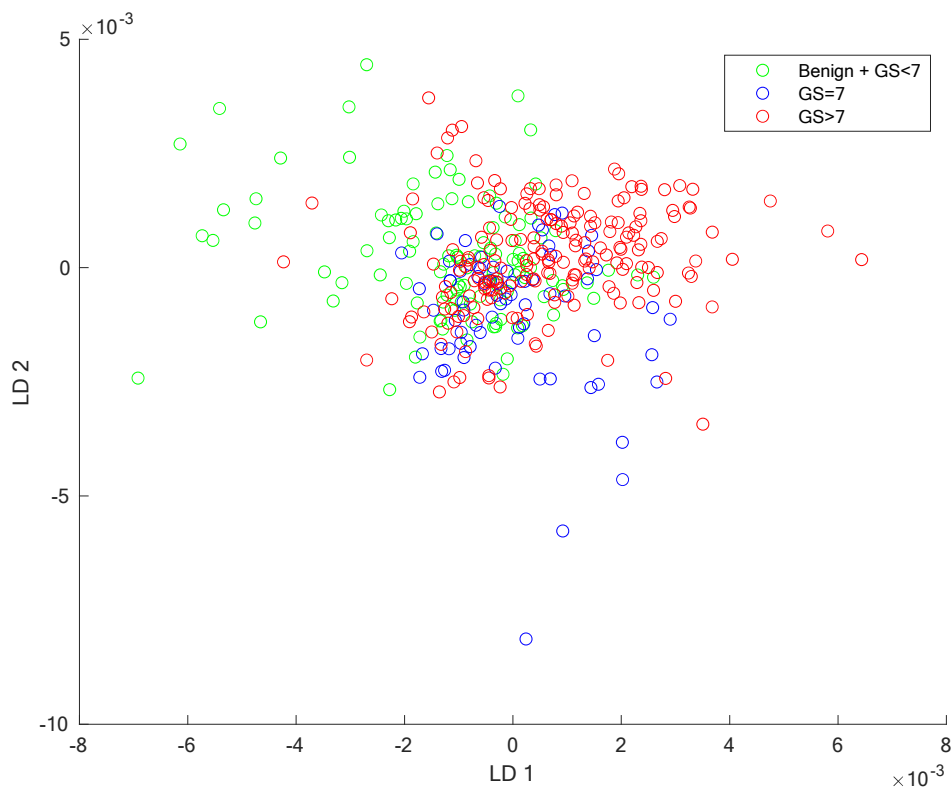


Fig. 5.19: Plot of the linear discriminant function of the scores for a three-group classification model using LDA for the Gleason risk stratification groups (benign + <7, 7 & >7). Each class spectrum were colour coded according to the histopathology report.

Histology Confirmed		Raman Predictions		
Class		Benign/GS = >7	GS = 7	GS = >7
1	Benign/ GS = <7	62	26	25
2	GS = 7	14	42	16
3	GS = >7	38	44	114
GS = Gleason Score, N=381				
Overall accuracy = 57.22 %				

Table 5.2a: Training classification in a three-group PC-LDA model with Gleason <7, 7 & >7 with histology versus Raman predictions.

Training Classification Performance	
Class	% Accurate Prediction
1	54.87
2	58.33
3	58.16
Training Performance = 57.22 %	

Table 5.2b: Showing the training classification performance in a three-group PC-LDA model with Gleason <7, 7 & >7.

5.1.7: Four Group classification Model (Gleason grade group scoring system)

The four-group classification model demonstrated 100% prediction accuracy for Class 4 (Gleason grade group 5) tumours. However, the other classes did not have excellent prediction accuracy, as shown in figure 5.20, table 5.3a, and 5.3b below.

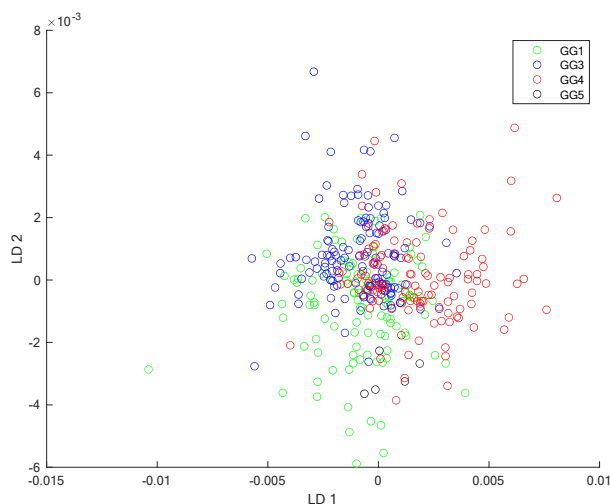


Fig. 5.20: Plot of the linear discriminant function of the scores for a four-group classification model using LDA for the Gleason grade group scores. Each class spectrum were colour coded according to the histopathology report.

Histology Confirmed		Raman Predictions			
Class		GG 1	GG 3	GG 4	GG 5
1	GG 1	59	26	20	8
2	GG 3	22	93	20	2
3	GG 4	23	29	70	4
4	GG 5	0	0	0	5
Overall accuracy = 59.58 %, N=381					

Table 5.3a: Showing the training classification performance for Raman versus histology in a four-group PC-LDA model with Gleason grade group 1, 3, 4 & 5.

Training Classification Performance	
Class	% Accurate Prediction
1	52.21
2	67.88
3	55.56
4	100
Training Performance =59.58 %	

Table 5.3b: Showing the training classification performance in a four-group PC-LDA model with Gleason grade group 1, 3, 4 & 5.

5.1.8: Three Group classification Model (Gleason grade group scores)

The three-group classification model involving Gleason grade groups 1, 2 & 4/5 shows inadequate separation between the groups, as seen in figure 5.21 below.

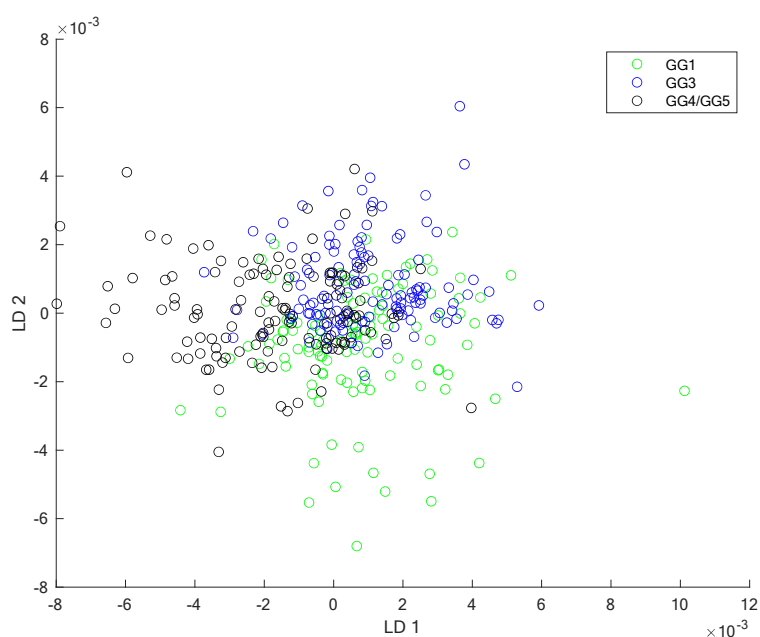


Fig. 5.21: Plot of the linear discriminant function of the scores for a three-group classification model using LDA for the Gleason grade group scores with spectra from Gleason grade group 4 merged with 5.

Histology Confirmed		Raman Predictions		
Class		GG = 1	GG = 3	GG = 4/5
1	GG = 1	60	29	24
2	GG = 3	26	87	24
3	GG = 4/5	25	31	75
GG = Grade Group score				
Overall accuracy = 58.27 %				

Table 5.4a: Raman prediction accuracy against histology in a three-group PC-LDA model with Gleason grade group 1, 3 & 4+5.

Training Classification Performance	
Class	% Accurate Prediction
1	53.10
2	63.50
3	57.25
Training Performance = 58.27%	

Table 5.4b: Showing the training classification performance in a three-group PC-LDA model with Gleason grade group 1, 3 & 4+5.

When a 5-fold leave-one-out cross-validation was applied for the predominant three groups (original Gleason risk stratification) LDA model, the overall prediction accuracy was recorded at 52.5%, but the Area under the curve was recorded as 0.73 (figure 5.22). This model is not perfect for discriminating the spectra into three different classes, but it is a reasonably good model. The ROC curve of the pathology of interest is demonstrated in figure 5.22 below.

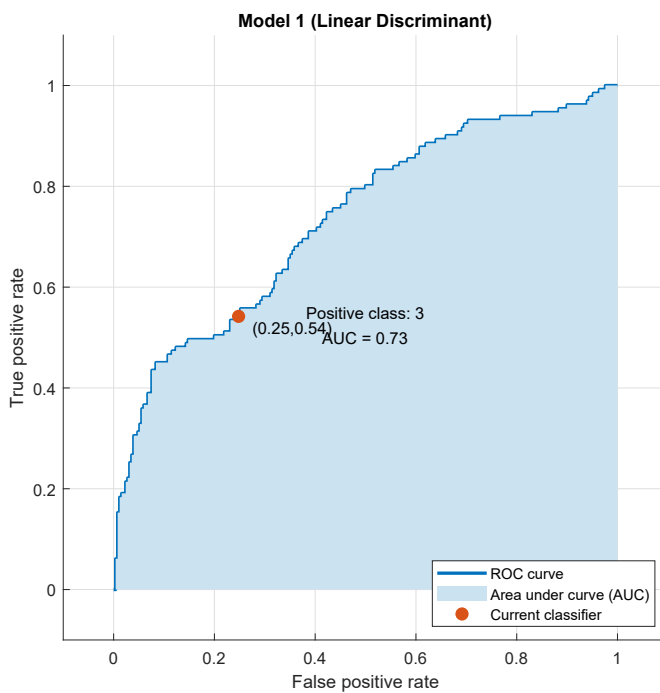


Fig. 5.22: Three group classification LDA and a 5-fold cross validation model showing the AUC of 0.73 and overall accuracy of 52.5% (Gleason 7, <7 & >7).

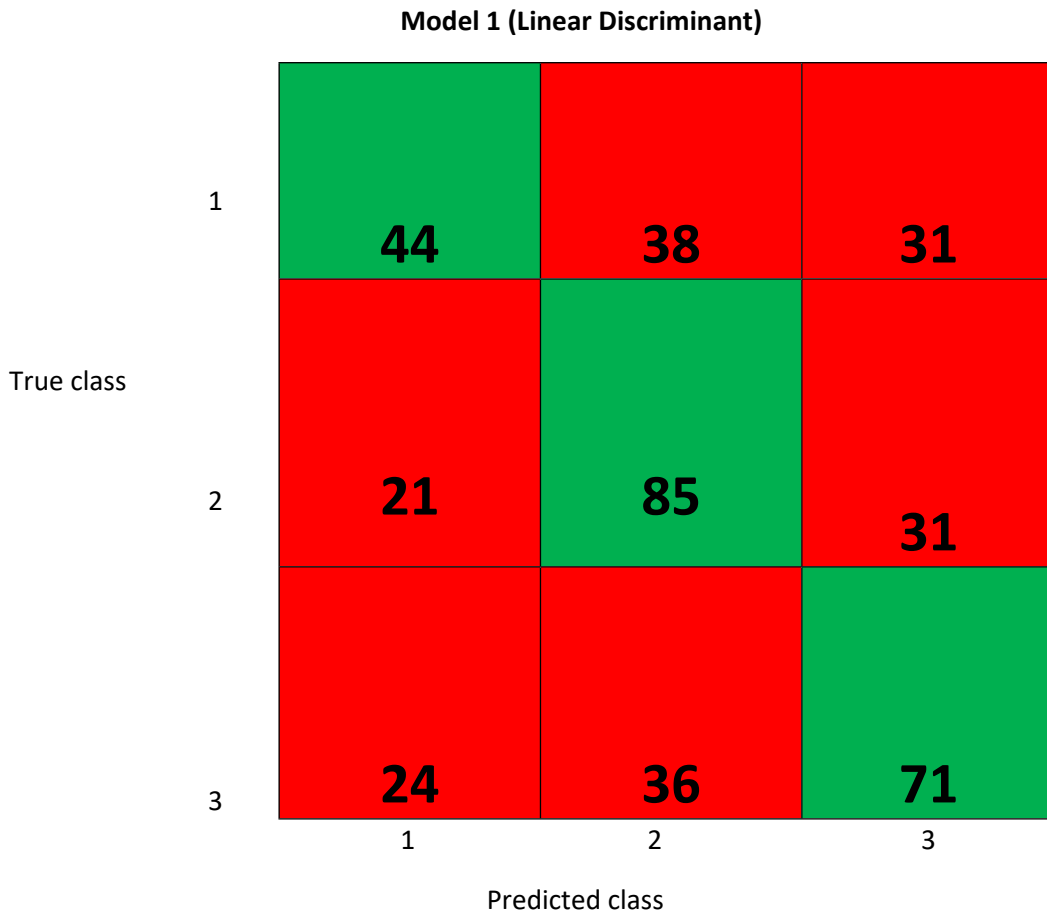


Fig. 5.23: A confusion matrix of a three-group classification LDA and a 5-fold cross validation model showing the AUC of 0.73 and overall accuracy of 52.5% (Gleason 7, <7 & >7) .

Quadratic Support vector machine learning was also utilised to further assess the performance of the classification into the three classes that could assist in the risk stratification of prostate cancer (Gleason <7, 7, >7). As seen in figure 5.24 below, the AUC was 0.79, with overall prediction accuracy of 64.6%, as shown in the figures below. The quadratic SVM model demonstrated a better ability to discriminate the spectra into these three risk stratification classes than the LDA model. Nevertheless, the quadratic SVM learning algorithm was not a perfect model for the discrimination of prostate cancer tissue for risk stratification purposes. The ROC curve below is for the more advanced disease (Gleason >7).

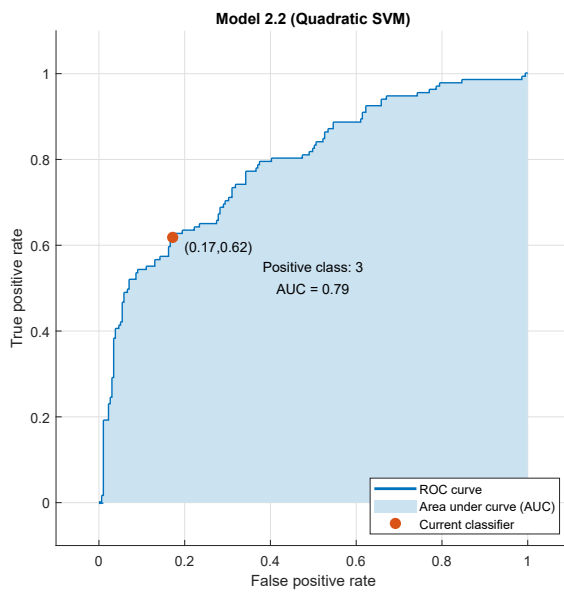


Fig. 5.24: Three group classification Quadratic SVM and a 5-fold cross validation model showing the AUC of 0.79 and overall accuracy of 64.6% (Gleason 7, <7 & >7).

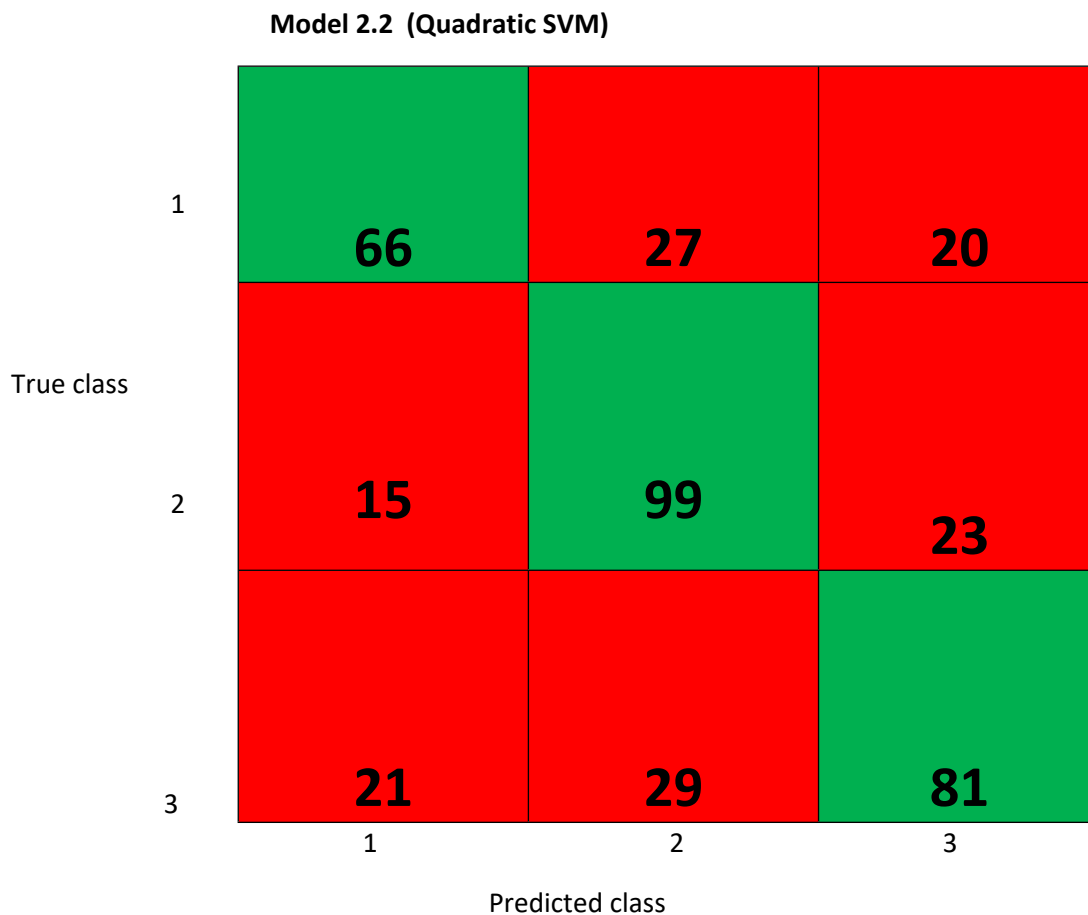


Fig. 5.25: Confusion matrix of a three-group classification using Quadratic SVM and a 5-fold cross validation model (Gleason 7, <7 & >7).

5.1.9: Four-group classification (Gleason grade group 1, 3, 4 & 5)

The same was also done for a four-group classification model for the Gleason grade group (1,3,4,5) with two linear discriminant functions to assess the level of separation between the four groups for visualization of the separation between the groups. It was not a good model, as the overall accuracy was less than 50%. Figure 5.26 and Tables 5.5a & 5.5b below show the separation between the groups and the overall accuracy rate.

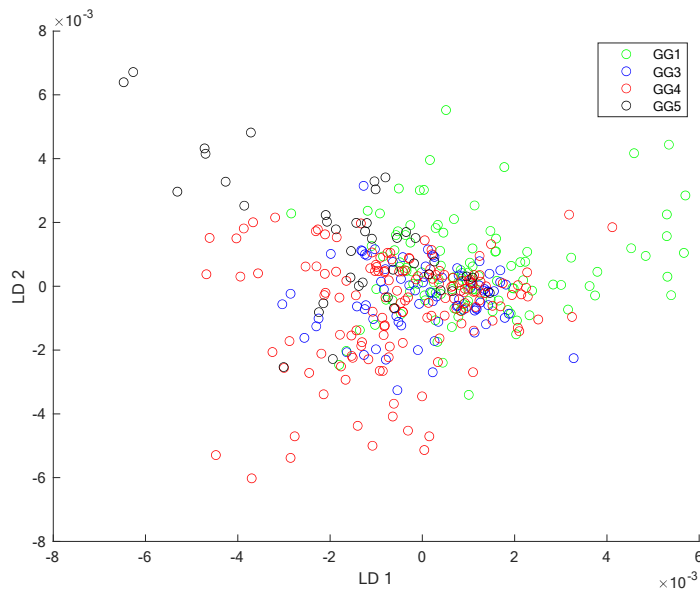


Fig. 5.26: Plot of the linear discriminant function of the scores for a four-group classification model using LDA for GG1, GG3, GG4 & GG5.

Histology Confirmed		Raman Predictions			
		GG =1	GG =3	GG = 4	GG = 5
1	GG = 1	53	28	15	17
2	GG = 3	13	50	8	6
3	GG = 4	35	33	58	25
4	GG = 5	1	9	8	22
Overall accuracy = 48.03% GG =Grade Group score					

Table 5.5a: Raman prediction against histology prediction in a 4-group model

Training Classification Performance	
Class	% Accurate Prediction
1	46.90
2	64.93
3	38.41
4	55.00
Training Performance = 48.03%	

Table 5.5b: Showing the training classification performance in a four-group PC-LDA model with Gleason Grade Group score 1, 3, 4 & 5.

5.1.10: Five group classification model (Gleason grade group scores)

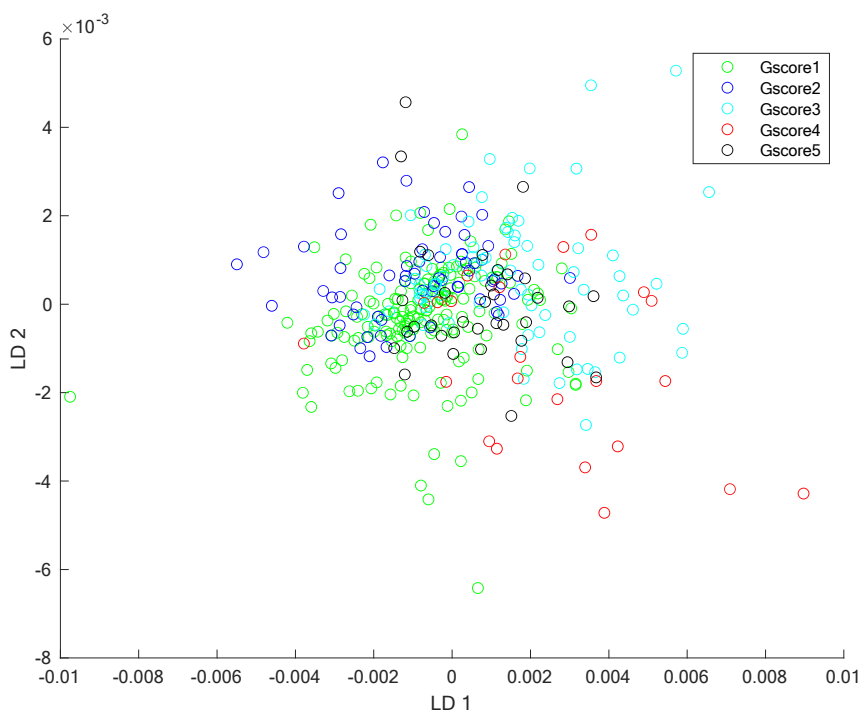


Fig. 5.27: Plot of the linear discriminant function of the scores for a five-group classification model using LDA for the Gleason grade group scores (GG1, GG2, GG3, GG4 & GG5) spectra.

Histology Confirmed		Raman Predictions				
Class		GGs = 1	GGs = 2	GGs = 3	GGs = 4	GGs = 5
1	GGs = 1	97	28	20	12	24
2	GGs = 2	20	25	8	0	11
3	GGs = 3	19	6	31	9	8
4	GGs = 4	2	2	3	13	4
5	GGs = 5	7	6	4	1	17
Overall accuracy = 42 %						

Table 5.6a: Raman prediction accuracy against histology predictions for a 5-group training model.

Training Classification Performance	
Class	% Accurate Prediction
1	52.49
2	39.06
3	41.09
4	50.00
5	37.14
Training Performance = 44%	

Table 5.6b: Showing the training classification performance in a five-group PC-LDA model with Gleason grade group score 1-5.

The worst outcome was observed in a five-group classification model with overall prediction accuracy of 45.9%, as seen in tables 5.6a & 5.5b above; hence not a great model with the tissue samples.

5.1.11: Comparison between two sets of two-group classification models:

When the background was subtracted from the raw data, the LDA model for distinguishing Raman spectra into two groups (benign versus cancer) demonstrated an overall prediction accuracy of about 60.8%, as shown in tables 5.7a & 5.7b below. Nevertheless, when spectra were classified into the different Gleason risk stratification groups, the prediction accuracy dropped below 50%. However, the overall prediction power for low versus high-grade tumours was recorded at about 59%. Shows that the model is not ideal for risk stratification, particularly when the background was subtracted.

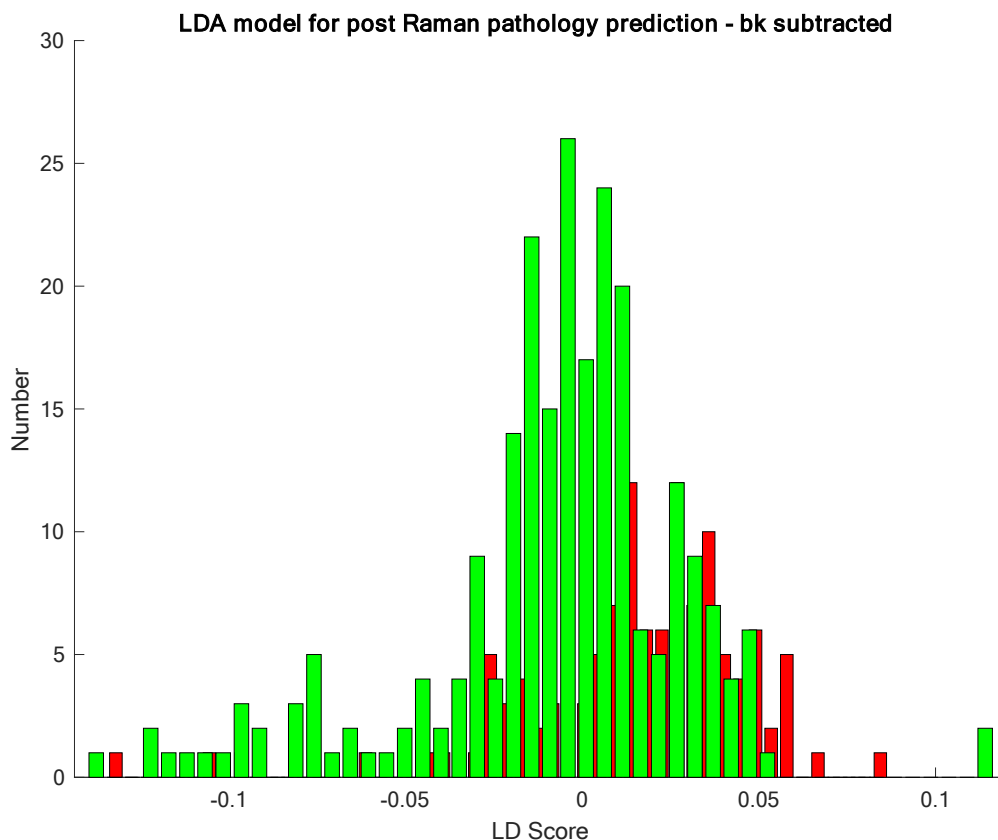


Fig. 5.28: Bar chart showing the Raman spectroscopy prediction power of a two group (benign vs cancer) with the aid of PC-LDA model with normalisation of the raw data to the area under the curve.

Histology Confirmed	Raman Prediction	
	Benign	Cancer
	Benign	143
Cancer	46	74

Table 5.7a: Raman prediction accuracy against histology in a 2-group training model.

Training Classification Performance	
Class	% Accurate Prediction
1	60.42
2	61.67
Training Performance = 60.83 %	

Table 5.7b: Showing the training classification performance in a two-group PC-LDA model with benign versus malignant tumours.

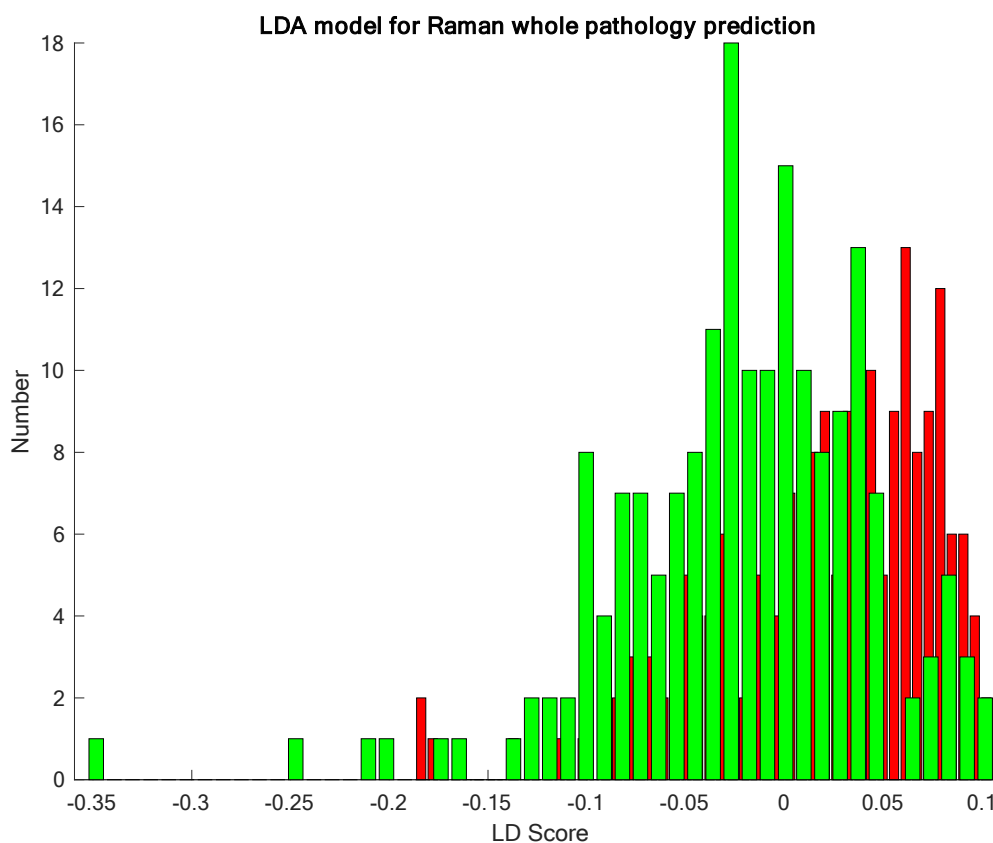


Fig. 5.29: Bar chart showing the Raman spectroscopy prediction power of a two group (benign & GS<7 vs GS 7 & >7) with the aid of PC-LDA model with normalisation of the raw data to the area under the curve.

Histology Confirmed		Raman Prediction	
		Benign/GS = <7	GS = ≥7
	Benign/GS = <7	102	83
	GS = ≥7	73	123

Table 5.8a: Raman prediction accuracy against histology in a two-group model (low grade versus high grade tumours).

Training Classification Performance	
Class	% Accurate Prediction
1	55.14
2	62.76
Training Performance = 59.06 %	

Table 5.8b: Showing the training classification performance in a two-group PC-LDA model with low grade tumours versus intermediate and high-grade tumours.

5.1.12: Partial least square analysis:

The partial least square analysis is often utilised to assess the prognostic impact of various factors. It is a method used for constructing prediction models that are many and highly collinear. It finds a linear regression model by projecting the predicted and observable variables to a new space.

PLS - PSA

RMSEP =

7.3840

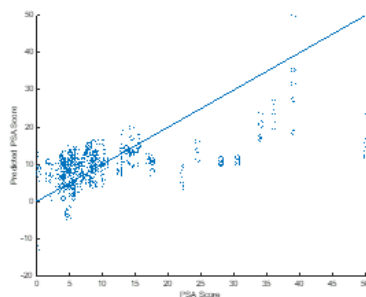


Fig. 5.30: Partial Least squares regression of the PSA showing a RMSEP of 7.3840

The Root mean square error of prediction calculated by summing all the squared prediction errors during cross validation. It is an indication of the reliability and predictive ability of the model. The lower

the root mean square value error of prediction (RMSEP), the higher the prediction ability of the model. The RMSEP of this model is 7.3840 as demonstrated in figure 5.30 above.

5.2: Serum Spectral analysis:

The Raman spectroscopy maps were recorded with the aid of the InVia Raman system and were loaded into MATLAB R2019a (the MathWorks inc Natick, Massachusetts, USA) for data pre-processing. These data were subjected to baseline correction using a 23-point Savitzky-Golay filter for smoothing, and cosmic ray contributions were removed. The noise in the Principal Components was individually eliminated by inspection and subsequently by an objective method, therefore, filtering off noise level. Data with an intensity of fewer than 400 counts at 1650 cm^{-1} were eliminated. PC noise reduction assisted in reducing the noise in a set of spectra by ensuring that only noise-free components were reconstructed. This process ensured that all the background noises were filtered out from the data set while vital spectral information was preserved.

After the pre-processing stage, the mean intensity on the y-axis was calculated to compare the values between the different maps. Data were validated with a 5-fold cross-validation. All spectra were mean centred, and 25 principal components were utilised to compress the data before discriminant classification at each training run. 20% of the data were held back from the training and utilised to test the model's performance in each fold (5 times).

Figure 5.31 below shows the separation between the mean spectra of benign and malignant samples. There was not a great deal of separation between both spectra.

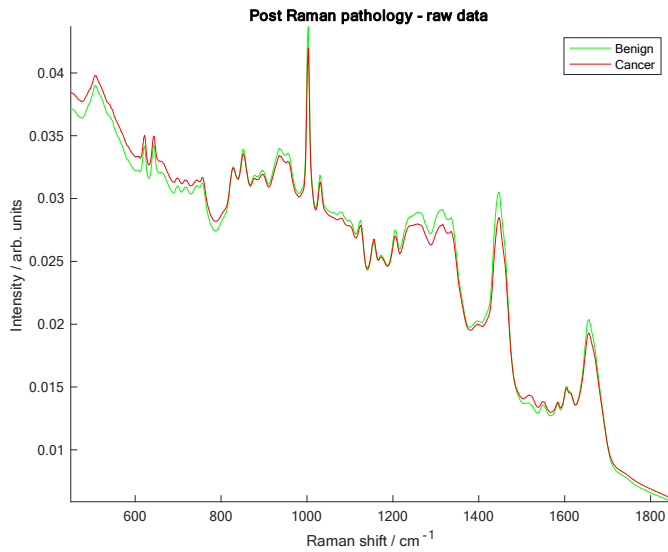


Fig. 5.31: Spectral differences between benign and cancer from the raw data after histology assessment was carried out.

5.2.1: Two group pathology training classification model

Prediction accuracy for the two pathology groups using PC-LDA algorithm for benign and cancer group. This is demonstrated in figure 5.32 with benign in green and cancer in red. Overall prediction accuracy of 72.3% is shown in table 5.9a & b below.

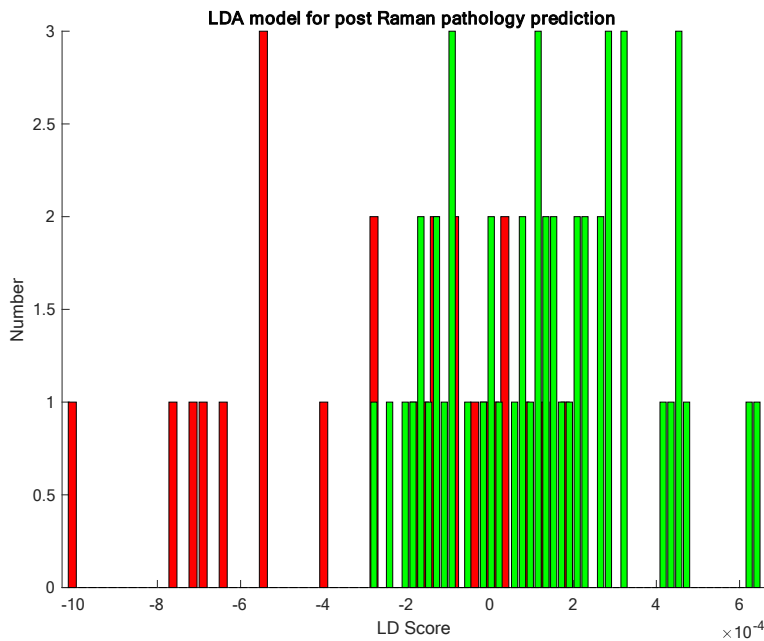


Fig. 5.32: Bar chart showing the training classification model for two pathology groups (benign vs cancer) with the aid of PC-LDA model.

Histology Confirmed	Raman Prediction	
	Benign	Cancer
	Benign	38
Cancer	8	17

Table 5.9a: Raman prediction accuracy against histology in a two training PC-LDA model in blood serum samples.

Training Classification performance	
Class	% Correct
1 (Benign)	74.51
2 (Cancer)	68.00
Training Performance = 72.37%	

Table 5.9b: Showing the training classification performance in a two-group PC-LDA model with benign versus malignant tumours.

5.2.2: Four Group training model:

Prediction accuracy for the two pathology groups using the PC-LDA algorithm for benign and cancer groups, which is demonstrated in figure 5.32 with benign in green and cancer in red, the overall prediction accuracy of 72.3% is shown in Tables 5.9a & b below.

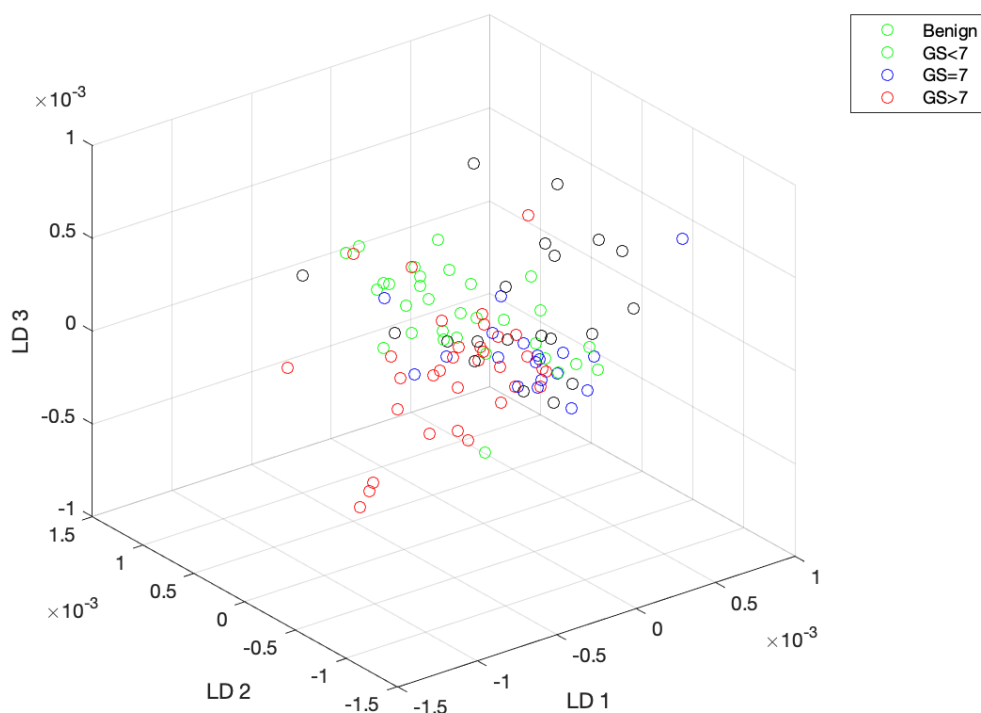


Fig. 5.33: Training classification model showing a 3-Dimensional (3D) Plot of the linear discriminant function of the scores for each class spectrum (Benign, GS<7, GS=7, GS>7).

Histology Confirmed		Raman Predictions			
		Benign	GS = <7	GS = 7	GS = >7
1	Benign	18	8	2	2
2	GS = <7	3	14	1	1
3	GS = 7	7	6	16	4
4	GS = >7	2	4	3	11
Overall accuracy = 55.34 %					

Training Classification Performance	
Class	% Accurate Prediction
1	56
2	68.42
3	48.49
4	55
Training Performance = 55.34%	

Table 5.10a & b: Showing the training classification performance in a four-group PC-LDA model with Benign, GS <7, GS =7, GS >7.

5.2.3: Two Pathology Group training classification model: Low versus high grade tumours

A training classification model was built using the two pathology diagnostic groups (low versus high-grade tumours). Better outcome was shown with the low-grade tumours (benign/GS = <7) with accurate class prediction of 77.6%, while the second class recorded prediction accuracy of 52.8% with an overall training performance of 64.1% as demonstrated in figure 5.34 and tables 5.11a & b below.

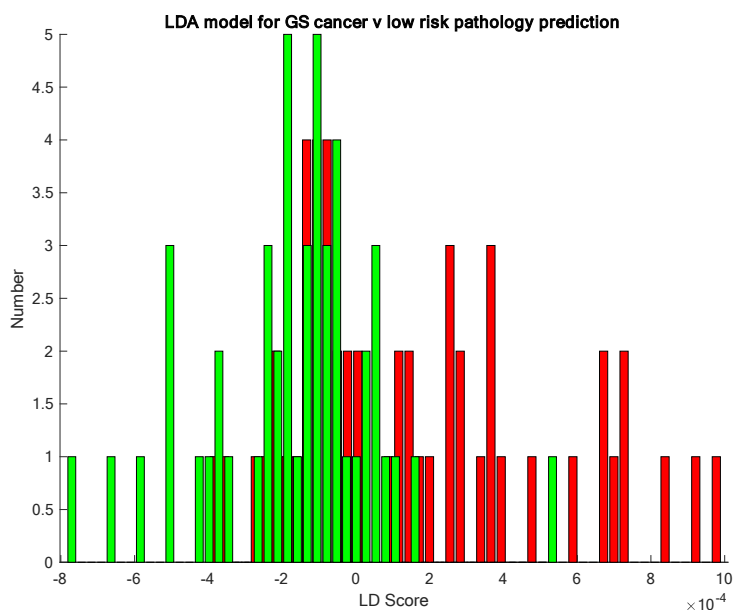


Fig. 5.34: Bar chart showing the Raman spectroscopy prediction power of a two group (low risk vs intermediate and high-risk tumours) with the aid of PC-LDA model.

Histology Confirmed	Raman Prediction	
	Benign / GS = <7	GS = 7 / GS = >7
	Benign / GS = <7	39
GS = 7 / GS = >7	24	29

Training Classification performance	
Class	% Correct
1 (Benign / GS = <7)	77.55
2 (GS = 7 / GS = >7)	52.83
Training Performance = 64.07%	

Table 5.11a & b: Showing the training classification performance in a two-group PC-LDA model with low-risk vs intermediate / high risk tumours.

5.2.4: Three Group training classification model

The figure 5.34 below shows a three-group training classification model demonstrating the ability of Raman spectroscopy to distinguish between the low-grade tumours, intermediate & high-grade tumours. Although the overall accuracy of this diagnostic model was recorded at 56.3%. Nonetheless, the prediction accuracy of the intermediate-grade tumours (73.63%) was somewhat better than that of low-grade tumours (56.67%) and high-grade tumour (50.94%) as shown in table 5.12a & b below.

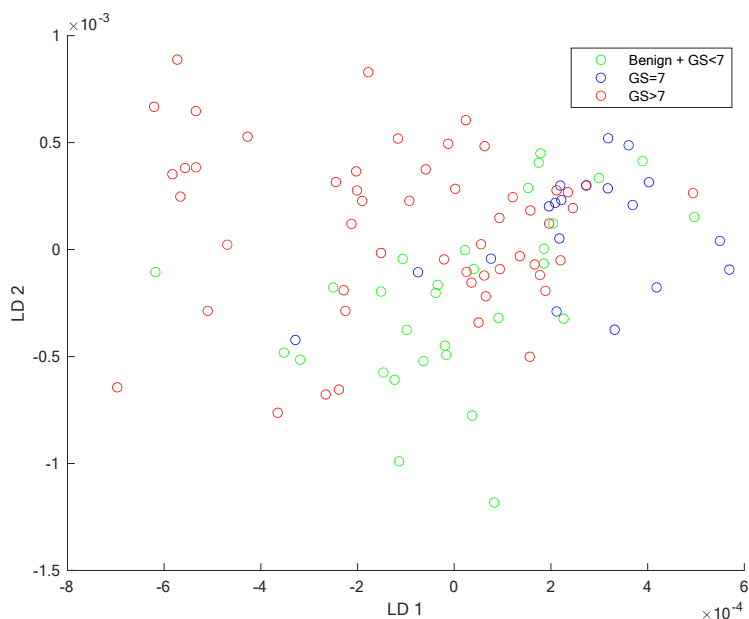


Fig. 5.35: Plot of the linear discriminant function of the scores for a three-group training classification model using LDA for the Gleason risk stratification groups (benign + Gleason <7, 7 & >7).

Histology Confirmed		Raman Predictions		
		Benign/ GS = <7	GS = 7	GS = >7
1	Benign / GS = <7	18	8	4
2	GS = 7	4	15	0
3	GG = >7	14	12	27
GS = Grade Score				
Overall accuracy = 56.31%				

Table 5.12a: Showing the training classification performance in a three-group PC-LDA model with Gleason Risk stratification scores using blood serum samples.

Training Classification Performance	
Class	% Accurate Prediction
1	56.67
2	73.68
3	50.94
Training Performance = 56.31 %	

Table 5.12b: Showing the training classification performance in a three-group PC-LDA model with Gleason Risk stratification scores using blood serum samples.

5.2.5: The two-group pathology classification (after training)

A two-group classification model was built to assess the prediction accuracy of the PC-LDA model for distinguishing spectra into two groups (low grade + intermediate versus high grade tumours), the receiver operating characteristics curve is shown in figure 5.36 below.

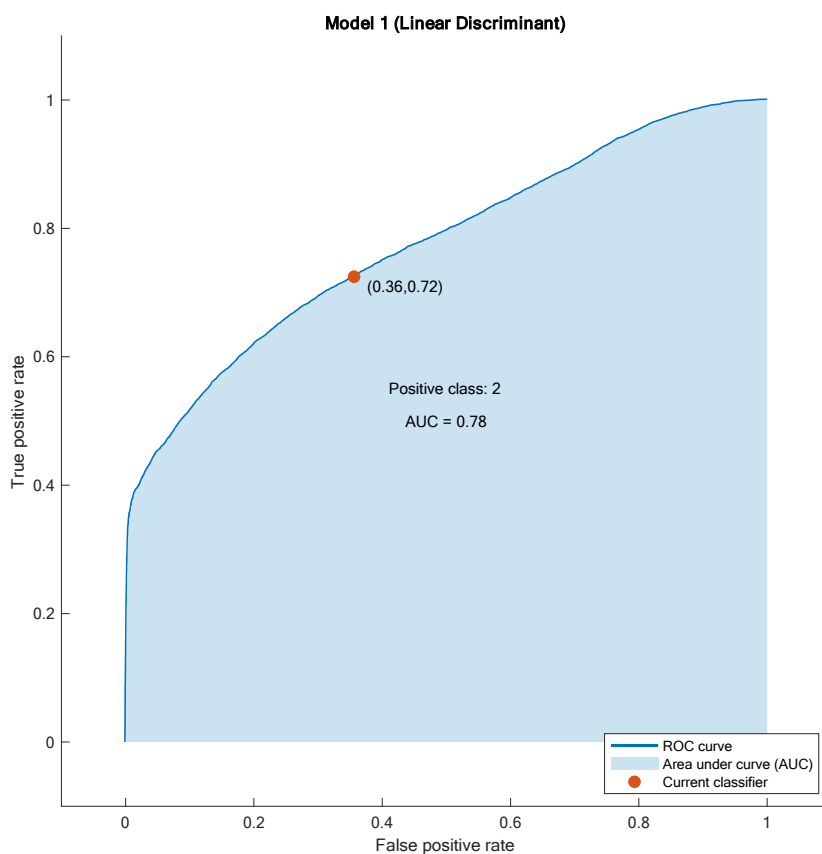


Fig. 5.36: Two group classification LDA and a 5-fold cross validation model showing the AUC of 0.78.

In order to further assess the performance of this model, a confusion matrix was constructed. The diagonal elements in green depicted correctly classified observations (figure 5.36), true positive and true negative. However, the diagonal elements on pink (figure 5.36) were the elements that were falsely predicted. The true positive rates for classes 1 & 2 were 64% and 72% respectively while the false negative rates for classes 1 & 2 were 36% and 28% respectively. The negative predictive value was recorded as 64% and 72% seen in the figure 5.38 below.

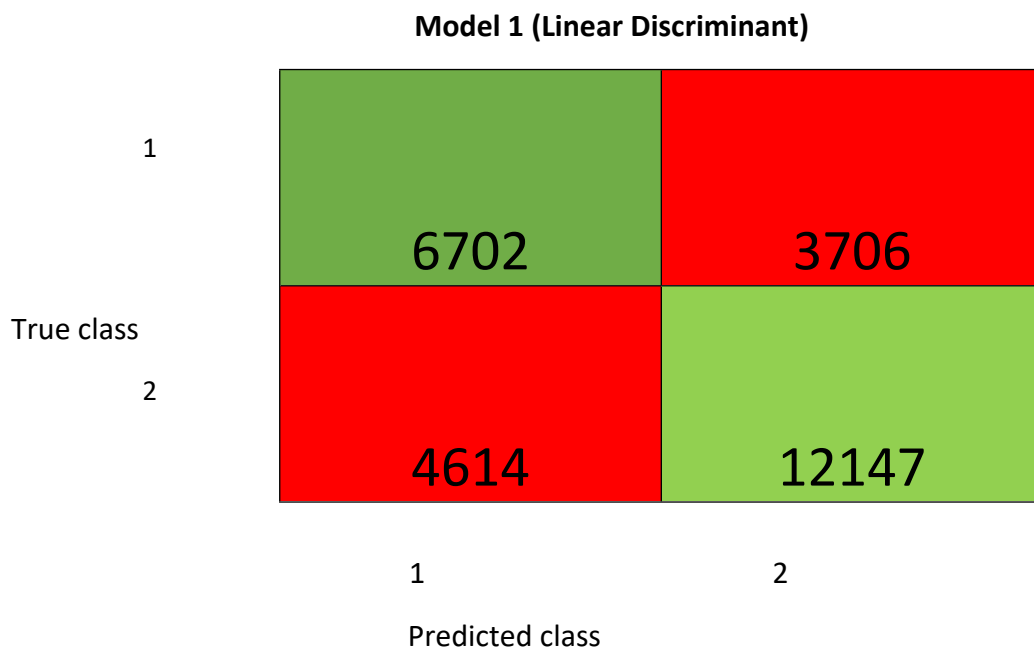


Fig. 5.37: Confusion matrix used to evaluate the performance of the LDA model as classification model of the group (Low-grade tumours versus intermediate and high-grade tumours).

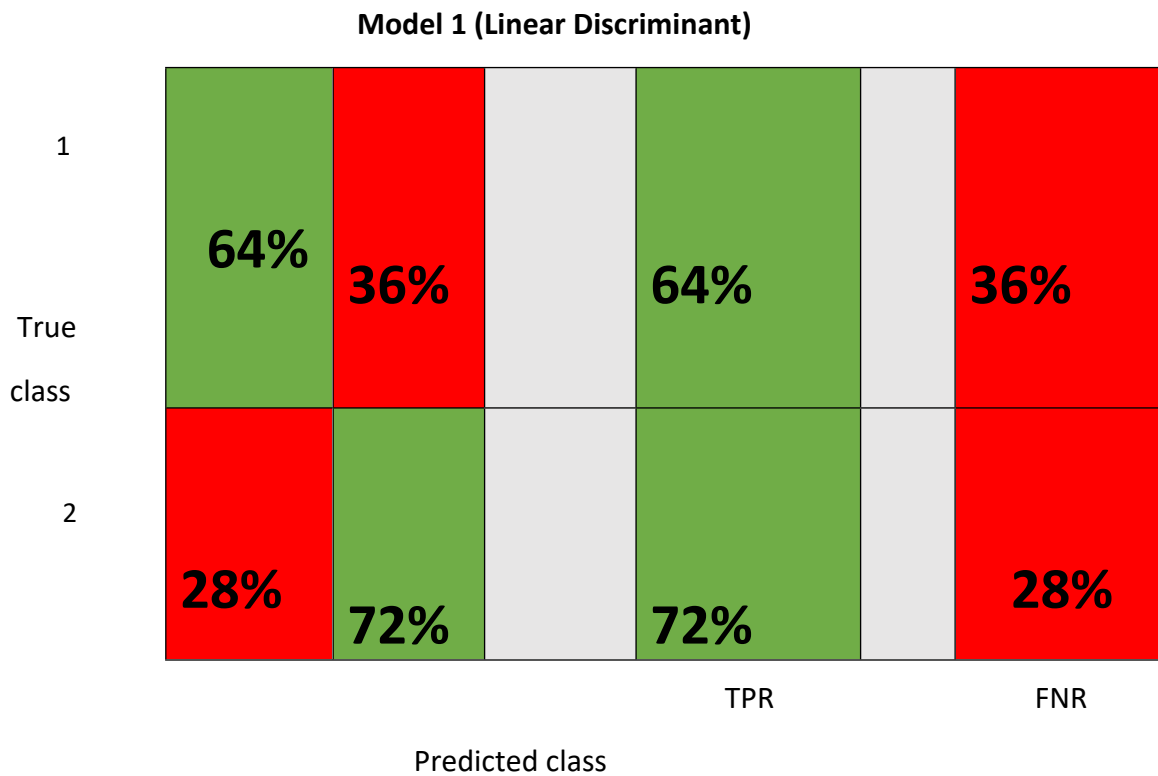


Fig. 5.38 The confusion matrix of a two-class prediction model showing the true positive and false negative rates low grade versus intermediate & high-grade tumours.

Model 1 (Linear Discriminant)

True class	1	59%	23%
	2	41%	77%
Positive Predictive Value		59%	77%
False Discovery Rate		41%	23%
		1	2
		Predicted class	

Fig. 5.39: The confusion matrix of a two-class (low grade versus intermediate & high-grade tumours) prediction model showing the positive predictive value and false discovery rates.

The model above depicted a positive predictive value of 59% and 77% (figure 5.39) respectively with a false discovery rate of 41% and 23% (5.38) respectively for both class 1 and 2 pathology groups.

Support vector was utilised to also evaluate the performance of this model as a classification tool to distinguish the spectra into two groups of low grade versus intermediate + high grade tumours. The support vector machine demonstrated an overwhelming 0.97 (figure 5.40) area under the receiver operating characteristic curve for a two-class prediction (low grade versus intermediate + high grade tumours) as demonstrated in the figure 5.40 below. This has been able to show that with the aid of the cubic support vector machine learning algorithm, an outstanding diagnostic performance can be

achieved for the discrimination between low-grade versus intermediate + high-grade tumours. The overall accuracy of 94% was demonstrated with the cubic Support vector machine learning algorithm.

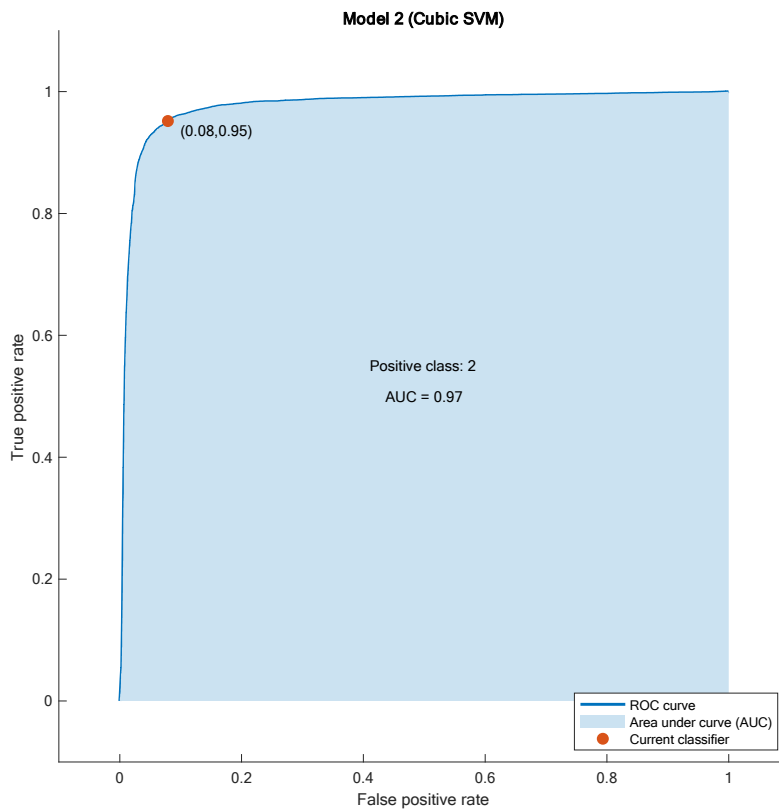


Fig. 5.40: Receiver Operating Characteristic curve with a five-fold leave one out cross validation for a 2 group mean spectral (low grade versus intermediate and high-grade tumours) cubic SVM model showing an area under the curve of 0.97 with an overall accuracy of 94%.

A confusion matrix was also constructed to further quantify how good this classification model was for discrimination between the low grade and intermediate + high grade tumours. This demonstrated a positive predictive value of 95% and a false discovery rate of 5% as demonstrated in the figure 5.40 below. This is quite impressive as outstanding diagnostic model aimed at differentiating between the low-grade tumours and intermediate / high grade tumours. The negative predictive value was also recorded as 92% while the false omission rate was 8% as seen in the figure 5.41 below.

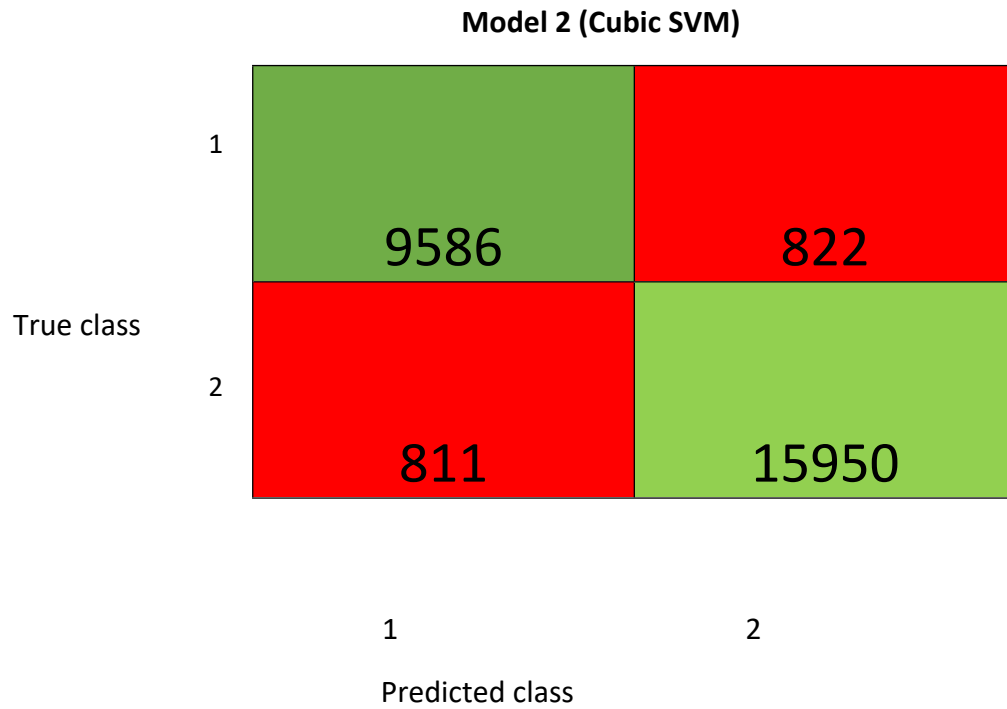


Fig. 5:41: Confusion matrix for a 2 group SVM classification model (Benign / GS = <7 VS GS7 / GS = >7).

The true positive rates of 92% and 95% was documented for this discriminatory model as shown in figure 5.42 below. Furthermore, positive predictive value of 92% and 95% were recorded for class 1 & 2 respectively (figure 5.42).

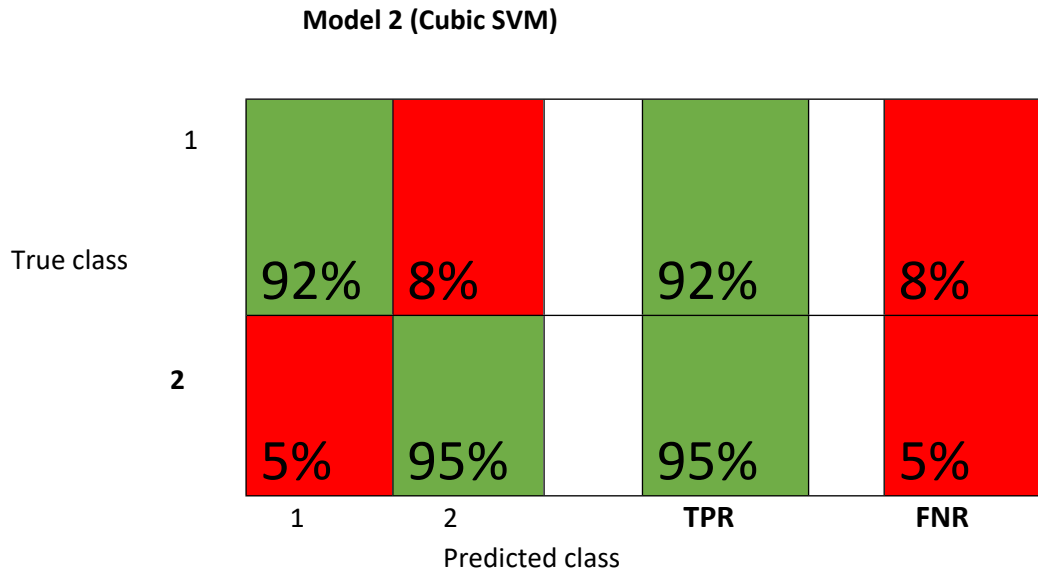


Fig. 5.42: Confusion matrix for a 2 group SVM classification model (Benign / GS = <7 VS GS7 / GS = >7).



Fig. 5.43: Confusion matrix for a 2 group SVM classification model (Benign / GS = <7 VS GS7 / GS = >7).

Linear discriminant analysis was utilized to assess the discrimination ability of the model in distinguishing between the high-grade tumours (GG 4 & 5) and low + intermediate grade tumour (GG 1-3). With this model, an overall accuracy rate of 74.9% was recorded with an area under the curve of 0.81 as shown in the figure 5.44 below. An interpretation of the area under the curve for discriminating between the high-grade tumours and low-grade tumours (Gleason grade group score of 1, 2 and 3) depicted a good classification model.

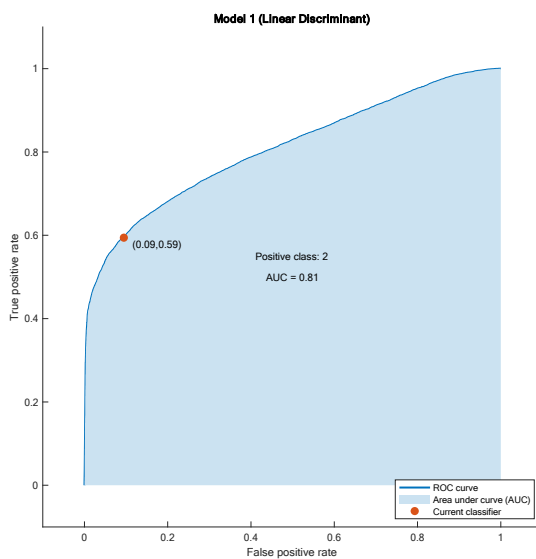


Fig. 5.44: Two group classification LDA and a 5-fold cross validation model showing the AUC of 0.81 (Gleason grade group score of (1, 2, 3) vs (4 &5)).

A confusion matrix was also constructed to further quantify how good this classification model was for discrimination between the low grade and intermediate + high grade tumours. This demonstrated a positive predictive value of 91% and a false discovery rate of 9% as demonstrated in the figure below. However, the negative predictive value was also recorded as 59% while the false omission rate was 41% as seen in the figure 5.45 below.

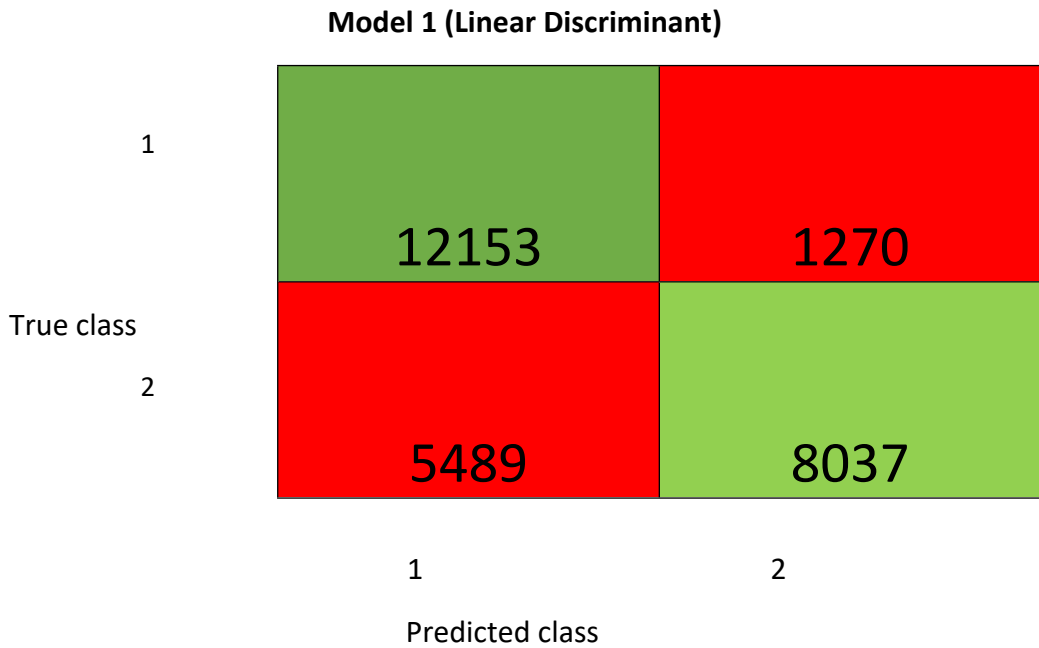


Fig. 5.45: Confusion matrix for a 2 group LDA classification model (Gleason grade group score of (1, 2, 3) vs (4 &5)).

The true positive rate for prediction into class 1 and 2 were 91% and 59% respectively while the false negative rates for class 1 and 2 were 9% and 41% respectively (figure 5.46) The positive predictive values for class 1 and 2 were 69% and 86% respectively as shown in figure 5.47 below.

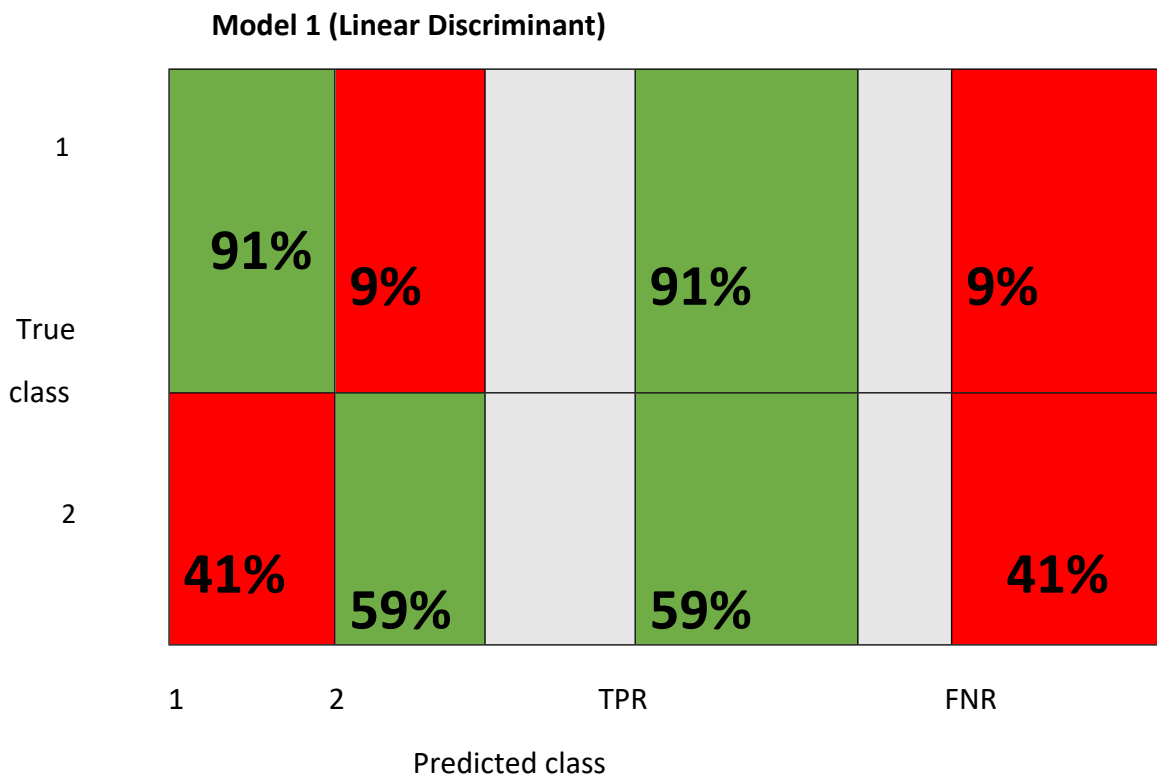


Fig. 5.46: Confusion matrix for a 2 group LDA classification model.



Fig. 5.47: Confusion matrix for a 2 group LDA classification model showing positive predictive values and false discovery rates for class 1 and 2.

The cubic support vector machine was also used to differentiate between the high- and low-grade tumours. An overall accuracy of 94.6% with the area under the curve of 0.98, which depicted an outstanding discriminating model at classification of spectra into different classes as shown in the figure 5.48 below.

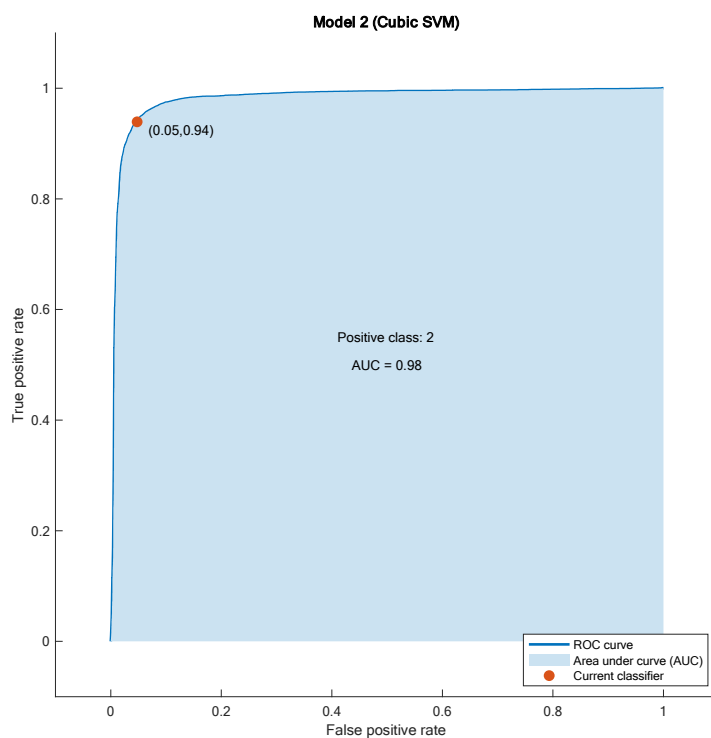


Fig. 5.48: Two group classification (Low grade vs high grade tumours) Support vector machine and a 5-fold cross validation model showing the AUC of 0.98 with overall accuracy of 94.6%.

A confusion matrix was also constructed (figure 5.49) to quantify further how good the classification model was for discrimination between the low-grade and intermediate + high-grade tumours, demonstrating a positive predictive value of 95% and a false discovery rate of 5% as demonstrated in the figure 5.49 below. It is impressive as an outstanding diagnostic model aimed at differentiating between low-grade and intermediate/high-grade tumours. The negative predictive value was also recorded as 94%, while the false omission rate was 6%, as seen in figure 5.50 below.

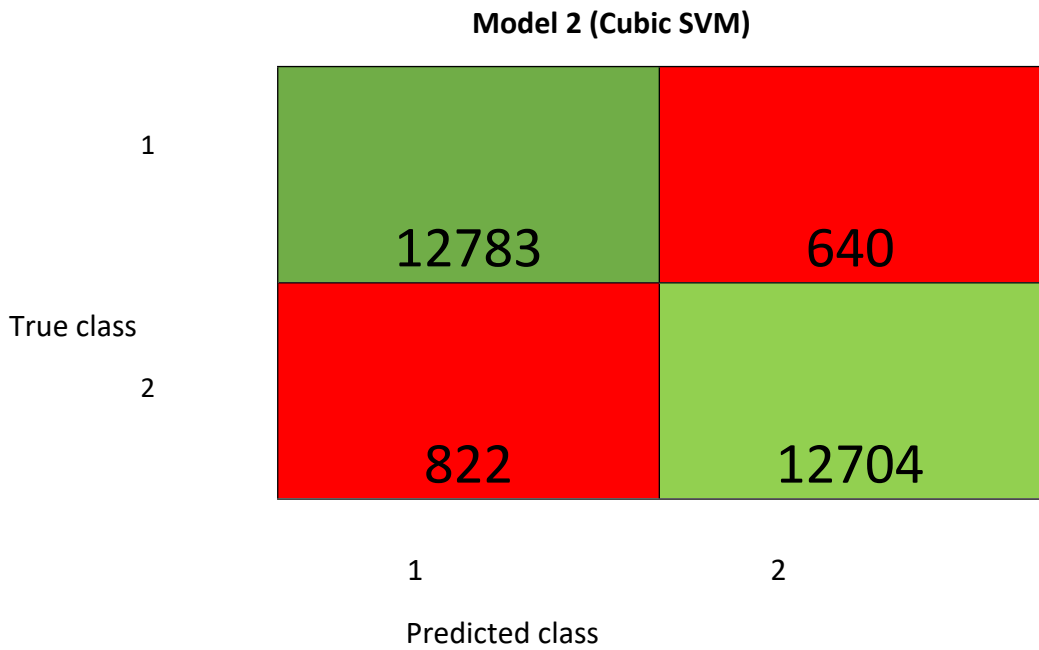


Fig. 5.49: Confusion matrix for a 2 group SVM classification model

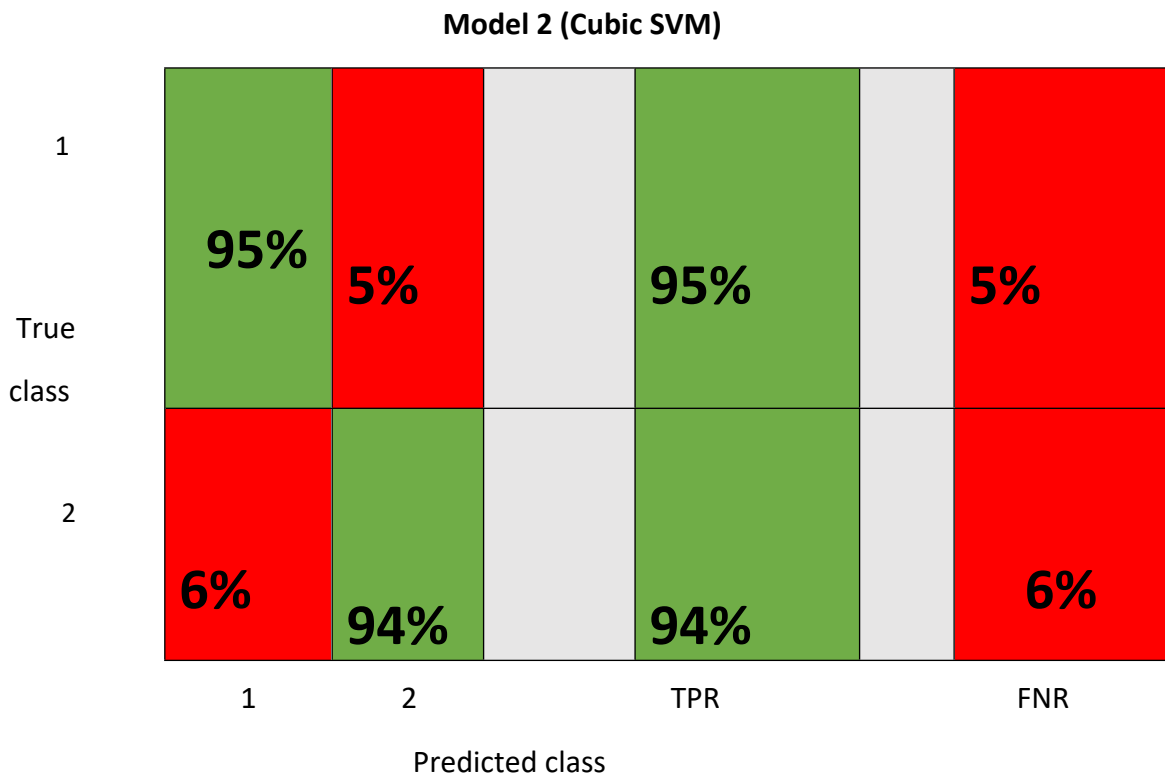


Fig. 5.50: Confusion matrix for a 2 group SVM classification model showing True positive and false negative rates.

Confusion matrix for multiple classes calculations and interpretation:

The diagonal values in the green boxes were the true positive rates or the sensitivity for the respective classes.

The total number of the values for any class was calculated as the sum of the values for the corresponding row, which was the same as true positive + False negative values for that class.

The number of false negatives for a class was the sum of the values in the corresponding rows, excluding the true positive value.

The number of false positives for a class was the sum of the values in the corresponding columns, excluding the true positive value.

The number of true negatives for a particular class was the sum of all the columns and rows, excluding that class's column and row.

Sensitivity is the true positive rate = $TP/(TP+FN)$, which in this case is the true positive divided by the sum of the values on the row of that particular class in our confusion matrix.

Specificity, also known as the true negative rate, was calculated by: $TN/(TN+FP)$. TN (true negatives) for a particular class was regarded as the sum of all the values in the columns and rows, excluding that class's column and row. False positive was the sum of the values in the corresponding columns, excluding the TP.

N/B:

For this study, the positive class was regarded as cancer, while the benign class was regarded as negative. High Gleason grades and high Gleason grade group were regarded as positive classes.

True positive indicated that the classification model predicted cancer or high-grade tumour consistent with the gold standard technique. False positives indicated that the classification model predicted the presence of cancer or a high-grade tumour. In contrast, the gold standard technique indicated the presence of a benign or low-grade tumour. True negative values indicated the situation where the classification model predicted the absence of cancer or a high-grade tumour, which corresponded well with the prediction of gold standard techniques.

5.2.6: Three group classification model

LDA was used to classify the spectra into three distinct groups, which included benign, low- and high-grade tumours. Although the overall accuracy was recorded as 64.6%, the area under the receiver operating characteristics curve was 0.80 for the more advanced disease (figure 5.51 below), which was a good model by interpretation.

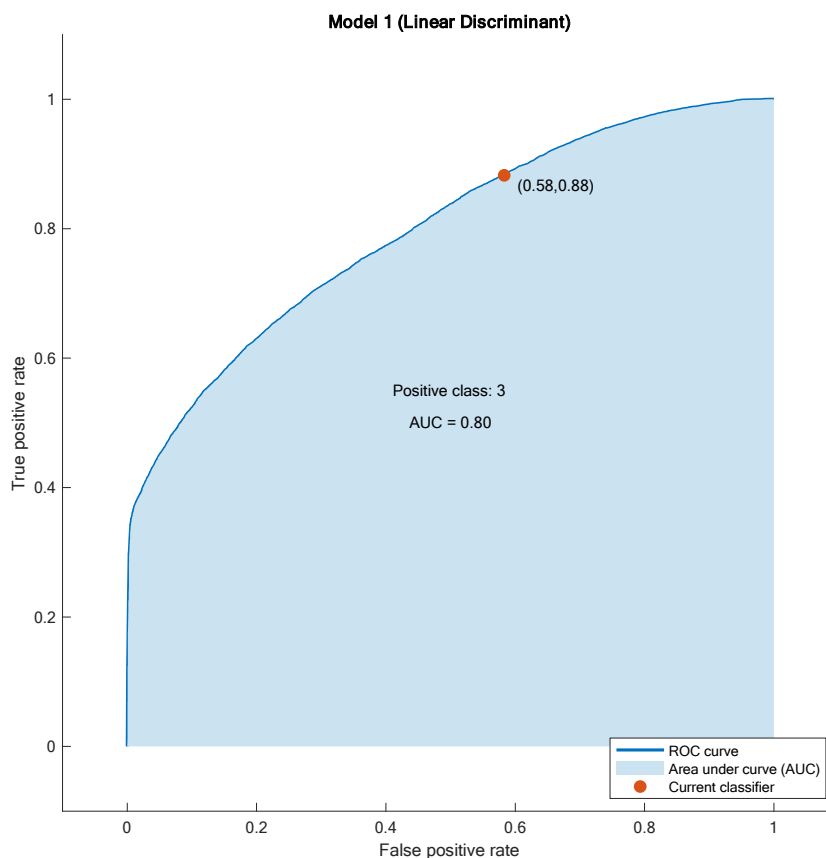


Fig. 5.51: Three group classification (Low grade vs high grade tumours) LDA and a 5-fold cross validation model showing the AUC of 0.80 with overall accuracy of 64.6%.

The confusion matrix used to quantify the level of accuracy of the LDA classification model demonstrated positive predictive values for the three classes were 47%, 37%, and 71% for classes 1 to 3 (figure 5.54), respectively. In comparison, the true positive rates (sensitivity) for the three classes (1-3) were 32%, 18% & 88%, respectively, as shown in figure 5.53 below.

Model 1 (Linear Discriminant)

	1	2	3
True class	1	2	3
1	2067	605	3834
2	903	706	2233
3	1377	583	14791
	1	2	3
	Predicted class		

Fig. 5.52: Confusion matrix with absolute values for a three-group discrimination with the aid of LDA model.

Model 1 (Linear Discriminant)

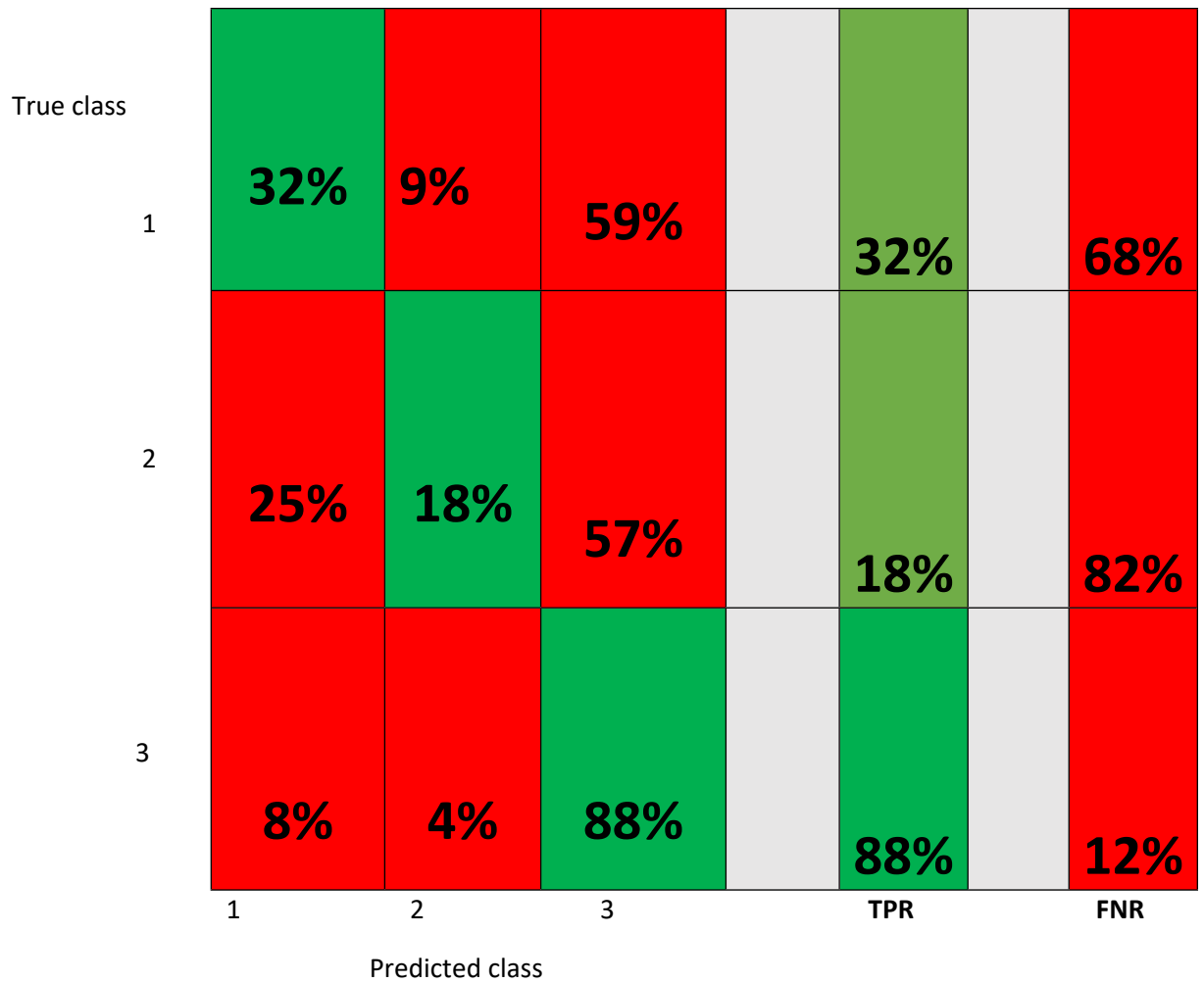


Fig. 5.53: Confusion matrix for a three-group discrimination with the aid of LDA model showing True positive rates and False negative Rates.



Fig. 5.54: Confusion matrix for a three-group discrimination with the aid of LDA model showing positive predictive values and False discovery rates.

Support vector machine learning was also utilised to distinguish between benign-, low- and high-grade tumours for risk stratification. The model can allow clinicians to identify the correct level of care to

administer to the different subgroups. With the cubic SVM for the three-group classification, an overall accuracy at discrimination was recorded as 93.2%, while the AUC of the receiver operating characteristic curve was 0.98. A brilliant discriminating model for three-group classification is shown in figure 5.55 below. The ROC curve shown below was for the pathology of interest in this model.

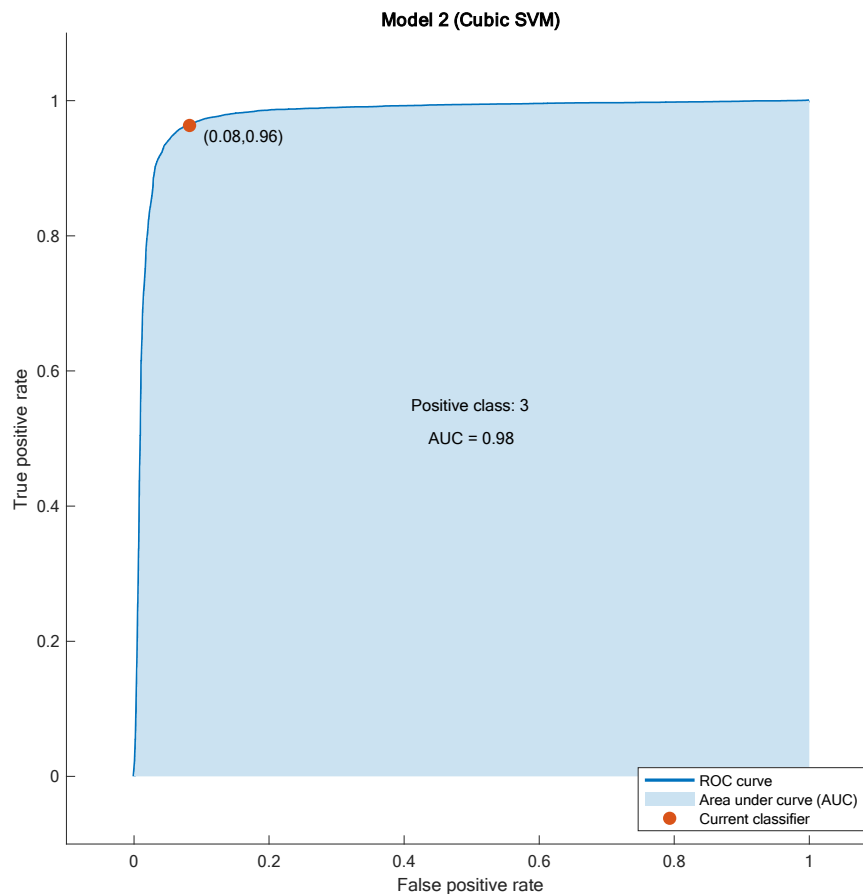


Fig. 5.55: Three group classification (benign vs Low grade vs high grade tumours) Support vector machine and a 5-fold cross validation model showing the AUC of 0.98 with overall accuracy of 93.2%.

A confusion matrix (figure 5.57) was plotted to evaluate further this classification model's performance for the three pathological groups. This further demonstrated a positive predictive value for class 1, 2, & 3 as 92%, 87% and 95% respectively with a corresponding false discovery rate of 8%, 13% & 5% respectively as demonstrated in figure 5.56 below. On the hand, the true positive rate for the three classes (1-3) were 89%, 86%, and 96%, respectively (figure 5.58 below).

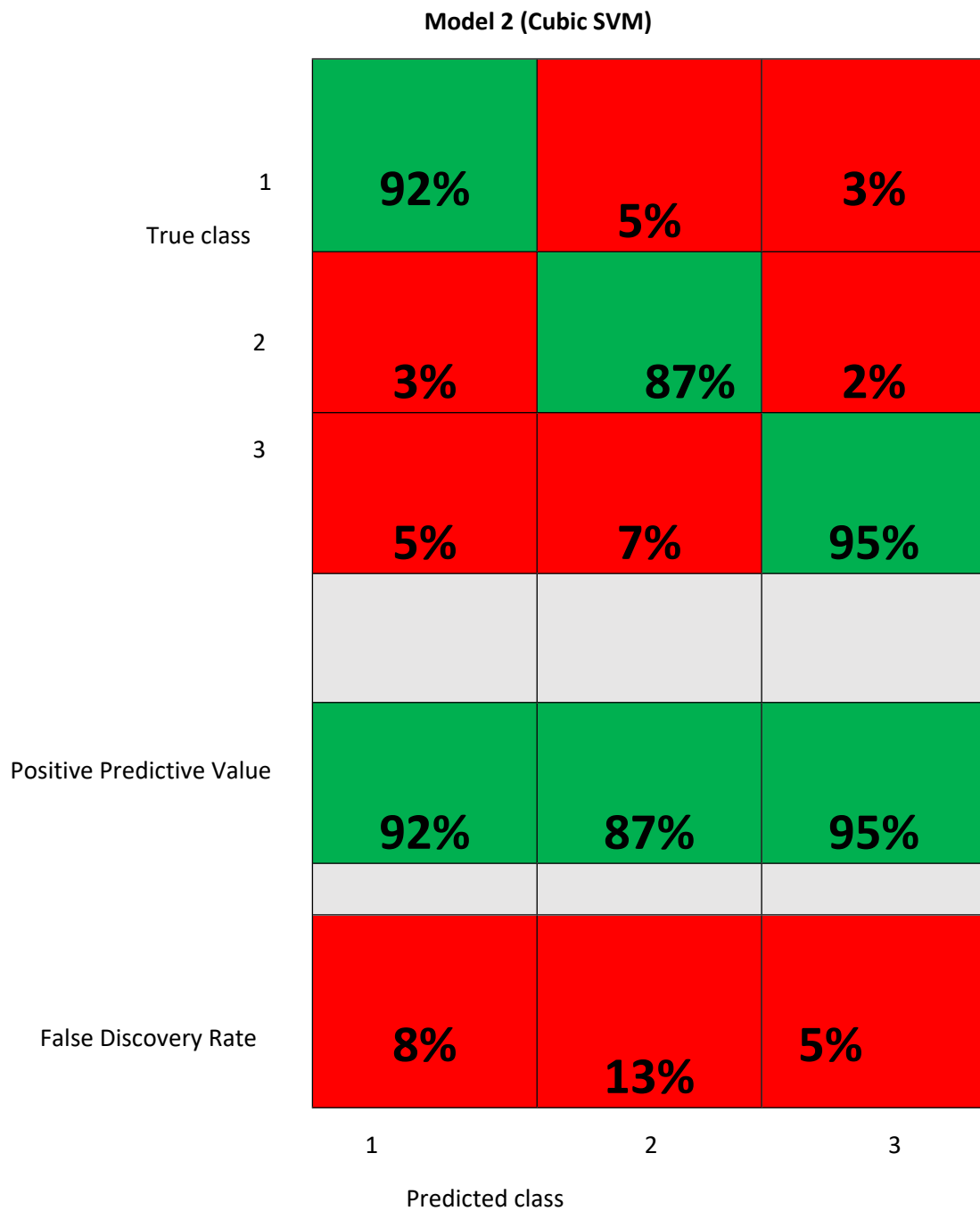


Fig. 5.56: Confusion matrix for a 3 group SVM classification model

Model 2 (Cubic SVM)

	1	2	3
1	5816	201	489
2	170	3365	367
3	330	285	16146
True class	1	2	3
	Predicted class		

Fig. 5.57: Confusion matrix for a 3 group SVM classification model

Model 2 (Cubic SVM)

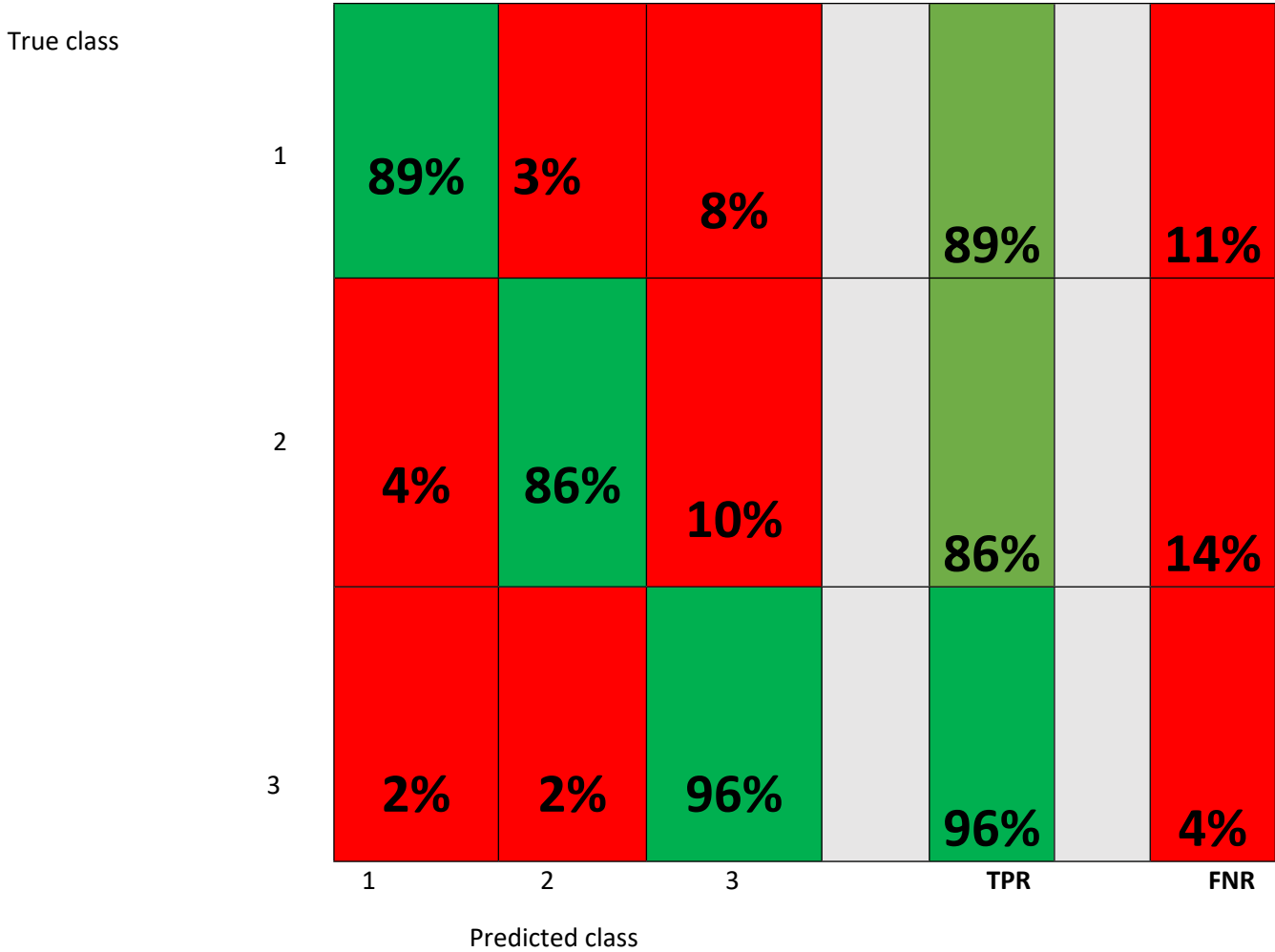


Fig. 5.58: Confusion matrix for a 3 group SVM classification model

Figures 5.59, 5.60 & 5.61 below demonstrate the spectral features that discriminate spectra into different groups.

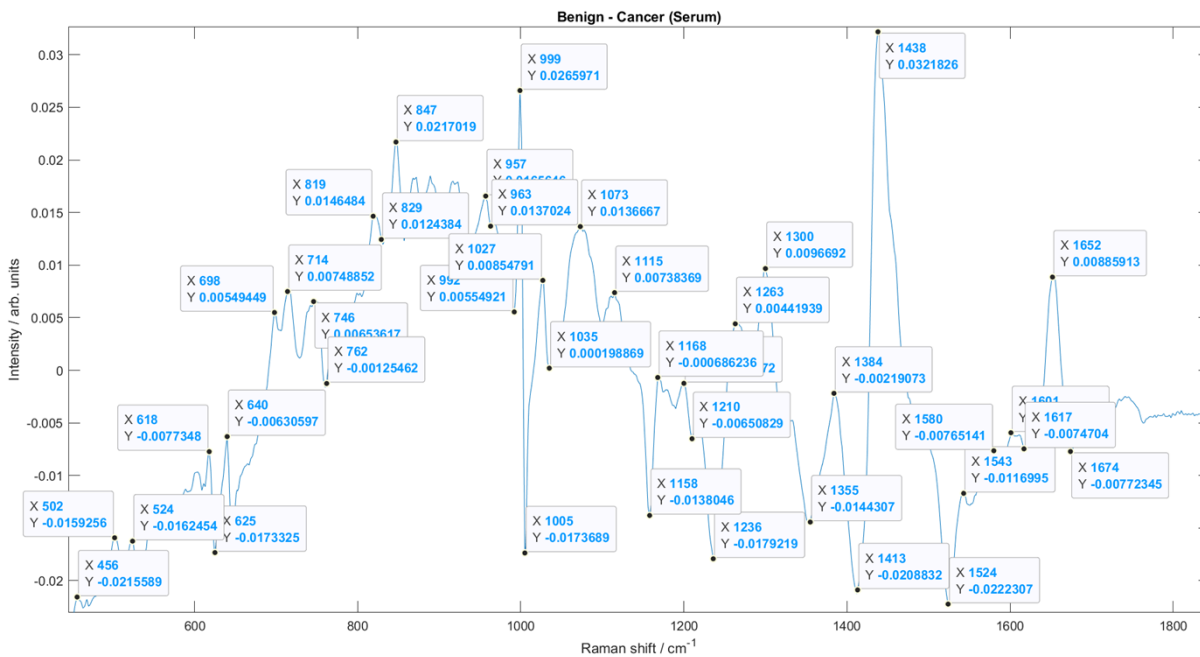


Fig. 5.59: The spectral features used for discrimination.

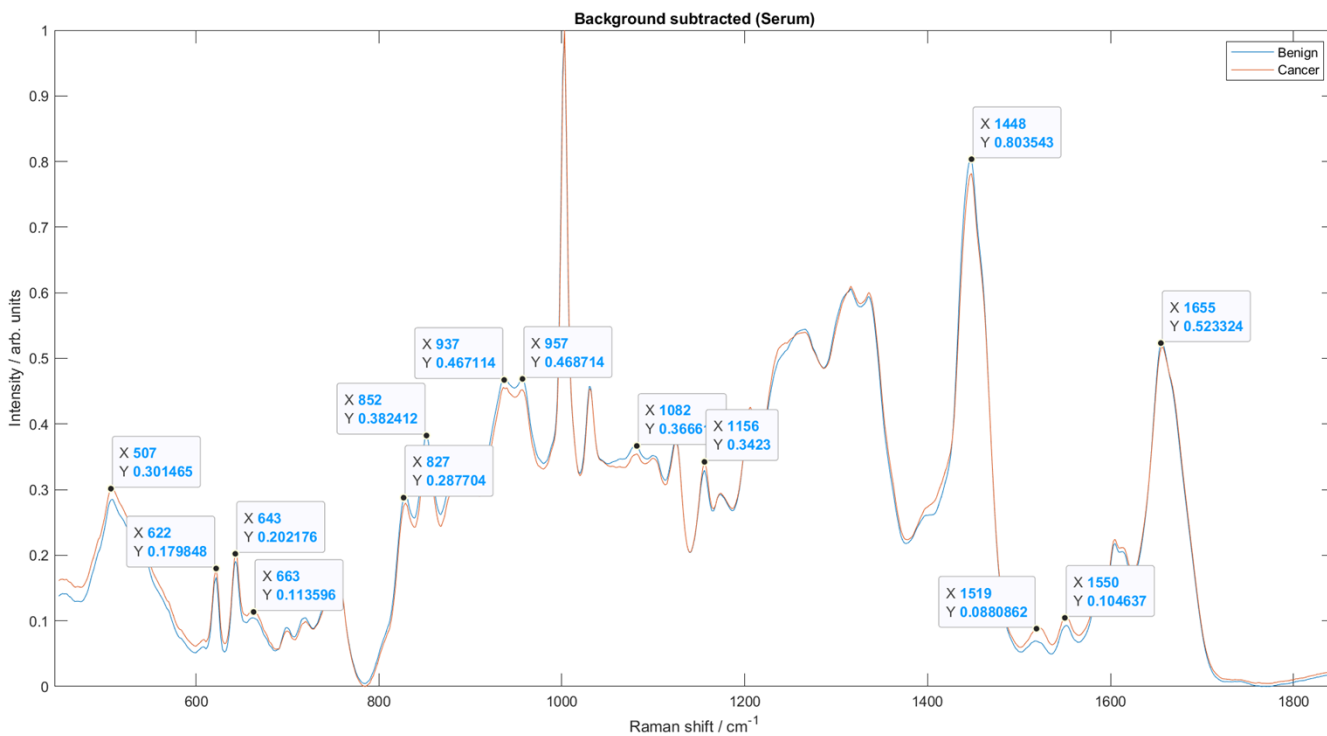


Fig. 5.60: Spectra difference between benign and cancer serum samples with peak assignment.

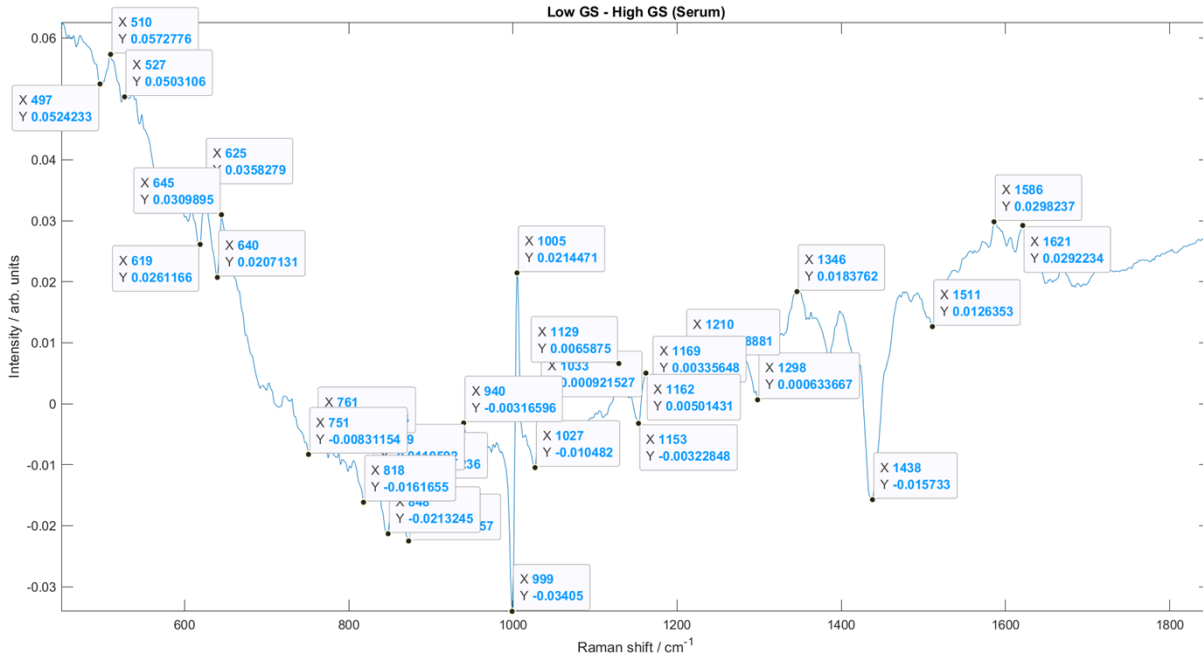


Fig. 5.61: Spectral differences between the low Gleason score (mean) and high Gleason score (mean).

11.3 Blood Plasma analysis:

The blood plasma spectra were all processed in the same manner, with all spectra with an intensity of fewer than 400 counts removed because they were outside the biological fingerprint region. 25 PCs were utilised to compress the data before discriminant classifications were carried out at each training run. 20% of the data were held out from the training and utilised to test in each fold (5 times). The mean spectra for benign and cancer are displayed in figure 5.62 below.

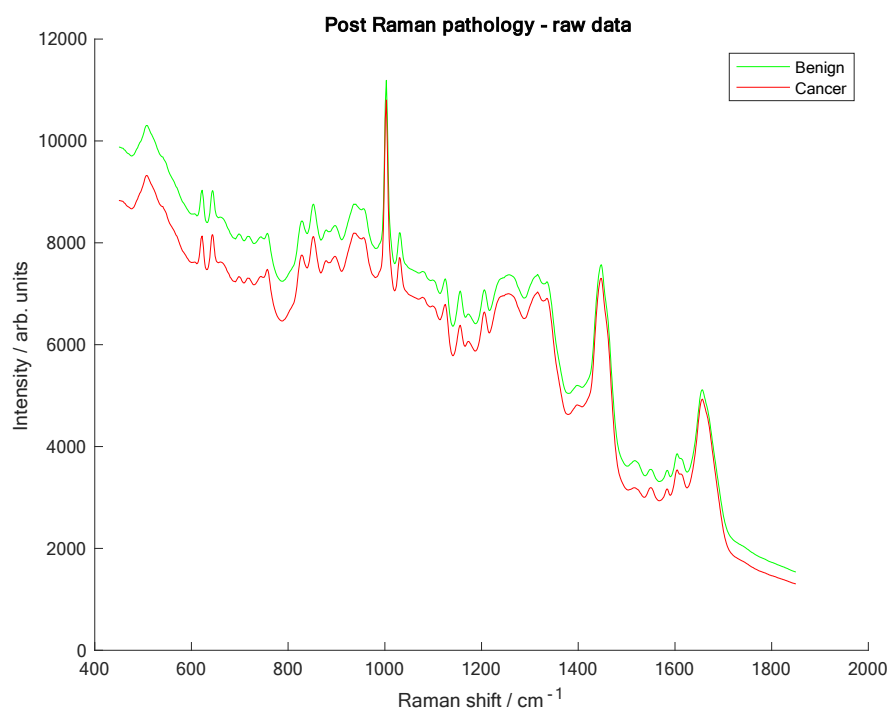


Fig: 5.62: Showing the separation between the mean spectra of the benign and the malignant samples.

5.3.1: Two Class discrimination Models:

Firstly, the linear discriminant analysis was utilised to discriminate the spectra into two pathology groups. Class 1 comprised all spectra from benign and low-grade Gleason <7 tumours. On the other hand, class 2 tumours consisted of all intermediate-grade tumours (Gleason 7) and high-grade (Gleason >7) tumour spectra. The area under the curve was 0.74 (threshold 0.49, 0.80), as shown in figure 5.63 below.

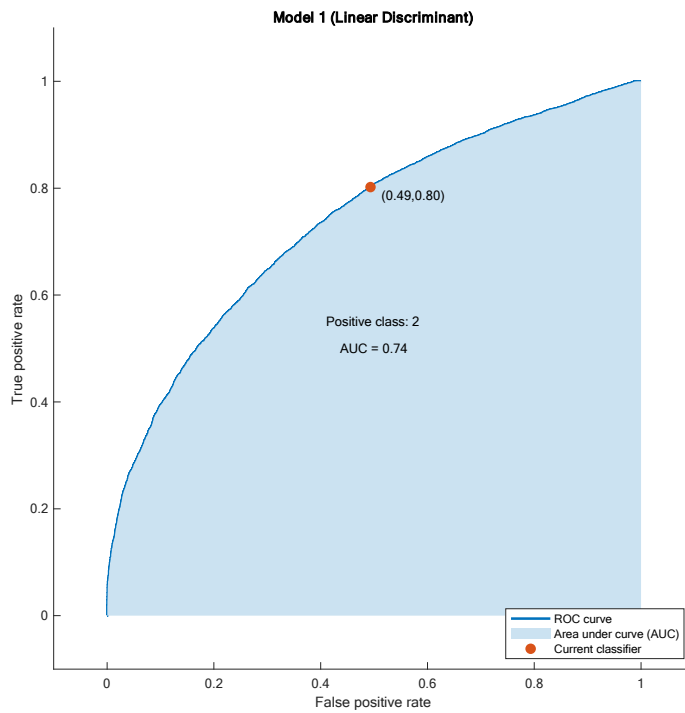


Fig. 5.63: Two class discrimination using PC-LDA with an AUC of 0.74 (threshold 0.49, 0.80). Low grade versus high grade tumour spectra.

The confusion matrix depicts the true positives and negatives in green, while the false positives and negatives are shown in red in figure 5.64 below.

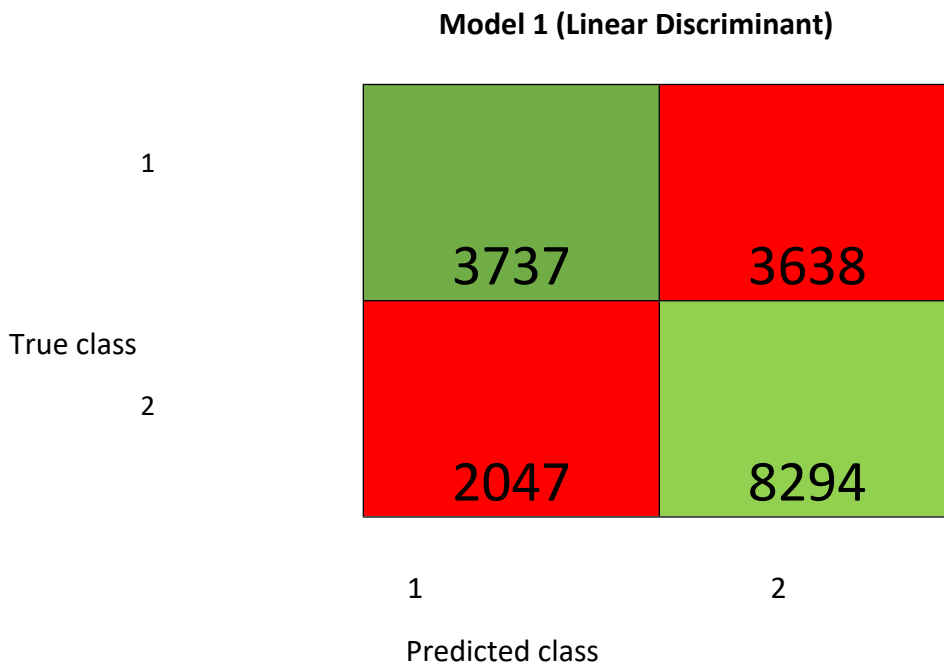


Fig. 5.64: Confusion matrix of the LDA classification model showing class 1 (benign & Gleason <7) and class 2 (Gleason 7 & >7).

The positive predictive values for classes 1 and 2 were 65% and 70%, respectively, while the false discovery rates for classes 1 and 2 were 35% and 30%, respectively, as demonstrated in figure 5.65 below. The sensitivity (true positive rates) for classes 1 and 2 were 51% and 80%, respectively, while the false negative rates for classes 1 and two were 49% and 20%, respectively, as shown in figure 5.66 below.

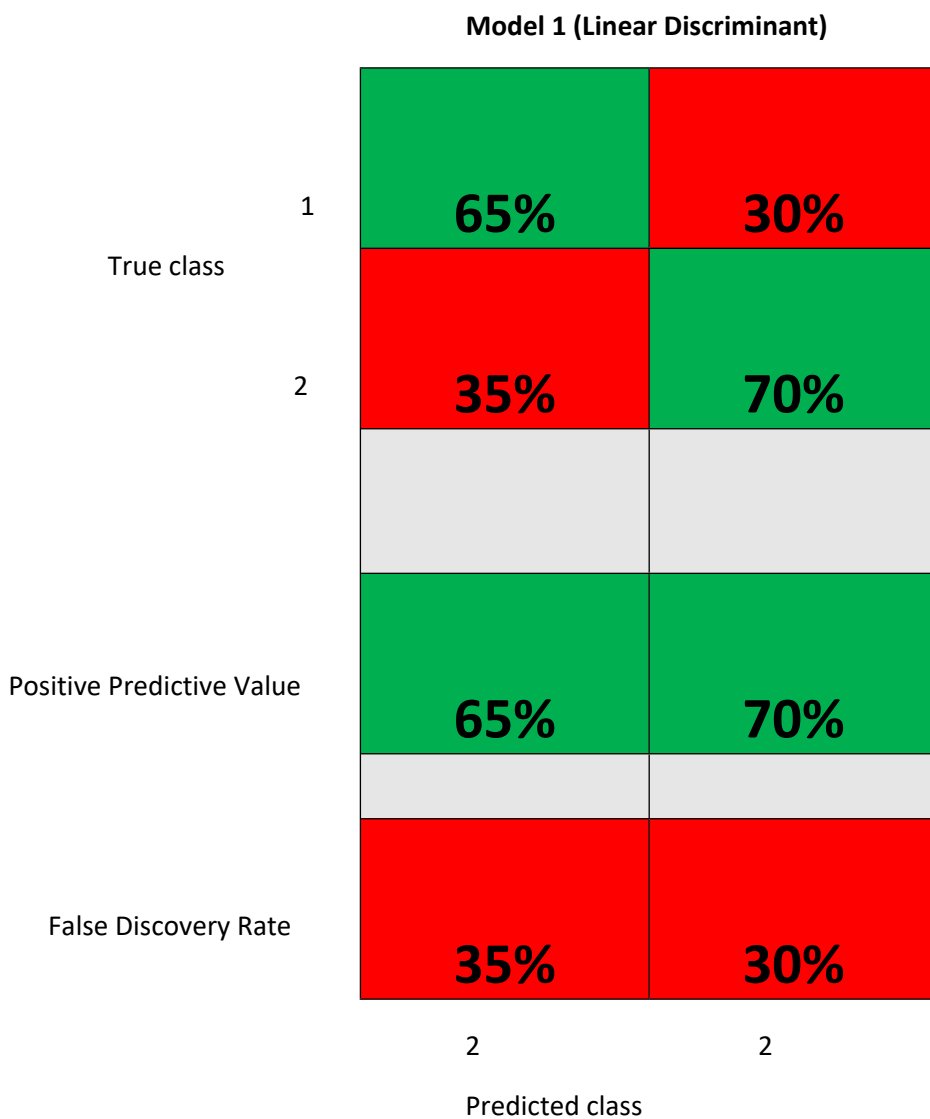


Fig. 5.65: Showing the Positive predictive values and False discovery rates for the two classes (Low grade vs high grade).

Model 1 (Linear Discriminant)

True class

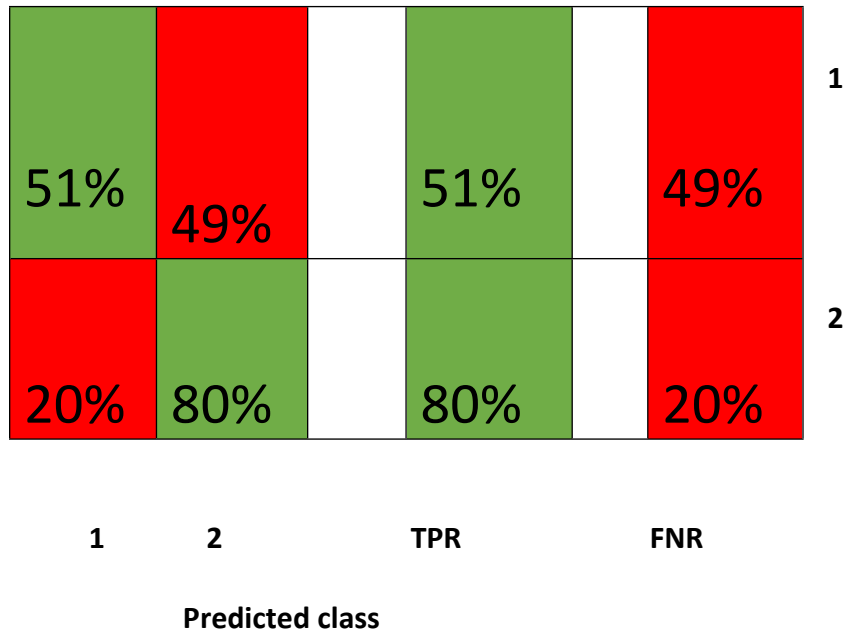


Fig. 5.66: Showing the True positive rates (sensitivity) and False Negative rates for two classes (low grade vs high grade).

SVM was also utilised as a discrimination model to classify the plasma spectra into benign & low-grade tumours (Class 1) and intermediate & high-grade tumours (class 2). As shown in figure 5.67 below, the area under the curve was 0.98 (threshold: 0.04, 0.97), which is an outstanding model.

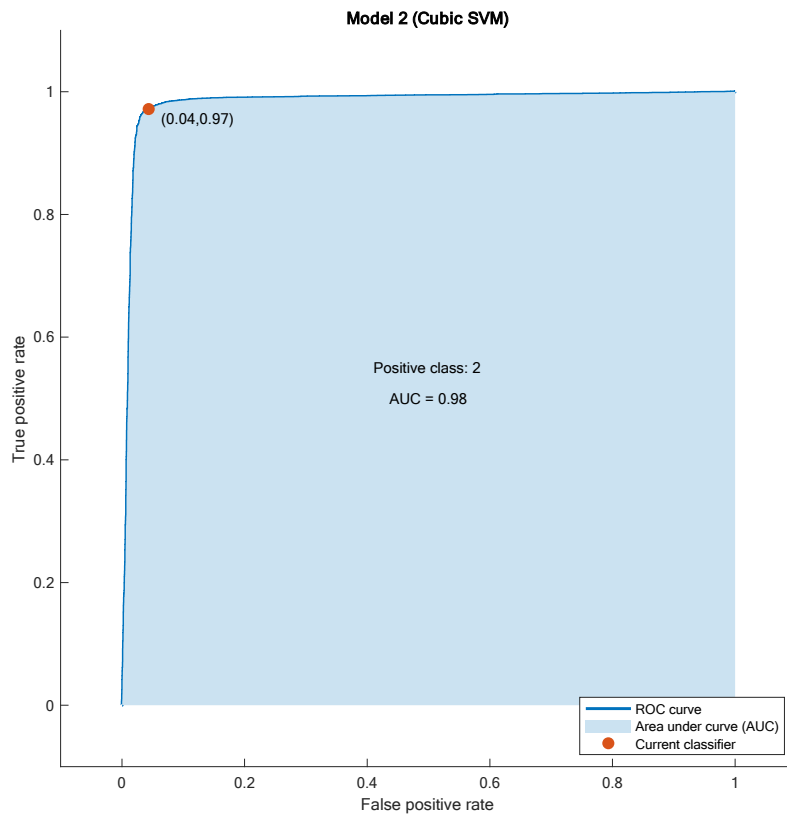


Fig. 5.67: Support Vector machine learning algorithm for a two class (benign + Gleason <7 versus Gleason 7 & >7) discrimination model showing an AUC of 0.98.

A confusion matrix (figure 5.68) was constructed to evaluate this classification model's performance further. The true positive rates were 96% and 97% for classes 1 and 2, respectively, while false negative rates are displayed in figure 5.69 below. The positive predictive values were 96% and 97% for classes 1 and 2, and false discovery rates are also demonstrated in figure 5.70 below, which further confirms that this model is excellent for discriminating between two pathology groups (benign +Gleason <7 vs. Gleason ≥7).

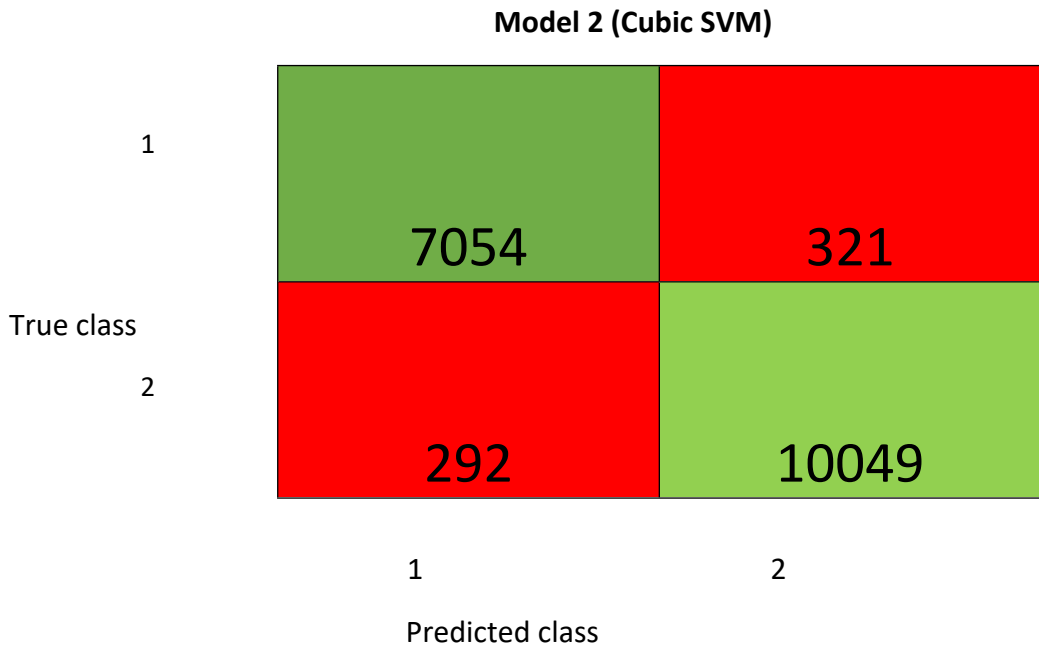


Fig. 5.68: The confusion matrix for a two class SVM model demonstrating the true positive and negative (green) and false positive and negative (pink) respectively.

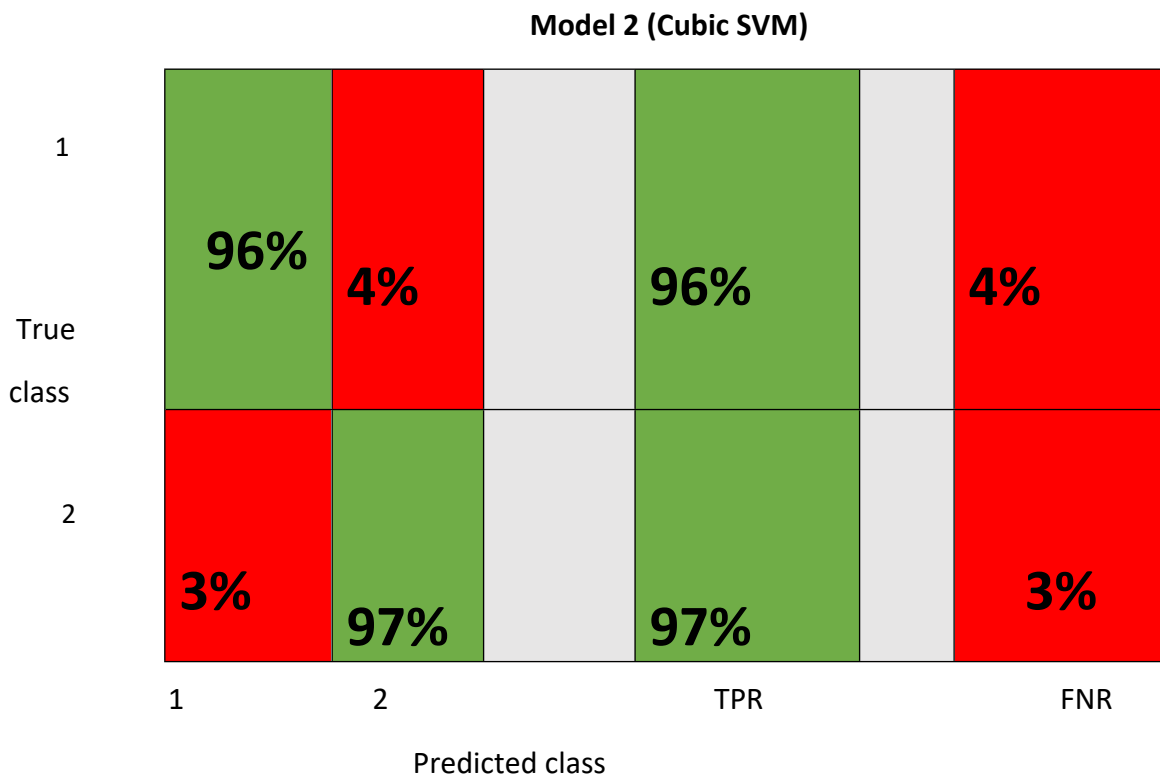


Fig. 5.69: The confusion matrix for a two class (Benign + < Gleason 7 vs Gleason ≥7) SVM model demonstrating the true positive rates and false negative rates (red) respectively.

Model 2 (Cubic SVM)



Fig. 5.70: The confusion matrix for a two class SVM model showing positive predictive values and false discovery rates respectively.

5.2.2: Two Group classification model with Low grade versus high grade tumours

Another two-group classification model assessed the Gleason grade group classification with Gleason grade groups 1, 2, & 3 classified as class 1 while Gleason grade groups 4 & 5 were classified as class 2 tumours. Both linear discriminant analysis and SVM learning algorithm were utilised to assess the performance of this two-group classification model.

When LDA was used to conduct the analysis, an AUC of 0.69 is shown in figure 5.71 below.

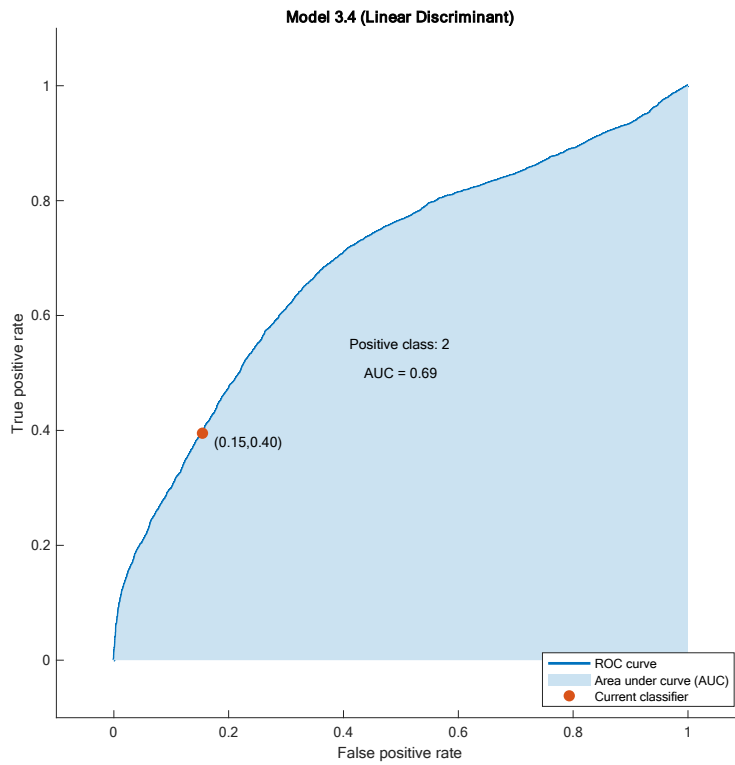


Fig. 5.71: Receiver operating characteristic curve showing an AUC of 0.69 in a two-group classification LDA model for low grade versus high grade tumours (Gleason grade group scores).

A confusion matrix was constructed to summarise the classification algorithm's performance further. The true positive rates for classes 1 and 2 were 85% and 40%, respectively, as shown in figure 5.73 below. Conversely, 15% and 60% false negative rates were recorded for classes 1 and 2, respectively, as demonstrated in figure 5.73 below.

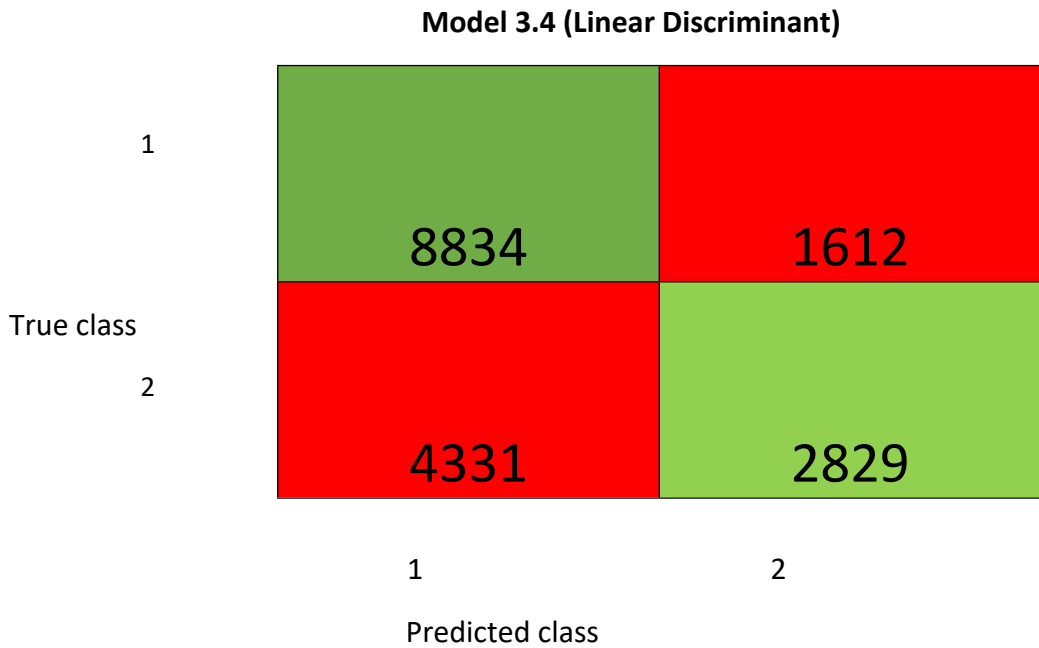


Fig. 5.72: Confusion matrix showing the true positive and false positives as well as the true and false negatives for Gleason 1,2 & versus Gleason 4 & 5 using LDA classification model.

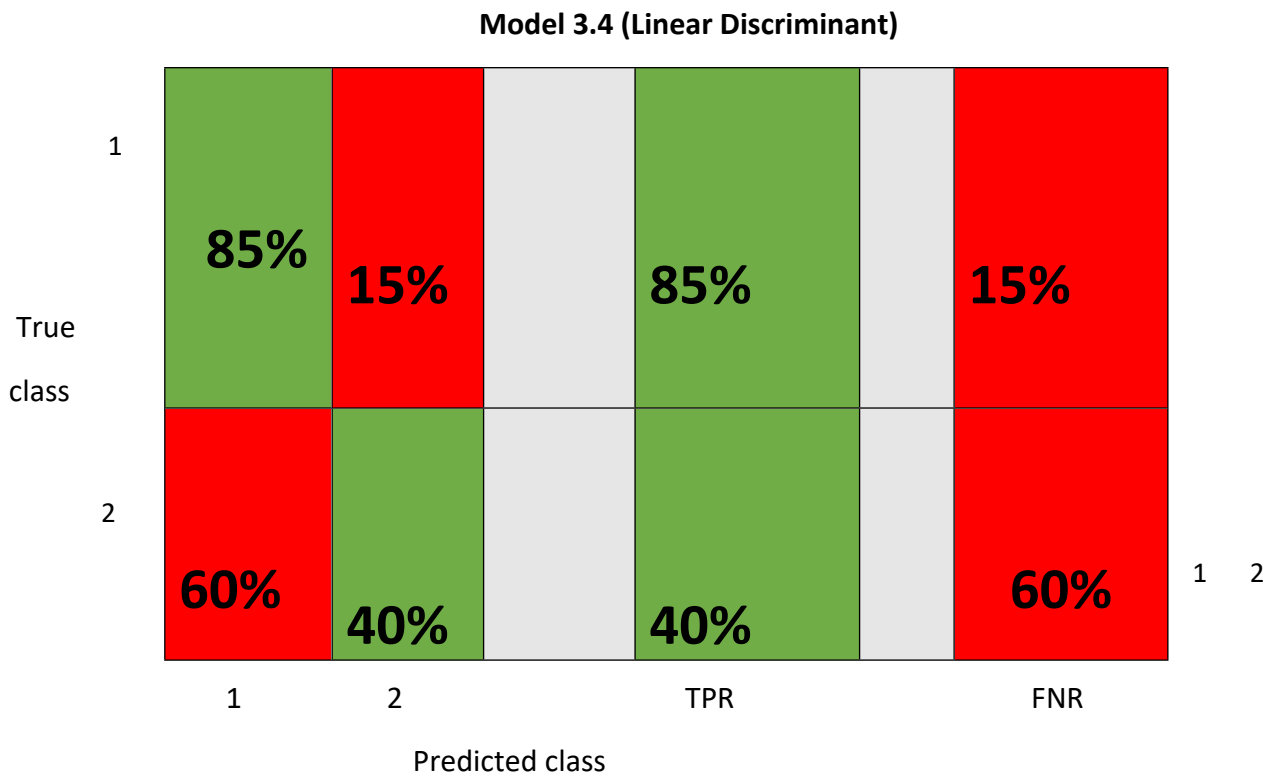


Fig. 5.73: Confusion matrix showing the true positive and false positives rates for Gleason 1,2 & 3 versus Gleason 4 & 5 using LDA classification model.

Support vector machine learning was also exploited to classify the spectra into two groups (Gleason grade groups 1, 2 & 3 versus Gleason 4 & 5). The figure below shows the receiver operating characteristics curve with an area under the curve of 0.98, which is an outstanding model for classification into two groups (Gleason grade groups 1-3 vs. Gleason grade groups 4-5).

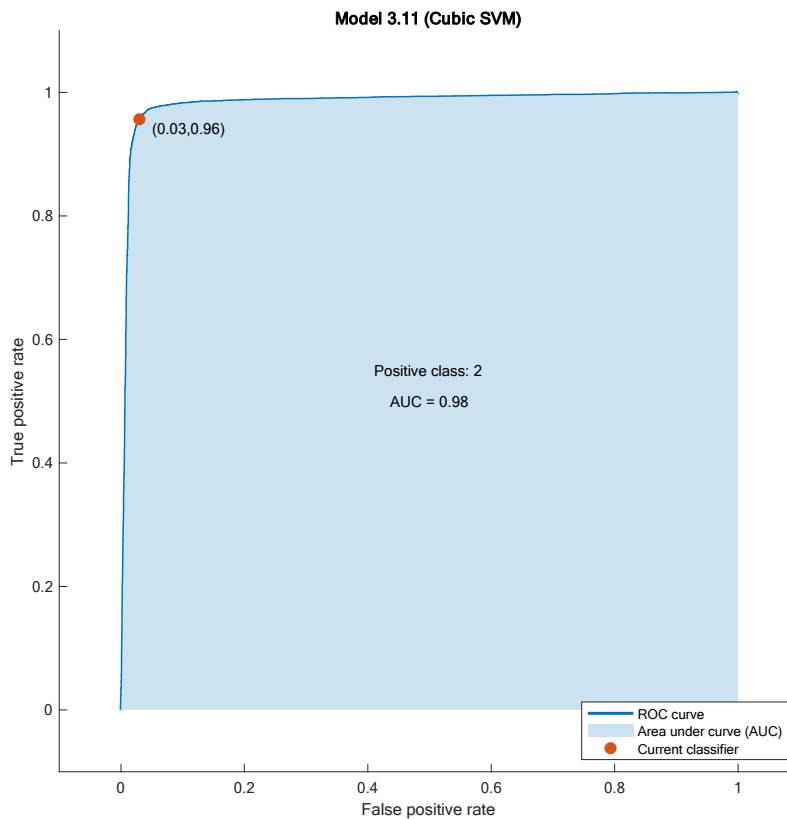


Fig. 5.74: Receiver operating characteristic curve showing an AUC of 0.98 in a two-group classification SVM model for low grade versus high grade tumours (Gleason grade group scores 1, 2, & 3 vs 4 & 5).

Confusion matrix (figure 5.75) was constructed to further assess the performance of this classification model. True positive rates of 97% and 96% respectively were recorded for class 1 and 2 respectively as shown figure 5.76 below. However, false negative rates of 3% and 4% for classes 1 and 2 respectively as shown in the figure 5.76 below.

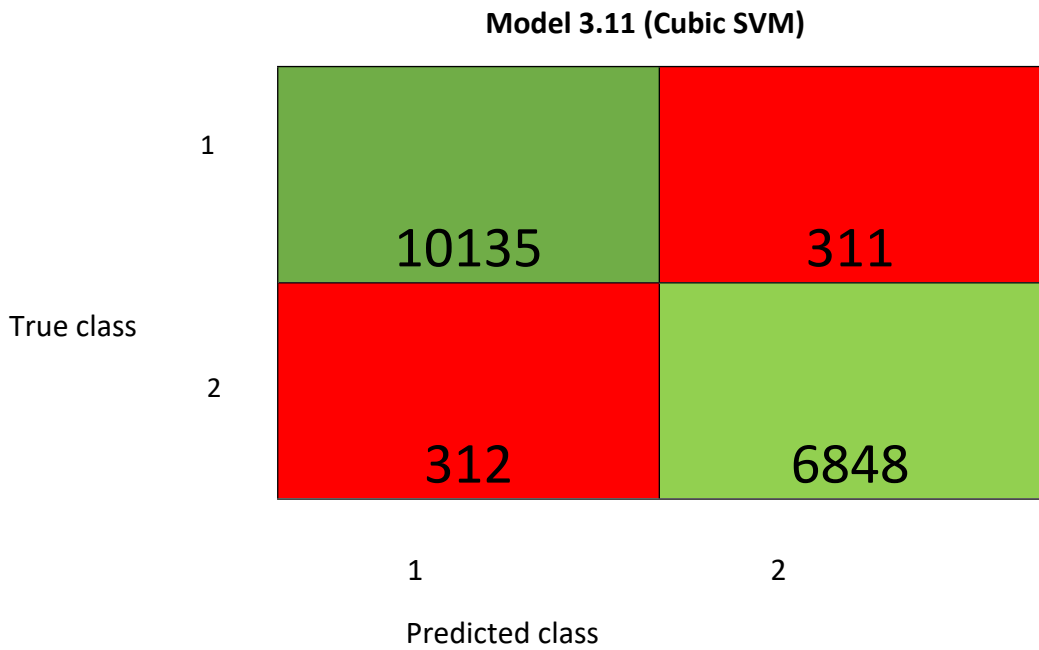


Fig. 5.75: Confusion matrix with correct prediction in green while false prediction in pink for Gleason 1,2 &3 versus Gleason 4 & 5 using SVM classification model.

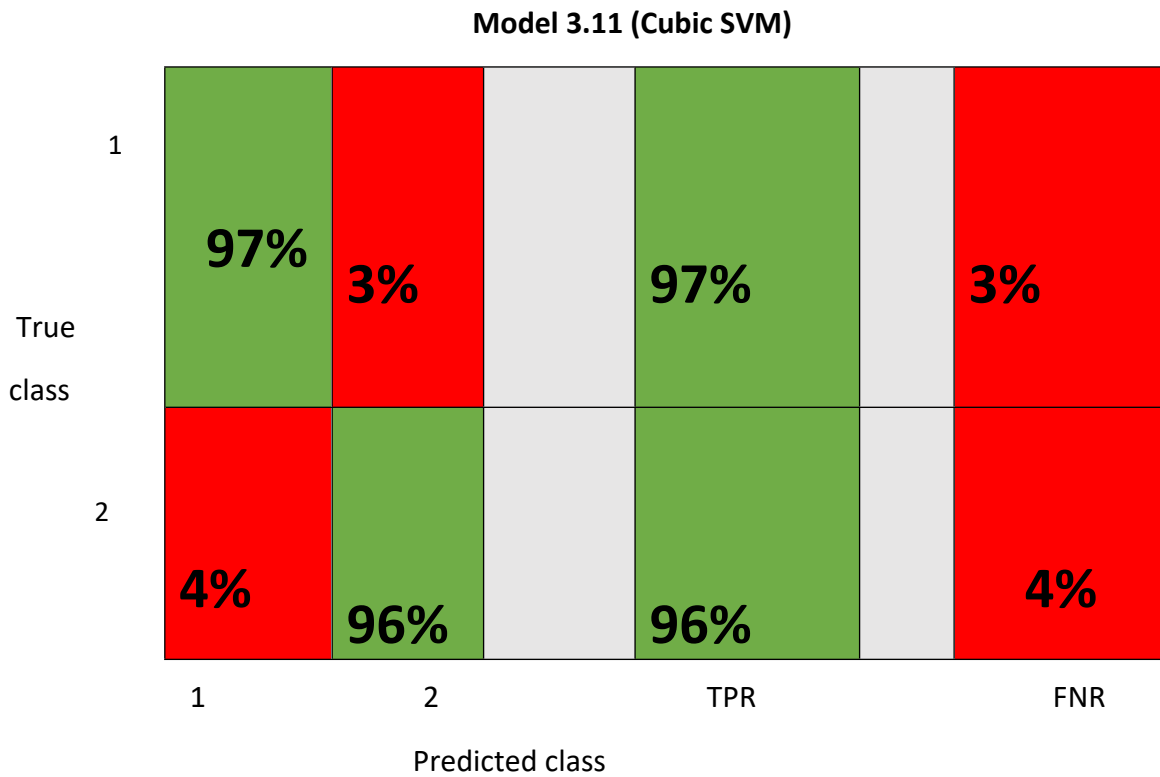


Fig. 5.76: Confusion matrix showing the true positive and false positives rates for Gleason 1,2 & 3 versus Gleason 4 & 5 using SVM classification model.

5.3.3: Three Group Classification model

LDA and SVM algorithms were also used to classify the spectra into three different pathology groups.

The three pathology groups in focus were benign, low-grade tumour, and high-grade tumours.

When LDA was exploited, the area under the curve of 0.68 was recorded, as shown in figure 5.77 below. A confusion matrix was utilised to assess the performance of this diagnostic model, necessary to give us an understanding of what the model was getting right and what types of errors it was making, demonstrated in figure 5.78 below. The ROC curve is shown below for the high-grade tumour class, which was the pathology of interest.

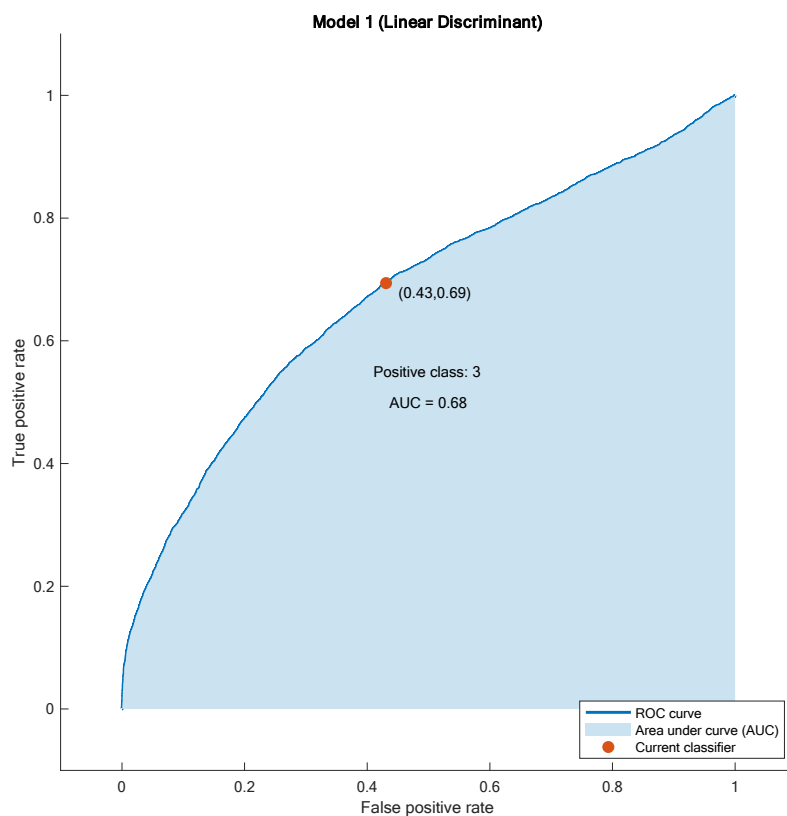


Fig. 5.77: Receiver operating characteristic curve showing an AUC of 0.68 in a three-group LDA classification model for benign, low grade & high-grade tumours.

Model 1 (Linear Discriminant)

			1
	1881	1202	1846
True class			
	1351	1513	2653
			2
	960	1231	4969
			3
	1	2	3
	Predicted class		

Fig. 5.78: Confusion matrix showing correct (green) and false (pink) predictions for benign, low-grade, and high-grade tumours using LDA classification model.

The confusion matrix demonstrated true positive rates of 38%, 27%, and 69% for classes 1,2 & 3, respectively. In comparison, 62%, 73%, and 31% false negative rates were recorded for classes 1-3, as shown in figure 5.79 below.

Model 1 (Linear Discriminant)

True class

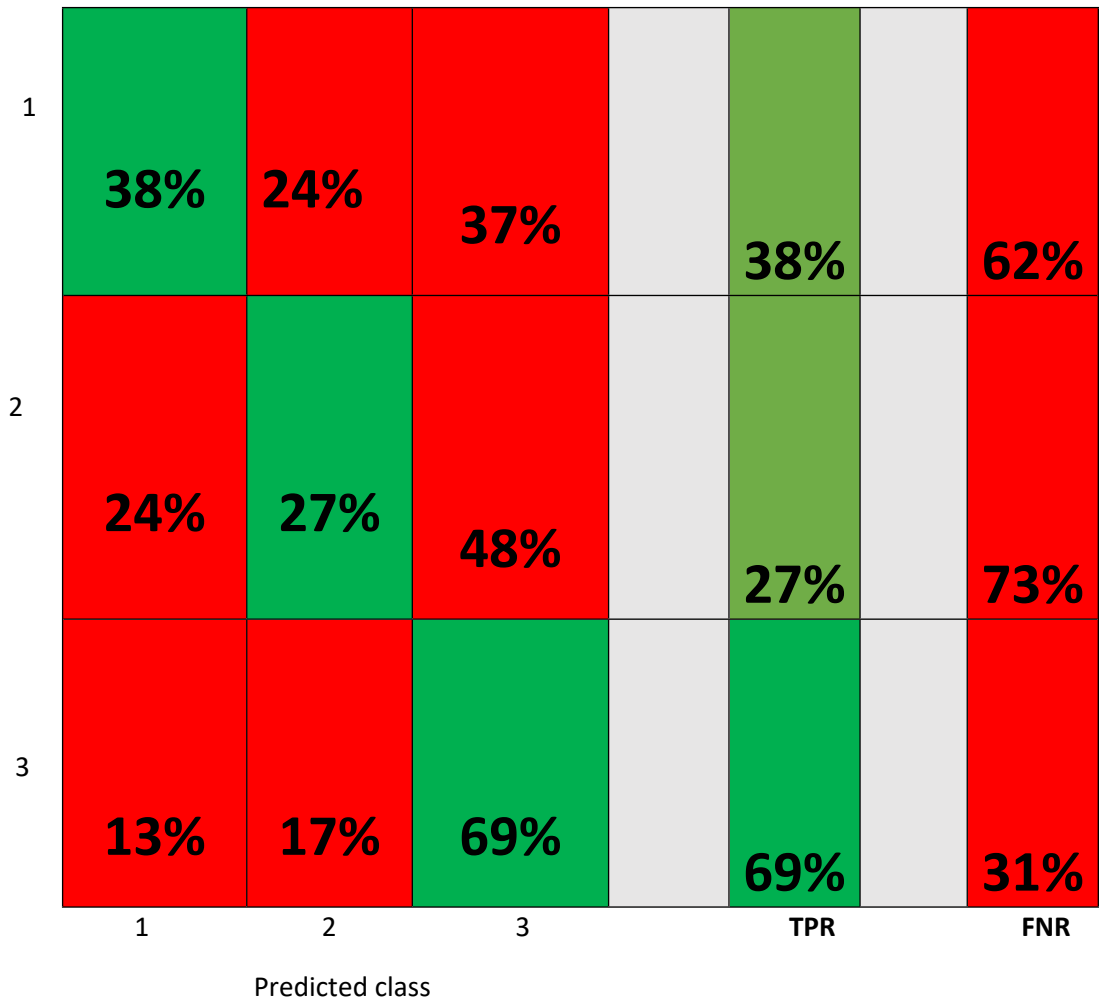


Fig. 5.79: Confusion matrix showing the true positive rates and false negative rates for discrimination into benign, low-grade, and high-grade tumour classes using LDA classification model.

Model 1 (Linear Discriminant)

True class	1	45%	30%	20%
	2	32%	38%	28%
	3	23%	31%	52%
Positive Predictive Value		45%	38%	52%
False Discovery Rate		55%	62%	48%
		1	2	3
		Predicted class		

Fig. 5.80: Confusion matrix showing the positive predictive values and the false discovery rates for the three group LDA classification model.

SVM was also utilised to discriminate the spectra into three pathology groups (benign, low-grade, and high-grade tumours). The receiver operating characteristic curve demonstrates an AUC of 0.98, as seen in figure 5.81 below. The ROC curve shown in figure 5.81 below was for the high-grade group.

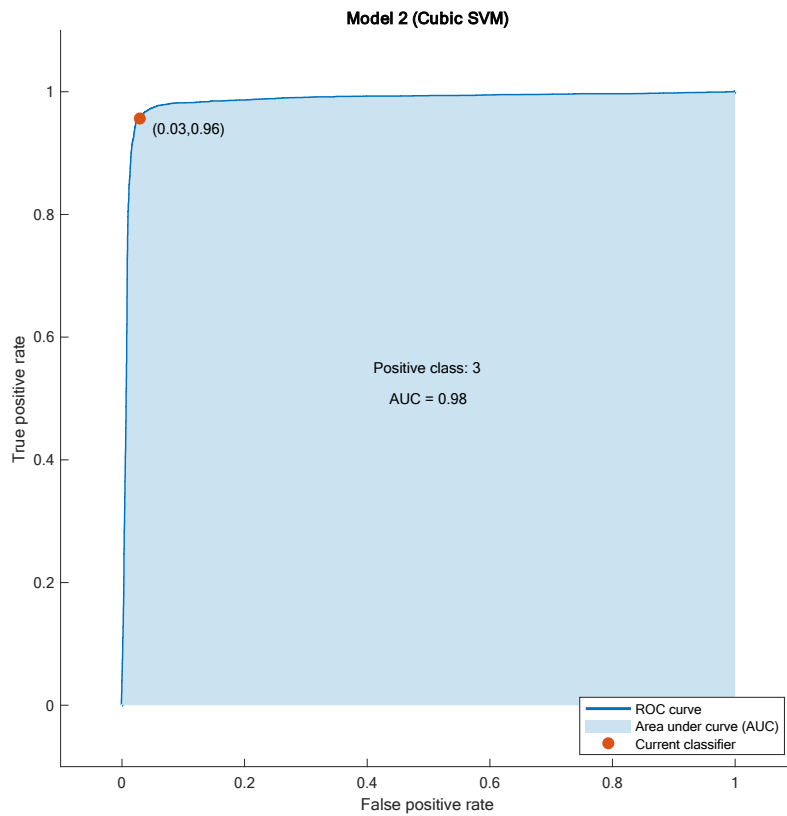


Fig. 5.81: Receiver operating characteristic curve showing an AUC of 0.98 in a three-group SVM learning classification model for benign, low grade & high-grade tumours.

A confusion matrix was constructed to assess this classification model's performance further. It demonstrated positive predictive values of 95%, 95% & 96%, respectively, with false negative rates of 5%, 5%, and 4% for classes 1, 2, and 3, respectively, as shown in the figure below. On the other hand, the true positive rates were 95%, 95% & 96%, while the false negative rates were 5%, 5%, and 4%, respectively, as shown in figure 5.82 below.

Model 2 (Cubic SVM)

	1	2	3
True class	1	2	3
1	4680	103	146
2	114	5245	158
3	133	180	6847
	1	2	3
	Predicted class		

Fig. 5.82: Confusion matrix for a three-group pathology showing the true positive and false positives SVM classification model.

Model 2 (Cubic SVM)

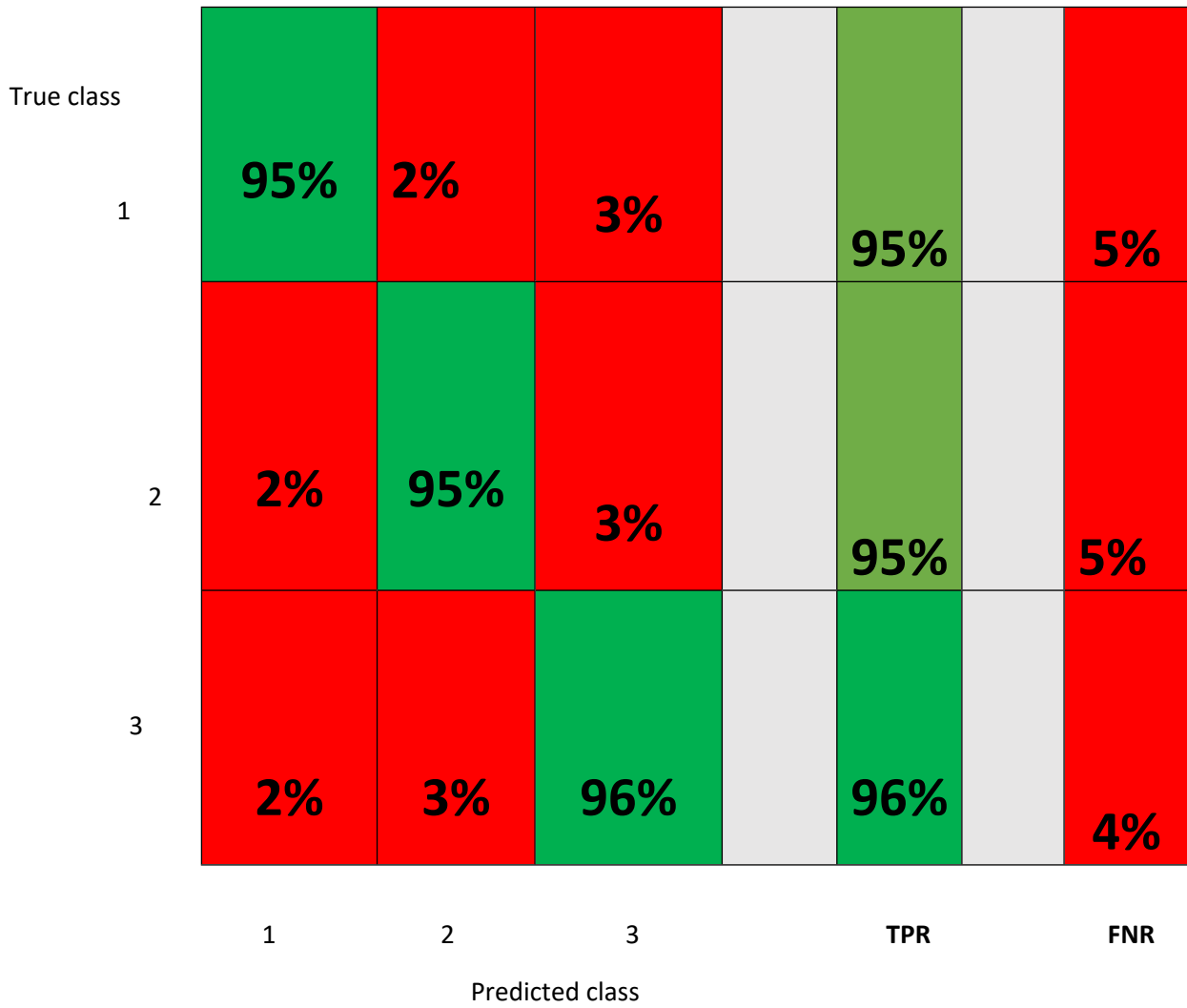


Fig. 5.83: Confusion matrix for a three-group pathology showing the true positive and false negative rates with the aid of SVM classification model.



Fig. 5.84: Confusion matrix showing the positive predictive values and the false discovery rates for the three group SVM learning classification model.

Spectral features found within the plasma samples are highlighted in Figures 5.85-5.87 below.

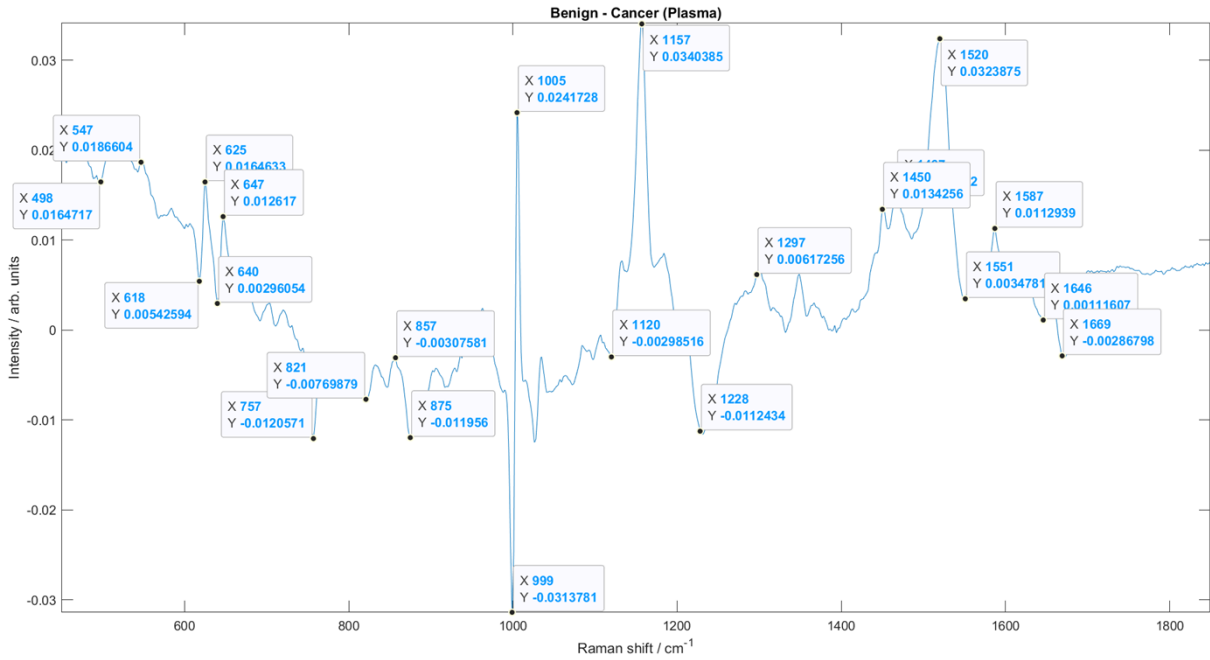


Fig. 5.85: Linear discriminant functions of the spectral features used for discrimination

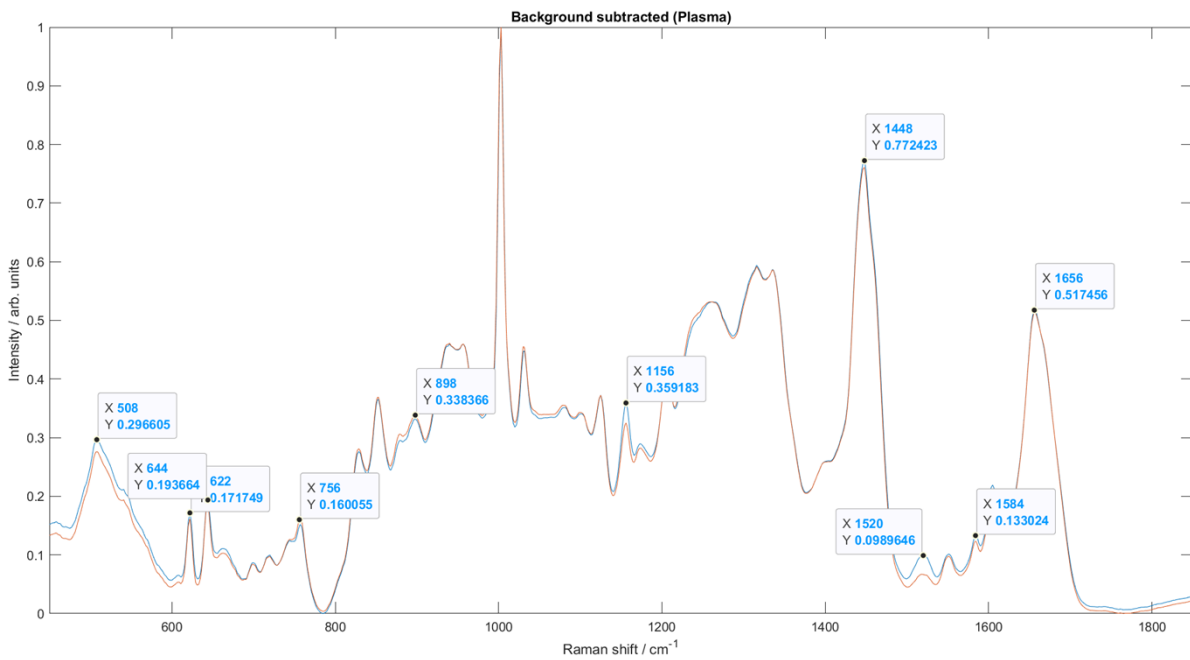


Fig. 5.86: Mean spectral differences between benign and cancer samples (Plasma).

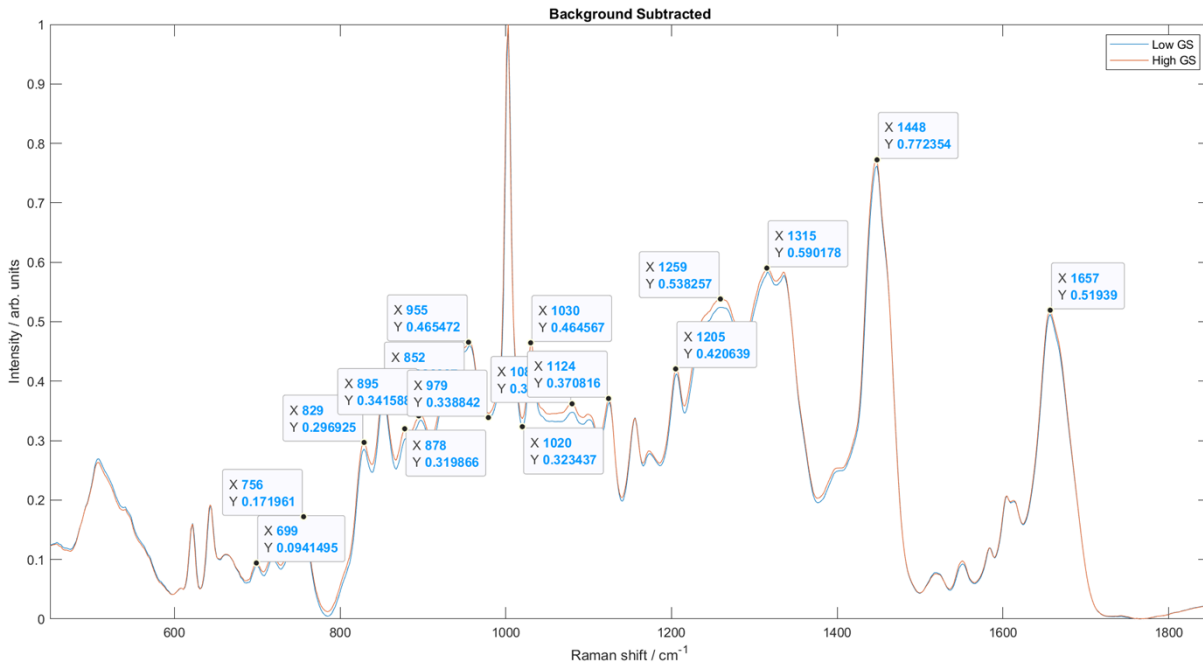


Fig. 5.87: Spectral difference between the low- and high-grade tumours (plasma).

In summary, we have shown the discriminate abilities of LDA and SVM algorithms for tissue, serum, and plasma spectra, considering 2, 3, 4, and 5 group classification models. We have shown that the models become less reliable as we move from 2 group classification to 5 group classification model. Better outcomes have been shown with SVM learning algorithms when compared to LDA models. The summary of the performance of the LDA and SVM classification models for two and three groups can be seen in tables 5.13-5.21 below for easy comparison. Spectral features have been shown for tissue, serum, and plasma, with higher peaks for nucleic acids such as DNA for the mean cancerous spectra compared to the benign group. The cancerous group observed lower carotenoid concentrations in the blood serum and plasma.

Tissue	LDA	SVM
Sensitivity	66%	87%
Specificity	78%	79%
AUC	0.77	0.82
PPV	53%	50%
NPV	86%	96%

Table 5.13: Two Group classification: Benign vs Malignant (Tissues)

Tissue	LDA	SVM
Sensitivity	60%	77%
Specificity	64%	73%
AUC	0.65	0.80
PPV	63%	73%
NPV	61%	76%

Table 5.14: Two Group classification: Low-grade tumour vs High-grade tumour (Tissues)

Tissue	LDA	SVM
Sensitivity: Class 1	49.4%	64.7%
Sensitivity: Class 2	53.5%	63.9%
Sensitivity: Class 3	53.4%	65.3%
Specificity: class 1	39%	58.4%
Specificity: class 2	62%	72.3%
Specificity: class 3	54.2%	61.8%
AUC	0.73	0.79
Overall accuracy	52.5%	64.6%

Table 5.15: Three-Group classification: Predominant 3g (Tissues)

Serum	LDA	SVM
Sensitivity: Class 1	64%	92%
Sensitivity: Class 2	72%	95%
False Negative Rate: Class 1	36%	5%
False Negative Rate: Class 2	28%	8%
Positive Predictive Value: Class 1	59%	95%
Positive Predictive Value: Class 2	77%	92%
False Discovery Rate: Class 1	41%	5%
False Discovery Rate: Class 2	23%	8%
AUC	0.78	0.94

Table 5.16: Two-group Classification model: Low-grade versus high-grade tumours

Serum	LDA	SVM
Sensitivity: Class 1	91%	95%
Sensitivity: Class 2	59%	94%
False Negative Rate: Class 1	9%	5%
False Negative Rate: Class 2	41%	6%
Positive Predictive Value: Class 1	69%	94%
Positive Predictive Value: Class 2	86%	95%
False Discovery Rate: Class 1	31%	6%
False Discovery Rate: Class 2	14%	5%
AUC	0.81	0.98

Table 5.17: Predominant 2 groups: Low-grade versus high-grade tumours

Serum	LDA	SVM
Sensitivity: Class 1	32%	89%
Sensitivity: Class 2	18%	86%
Sensitivity: Class 3	88%	96%
False Negative Rate: Class 1	68%	11%
False Negative Rate: Class 2	82%	14%
False Negative Rate: Class 3	12%	4%
Positive Predictive Value: Class 1	47%	92%
Positive Predictive Value: Class 2	37%	87%
Positive Predictive Value: Class 3	71%	95%
False Discovery Rate: Class 1	53%	8%
False Discovery Rate: Class 2	63	13%
False Discovery Rate: Class 3	29%	3%
AUC	0.80	0.98

Table 5.18: 3-group classification model: Benign, low-grade versus high-grade tumours

Plasma	LDA	SVM
Sensitivity: Class 1	51%	96%
Sensitivity: Class 2	80%	97%
False Negative Rate: Class 1	49%	4%
False Negative Rate: Class 2	20%	3%
Positive Predictive Value: Class 1	65%	96%
Positive Predictive Value: Class 2	70%	97%
False Discovery Rate: Class 1	35%	4%
False Discovery Rate: Class 2	30%	3%
AUC	0.74	0.98

Table 5.19: 2-group classification mode: Benign + low-grade versus high-grade tumours

Plasma	LDA	SVM
Sensitivity: Class 1	51%	96%
Sensitivity: Class 2	80%	97%
False Negative Rate: Class 1	49%	4%
False Negative Rate: Class 2	20%	3%
Positive Predictive Value: Class 1	65%	96%
Positive Predictive Value: Class 2	70%	97%
False Discovery Rate: Class 1	35%	4%
False Discovery Rate: Class 2	30%	3%
AUC	0.74	0.98

Table 5.20: Low-grade versus high-grade (2 Group classification model).

Plasma	LDA	SVM
Sensitivity: Class 1	38%	95%
Sensitivity: Class 2	27%	95%
Sensitivity: Class 3	69%	96%
False Negative Rate: Class 1	62%	5%
False Negative Rate: Class 2	73%	5%
False Negative Rate: Class 3	31%	4%
Positive Predictive Value: Class 1	45%	95%
Positive Predictive Value: Class 2	36%	95%
Positive Predictive Value: Class 3	52%	96%
False Discovery Rate: Class 1	55%	5%
False Discovery Rate: Class 2	62%	5%
False Discovery Rate: Class 3	48%	4%
AUC	0.68	0.98

Table 5.21: 3-group classification model (benign versus low-grade versus high grade tumours).

Please note that all sensitivity, specificity, positive predictive values in this study were calculated as shown the table 5.22 below.

	Disorder	No Disorder
Positive Test Result	True Positive (TP)	False Positive (FP)
Negative Test Result	False Negative (FN)	True Negative (TN)

$$\text{Sensitivity} = \text{TP}/(\text{TP}+\text{FN})$$

$$\text{Specificity} = \text{TN}/(\text{TN}+\text{FP})$$

$$\text{PPV} = \text{TP}/(\text{TP}+\text{FP})$$

$$\text{NPV} = \text{TN}/(\text{TN}+\text{FN})$$

Table 5.22 : Calculation of sensitivity, specificity, positive and negative predictive values

Chapter 6– Discussion

6.0: Contribution to knowledge:

Raman spectroscopy has been shown to have the ability to probe the molecular fingerprints of different disease conditions. It can assess the biochemical compositions and functions of different biological samples in a non-destructive and label-free fashion. Therefore, it could be utilised to assess early molecular changes resulting from prostate cancer before structural changes are seen. The work in this thesis was set out to see if Raman spectroscopy can provide a more accurate prediction of the presence of prostate cancer than PSA and allow for blood sample triage of patients into at-risk groups. Secondly, the usefulness of Raman spectroscopy as a minimally invasive diagnostic tool to assess real-time, molecular specific fingerprints of prostate disease such as tumour was also assessed.

The testing of liquid and tissue biopsies was proposed to measure the disease-specific molecular fingerprints found within blood plasma, serum, and prostate tissues. Raman spectroscopy has been demonstrated to have the ability to distinguish between prostate disease at the cellular level. Nevertheless, bodily fluids have not been used to date except for the recent work of Medipally D K R et al. (2020); who utilised the blood samples of plasma and lymphocytes to differentiate spectra into different groups with Fourier Transform Infrared Spectroscopy and Raman spectroscopy from healthy controls and cancer patients. We initiated a feasibility study whereby we measured specimens from patients exhibiting both malignant and benign diseases within the prostate gland. We compared the molecular fingerprints obtained from Raman spectroscopy with histopathology (a gold standard technique for diagnosis of prostate cancer) and PSA levels. We utilised advanced data analysis methods to identify the differences in the pathology groupings, enabling an initial diagnostic algorithm to be demonstrated and tested.

6:1: Performance of the classification models:

A classification model can only be considered as good as the data used in building the model. Therefore, it is paramount that high-quality data are obtained and processed carefully since an error in the data acquisition or analysis could impact quite severely on the outcome. An experienced and board-certified consultant histopathologist reviewed and reported on all the samples used for this study.

6.2: Tissue Samples analysis:

Histological findings concerning tumours in the prostate gland are usually based on the structural changes found within prostate tissues, which may vary from the abnormal architecture of the glandular

tissue to the loss of basal membrane cells or changes in the nuclear, among other features. On the other hand, Raman spectroscopy relies on the biochemical variation within the cell or tissue or biofluids to distinguish between the different pathological groupings. The classification models utilised to distinguish the different pathology groups were therefore trained with a gold standard histology technique, including the benign and malignant groups. Leave one out cross-validation was statistically significant at $p < 0.1$, which indicated that there was a 10% possibility of a chance occurrence of variance between the training model and the test model. Demonstrated that the training dataset was probably slightly overfitting using spectral components irrelevant to the differences in pathology.

Furthermore, a more extensive sample set would have enabled more inter-patient variation to be described, which may have led to more robust models when tested with independent sampling. It is important to note that in the protocol employed between the experimental and clinical centres, the tissue pathology could not consider the location from which the spectra were measured. Also, the prostate tissues were highly heterogenous, including regions of glandular and stromal tissues that could have been independently sampled by the few-micron laser beam used for illumination.

The classification model developed performed well compared with the gold standard technique of histopathology assessment. Twenty-five principal components were utilised for data compression before discriminant classification at each run. 20% of the spectra were held back from the training and used to test the model in each fold (5 times). It further confirmed the robustness of the model, although some variances among the benign and malignant spectra were not considered.

The same model as above was further utilised for analysis. However, this time only significant principal components were utilised, minimising the risk of the model predicting the pathology used in the principal components that were not relevant to the pathology. A high sensitivity of 84.6% with a specificity of 76.2% was achieved, giving a positive predictive value of 89.8% with a negative predictive value of 67.0%. It further substantiated the possibility of utilizing Raman spectroscopy as a measuring and discriminating tool in distinguishing spectra into two pathology groups, from benign and malignant lesions within the prostate gland.

Both linear discriminant analysis and support vector machine learning classification models were used to distinguish between the different pathology groups from the spectra acquired from the biopsy tissues.

The data analysis was done using the raw data, with only normalisation applied. Further pre-processing steps, such as EMSC correction and background subtraction, were also tested. However, these pre-processing steps did not add any value to the classification performance. Hence the data were not used for the presented analysis results.

The two-pathology group comprising benign and malignant tissue samples with an LDA model consisting of 381 spectra taken from 79 patients was correctly classified with a prediction accuracy of 75% with an area under the receiver operating characteristic curve of 0.77. The sensitivity and specificity of 78.4% and 65.6% were recorded. Moreover, when the MATLAB classification app was utilised to distinguish the spectra into the two pathology groups with a 5-fold leave one out cross-validation for the group mean spectra with the LDA model, 72.6% prediction accuracy was documented with sensitivity and specificity of 76.4% and 61.1% respectively with a corresponding AUC of 0.70.

Overall prediction accuracy of 80.8%, a sensitivity of 79.4%, and a specificity of 87.0% with the Support Vector Machine Learning algorithm, the AUC was 0.82.

When the MATLAB classification app was utilised to cross-validate (5-fold leave one out) the data for the group mean spectra SVM model, the prediction accuracy of 72.6% with a sensitivity of 74.6% and specificity of 64.3%. Overall prediction accuracy was also dropped to 0.69 showing better outcomes for benign spectra, and worse outcomes for malignant spectra since only a small number of cancer tissue samples were used. Although there was a decline in the performance of the SVM when 20% of the data were withheld for validation of the data, nevertheless, the SVM algorithm demonstrated better prediction ability at the classification of the Raman spectra into two different pathology groups (benign versus cancer) than the LDA model.

Another method of assessing a two-pathology group was also conducted. However, this time, instead of distinguishing the spectra into either benign or malignant groups, spectra were classified into low-grade or high-grade tumours. For this analysis, spectra from intermediate-grade tumours were also classified as high-grade. Therefore, spectra from Gleason 7 tumours were classified with spectra from high-grade tumours. Class 1 comprised benign lesions and Gleason grade <7, while the class 2 group comprised Gleason 7 and >7 tumours. Analysis with the raw data using the LDA classification model depicted an overall prediction accuracy of 63.3%, with 52.6% correctly classifying spectra into class 1 and class 2 with an overall prediction accuracy of 75%. This model demonstrated a better accuracy at

predicting spectra in the high-grade tumours group than in the low-grade ones. The sensitivity and specificity in distinguishing the spectra into low-grade or high-grade groups were 70.0% and 64.6%, respectively. However, the training dataset demonstrated a 68.8 % overall prediction accuracy, while sensitivity and specificity were 66.8% and 70.8 %, respectively.

Moreover, when the MATLAB classification app was utilised to distinguish the spectra into the two pathology groups (low grade versus high grade) with a 5-fold leave-one-out cross-validation for the group mean spectra with the LDA model, the overall prediction accuracy was 61.9 %. The area under the curve of 0.65 was observed, while the sensitivity and specificity were 60.4% and 63.5%, respectively.

Support vector machine learning was also utilised to discriminate the spectra into these two pathology groups – low-grade versus high-grade tumours. The overall prediction accuracy of 74.8% when a 5-fold cross-validation was applied, holding back 20% of the data using the MATLAB app for classification. A sensitivity of 73.0% and a specificity of 75.6% were documented, respectively. Slightly higher prediction performance was observed with the SVM model compared to the LDA model.

A three-pathology group prediction model was also assessed with a PC-LDA model to discriminate the spectra into benign, Gleason score <7, and Gleason score ≥ 7 . 69.6% of the spectra were correctly classified into the benign group. In comparison, 53.3% were correctly classified into the low-grade cancer group (Gleason <7), and 75% were correctly classified into Gleason ≥ 7 group, giving an overall prediction accuracy of 68.4%. When a 5-fold leave-one-out cross-validation was used with a MATLAB classification app, an overall accuracy of 57% was documented, with 55% of spectra correctly classified into class 1 and 58% classified into class 2. In comparison, 58% were accurately classified into class 3.

When the data were normalised to the spectrum with a 5-fold leave-one-out cross-validation, the PC-LDA model demonstrated an AUC of 0.73. The overall prediction accuracy of 52.5% was observed with 49.4%, 53.5% and 53.4% sensitivity for classes 1, 2 & 3. While the specificity were 39%, 62% & 54.2% for the classes 1 – 3, respectively.

Quadratic SVM was also used to assess the data; the overall prediction accuracy of 64.6%, and an AUC was 0.79 for the three-group pathology analysis. Sensitivity for the respective 3 classes from 1 to 3 were recorded as 64.7%, 63.9% & 65.3% respectively. However, specificity were recorded as 58.4%, 72.3% & 61.8% for the 3 respective classes.

The four-pathology group biopsy targeting PC-LDA model comprised the benign group as the first group, a Gleason score <7 as the second group, a Gleason score of 7 was assigned to the third group, while a Gleason scores greater than 7 was classified as the fourth group. The overall prediction accuracy of 57.0% with the percentage of correctly classification into classes (groups 1, 2, 3 & 4) recorded as 52.2%, 60%, 64.3%, 50.0%, respectively. However, when the MATLAB classification app was utilised to normalise the data using 25 principal components, and 5-fold cross-validation was applied, the total prediction accuracy declined to 50.4%, which was about a 6% drop from the raw data. The percentages of the spectra correctly classified into different pathology groups were as follows: Class 1, 2, 3 & 4 were correctly classified at 47.8%, 55.6%, 46.7%, and 57.6%, respectively.

Another four-group classification was also assessed. However, this time, the predominant Gleason grade group scores were assessed, which comprised Gleason grade groups 1, 3, 4 & 5. Correctly classified spectra into class 1, 2, 3 & 4 was 52.2%, 67.9%, 55.6%, 100% respectively. Sensitivity was 56.7%, 62.8%, 63.6%, 35.7% respectively while specificity was 52.2%, 67.9%, 55.6%, 100%.

Nevertheless, merging the spectra from Gleason grade group scores 4 and 5 to form one group, thereby reducing the classification model to three groups, did not improve the classification precision. Instead, there was a slight depletion in the performance accuracy, showing an overall prediction accuracy of 58.3% (class 1, 2 & 3), while the four-group classification model's overall prediction accuracy was 59.6%.

6.3: Classification performance for the Liquid biopsy spectra

Liquid biopsies are tests carried out on blood samples to rule out the presence of cancer cells from tumours circulating within the blood or pieces of biomolecules from tumour cells found in the blood. Liquid biopsy can be utilised for early cancer detection, monitoring disease progression, treatment efficacy, or assessing disease recurrence. Biomolecular content variations in the blood have been known to occur due to the presence of tumour cells. The variations in oncological metabolites can be quantity depletion or an increase in the quantity of the metabolites depending on the metabolite in question and the disease condition assessed. Therefore, oncometabolite are metabolites found in large quantities in the presence of cancer cells. These are when a distinct mechanism links a particular mutation in the tumour to the large concentration of the metabolites.

Raman spectroscopy of blood plasma and serum has recently been accepted as a technique of choice in the early detection of cancer within the body since it is a minimally invasive technique and easy

accessibility of the blood samples can be achieved from potential subjects. Furthermore, biomarkers secreted from the tumour cells into the general blood circulation can be obtained from the blood plasma and serum. Although near-infrared Raman signals are often weak, both serum and plasma are known to be affected by the fluorescence background, mainly when Raman spectra are acquired. Nevertheless, technological advancement has increased the signal intensity of Raman scattered light and alleviated the burden upon the Raman signals from fluorescence interferences. The deposition of a small volume of blood plasma or serum on a substrate such as calcium fluoride or aluminium and subsequent solvent evaporation and formation of a coffee ring has been shown to enhance the intensity of the Raman scattered light with less interference from fluorescence. Therefore, an objective assessment of the biomolecular composition of the blood plasma/serum can be achieved with Raman spectroscopy and multivariate analysis. This technique can be used as a complimentary screening tool to PSA in assessing an asymptomatic patient with suspicion of the presence of cancer within the prostate gland.

We attempted to discriminate the Raman spectra acquired in our study into different pathology groups to assess the prediction accuracy of the classification model for PC-LDA and SVM algorithms. Two group pathology models comprising benign and malignant samples from blood serum comprising 300 spectra obtained from 100 patients were utilised for training to assess the model's performance. During the training process, the overall diagnostic accuracy for the LDA model of the blood serum spectra utilised to discriminate the spectra into the two classes was 72.4 %, with higher prediction accuracy in the benign group (74.5%) compared to the malignant group (68%). The sensitivity and specificity were recorded as 82.6% and 56.7%, respectively.

A training model was also built for a four-group LDA model, consisting of benign, Gleason score <7, Gleason score 7, and Gleason >7. The overall prediction accuracy was recorded as 55.3%, with the spectra correctly classified into the low-grade tumour with Gleason score <7 having the highest prediction accuracy of 68.4%, while spectra from intermediate tumour grade of Gleason score 7 had the lowest prediction accuracy of 48.5%. Sensitivity for the four groups were 60.0%, 44.0%, 73.0%, 61.0% respectively. However, this training model was poor, possibly because there were not enough spectra in some groups compared to others.

Another training performance was assessed for a two-group PC-LDA model that was conducted using low-grade tumours (benign + Gleason <7) and high-grade tumours (Gleason 7 and >7). This model gave

an overall prediction accuracy of 64%. The low-grade tumours were correctly classified by 77%, while high-grade tumours were correctly classified with accuracy recorded at 52.8%. The sensitivity and specificity for this classification were 62% and 74.3%, respectively.

Three class training performance models included benign and Gleason <7 in class 1, Gleason 7 in class 2, and Gleason >7 were classified into class 3. Overall prediction accuracy of 56.3%. However, Gleason score 7 spectra were correctly classified by 73.7%, while Gleason score >7 had the lowest prediction accuracy of 50.9 %. The sensitivity for the three classes were 50.0%, 42.0% and 87.0% respectively.

After assessing the data with PC-LDA with different groups of data, intensity less than 400 counts at 1650 cm^{-1} (Amide 1) were removed from the data set. Five-fold cross-validation was carried out to test the validity of the classification models. All data were mean-centred, and 25 principal components were used for data compression before discriminant classification at each training run. Since blood sera and plasma were classified separately, a comparison was carried out. Compared to the sera samples, a better mean spectra separation between cancer and benign was observed for the plasma samples.

The two-group LDA classification model was made up of low-grade (benign & Gleason <7) and high-grade (Gleason 7 & >7) tumours for the mean centred spectra of the blood serum samples. These included 300 spectra taken from 100 samples taken from 100 patients. The receiver operator characteristic curve was generated to assess the performance of the PC-LDA model for blood serum classification by consecutively changing the thresholds to determine the correct classification of all the subjects. The AUC of 0.78 (threshold of 0.38, 0.72) was recorded with a sensitivity and specificity of 50.2 % and 76.6 %, respectively. At the same time, the positive predictive rate and the negative predictive value were 64.4 % and 72.5 %, respectively.

A close comparison of this PC-LDA with the performance of the blood plasma for the same two pathology group classifications (Low-grade versus high-grade tumours) for 300 spectra from 100 samples taken from 100 patients was carried out. The AUC demonstrated 0.74 (at threshold of 0.49, 0.80) with a sensitivity of 64.6 % and 69.5 % respectively. While the positive predictive value and negative values were 80.2 % and 64.7 %, respectively.

When the cubic support vector machine learning algorithm was used to analyse the two-group classification model, this was done for both serum and plasma with the same number of spectra and samples. Overall accuracy for classification of the serum spectra was 94% with an AUC of 0.97

(threshold 0.08, 0.95) for two group classification models (benign + Gleason <7 versus Gleason 7 + Gleason >7). The sensitivity and specificity were 92.2% and 95.1%, respectively, while the positive and negative predictive values were 92% and 95%, respectively.

On the other hand, the cubic SVM for the same two-sample model for the plasma depicted an AUC of 0.98 (threshold of 0.04, 0.97). The sensitivity and specificity were 96% and 96.9%, respectively, while the positive and negative predictive values of 95.7% and 97.2% were recorded.

The cubic support vector machine learning algorithm was superior to the PC-LDA for discriminating between class 1 and class 2 for both blood plasma and serum spectra; hence it is the preferred classification approach.

The performance of another two-pathology group classification model was also assessed with the blood serum spectra. This model included Gleason grade group scores 1-3 classified as class 1 tumours, while the Gleason grade group score 4 and 5 spectra were classified as class 2 tumours. This practical model could be used for treatment planning and avoiding the overtreatment of low-grade tumours. When PC-LDA was utilised to discriminate spectra into these two pathology groups for the blood serum spectra, overall prediction accuracy of 74.9% was recorded with an AUC of 0.8 (threshold 0.09, 0.59). The sensitivity and specificity were 69.0% and 86.4%, respectively, while the positive and negative predictive values of 90.5% and 59.4% were documented, respectively.

A comparison was made with the performance PC-LDA for the blood plasma, AUC of 0.69 (threshold 0.15, 0.4). Sensitivity and specificity were 67.1% and 63.7%, respectively, while the positive and negative predictive values were 84.6% and 39.5%, respectively.

Support vector machine learning was also used to assess the performance of the above two pathology group classification model for the serum spectra. The overall prediction accuracy was 94.6%, with an AUC of 0.98 (threshold of 0.05, 0.94). The sensitivity and specificity of 94.0% and 95.0%, respectively, while the positive and negative predictive values of 95.0% and 94.0% were recorded, respectively.

A close comparison of the Blood plasma spectra analysis with the support vector machine learning algorithm also demonstrated the AUC of 0.98 (threshold of 0.03, 0.96). Sensitivity and specificity were 97.0% and 96.0%, respectively, while the positive and negative predictive values were 97.0% and 96.0%.

Support vector machine learning algorithm has further proven to be a superior prediction model to classify the spectra into two groups Gleason grade group score 1-3 versus Gleason grade group score 4 & 5 both for the blood plasma and serum spectra with an area under the curve of the receiver operating characteristic curve of 0.98.

The three-pathology group classification model consisting of benign, low-grade, and high-grade spectra was also assessed using the PC-LDA classification model for the blood serum spectra. Overall prediction accuracy of 64 % was recorded. The sensitivity for the different classes included 47.0%, 37.0%, 71% respectively with a positive predictive values of 32%, 18%, 88% respectively and the AUC was 0.80 (threshold of 0.58, 0.88).

When the PC-LDA model was utilised to assess the ability to discriminate spectra into benign, low-grade, and high-grade tumour groups for the blood plasma samples, the sensitivity for classification into the respective classes (1-3) were 45%, 38%, and 52%, respectively. The positive predictive values for the different classes were 38%, 27%, and 69%, respectively.

Support vector machine learning algorithm was also utilised to assess the ability of the model to classify the spectra into the three different groups (benign, low-grade & high-grade) both for the serum and the plasma spectra. AUC was 0.98 (threshold of 0.08, 0.96) for serum samples with a sensitivity for prediction into the three classes of 92%, 87%, and 95%, respectively. At the same time, the positive predictive values were 89%, 86 %, and 96%, respectively. On the other hand, when blood plasma spectra were assessed, the area under the curve was 0.98 (0.03, 0.96), which was quite similar to the AUC for the serum spectra. The sensitivity for classification into the three pathology groups was 95%, 95%, and 96%, respectively, and the positive predictive values were 95%, 95%, and 96%, respectively.

The support vector machine learning algorithm is an excellent classification model for distinguishing between spectra from different pathology groups, as demonstrated unequivocally in tissue, serum, and plasma sample analysis. Although the PC-LDA model has shown some ability to classify the spectra into different pathology groups, its performance lacks consistency in providing a high prediction accuracy all through the different types of samples analysed. Therefore, to answer the first research question, can Raman spectroscopy provide a more accurate prediction of the presence and progression of prostate cancer than PSA and allow blood sample triage of patients into at-risk groups? It is evident that based on this study's findings, with the aid of a Drop coated deposited Raman spectroscopy of

blood plasma and serum; it is possible to provide a more accurate prediction of the presence of prostate cancer than PSA. The sensitivity and specificity of PSA in prostate cancer detection have been known to be around 21% and 91%, respectively. However, with Raman spectroscopy of blood serum and plasma, it is possible to detect the presence of prostate cancer and classify the same into two or three groups with sensitivity and specificity of 95%-96%. Therefore, it is possible to use this technique to triage patients into two or three pathology groups of benign, low-grade, and high-grade tumours with the aid of advanced data analysis techniques such as support vector machine learning algorithm.

Two other studies have used Raman spectroscopy in breast and prostate cancer (Medipally DKR et al., 2020) with liquid biopsy samples (Freitas DLD et al., 2020). Freitas DLD et al. conducted a breast screening program with liquid biopsy from blood plasma samples from 476 patients recruited over two years. Attenuated total reflection Fourier Transform infrared was utilised to analyse the spectrochemical fingerprints of the plasma samples. Sensitivity and specificity of 94.0% and 91%, respectively, were recorded compared to sensitivity (88-93%) and specificity (85-95%) of mammography.

Medipally D et al. utilised a high throughput Raman spectroscopy and Fourier Transform Infrared spectroscopy of liquid biopsies of blood plasma and lymphocytes to assess the presence of cancer among prostate cancer patients and healthy control subjects. Raman and FTIR spectra were recorded from blood plasma samples; nevertheless, only Raman spectra were recorded from the lymphocytes. Partial Least squares discriminant analysis was used to classify spectra into different pathology groups with sensitivity and specificity of 90%-99%. The team utilised classical least squares fitting analysis for detecting the main components involved in the development and progression of prostate cancer.

The primary purpose of establishing the Gleason grading system was to assess the prostate tumour cell's structural features. The Gleason grading system often decides prognosis prediction and adopts a suitable treatment pathway.

Ozkan and colleagues conducted a study to evaluate the interobserver concordance rate of two pathologists at histological grading of prostate tumours (Ozkan TA et al., 2016). Four hundred-seven pathology slides of prostate needle biopsies from 34 patients were re-evaluated by two pathologists blinded to each other's reports and previous reports. Both pathologists disagreed on the presence of tumours in 31 cores; however, 74% (n=23/31) were Gleason pattern 3 based on the initial histological

report. While Pathologist 1 reported the presence of a tumour in 202 cores, pathologist two reported tumours in 231 cores. The kappa (k) coefficient was utilised to assess the degree of concordance between the two pathologists. The concordance rate between the two observers was 63.96% ($k=0.34$) for the primary pattern, while the secondary Gleason pattern received a concordance of 63.45% ($k=0.37$), respectively. The agreement concerning the sum of the primary and secondary patterns was 57.8%, with a kappa score of 0.43.

On the other hand, the level of agreement was even lower for the Gleason grade group scoring (51.7%) with $k = 0.39$, demonstrating a low level of agreement between the two pathologists, which means that the precision in carrying out histological assessment can be less than reliable at all times. Suppose clinicians have to depend entirely on the result of the histological grading system to determine the most suitable treatment for prostate cancer and the prediction of prognosis. With a lack of precision in diagnosis as a result of poor reproducibility, therefore it means that false positives and false negatives would have been recorded.

Therefore, using the Gleason grading system to train the Raman models means training the model on an imperfect system with spatial discrepancies (in the biopsies) between pathology and potential errors in pathology classification to train and test the models. This thesis highlights that a classification model is only as good as the data used in training and testing the model.

6.4: Plasma Spectral features:

Prominent Raman peaks were observed in plasma samples with respective tentative biochemical assignments at the following locations. 455 cm^{-1} , 463, 473, 496, 519, 547 (cholesterol), 583, 617, 625 (guanine), 640 (guanine), 647, 757, 822, 877, 962, 999, 1005 (beta carotene), 1028, 1074 (triglycerides), 1133, 1156 (carotenoid), 1174, 1203 (collagen), 1210 (tryptophan), 1230 (amide 111), 1349, 1360, 1392, 1452 (CH_2 bending), 1467, 1520 (carotenoid), 1332, 1587, 1548, 1600. 1607 (phenylalanine), 1612 (C-C stretching), 1645 (amide 1 bending), 1656 (amide 1), 1674 cm^{-1} .

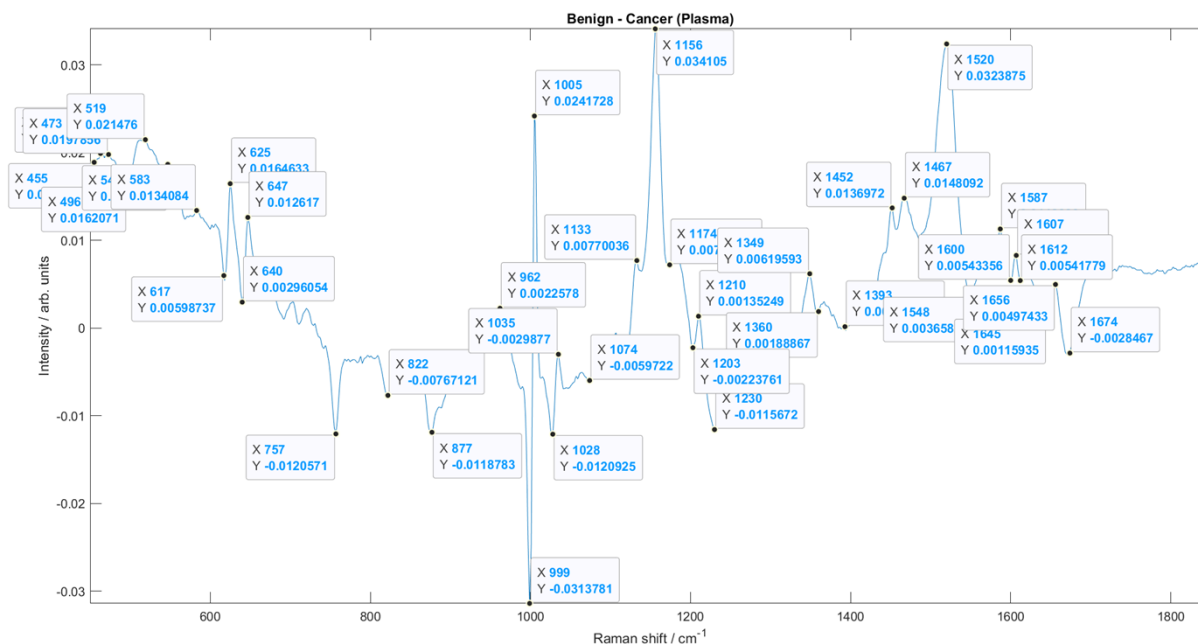


Fig. 6.1: Spectral assignment for benign minus cancer plasma data.

The highest intensities were observed at 1156 cm⁻¹, 1005 cm⁻¹, and 1520 cm⁻¹, consistent with carotenoid or beta carotenoids. Effectively demonstrated that carotenoid was responsible for differentiating benign and malignant plasma mean spectra. Therefore, a higher concentration of carotenoids was found in benign samples after cancer spectra were subtracted.

When molecular components of the mean of the low Gleason scores were subtracted from that of the mean high Gleason scores, prominent Raman peaks was observed in plasma spectra at the following locations 489, 618, 625, 640, 647, 692, 703, 711, 755, 874, 903, 918, 942, 999, 1005, 1026, 1034, 1043, 1103, 1119, 1131, 1144, 1158, 1169, 1282, 1300, 1332, 1347, 1436, 1436, 1452, 1468, 1517, 1578, 1586, 1597, 1648 cm⁻¹ as demonstrated in the figure below.

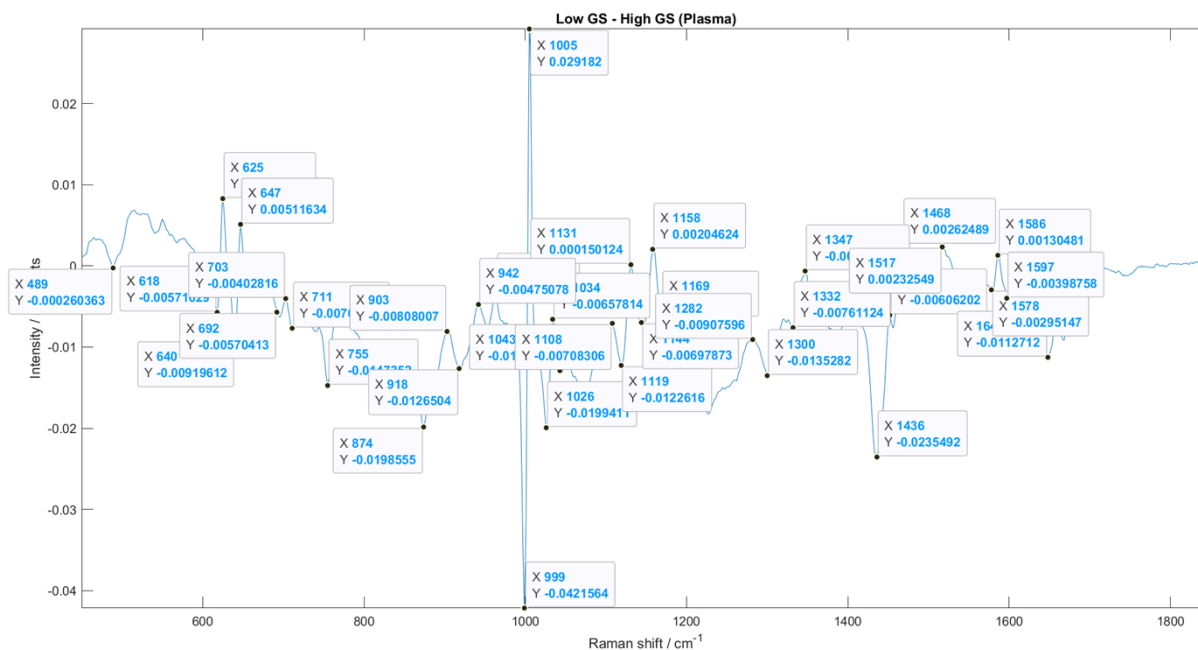


Fig. 6.2: Spectral assignment after subtraction of mean spectral intensity of high Gleason scores from the low Gleason scores.

Here the highest peak recorded was at 1005, which is in line with the highest amount of molecules, which was in a spectral position of carotenoids, while the lowest concentration was seen at peak position 999.

Despite the similarity in shape and intensity of the characteristic spectra of benign and cancer plasma, remarkable changes in Raman peak intensity were observed.

Firstly, when the benign group was compared with the cancer group, there were higher intensities depicted with the mean benign spectra at Disulphide (approx. 507 cm^{-1}), phenylalanine (approx. 622 cm^{-1}), tyrosine (approx. 644 cm^{-1}), carotenoid (approx. 1156 & 1517), CH_2 deformation (approx. 1448). On the other hand, higher intensities were seen at collagen (approx. 1030 cm^{-1}) at peak positions 757 cm^{-1} and 878 cm^{-1} for malignant mean spectra compared to the mean benign spectra.

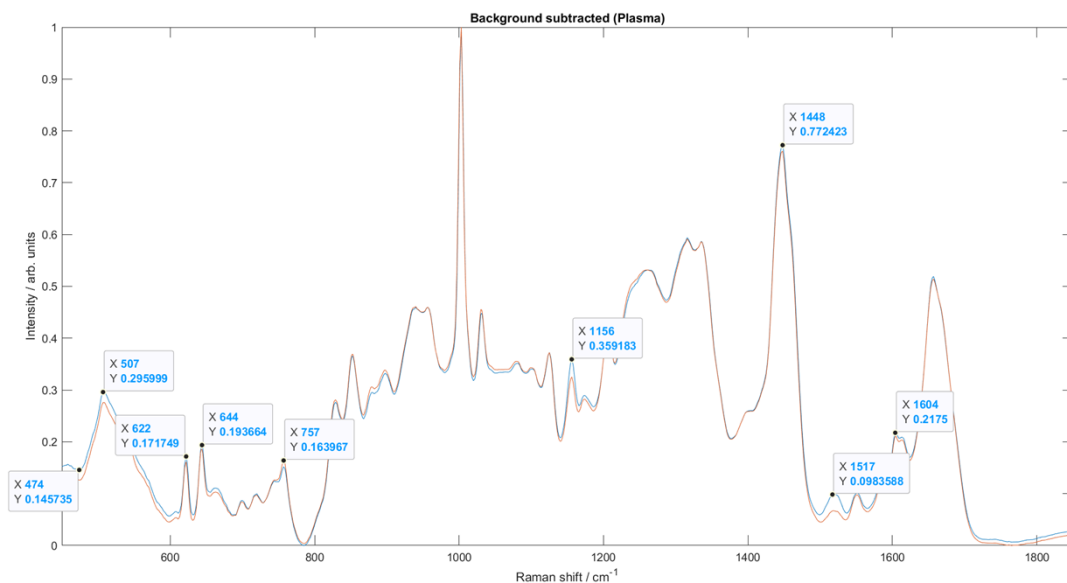


Fig. 6.3: Mean plasma spectra for benign and cancer groups

A comparison was also made between spectral intensities of the mean low Gleason scores with that of the mean high Gleason scores. The mean spectra for the low Gleason scores recorded high intensities at Disulphide (approx. 509 cm^{-1}). However, the mean high Gleason scores demonstrated a higher spectral intensity than the mean low Gleason scores at tyrosine (approx. 829 cm^{-1}), polysaccharides (approx. 851 cm^{-1}), lipids (approx. 1261), CH_2 twisting (approx. 1317), DNA (approx. 1335), Glycogen (approx. 1377) and CH_2 deformation as seen in figure 6.4 below.

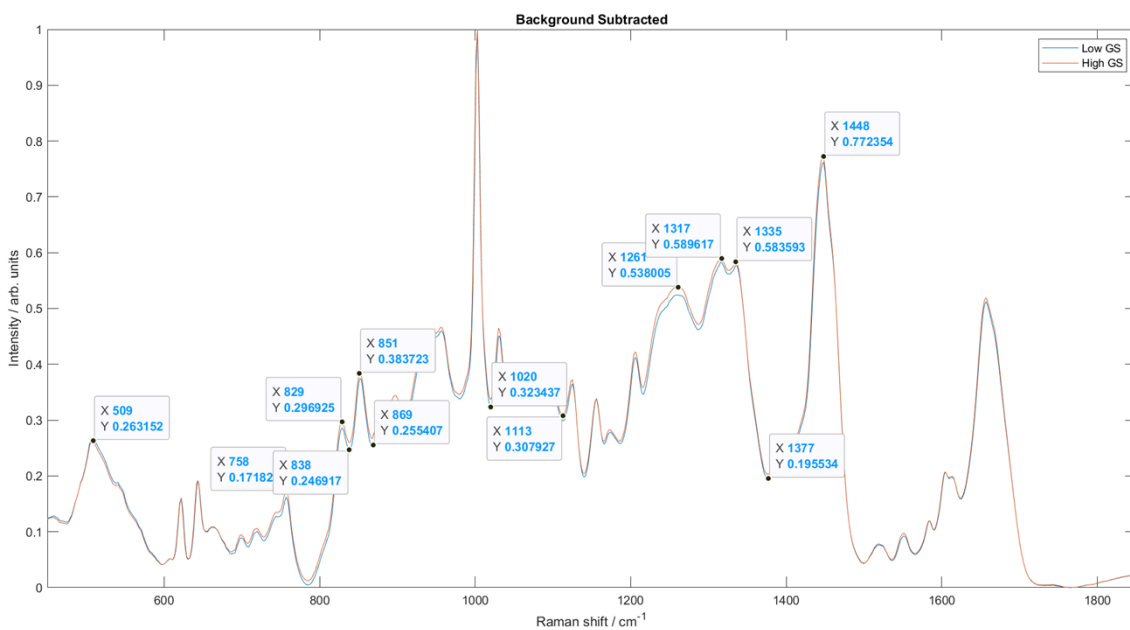


Fig. 6.4: Mean plasma spectral differences between low Gleason scores and high Gleason scores.

6.5: Serum spectral features:

Prominent Raman peaks were observed after subtracting mean cancer spectra from the benign mean spectra at the following locations with respective tentative biochemical assignments. 548 cm^{-1} (Cholesterol), 618 cm^{-1} (Phenylalanine) amino acid, 625 cm^{-1} (guanine), 717 cm^{-1} (Lipid), 878 cm^{-1} (Lipid), 1128 cm^{-1} (Heme vibration mode), 1235 cm^{-1} (Amide III), 1300 cm^{-1} (Lipid), 1358 cm^{-1} (Tryptophan), 1442 cm^{-1} (Lipid), 1525 cm^{-1} (Carotenoid), 1653 cm^{-1} (Amide 1) and 1676 cm^{-1} (C=C vibration mode). The highest spectral intensities were observed at peak positions 1300 and 1442, which were in the peak position for lipids, and 1653, which was at the amide I position. In contrast, the lowest spectral intensities were mostly related to carotenoids' spectral positions at 1525 cm^{-1} .

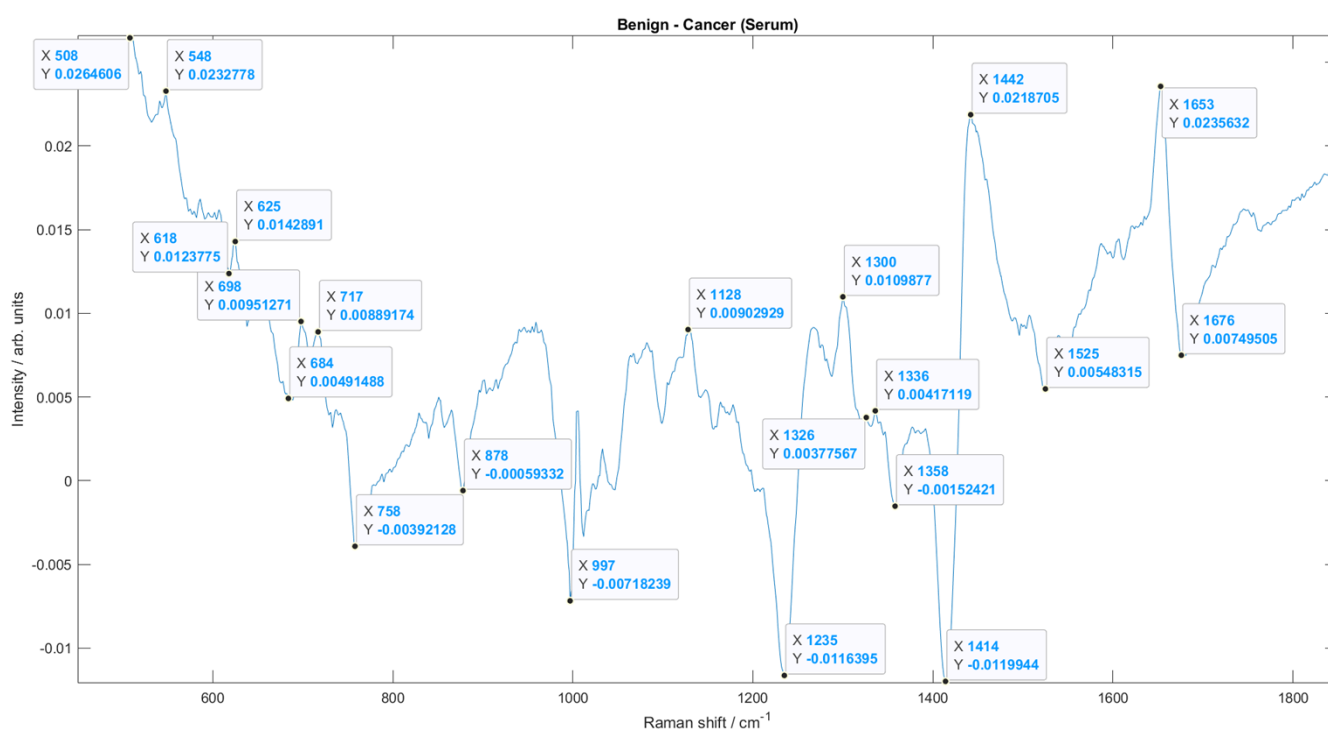


Fig. 6.5: Mean serum spectral difference between benign and cancer.

A comparison between the mean benign and cancer spectra was assessed, and there were some differences between the two mean spectra. In comparison, the benign group depicted higher intensities at Disulphide (approx. 510 cm^{-1}), phenylalanine (approx. 622 cm^{-1}), tyrosine (approx. 644 cm^{-1}), C-C stretch, and collagen (approx. 936 cm^{-1}), amide III (approx. 1264 cm^{-1}). However, the intensity was significantly highest in the cancer group at peak position 1003 cm^{-1} , which corresponded with phenylalanine (amino acid).

The increased intensities of the 1336 cm^{-1} and 1326 cm^{-1} peaks were in line with a higher content of cell-free DNA. Although the reason is unknown, several cancer patients' blood has been proven to have an increased level of cell-free nucleic acids.

A lower carotenoid level has been demonstrated in the population of patients with prostate cancer.

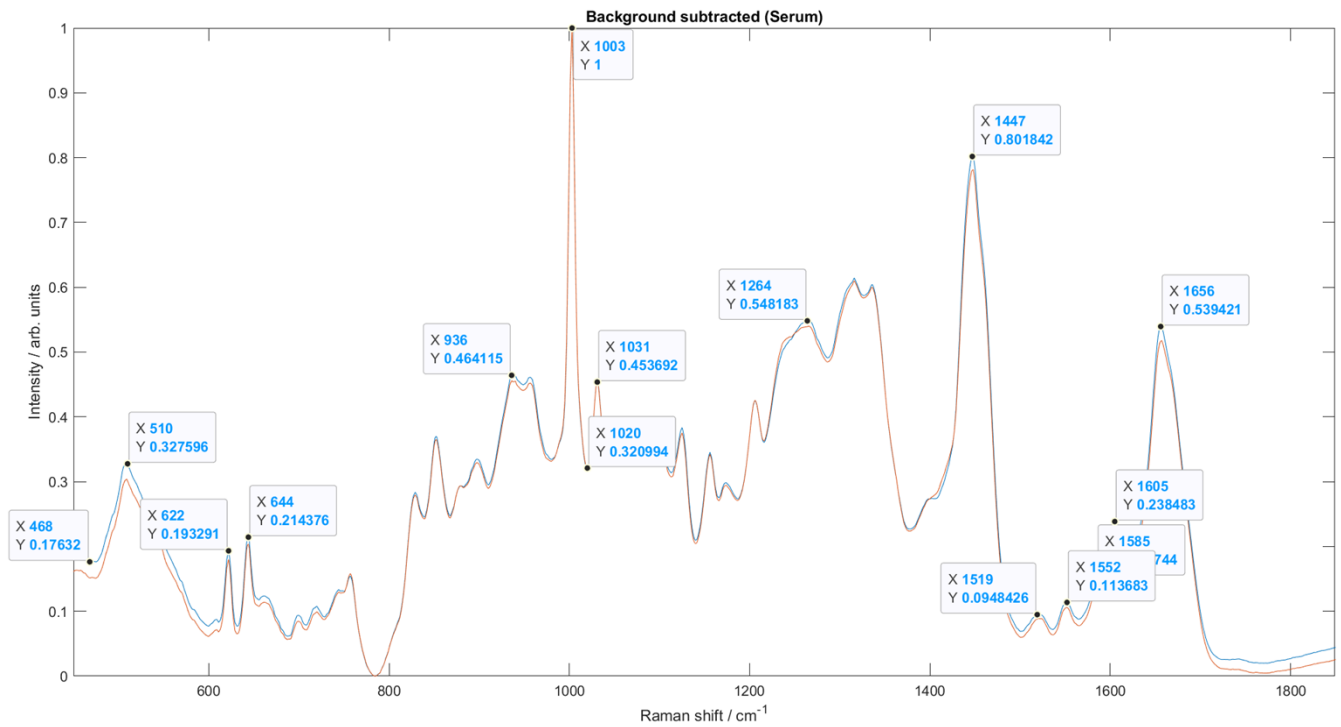


Fig. 6.7: Mean serum spectra of low Gleason scores and high Gleason scores.

However, high Gleason scores for the blood serum, when compared to low Gleason scores, demonstrated a higher intensity at CCH aromatic deformation (approx. 851 cm^{-1}), proline (approx. 896 cm^{-1} & 1031 cm^{-1}), α helix (approx. 937 cm^{-1}), hydroxyapatite (approx. 955 cm^{-1}), phenylalanine (approx. 1003 cm^{-1}), tyrosine & phenylalanine (approx. 1205 cm^{-1}), amide III (approx. 1260 cm^{-1}), CH_2 (approx. 1313 cm^{-1}), and amide I (approx. 1658 cm^{-1}).

The increased intensities of the 1335 cm^{-1} peak were associated with a higher content of cell-free DNA. Several cancer patients' blood has been proven to have an increased level of cell-free nucleic acids. Many studies have shown strong associations between a higher level of β -carotene and a reduced incidence of many forms of cancer. The increased intensity at 937 cm^{-1} demonstrated a higher concentration of α -helix proteins (e.g., histone, the main protein component that makes up the chromatin). The higher intensity of tryptophan at 881 and 1551 cm^{-1} in the serum of colorectal cancer has also been reported (Sahu A et al., 2013; Yang & Li S, 2012).

Therefore, to answer our second research question, can Raman spectroscopy of prostate tissue provide molecular signatures that may be used for real-time in vivo analysis? We have demonstrated the increased concentration of cell-free DNA in both blood plasma and serum studies with prostate cancer participants due to the process of apoptosis and necrosis or release of intact cells in the bloodstream. Nevertheless, decreased concentration of β -carotene was observed in blood plasma and serum studies among cancer cohorts due to a deficiency of antioxidant species. However, the tissue samples demonstrated a lower glycogen concentration in cancerous tissues because tumour cells absorbed glucose and, in turn, gave out lactate. Therefore, as the tumour cells advanced from benign to malignant tissues, there was a lower glycogen concentration. There was also an increased concentration of DNA as the tissues progressed from normal to malignant tissues due to the increased nuclear-to-cytoplasm ratio as the tissue advanced from normal to malignancy. Furthermore, reduced collagen concentration was observed within the extracellular matrix until the tumour became prominent, then more collagen was expected. With the above spectral features, it is possible to provide molecular signatures that can be used for real-time in vivo analysis.

6.6: Translation of vibrational Spectroscopy of blood plasma, serum and tissues into clinical practice.

It is well established that most biofluid and tissue studies conducted with the aid of Raman spectroscopy are purely research-based and have not gained access into the clinical environment for routine use. These are purely proof-of-concept studies with small population sizes demonstrating the potential of Raman spectroscopy in clinical practice. However, a few studies are using complementary techniques, such as infrared spectroscopy, gradually gaining momentum for translation into the clinical environment. Butler H J et al. (2019) developed a high throughput blood test with attenuated total reflection Fourier transform infrared (ATR-FTIR) spectroscopy to assess brain cancer patients. It was based on the fact that it can be challenging to decipher which patients with non-specific symptoms such as headache and dizziness were likely to have a brain tumour. Secondly, the NICE guideline for referral of patients for medical imaging with a suspected brain tumour was expected to discover brain tumours at a rate of 3% in the referral population. ATR-FTIR spectroscopy is a simple, label-free, non-invasive, and non-destructive technique that can be utilised to characterise the biochemical profile of blood samples to rule out the presence of tumour cells. Four hundred thirty-three patients' blood samples were collected from the biobank for the control group (normal) and glioma participants. Machine learning algorithms were utilised to learn the infrared signatures that assisted in the discrimination of the spectra into cancer and non-cancer with a sensitivity and specificity of 93.2% and 92.8%,

respectively. The cancer cohort was further separated into high-grade gliomas, glioblastoma, and low-grade gliomas, with a sensitivity and specificity of 83.3% and 87%, respectively. The value of sensitivity and specificity were found to be within the threshold of cost-effectiveness (80%). By implication, this indicates that the test has the potential to provide cost savings to both UK and US health services if used to triage patients and detect those that urgently need brain scans. It saves the UK about £6-12 million annually due to its high specificity. While from the patients' point of view, the high sensitivity of the test could help in the early detection of the tumour, and when treatment is offered on time, it could result in improved quality of life. This technique is currently undergoing clinical translation (Butler HJ et al., 2019).

Jenkins C A et al. (2018) developed a high throughput test using liquid and dry serum Raman spectroscopy to rule out the presence of colorectal cancer in symptomatic patients. Because only 3-5% of patients referred for colonoscopy end up having colorectal cancer, there was a need to develop a simple, rapid, and non-invasive test that can assist in triaging patients and identifying those patients that require a colonoscopy. The team recruited 60 participants. Thirty were cancer patients, while the other 30 were healthy participants as the control group. Sensitivity and specificity of 83% and 83% were recorded in discriminating between healthy controls and colorectal cancer (Jenkins CA et al., 2018)

6.7: Conditions for translation into clinical application

Many factors are responsible for the lack of translation of vibrational spectroscopy techniques from just a research tool to a valuable tool for routine clinical practices. One such factor includes the imperfections in the methodology of these techniques. Many variations are found in many biological fluids and tissue studies, and everyone claims to have valid methods for assessing different disease conditions. Rigorous efforts are therefore necessary to establish a methodology that can withstand the test of time and can be utilised across different equipment manufacturers and laboratories. Current practices in medical imaging techniques could be seen whereby there is a standardization of methodology for investigations across different equipment manufacturers.

The other crucial point for translation is ascertaining the ideal sample size required to build an ideal classifier (diagnostic model) with specified performance. Beleites and colleagues in 2013 had put forward that learning curves could be exploited to ascertain the ideal sample size necessary to build good classifiers alongside specified performances. It is essential to bear in mind that when the sample size is too small to divide the population into a training set and the other independent validation set,

cross-validation methods should be utilized to avoid the challenge of overfitting. A small sample size of about 5-25 independent samples per class could be utilised to build a diagnostic model, although the classification could accomplish an acceptable performance. Nevertheless, the learning curve could be obscured by the random testing variability as a result of the small test sample size. Therefore, to ascertain the sample size necessary to achieve reasonable precision in the validation, the authors discovered that a population size of 75-100 samples was necessary to determine if a classifier was good enough. Nevertheless, this is not the same as a perfect classifier (which requires a larger sample size). A good classifier, therefore, requires advanced sample size planning based on the performance achieved (Beleites C et al., 2013).

In our study, the analysis of tissue samples could have been good at discrimination into the different pathology groups if sufficient sample sizes had been utilised. A sample size of 100 participants was planned as stipulated by Beleites C et al. in 2013. Therefore, 100 participants were recruited (included in the study). Nevertheless, some tissue samples were suboptimal during histological assessment and Raman measurements, primarily because the biopsy needle did not retrieve enough tissue samples for histological assessment. With a small tissue biopsy, it became difficult to embed the tissue in paraffin wax and cut it. It was also observed that some of the tissue samples were fragmented and curved, making it difficult to include such in the pathological evaluation. The histopathologist considered the tissue biopsies adequate if at least a single prostate gland was present in the tissue. Therefore, if only stromal tissues were seen, the biopsy samples were considered inadequate or inappropriate for diagnosis or analysis. This study has highlighted the importance of the biopsy technique and the skill of the urologist, as these can significantly impact the number of biopsy samples obtained that are of diagnostic quality. Therefore, with an original sample size of 100, only 49 tissue samples were helpful for histological analysis. The dataset size of 49 tissue samples was insufficient to describe all the variances in each group to represent the patient population and the variability of the gold standard technique, leading to an inability to distinguish between many subcategories of pathology. Nevertheless, for large sample sizes with reproducible homogeneous blood samples, such as dried liquid biopsy samples, and a smaller number of pathology groups, such as 2 and 3 groups, it was possible to distinguish between the different classes with high sensitivity, specificity, positive and negative predictive values respectively.

Future studies should aim for at least 25 independent samples in each class to enable accurate classification into 4- and 5-group classification models. Therefore, an ideal sample size for a feasibility

study of this nature should be between 100 and 150, based on our experience. A competent clinical histopathologist should access each sample before inclusion into the study.

6.8: Limitations of Raman spectroscopy in clinical applications

Fluorescence caused by fluorophores and chromophores within the sample can sometimes impact significantly on the quality of the data measured with RS of human tissues. Sometimes, the fluorescence emission spectrum masks the weaker Raman spectrum. While the Raman effect is due to a scattering process, the fluorescence effect is due to photon absorption. In order to tackle this problem of masking the Raman spectrum, some methods have been developed.

Firstly, the choice of excitation wavelength can minimize tissue fluorescence. The photons in the Near InfraRed (NIR) wavelength region (750-1400nm) have lower energy and rarely induce fluorescence (Stone N et al., 2007a). However, the Charge Couple Device (CCD) cameras that detect the signals become less sensitive at longer wavelengths. Raman scattering signals also reduce since they depend on the wavelength by a factor of $1/\lambda^4$ (Matousek P, 2016). Therefore, a compromise has to be found. On the other hand, fluorescence from UV light (10-380nm) has significantly different energy from the Raman scattering, allowing separation of fluorescence and Raman signal. However, in vivo safety is a concern, and UV light does not penetrate far into tissues, reducing the signals to the surface cells only (Kast RE et al., 2014).

The use of lasers to measure tissues may raise some concerns, although lasers are just coherent beams of light. Several factors contribute to the threshold of damage for a given application. These include tissue type, excitation wavelength (i.e., does the tissue readily absorb it), exposure time, and fluency (energy by unit area). Minimally absorbing and non-carcinogenic NIR light enables safe in vivo measurements at much higher light fluency levels than visible and ultraviolet wavelengths (Ibid, 2014).

The translation of the Raman-based technique from a research tool into clinical practice would require that a detailed spectral database is developed for easy assessment of the molecular fingerprints of the subtle changes within the biological samples. Standardizing best practice techniques for image acquisition, data processing, and classification is also necessary to enhance consistent results.

6.9: Clinical Validity:

Defining the diagnostic performance of a given biomarker test is crucial in managing patients concerning any particular disease condition. In order to assess the clinical validity of a particular test or biomarker, a large population size is necessary (Baker M et al., 2015). Large multicentre randomized control trials are usually necessary, whereby the sensitivity and specificity of the diagnostic or screening tool are tested against a gold standard diagnostic or screening test. The studies are often designed to recruit both the study group and control group to ensure that the biomarker reflects the very essence of the test (Baker M et al., 2015). Therefore, the test could be for screening, prognostic, diagnostic, treatment response prediction, or disease monitoring. In the context of a screening test, high sensitivity and specificity are crucial to ensure a reduction in the number of false positives, which often result in a further investigation on the part of the patient (Ibid, 2015). During the recruitment process, it is of paramount importance to ensure that bias is not introduced during this process. One quick method of achieving this is carrying out a prospective study without knowing the final result (Ibid, 2015). In our study, we could see the potential of this test with the blood plasma and serum, which could be utilised as a screening test to rule out the presence of prostate cancer following a sizeable multicentre study conducted to confirm the findings of this study. With the aid of a support vector machine learning algorithm, high sensitivity and specificity were achieved. For a screening test, discriminating between normal or benign cancer patients is paramount. This model has been able to differentiate between the two classes of spectra, benign versus malignant. The study could also discriminate between low-grade and high-grade tumours with high sensitivity and specificity.

On the other hand, due to multiple factors, the tissue sample analysis could not do the same; hence, lower sensitivity and specificity were observed. The reason for low prediction accuracy could be due to multiple factors. Firstly, the population size was smaller for the tissue samples than those utilized for the blood sample analysis. However, the tissue and blood samples were collected from the same cohort. However, during histological and Raman assessments, it was discovered that some tissue samples were suboptimal for diagnosis and measurements. Secondly, the histological assessments were given on the overall tissue, while Raman measurements were taken from five random positions within the tissue samples. Future studies could benefit from taking the histological assessment and Raman spectroscopy measurements from the same positions on the tissue samples. Thirdly, only one histopathologist provided an assessment of all the tissue samples included in the study. Future studies could benefit from having more than one histopathologist to conduct tissue analysis.

6.10: Clinical utility

The clinical utility of a diagnostic test refers to the extent to which a diagnostic test improves health outcomes compared to the existing gold standard technique or by measuring outcomes in randomised controlled trials. However, this can be difficult for diagnostic purposes since one has to wait until cancer develops before we can assess the test's clinical utility. Nevertheless, this can be handy for a screening test since the disease can be discovered early before the tumour progresses to an advanced stage. Doctors must distinguish between clinically significant and insignificant tumours, reducing the burden of overdiagnosis, overtreatment, and attendant complications.

Furthermore, clinical utility is one of the metrics that define the usefulness of a biomarker in making clinical decisions at an acceptable cost to society (Baker M et al., 2015). Therefore, the laboratory director is always in a dilemma of offering a helpful test that is also cost-effective. Before a biomarker test can be routinely implemented in clinical practice, the test's positive and negative predictive values must be assessed in real-life patients (Ibid, 2015). Drop coating deposition Raman spectroscopy has shown a high positive and negative predictive value, especially with support vector machine learning algorithm as a potential screening tool that can be utilised in discriminating between low-grade and high-grade tumours. Nevertheless, the tissue samples have been able to show lower positive predictive and negative predictive values due to low population size and the inability to target Raman measurement to the location where histological tissue assessments were taken. It is, therefore, essential to verify the findings of this feasibility study with a large independent population both for the tissue biopsy samples and the liquid biopsy samples. After these findings are confirmed, it is also paramount to conduct a large multicentre study to validate or substantiate them. The next step to translation should involve an assessment of the usefulness of these findings in a clinical decision-making capacity, considering the cost and the benefit to the clinical environment and the patients.

Chapter 7 – Conclusion

Raman spectroscopy is an optical technique that can potentially impact the clinical environment, especially urology. With high chemical specificity and the ability to provide molecular-specific fingerprints of the composition of biological samples under interrogation, Raman spectroscopy can provide precision in screening for early tumours, tissue diagnosis, metastasis, treatment efficacy, and the assessment of tumour margins following radical prostatectomy. A minimally invasive technique can provide objective results in real-time within the clinical environment, thereby removing the adverse impact of interobserver variability and delays to diagnosis. The current study has demonstrated that it is possible to distinguish between patients with cancer and those with benign prostate conditions alongside healthy participants using biopsy tissue samples, blood serum, and plasma. The highest intensities at 1003 cm^{-1} in the mean serum Raman spectrum were higher in the cancer group due to the phenylalanine.

The highest intensities were observed at peak positions consistent with carotenoid or beta carotenoids within the blood serum and plasma spectra; this effectively demonstrated that carotenoid was responsible for the discrimination between benign and malignant plasma and mean serum spectra. A lower level of β -carotene was demonstrated in the population of blood plasma with prostate cancer, with a corresponding higher concentration among the benign group. The concentration of Disulphide, phenylalanine, tyrosine and CH_2 deformation was also seen to be higher among benign mean spectra. On the other hand, higher intensities were seen at collagen at peak positions for malignant mean spectra compared to the mean benign spectra.

The disease-specific molecular fingerprints found in the prostate tissue can be measured with this technique which can be utilised in risk stratification of prostatic tumours. This study has shown that a high concentration of lipids and amide 1 was observed in benign tissues compared to the malignant spectra. On the other hand, a higher concentration of cholesterol, phenylalanine, collagen, α helix, tryptophan, and DNA were observed in the malignant mean spectra compared to benign spectra.

Sensitivity, specificity, and positive and negative predictive values of above 90% can be achieved using this technique with the SVM learning algorithm in discriminating blood samples (serum & plasma) spectra into two groups, benign versus malignant or low-grade versus high-grade tumours.

Automation can ensure quick and effective complementary tools in prostate cancer risk stratification alongside histopathology.

A minimally invasive technique that can be quickly used to assess the malignant status of the prostate gland that can act as a screening tool can be developed from the blood serum/ plasma assay, which essentially allows for early detection of prostate cancer. It can also be utilized in monitoring patients for disease progression or the efficacy of a particular therapy.

The translation of Raman spectroscopy from a research tool into clinical practice will require a well-defined clinical need by Clinicians, well-demonstrated patient safety, and reliable and reproducible results achieved through extensive clinical trials. Furthermore, regulatory bodies will need to approve this technique's translation into clinical use after a large multi-centre study has been conducted with large population size.

References

- A, F. R. (1936) 'THE USE OF MULTIPLE MEASUREMENTS IN TAXONOMIC PROBLEMS', *Annals of Eugenics*, 7(2), pp. 179–188.
- A, S. *et al.* (2019) 'Comparison of PI-RADS v1 and v2 for multiparametric MRI detection of prostate cancer with whole-mount histological workup as reference standard', *European Journal of Radiology*, 116(1), pp. 180–185.
- Aaron LT, Franco O, H. S. (2016) 'Review of Prostate Anatomy and Embryology and the Etiology of BPH', *Urology Clinician of Northern America*, 43(3), pp. 279–288.
- Abdi H, Pourmalek F, Zargar H, Walshe T, Harris AC, Chang SD, Eddy C, So AI, Gleave ME, Machan L, Goldenberg SL, B. P. (2015) 'Multiparametric magnetic resonance imaging enhances detection of significant tumor in patients on active surveillance for prostate cancer.', *Urology*, 85(2), pp. 423–428.
- Alemezaffar M, Regan MM, Cooperberg MR, Wei JT, Michalski JM, Sandler HM, Hembroff L, Sadetsky N, Saigal CS, Litwin MS, Klein E, Kibel AS, Hamstra DA, Pisters LL, Kuban DA, Kaplan ID, Wood DP, Ciezki J, Dunn RL, Carroll PR, S. M. (2011) 'Prediction of erectile function following treatment for prostate cancer', *JAMA*, 306(11), pp. 1205–1214.
- Ali TZ, E. J. (2005) 'Perineural involvement by benign prostatic glands on needle biopsy', *American Journal of Surgical Pathology*, 29(1), pp. 1159–1163.
- Allard WJ, Matera J, Miller MC, Repollet M, Connelly MC, Rao C, Tibbe AG, Uhr JW, T. L. (2004) 'Tumor Cells Circulate in the Peripheral Blood of All Major Carcinomas but not in Healthy Subjects or Patients With Nonmalignant Diseases', *Clinical Cancer Research*, 10(20), pp. 6897–6904.
- Amis, E. (1994) *The Radiology of the Lower Urinary tract*. Edited by L. E. K. Berlin, Heidelberg.
- Angelo M. De Marzo, Valerie L. Marchi, Jonathan I. Epstein, and W. G. N. (1999) 'Proliferative Inflammatory Atrophy of the Prostate Implications for Prostatic Carcinogenesis', *American Journal of Pathology*, 155(6), pp. 1985–1992.
- Aubertin K, Trinh VQ, Jermyn M, Baksic P, Grosset AA, Desroches J, St-Arnaud K, Birlea M, Vladioiu MC, Latour M, Albadine R, Saad F, Leblond F, T. D. (2018) 'Mesoscopic characterization of prostate cancer using Raman spectroscopy: potential for diagnostics and therapeutics.', *British Journal of Urology International*, 122(2), pp. 326–336.

- Auner GW, Koya SK, Huang C, Broadbent B, Trexler M, Auner Z, Elias A, Mehne KC, B. M. (2018) 'Applications of Raman spectroscopy in cancer diagnosis', *Cancer and Metastasis Reviews*, 37(4), pp. 691–717. doi: 10.1007/s10555-018-9770-9.
- Baisden BL, Kahane H, E. J. (1999) 'Perineural invasion, mucinous fibroplasia, and glomerulations: diagnostic features of limited cancer on prostate needle biopsy.', *American Journal of Surgical Pathology*, 23(8), pp. 918–924.
- Baker M, Hussainb SR, Lovergnea L, Untereiner V, H. C. and Roman A. Lukaszewskif RA, Thiéfinb G, S. G. (2015) 'Developing and Understanding Biofluid Vibrational Spectroscopy: A Critical Review', *Chem. Soc. Rev.*, 45(1), pp. 1803–1818.
- Barentsz JO, Richenberg J, Clements R, et al. (2012) 'ESUR prostate MR guidelines 2012', *Eur Radiol.*, 22(4), pp. 746–757.
- Beleites C, Neugebauer U, Bocklitz T, Krafft C, P. J. (2013) 'Sample size planning for classification models', *Analytica Chimica Acta*, 760(1), pp. 25–33.
- Bergholt MS, St-Pierre J, Offeddu GS, Parmar PA, Albro MB, Puetzer JL, Oyen ML, S. M. (2016) 'Raman Spectroscopy Reveals New Insights into the Zonal Organization of Native and Tissue-Engineered Articular Cartilage', *ACS*, 2(12), pp. 885–895.
- Bergholt MS, H. S. (2009) 'Quantification of C-reactive protein in human blood plasma using near-infrared Raman spectroscopy', *Analyst*, 134(10), pp. 2123–2127.
- Bismar TA, Lewis JSJr, Vollmer RT, H. P. (2002) 'Multiple measures of carcinoma extent versus perineural invasion in prostate biopsy tissue in prediction of pathologic stage in a screening population', *American Journal of Surgical Pathology*, 27(1), pp. 432–440.
- Butler HJ, Brennan PM, Cameron JM, Finlayson D, Hegarty MG, Jenkinson MD, Palmer DS, Smith BR, B. M. (2019) 'Development of high-throughput ATR-FTIR technology for rapid triage of brain cancer', *Nature Communications*, 10(1), p. 4501. doi: doi: 10.1038/s41467-019-12527-5.
- Byar DP, M. F. (1972) 'Carcinoma of the prostate: Prognostic evaluation of certain pathologic features in 208 radical prostatectomies.', *Cancer*, 30(1), pp. 5–13.
- C, K. (2002) *A study of Raman spectroscopy of early detection and classification of malignancy in oesophageal tissue.*

- Carneiro A, Barbosa ARG, Takemura LS, et al. (2018) 'The Role of Immunohistochemical Analysis as a Tool for the Diagnosis, Prognostic Evaluation and Treatment of Prostate Cancer: A Systematic Review of the Literature', *Frontiers in Oncology*, 8(377). doi: 10.3389/fonc.2018.00377.
- Catalona WJ, Richie JP, Ahmann FR, Hudson MA, Scardino PT, Flanigan RC, DeKernion JB, Ratliff TL, Kavoussi LR, Dalkin BL, Waters WB, MacFarlane MT, S. P. (2017) 'Comparison of digital rectal examination and serum prostate specific antigen in the early detection of prostate cancer: results of a multicenter clinical trial of 6,630 men.', *Journal of Urology*, 151(5), pp. 1283–1290.
- Celma A, Servián P, Planas J, Placer J, Quilez MT, Arbós MA, de Torres I, M. J. (2014) 'Clinical significance of proliferative inflammatory atrophy in prostate biopsy.', *Actas Urologicas Espanoles*, 38(3), pp. 122–126.
- Cookson MS, C. S. (2010) 'Margin control in open radical prostatectomy: What are the real outcomes?', *Urologic Oncology: Seminars and Original Investigations*, 28(2), pp. 205–209.
- Correas JM, Tissier AM, Khairoune A, Khourya G, Eiss D, H. O. (2013) 'Ultrasound elastography of the prostate: State of the art', *Diagnostic and Interventional Imaging*, 94(5), pp. 551–560.
- Corsetti S, Rabl T, McGloin D, N. G. (2017) 'Raman spectroscopy for accurately characterizing biomolecular changes in androgen-independent prostate cancer cells', *Journal of Biophotonics*, p. <https://doi.org/10.1002/jbio.201700166>.
- Crow P, Stone N, Kendall C A, Uff J S, Farmer J A M, B. H. and W. M. P. J. (2003) 'The use of Raman spectroscopy to identify and grade prostatic adenocarcinoma in vitro', *British Journal of Cancer*, 89(1), pp. 106–108.
- Danila DC, Heller G, Gignac GA, Gonzalez-Espinoza R, Anand A, Tanaka E, Lilja H, Schwartz L, Larson S, Fleisher M, S. H. (2007) 'Circulating tumor cell number and prognosis in progressive castration-resistant prostate cancer.', *Clinical Cancer Research*, 13(23), pp. 7053–7058.
- Day JC, S. N. (2013) 'A subcutaneous Raman needle probe', *Applied Spectroscopy*, 67(3), pp. 349–354.
- Delongchamps NB, Portalez D, Malavaud B, Renard-Penna R, Mozer P, Cornud F1, B. L. (2013) 'TRUS-MRI image registration: a paradigm shift in the diagnosis of significant prostate cancer.', *Abdominal Imaging*, 38(6), pp. 1447–1463.
- Descotes, J.-L. (2019) 'Diagnosis of prostate cancer', *Asian Journal of Urology*, 6(2), pp. 129–136.

- Desroches J, Lemoine É, Pinto M, Marple E, Urmey K, Diaz R, Guiot MC, Wilson BC, Petrecca K, L. F. (2019) 'Development and first in-human use of a Raman spectroscopy guidance system integrated with a brain biopsy needle', *Journal of Biophotonics*, 12(3), pp. 1–7.
- Djavan B, Susani M, Bursa B, Basharkhah A, Simak R, M. M. (1999) 'Predictability and significance of multifocal prostate cancer in the radical prostatectomy specimen', *Techniques in Urology*, 5(3), pp. 139–142.
- Downing A, Wright P, Hounscome L, Selby P, Wilding S, Watson E, Wagland R, Kind P, Donnelly DW, Butcher H, Catto JWF, Cross W, Mason M, Sharp L, Weller D, Velikova G, McCaughan E, Mottram R, Allen M, Kearney T, McSorley O, Huws DW, Brewster DH, McNair E, G. G. A. (2019) 'Quality of life in men living with advanced and localised prostate cancer in the UK: a population-based study', *The Lancet. Oncology*, 20(3), pp. 436–447.
- Esmonde-White K, Esmonde-White FW, M. M. and R. B. (2014) 'Characterization of Biofluids Prepared by Sessile Drop Formation', *Analyst*, 139(11), pp. 2734–2741.
- Fady B. Geara, Muhammad Bulbul, Raja B. Khauli, Therese Y. Andraos, Mirna Abboud, Abdelatif Al Mousa, Nasim Sarhan, Ahmed Salem, Hamza Ghatasheh, Anoud Alnsour, Zeina Ayoub, Ibrahim Abu Gheida, Maya Charafeddine, Mohammed Shahait, Ali Shamseddine, Rami Ab, and J. K. (2017) 'Nadir PSA is a strong predictor of treatment outcome in intermediate and high risk localized prostate cancer patients treated by definitive external beam radiotherapy and androgen deprivation', *Radiation Oncology*, 12(149).
- Fajkovic H, Mathieu R, Lucca I, Hiess M, Hubner N, A., Hussein Al Awamlh B, Lee R, Briganti A, K. P. and Lotan Y, et al. (2016) 'Validation of lymphovascular invasion is an independent prognostic factor for biochemical recurrence after radical prostatectomy. Urol', *Urological Oncology*, 34(233), pp. e1–e6.
- Faria R, Soares MO, Spackman E, et al. (2018) 'Optimising the Diagnosis of Prostate Cancer in the Era of Multiparametric Magnetic Resonance Imaging: A Cost-effectiveness Analysis Based on the Prostate MR Imaging Study (PROMIS)', *European Urology*, 73(1), pp. 23–30.
- Fawcett, T. (2006) "An Introduction to ROC Analysis", *Pattern Recognition Letters*, 27(8), pp. 861–874. doi: 10.1016/j.patrec.2005.10.010.
- Feld MS, Boustany NN, Crawford JM, Manoharan R, D. R. (1999) 'Analysis of nucleotides and aromatic amino acids in normal and neoplastic colon mucosa by ultraviolet resonance raman spectroscopy',

Laboratory Investigations, 79(10), pp. 1201–1214.

Ferlay, J. *et al.* (2018) 'Cancer incidence and mortality patterns in Europe: Estimates for 40 countries and 25 major cancers in 2018', *European Journal of Cancer*, 103, pp. 356–387. doi: 10.1016/j.ejca.2018.07.005.

Gleason D F (1966) 'Classification of prostatic carcinomas', *Classification of prostatic carcinomas*, 50(3), pp. 125–128.

Globocan (2020) *Estimated number of new cases in 2020 worldwide, males, all ages.*, *GLOBOCAN 2020: New Global Cancer Data*.

de Grauw CJ, Otto C, G. J. (1997) 'Line-scan Raman microspectrometry for biological applications', *Applied Spectroscopy*, 51(11), pp. 1607–1612.

Haar G, Rivens I, Chen L, R. S. (1991) 'High intensity focused ultrasound for the treatment of rat tumours', *Physics in Medicine and Biology*, 36(11), pp. 1495–1501.

Haka A, Volynskaya Z, Gardecki J, and N. J. (2009) 'Diagnosing breast cancer using Raman spectroscopy: prospective analysis', 14(5), p. doi: 10.1117/1.3247154.

Halpern JA, Oromendia C, Shoag JE, Mittal S, Cosiano MF, Ballman KV, Vickers AJ, H. J. (2018) 'Use of Digital Rectal Examination as an Adjunct to Prostate Specific Antigen in the Detection of Clinically Significant Prostate Cancer.', *Journal of Urology*, 199(4), pp. 947–953.

Harder SJ, Matthews Q, Isabelle M, Brolo AG, Lum JJ, J. A. (2015) 'A Raman Spectroscopic Study of Cell Response to Clinical Doses of Ionizing Radiation', *Applied Spectroscopy*, 69(2), pp. 193–204.

Hou JM, Krebs M, Ward T, Sloane R, Priest L, Hughes A, Clack G, Ranson M, Blackhall F, D. C. (2011) 'Circulating tumor cells as a window on metastasis biology in lung cancer', *The American Journal of Pathology*, 178(3), pp. 989–996.

Huang N, Short M, Zhao J, Wang H, Lui H, Korbelik M, Z. H. (2011) 'Full Range Characterization of the Raman Spectra of Organs in a Murine Model', *Optic Express*, 19(23), pp. 22892–22909.

Humphrey PA (2003) *In Prostate pathology*.

Issaq H, Xiao Z, and V. T. D. (2007) 'Serum and Plasma Proteomics', *Chemica Review*, 107(8), pp. 3601–3620.

- Izadifar Z, Izadifar Z, Chapman D, B. P. (2020) 'An Introduction to High Intensity Focused Ultrasound: Systematic Review on Principles, Devices, and Clinical Applications', *Journal of Clinical Medicine*, 9(2), p. 460.
- Jang HJ, Lee JY, Lee D, Kim W, H. J. (2010) 'Current and Future Clinical Applications of High-Intensity Focused Ultrasound (HIFU) for Pancreatic Cancer', *Gut and Liver*, 4(Supplement 1), pp. S57–S61.
- Jenkins CA , Jenkins RA , Pryse MM , Welsby KA , Jitsumura M , Thornton CA , Dunstan PR, H. DA (2018) 'A high-throughput serum Raman spectroscopy platform and methodology for colorectal cancer diagnostics', *Analyst*, 143(24), pp. 6014–6024.
- Jermyn M, Mok K, Mercier J, Desroches J, Pichette J, Saint-Arnaud K, Bernstein L, Guiot MC, Petrecca K, L. F. (2015) 'Intraoperative brain cancer detection with Raman spectroscopy in humans.', *Science of Translation Medicine*, 7(274), p. doi: 10.1126/scitranslmed.aaa2384.
- Kanter EM, Majumder S, Vargis E, Robichaux-Viehoever A, Kanter GJ, Shappell H, Jones HW 3rd, M.-J. A. (2009) 'Multiclass discrimination of cervical precancers using Raman spectroscopy.', *Journal of Raman Spectroscopy*, 40(2), pp. 205–211.
- Kast RE, Tucker SC, Killian K, Trexler M, Honn KV, A. G. (2014) 'Emerging technology: applications of Raman spectroscopy for prostate cancer', *Cancer and Metastasis Reviews*, 33(2–3), pp. 673–693.
- Kelloff G.J, Choyke P, C. D. S. (2009) 'Challenges in Clinical Prostate Cancer: Role of Imaging', *American Journal of Roentgenol*, 192(6), pp. 1455–1470.
- Koca O, Çalışkan S, Öztürk MI, Güneş M, and K. M. (2011) 'Significance of Atypical Small Acinar Proliferation and High-Grade Prostatic Intraepithelial Neoplasia in Prostate Biopsy', *Korean Journal of Urology*, 52(11), pp. 736–740.
- Li P; Chen C; Deng X, Mao H, J. S. (2015) 'Drop coating deposition Raman spectroscopy of blood plasma for the detection of colorectal cancer', *Journal of Biomedical Optics*, 20(3), pp. 037004–1.
- Litjens G, Sánchez CI, Timofeeva N, Hermsen M, Nagtegaal I, Kovacs I, Hulsbergen - van de Kaa C, Bult P, van G. B. van der L. J. (2016) 'Deep learning as a tool for increased accuracy and efficiency of histopathological diagnosis.', *Scientific Report*, 6(26286). doi: 10.1038/srep26286.
- Liu Y, Kyne M, Wang C, and Y. X. (2020) 'Data mining in Raman imaging in a cellular biological system', *Comput Struct Biotechnol Journal*, 18, pp. 2920–2930.

- Lovergne L, Clemens G, Untereiner V, Lukaszewski RA, S. G. and B. M. (2015) 'Investigating optimum sample preparation for infrared spectroscopic serum diagnostics', *Analytical Methods*, 7(17), pp. 7140–7149.
- Lyng FM, Traynor D, Nguyen TNQ, Meade AD, Rakib F, Al-Saad R, Goormaghtigh E, Al-Saad K, A. M. (2019) 'Discrimination of breast cancer from benign tumours using Raman spectroscopy', *PLoS one*, 13(2), p. e0212376.
- M, Z. (2018) 'High-grade prostatic intraepithelial neoplasia, PIN-like carcinoma, ductal carcinoma, and intraductal carcinoma of the prostate.', *Modern Pathology*, 31(S1), pp. S71–S79.
- Magbanua MJ, Sosa EV, Scott JH, Simko J, Collins C, Pinkel D, Ryan CJ, P. J. (2012) 'Isolation and genomic analysis of circulating tumor cells from castration resistant metastatic prostate cancer', *Biomedical Central Cancer*, 12(78).
- Mahadevan-Jansen A, R.-K. R. (1996) 'Raman Spectroscopy for the detection of cancers and precancers', *Journal of Biomedical Optics*, 1(1), pp. 31–70.
- Mahadevan-Jansen A1, Mitchell MF, Ramanujam N, Malpica A, Thomsen S, Utzinger U, R.-K. R. (1998) 'Near-infrared Raman spectroscopy for in vitro detection of cervical precancers', *Photochemistry and photobiology*, 68(1).
- Marrinucci D, Bethel K, Lazar D, Fisher J, Huynh E, Clark P, Bruce R, Nieva J, K. P. (2010) 'Cytomorphology of circulating colorectal tumor cells:a small case series.', *Journal of Oncology*.
- De Marzo AM, Marchi VL, Epstein JI, and N. W. (1999) 'Proliferative Inflammatory Atrophy of the Prostate Implications for Prostatic Carcinogenesis', *American Journal of Pathology*, 155(6), pp. 1985–1992.
- Mathew J, Sankar P, V. M. (2020) 'Physiology, Blood Plasma', In: *StatPearls. Treasure Island (FL): StatPearls Publishing;*, 30285399.
- Matousek P, S. N. (2016) 'Development of deep subsurface Raman spectroscopy for medical diagnosis and disease monitoring.', *Chemical Society Reviews*, 45(7), pp. 1794–1802.
- McNeal, J. E. (1981) 'The zonal anatomy of the prostate', *The Prostate*, 2(1), pp. 35-49+.
- Meng S, Tripathy D, Frenkel EP, Shete S, Naftalis EZ, Huth JF, Beitsch PD, Leitch M, Hoover S, Euhus D, Haley B, Morrison L, Fleming TP, Herlyn D, Terstappen LW, Fehm T, Tucker TF, Lane N, Wang J, U. J.

- (2004) 'Circulating Tumor Cells in Patients with Breast Cancer Dormancy', *Clinical Cancer Research*, 10(24), pp. 8152–8162.
- Montironi R, Scattonib V, Mazzucchellia R, Lopez-Beltranc A, Bostwickd DG, M. F. (2006) 'Atypical Foci Suspicious but not Diagnostic of Malignancy in Prostate Needle Biopsies', *European Urology*, 50(4), pp. 666–674.
- Naji L, Randhawa H, Sohani Z, Dennis B, Lautenbach D, Kavanagh O, Bawor M, Banfield L, P. J. (2018) 'Digital Rectal Examination for Prostate Cancer Screening in Primary Care: A Systematic Review and Meta-Analysis', *Annals of Family Medicine*, 16(2), pp. 149–154.
- Nyberg M, Jalkanen V, Ramser K, Ljungberg B, B. A. & L. O. (2015) 'Dual-modality probe intended for prostate cancer detection combining Raman spectroscopy and tactile resonance technology—discrimination of normal human prostate tissues ex vivo', *Journal of Medical Engineering & Technology*, 39(3), pp. 198–207. doi: 10.3109/03091902.2015.1021430.
- O'Brien CM, Rood K, Sengupta S, Gupta SK, DeSouza T, Cook A, V. J. (2011) 'Detection and isolation of circulating melanoma cells using photoacoustic flowmetry.', *Journal of Visualised Experiment*, 25(57). doi: 10.3791/3559.
- Obort A, Ajadi M, A. O. (2013) 'Prostate-Specific Antigen: Any Successor in Sight?', *Reviews in Urology*, 15(3), pp. 97–107.
- Oesterling JE, Rice DC, Glenski WJ, B. E. (1993) 'Effect of cystoscopy, prostate biopsy, and transurethral resection of prostate on serum prostate-specific antigen concentration', *Urology*, 42(3), pp. 276–282.
- Olson DO, Baisden JM, Groten DL, T. C. (2019) 'Pursuing an Elusive Prostate Carcinoma: A Case Report Involving Multiparametric MR and CT-Guided Biopsy', *Case Reports in Oncology*, 12(3), pp. 737–741.
- Oshima Y, Sato H, Kajiura-Kobayashi HK, Kimura T, Naruse K, and N. S. (2012) 'Light Sheet-excited Spontaneous Raman Imaging of a Living Fish by Optical Sectioning in a Wide Field Raman Microscope', *Optic Express*, 20(15), pp. 16195–16204.
- Ozaki Y, Dou x, Yamaguchi Y, Yamamoto H, U. H. (1996) 'Biological Applications of Anti-Stokes Raman Spectroscopy: Quantitative Analysis of Glucose in Plasma and Serum by a Highly Sensitive Multichannel Raman Spectrometer', *Applied Spectroscopy*, 50(10), pp. 1301–1306.

- Ozkan TA, Erucar AT, Cebeci OO, Memik O, Ozcan L, K. I. (2016) 'Interobserver variability in Gleason histological grading of prostate cancer', *Scand J Urol*, 50(6), pp. 420–424.
- Pallwein L, Mitterberger M, Pelzer A, Bartsch G, Strasser H, Pinggera GM, Aigner F, Gradl J, Zur Nedden D, F. F. (2008) 'Ultrasound of prostate cancer: recent advances.', *European Radiology*, 18(4), pp. 707–715.
- Phan LM, Sai-Ching Jim Yeung SJ, L. M. (2014) 'Cancer metabolic reprogramming: importance, main features, and potentials for precise targeted anti-cancer therapies', *Cancer Biology & Medicine*, 11(1), pp. 1–19.
- Puppels GJ, de Mul FFM, Otto C, Greve J, Robert-Nicoud M, A.-J. D. & J. T. (1990) 'Studying single living cells and chromosomes by confocal Raman microspectroscopy', *Nature*, 347, pp. 301–303.
- Gautam R, Vanga S and , Ariese F, and U. S. (2015) 'Review of multidimensional data processing approaches for Raman and infrared spectroscopy', *EPJ Techniques and Instrumentation*, 2(8), pp. 1–38.
- Rau JV, Marini F, Fosca M, Cippitelli C, Rocchia M, D. N. A. (2019) 'Raman spectroscopy discriminates malignant follicular lymphoma from benign follicular hyperplasia and from tumour metastasis', *Talanta*, 194(1), pp. 763–770.
- Rizzo FM, Vesely C, Childs A, Marafioti T, Khan MS, Mandair D, Cives M, Ensell L, Lowe H, Akarca AU, Luong T, Caplin M, Toumpanakis C, Krell D, Thirlwell C, Silvestris F, Hartley JA, M. T. (2019) 'Circulating tumour cells and their association with bone metastases in patients with neuroendocrine tumours.', *British Journal of Cancer*, 120(3).
- Ross JS, S. E. (2009) 'Circulating and disseminated tumor cells in the management of breast cancer.', *American Journal of Clinical Pathology*, 132(2), pp. 237–245.
- Saha A, Barman I, Dingari NC, Galindo LH, Sattar A, Liu W, Plecha D, Klein N, Dasari RR, F. M. (2012) 'Precision of Raman spectroscopy measurements in detection of microcalcifications in breast needle biopsies.', *Analytical Chemistry*, 84(15), pp. 6715–6722.
- Sahu A, Nandakumar N, Sawant S, K. C. (2015) 'Recurrence prediction in oral cancers: a serum Raman spectroscopy study', *Analyst*, 140(7), pp. 2294–2301.
- Sahu A, Sawant S, Mamgain H, K. C. M. (2013) 'Raman Spectroscopy of Serum: An Exploratory Study

for Detection of Oral Cancers', *Analyst*, 138(13), pp. 4161–4174.

Sahu AK, Dhoot S, Singh A, Sawant SS, Nandakumar N, Talathi-Desai S, Garud M, Pagare S, Srivastava S, Nair S, Chaturvedi P, M. K. (2015) 'Oral cancer screening: serum Raman spectroscopic approach', *Journal of Biomedical Optics*, 20(11), p. 115006.

Shipp DW, Rakha EA, Koloydenko AA, Macmillan RD, Ellis IO, N. I. (2018) 'Intra-operative spectroscopic assessment of surgical margins during breast conserving surgery.', *Breast Cancer Research*, 20(1).

SHUFORD M D, COOKSON M S, CHANG S S, SHINTANI A K, TSIATIS A, SMITHJR J A, S. S. B. (2004) 'Adverse prognostic significance of capsular incision with radical retropubic prostatectomy', *Journal of Urology*, 172(1), pp. 119–123.

Siddiqui MM, Truong H, Rais-Bahrami S, Stamatakis L, Logan J, Walton-Diaz A, Turkbey B, Choyke PL, Wood BJ, Simon R, P. P. (2015) 'Clinical implications of a multiparametric magnetic resonance imaging based nomogram applied to prostate cancer active surveillance.', *Journal of Urology*, 193(6), pp. 1943–1949.

Skove SL, Howard LE, Aronson WJ, Terris MK, Kane CJ, Amling CL, Cooperberg MR, Moreira DM, F. S. (2017) 'Timing of PSA nadir after radical prostatectomy and risk of biochemical recurrence', *Urology*, 108, pp. 129–134.

Stabile A, Giganti F, Emberton M, M. C. (2018) 'MRI in prostate cancer diagnosis: do we need to add standard sampling? A review of the last 5 years.', *Prostate Cancer and Prostatic Diseases*, 21(4), pp. 473–487.

Stamey TA, Yang N, Hay AR, McNeal JE, Freiha FS, R. E. (1987) 'Prostate-specific antigen as a serum marker for adenocarcinoma of the prostate.', *New England Journal of Medicine*, 317(15), pp. 909–916.

Stone N, Hart Prieto MC, Crow P, Uff J, R. A. (2007a) 'The use of Raman spectroscopy to provide an estimation of the gross biochemistry associated with urological pathologies.', *Analytical and Bioanalytical Chemistry*, 387(5), pp. 1657–1668.

Stone N, Hart Prieto MC, Crow P, Uff J, R. A. (2007b) 'The use of Raman spectroscopy to provide an estimation of the gross biochemistry associated with urological pathologies', *Analytical and*

Bioanalytical Chemistry, 387(5), pp. 1657–1668.

Stone N, Kendall C, Smith J, Crow P, B. H. (2004) 'Raman spectroscopy for identification of epithelial cancers', *Faraday Discussions*, 126(141–157), pp. 169–183.

Stone N, Stavroulaki P, Kendall C, Birchall M, B. H. (2000) 'Raman Spectroscopy for Early Detection of Laryngeal Malignancy: Preliminary Results', *The Laryngoscope*, 110(10), pp. 1756–1763.

Svetec D, McCabe K, Peretsman S, Klein E, Levin H, Optenberg S, T. I. (1998) 'P De Visschere 1, W Oosterlinck, G De Meerleer, G Villeirs', *Journal of Urology*, 159(5), pp. 1606–1608.

Thompson IM, Pauler DK, Goodman PJ, Tangen CM, Lucia MS, Parnes HL, Minasian LM, Ford LG, Lippman SM, Crawford ED, Crowley JJ, C. C. J. (2004) 'Prevalence of prostate cancer among men with a prostate-specific antigen level \leq 4.0 ng per milliliter.', *N Engl J Med.*, 350(22), pp. 2239–2246.

TR, A. (1869) 'A case of cancer in which cells similar to those in the tumours were seen in the blood after death.', *The Medical Journal of Australia*, 14(1), pp. 146–147.

De Visschere P, Oosterlinck W, De Meerleer G, V. G. (2010) 'Clinical and imaging tools in the early diagnosis of prostate cancer, a review', *JBR-BTR*, 93(2), pp. 62–70.

VV, T. (2015) 'Tissue Optics and Photonics: Light-Tissue Interaction', *Journal of Biomedical Photonics & Eng*, 1(2), pp. 98–134.

Wang L, He D, Zeng J, Guan Z, Dang Q, Wang X, Wang J, Huang L, Cao P, Zhang G, Hsieh J, F. J. (2013) 'Raman spectroscopy, a potential tool in diagnosis and prognosis of castration-resistant prostate cancer.', *Journal OF Biomedical Optometrics*, 18(8).

Wang X, Qian X, Beitler JJ, Chen ZG, Khuri FR, Lewis MM, Shin HJ, Nie S, S. D. (2011) 'Detection of circulating tumor cells in human peripheral blood using surface-enhanced Raman scattering nanoparticles.', *Cancer Research*, 71(5), pp. 1526–1532.

Widjaja E, Zheng W, H. Z. (2008) 'Classification of colonic tissues using near-infrared Raman spectroscopy and support vector machines.', *International Journal of Oncology*, 32(3), pp. 653–662.

Y, Z. (2011) 'High intensity focused ultrasound in clinical tumor ablation', *World Journal of Clinical Oncology*, 2(1), pp. 8–27.

Yu L, Ng SR, Xu Y, Dong H, Wang YJ, L. C. (2013) 'Advances of lab-on-a-chip in isolation, detection and

post-processing of circulating tumour cells', *Lab on a chip*, 13(16), pp. 163–182.

Yuan Y., L. T. R. (2013) *Contact Angle and Wetting Properties*. Springer, Berlin, Heidelberg. doi: https://doi.org/10.1007/978-3-642-34243-1_1.

Zhang D, Mrozek MF, Xie Y, B.-A. D. (2004) 'Chemical segregation and reduction of Raman background interference using drop coating deposition.', *Applied Spectroscopy*, 58(8), pp. 929–933.

Zhang D, Xie Y, Mrozek MF, Ortiz C, Davisson V J, B.-A. D. (2003) 'Raman Detection of Proteomic Analytes', *Analytical Chemistry*, 75(21), pp. 5703–5709.

Zhang J, Fan Y, Song Y, X. J. (2018) 'Accuracy of Raman spectroscopy for differentiating skin cancer from normal tissue', *Medicine*, 97(34), p. e12022.

Zhao J, Lui H, McLean D, Z. H. (2008) 'Real-time Raman spectroscopy for non-invasive skin cancer detection - preliminary results.', *IEEE Xplore*, p. doi: 10.1109/IEMBS.2008.4649861.

Appendices:

Appendix A : Ethical approval



Health Research Authority

Email:
hra.approval@nhs.net

Mr Basseyy Ndiyo
Department of Physics & Astronomy
University of Exeter
EX4 4QL

26 February 2018

Dear Mr Ndiyo

Letter of HRA Approval

Study title:	An evaluation of Raman Spectroscopy for the diagnosis and risk stratification of prostate cancer
IRAS project ID:	236129
REC reference:	18/LO/0135
Sponsor	University of Exeter

*I am pleased to confirm that **HRA Approval** has been given for the above referenced study, on the basis described in the application form, protocol, supporting documentation and any clarifications noted in this letter.*

Participation of NHS Organisations in England

The sponsor should now provide a copy of this letter to all participating NHS organisations in England.

*Appendix B provides important information for sponsors and participating NHS organisations in England for arranging and confirming capacity and capability. **Please read Appendix B carefully**, in particular the following sections:*

- *Participating NHS organisations in England* – this clarifies the types of participating organisations in the study and whether or not all organisations will be undertaking the same activities
- *Confirmation of capacity and capability* - this confirms whether or not each type of participating NHS organisation in England is expected to give formal confirmation of capacity and capability. Where formal confirmation is not expected, the section also provides details on the time limit given to participating organisations to opt out of the study, or request additional time, before

their participation is assumed.

- *Allocation of responsibilities and rights are agreed and documented (4.1 of HRA assessment criteria)* - this provides detail on the form of agreement to be used in the study to confirm capacity and capability, where applicable.

Further information on funding, HR processes, and compliance with HRA criteria and standards is also provided. It is critical that you involve both the research management function (e.g. R&D office) supporting each organisation and the local research team (where there is one) in setting up your study. Contact details and further information about working with the research management function for each organisation can be accessed from the [HRA website](#).

Appendices

The HRA Approval letter contains the following appendices:

- A – List of documents reviewed during HRA assessment
- B – Summary of HRA assessment

After HRA Approval

The document “*After Ethical Review – guidance for sponsors and investigators*”, issued with your REC favourable opinion, gives detailed guidance on reporting expectations for studies, including:

- Registration of research
- Notifying amendments
- Notifying the end of the study

The HRA website also provides guidance on these topics, and is updated in the light of changes in reporting expectations or procedures.

In addition to the guidance in the above, please note the following:

- HRA Approval applies for the duration of your REC favourable opinion, unless otherwise notified in writing by the HRA.
- Substantial amendments should be submitted directly to the Research Ethics Committee, as detailed in the *After Ethical Review* document. Non-substantial amendments should be submitted for review by the HRA using the form provided on the [HRA website](#), and emailed to hra.amendments@nhs.net.
- The HRA will categorise amendments (substantial and non-substantial) and issue confirmation of continued HRA Approval. Further details can be found on the [HRA website](#).

Scope

HRA Approval provides an approval for research involving patients or staff in NHS organisations in England.

If your study involves NHS organisations in other countries in the UK, please contact the relevant national coordinating functions for support and advice. Further information can be found through [IRAS](#).

If there are participating non-NHS organisations, local agreement should be obtained in accordance with the procedures of the local participating non-NHS organisation.

User Feedback

The Health Research Authority is continually striving to provide a high quality service to all applicants and sponsors. You are invited to give your view of the service you have received and the application procedure. If you wish to make your views known please use the feedback form available on the [HRA website](#).

Appendix B: Research Ethics Committee favourable Opinion



Health Research Authority

London – Stanmore Research Ethics Committee
Health Research Authority

Skipton House 80 London Road

London SE1 6LH

Telephone: 020 7972 2561

Please note: This is the favourable opinion of the REC only and does not allow you to start your study at sites in England until you receive HRA Approval

26 February 2018

Mr Basseyy Ndiyo
Department of Physics &
Astronomy University of Exeter
EX4 4QL

Dear Mr Ndiyo

Study title: An evaluation of Raman Spectroscopy for the diagnosis and risk stratification of prostate cancer
REC reference: 18/LO/0135
IRAS project ID: 236129

Thank you for your letter responding to the Committee's request for further information on the above research and submitting revised documentation.

The further information has been considered on behalf of the Committee by the Chair.

We plan to publish your research summary wording for the above study on the HRA website, together with your contact details. Publication will be no earlier than three months from the date of this opinion letter. Should you wish to provide a substitute contact point, require further information, or wish to make a request to postpone publication, please contact hra.studyregistration@nhs.net outlining the reasons for your request.

Confirmation of ethical opinion

On behalf of the Committee, I am pleased to confirm a favourable ethical opinion for the above research on the basis described in the application form, protocol and supporting documentation as revised, subject to the conditions specified below.

Conditions of the favourable opinion

The REC favourable opinion is subject to the following conditions being met prior to the start of the study.

Management permission must be obtained from each host organisation prior to the start of the study at the site concerned.

Management permission should be sought from all NHS organisations involved in the study in accordance with NHS research governance arrangements. Each NHS organisation must confirm through the signing of agreements and/or other documents that it has given permission for the research to proceed (except where explicitly specified otherwise).

Guidance on applying for NHS permission for research is available in the Integrated Research Application System, www.hra.nhs.uk or at <http://www.rdforum.nhs.uk>.

Where a NHS organisation's role in the study is limited to identifying and referring potential participants to research sites ("participant identification centre"), guidance should be sought from the R&D office on the information it requires to give permission for this activity.

For non-NHS sites, site management permission should be obtained in accordance with the procedures of the relevant host organisation.

Sponsors are not required to notify the Committee of management permissions from host organisations

Registration of Clinical Trials

All clinical trials (defined as the first four categories on the IRAS filter page) must be registered on a publically accessible database within 6 weeks of recruitment of the first participant (for medical device studies, within the timeline determined by the current registration and publication trees).

There is no requirement to separately notify the REC but you should do so at the earliest opportunity e.g. when submitting an amendment. We will audit the registration details as part of the annual progress reporting process.

To ensure transparency in research, we strongly recommend that all research is registered but for non-clinical trials this is not currently mandatory.

If a sponsor wishes to request a deferral for study registration within the required timeframe, they should contact hra.studyregistration@nhs.net. The expectation is that all clinical trials will be registered, however, in exceptional circumstances non registration may be permissible with prior agreement from the HRA. Guidance on where to register is provided on the HRA website.

It is the responsibility of the sponsor to ensure that all the conditions are complied with before the start of the study or its initiation at a particular site (as applicable).

Ethical review of research sites

NHS sites

The favourable opinion applies to all NHS sites taking part in the study, subject to management permission being obtained from the NHS/HSC R&D office prior to the start of the study (see "Conditions of the favourable opinion" below).

Appendix C : Confirmation of capacity and capability

25 April 2018

Ms P Baxter

*Senior Research Governance Officer
University of Exeter
Research Ethics & Governance office
Lafrowda House
St Germans Road
Exeter*

EX4 6TL

Dartford & Gravesham

NHS Trust

*Darent Valley Hospital
Darenth Wood Road
Dartford
d Kent DA2
8DA*

Direct Line Tel: 01322 428393

Email: bridget.fuller@nhs.net

Website: www.dvh.nhs.uk

PROJECT TITLE: An evaluation of Raman Spectroscopy for the diagnosis and risk stratification of prostate cancer.
REC Reference: 18/LO/0135
IRAS Reference: 236129

Dear Pam,

RE: IRAS 236129 Confirmation of Capacity and Capability at Dartford & Gravesham NHS Trust.

*Following review I can confirm that **Dartford & Gravesham NHS Trust** has the capacity and capability to deliver the above referenced study. Please find attached our agreed Statement of Activities as confirmation. It is noted that the research core biopsies will be frozen in liquid nitrogen in theatres and transported to the local labs for storage in the -70 freezer prior to transport to Exeter hospital for histopathology processing.*

We agree to start this study on a date to be agreed when you as sponsor give the green light to begin, although the researcher will need to complete training in the safe use of liquid nitrogen as part of the protocol tissue collection activities.

The approved documents are those listed on the Letter from London — Stanmore Research Ethics Committee, dated 28 February 2018 and the HRA approval letter dated 26 February 2018.

Please note under the terms of the research governance framework the study will be subject to monitoring and audit and you will be contacted later in the year regarding this.

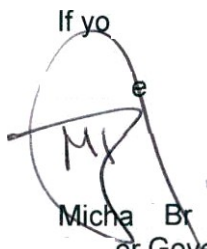
If you wish to discuss further, please do not hesitate to contact me.

Kind regards

Michael Brand

Senior Governance Manager

If yo
e
My
Micha Br
or Gove

A handwritten signature in black ink, appearing to be 'My' or 'Micha', is written over a circular stamp. The stamp contains the text 'Micha Br' and 'or Gove'.

RESEARCH IN HUMAN SUBJECTS OTHER THAN CLINICAL TRIALS OF INVESTIGATIONAL MEDICINAL PRODUCTS

After ethical review – guidance for sponsors and investigators

This document sets out important guidance for sponsors and investigators on the conduct and management of research with a favourable opinion from a Research Ethics Committee. Please read the guidance carefully. A failure to follow the guidance could lead to the committee reviewing its opinion on the research.

1. Commencement of the research

1.1 It is assumed that the research will commence within 12 months of the date of the favourable ethical opinion.

1.2 The research should not commence at any site until the local Principal Investigator (PI) or research collaborator has obtained management permission from the organisation with responsibility for the research participants at the site.

1.3 If the research does not commence within 12 months of the favourable opinion being issued, the Chief Investigator should send a written explanation for the delay. A further written explanation should be sent after 24 months if the research has still not commenced.

1.4 If the research does not commence within 24 months, the REC may review its opinion.

2. Duration of ethical approval

2.1 The favourable ethical opinion of the REC for a specific research study applies for the duration of the study, except where action is taken to suspend or terminate the opinion, subject to approved substantial amendments. Where the duration of the study is to be extended beyond the period specified in the application form, there is no need to notify or seek approval from the REC.

2.2 Where the research involves the use of “relevant material” for the purposes of the Human Tissue Act 2004, authority to hold the material under the terms of the ethical approval applies until the end of the period declared in the application and approved by the REC. In England, Wales and Northern Ireland, samples may be held after the declaration of the end of the research, for analysis or verification of research data for up to one year (this should be detailed in the application which is approved by the REC. After this period legal authority to hold any human tissue under the ethical approval for this project will expire. To ensure that any continued storage is lawful, either the tissue must be held on premises with a storage licence from the Human Tissue Authority, or an application made for ethical approval of another project before the favourable ethical opinion (including the one year after the declaration of the end of study, if applicable) of the existing project expires. Otherwise the tissue would need to be destroyed in accordance with the HTA Codes of Practice.

3. Progress reports

3.1 Research Ethics Committees can review a favourable opinion in the light of progress reports and any developments relevant to the study. The Chief Investigator is responsible for ensuring the research remains scientifically sound, safe, ethical, legal and feasible throughout its duration. The Chief Investigator should submit a progress report to the REC 13 months after the date on which the favourable opinion was given. Annual progress reports should be submitted thereafter.

3.2 Progress reports should be in the format prescribed by the HRA and published on the website <http://www.hra.nhs.uk/resources/during-and-after-your-study/nhs-rec-annual-progress-report-forms/>

4. Amendments

4.1 If it is proposed to make a substantial amendment to the research, the Chief Investigator should submit a Notice of Substantial Amendment to the REC by accessing the original application form on the Integrated Research Application System (IRAS)

4.2 A substantial amendment is any amendment to the terms of the application for ethical review, or to the protocol or other supporting documentation approved by the REC that is likely to affect to a significant degree:

(a) the safety or physical or mental integrity of the research participants

(b) the scientific value of the research

(c) the conduct or management of the research, including its ongoing legality and feasibility.

4.3 A substantial amendment should not be implemented until a favourable ethical opinion has been given by the Committee, unless the changes to the research are urgent safety measures (see section 8). The Committee is required to give an opinion within 35 days of the date of receiving a valid notice of amendment.

4.4 Amendments that are not substantial amendments (“minor amendments”) may be made at any time and do not need to be notified to the Committee. However, changes to contact details of the CI, sponsor or R&D contact are helpful and can be notified by letter or email.

4.5 Further guidance on amendments is available at. <http://www.hra.nhs.uk/research-community/during-your-research-project/amendments/>

5. Changes to sites

Management permission (all studies)

5.1 For all studies, management permission should be obtained from the participating organisation where it is proposed to:

- include a new site in the research, not included in the list of proposed research sites in the original REC application
- appoint a new PI or Local Collaborator at a research site
- make any other significant change to the conduct or management of a research site.

In the case of any new NHS/HSC site, the Site-Specific Information (SSI) Form should be submitted

to the R&D office for review as part of the R&D application.

Site-specific assessment (where required)

5.2 The following guidance applies only to studies requiring site-specific assessment (SSA) as part of ethical review.

5.3 In the case of NHS/HSC sites, SSA responsibilities are undertaken on behalf of the REC by the relevant R&D office as part of the research governance review. The REC's favourable opinion for the study will apply to any new sites and other changes at sites provided that management permission is obtained. There is no need to notify the Research Ethics Committee (or any other REC) about new sites or other changes, or to provide a copy of the SSI Form.

5.4 Changes at non-NHS/HSC sites require review by the REC which reviewed the application for the research. Please submit the SSI Form (or revised SSI Form as appropriate) to the REC together with relevant supporting documentation. The REC will notify the Chief Investigator and sponsor of its opinion within a maximum of 25 days from the date on which a valid SSA application has been received.

Studies not requiring SSA

5.5 For studies designated by the REC as not requiring SSA, there is no requirement to notify the Committee of the inclusion of new sites or other changes at sites, either for NHS/HSC or non-NHS/HSC sites. However, management permission should still be obtained from the responsible participating organisation (see 7.1 above).

6. Urgent safety measures

6.1 The sponsor or the Chief Investigator, or the local Principal Investigator at a research site, may take appropriate urgent safety measures in order to protect research participants against any immediate hazard to their health or safety.

6.2 The REC should be notified within three days that such measures have been taken, the reasons why and the plan for further action.

7. Serious Adverse Events

7.1 A Serious Adverse Event (SAE) is an untoward occurrence that:

(a) results in death

(b) is life-threatening

(c) requires hospitalisation or prolongation of existing hospitalisation

(d) results in persistent or significant disability or incapacity (e) consists of a congenital anomaly or birth defect (f) is otherwise considered medically significant by the investigator.

7.2 A SAE occurring to a research participant should be reported to the Committee where in the opinion of the Chief Investigator the event was related to administration of any of the research

procedures, and was an unexpected occurrence.

7.3 Reports of SAEs should be provided to the REC within 15 days of the Chief Investigator becoming aware of the event, in the format prescribed by the HRA and published on the website:

<http://www.hra.nhs.uk/resources/during-and-after-your-study/progress-and-safety-reporting/>

8. Conclusion or early termination of the research

8.1 The Chief Investigator should notify the REC in writing that the research has ended within 90 days of its conclusion. The conclusion of the research is defined as the final date or event specified in the protocol, not the completion of data analysis or publication of the results.

8.2 If the research is terminated early, the Chief Investigator should notify the REC within 15 days of the date of termination. An explanation of the reasons for the early termination should be given.

8.3 Reports of conclusion or early termination should be submitted in the form prescribed by the HRA and published on the website: <http://www.hra.nhs.uk/research-community/end-of-study-and-beyond/notifying-the-end-of-study/>

9. Final report

9.1 A summary of the final report on the research should be provided to the REC within 12 months of the conclusion of the study. This should include information on whether the study achieved its objectives, the main findings, and arrangements for publication or dissemination of the research including any feedback to participants.

10. Review of ethical opinion

10.1 The REC may review its opinion at any time in the light of any relevant information it receives.

10.2 The Chief Investigator may at any time request that the REC reviews its opinion or seek advice from the REC on any ethical issue relating to the research.

11. Serious breaches of Good Clinical Practice or the protocol

11.1 To ensure that the REC is able to keep the favourable ethical opinion under review, the sponsor should report to the REC any serious breaches of the protocol or of the principles of Good Clinical Practice. A “serious breach” is defined as a breach of the protocol or, of the principles of Good Clinical Practice which is likely to affect to a significant degree the safety or physical or mental integrity of the research participants, or the scientific value of the research. There is no requirement to notify minor breaches of GCP or the protocol.

11.2 Reports of serious breaches should give details of when the breach occurred, the location, who was involved, the outcome and any information given to participants. An explanation should be given and the REC informed what further action the sponsor plans to take.

12. Long Term Studies

The sponsor and Chief Investigator are responsible for ensuring that the study procedures and documentation are updated in light of legislative or policy changes and also for reasons of good practice (e.g. standards for supporting documentation). This should be documented in the progress report to the REC (see above) and, where necessary, an amendment (see above) should be submitted to the REC. The REC may review its opinion in light of legislative changes or other relevant developments.

Participant Identification Number for this study:

Title of Project: **Rapid Assessment of prostate cancer (RAMAN).**

Name of Researcher: Bassey Ndiyo

**Please
initial box**

1. I confirm that I have read the information sheet dated 15/02/2018 (version 1.1) for the above study. I have had the opportunity to consider the information, ask questions and have had these answered satisfactorily.
2. I understand that my participation is voluntary and that I am free to withdraw at any time without giving any reason, without my medical care or legal rights being affected.
3. I understand that relevant sections of my medical notes and data collected during the study, may be looked at by individuals from University of Exeter and from the NHS Trust, where it is relevant to my taking part in this research. I give permission for these individuals to have access to my records.

Only initial boxes for those you wish to consent to for part a); b) and c):

- a) I understand that taking part involves an additional blood sample being taken for research purposes as part of this study only
- b) I agree to an additional prostate tissue sample being collected via biopsy for the purpose of this study, which is one extra sample to the standard care biopsy samples that will be collected.
- c) I agree for any residue sample that is not used for my diagnosis to be stored for future research studies and that if used further ethical approval would be obtained.

4. I agree to the options as initialled above only

5. I agree to take part in the above study.

6. I give express permission for my samples to be sent from Dartford to Exeter

Name of Participant

Date

Signature

Name of Person

Date

Signature taking consent

Study Title: Rapid AssessMent of prostAte caNcer (RAMAN)

Chief Investigator: Basseyy Ndiyo

We would like to invite you to take part in this research study which has been set up by the University of Exeter in collaboration with the Darent Valley Hospital NHS Trust. Please take time to read the following information carefully. Discuss it with friends and family if you wish.

You are free to decide whether to or not to take part in this research study. If you choose not to take part in the study, this will not affect the quality of care you receive from your doctor.

Kindly ask, if there are any concerns that you have and we will be happy to explain and give further information. This study is undertaken as part of a PhD study at the University of Exeter

Background to the study

Prostate cancer is now the most common cancer in men after non melanoma skin cancer in the United Kingdom (UK). This disease condition accounts for over 42,000 new cases diagnosed each year resulting in about 110 men being diagnosed of this disease condition every day (Cancer Research UK, 2017). This high incidence can also be seen in other nations of the world such as United States of America with an estimate of over 220,800 new cases every year (American Cancer Society 2017).

We are using blood samples and biopsy samples to assess the prostate. The aim of the study is to identify specific measurable signs (markers) that will assist in the diagnosis of both aggressive and non-aggressive cancers that some men suffer from and help to prevent the over treatment of patients found to have tumours that are found not to be clinically significant.

The Prostate Specific Antigen (PSA) test is a blood test that can be used to help diagnose prostate problems, including prostate cancer. PSA has been a very useful tool in detecting prostate cancer at the earlier stages of the disease. However, it can be difficult to distinguish between aggressive and non-aggressive prostate cancer using only PSA as a measurement. As a result, it may be difficult for your doctor to gauge sometimes that you do not need immediate treatment for your prostate cancer. This may be because the PSA result is specific to the prostate itself and yet not a specific pointer of a possible cancer in the prostate.

Currently the best available assessment tool for early detection of prostate cancer is Prostate Specific Antigen (PSA) test which involves taking your blood sample for histological assessment for the presence or absence of prostate cancer. In order to confirm the presence of cancer, a prostate biopsy (needle puncture sample) is also done. A prostate biopsy is where very thin sections of prostate tissue are removed using a special needle, although the test can be seen as a very invasive procedure by some patients. For this study, we will need one extra biopsy sample to the ones that are taken for routine purposes towards your diagnosis. About 100 participants will take part in this study.

Why have I been invited to take part?

We are inviting all patients to take part in the research study who have undergone the investigations of a PSA test; Transrectal Ultrasound guided biopsy and MRI scan of the prostate. These tests will have been requested by your clinician, because you have been informed about the suspicion of a growth in your prostate.

You will be eligible to take part in the study if you:

- Are a man aged 40 or above
- Have a raised PSA level.
- Have undergone a digital rectal examination of the prostate for suspected abnormal growth.
- Have had a biopsy taken of your prostate gland for pathological analysis.

You will not be eligible to take part in the study if you:

Had received any prior treatment for your prostate that could affect the results of blood samples or biopsy. This could include previous Radiotherapy, brachytherapy or hormonal therapy for your prostate.

How will the biopsy samples be taken?

An ultrasound probe will be used to scan your prostate and an image will appear on the screen. The image will be used as a guide to take the biopsy samples. A local anaesthetic will be given to make the procedure less painful. The doctor will insert a thin needle next to the ultrasound probe in your back passage into the prostate. 10 to 12 small pieces of prostate tissues will be taken from different areas of your prostate with an extra piece for research purpose. This whole procedure should take about 10 to 15 minutes.

What should I do if I am interested in taking part in this study?

If you think you would like to take part in this study, all you need to do is to take this information sheet to your next appointment with your Consultant and there you would be asked if you understand what the study is about and have the opportunity to ask any questions you may have, before you decide to take part in this study.

What does taking part in this research study involve?

Taking part in the research study involves having one additional core biopsy which will be obtained during your routine biopsy procedure and a 5ml blood sample (about a teaspoonful) will be obtained for analysis for the research. Your involvement in the study will not require anything else to be done after these samples have been collected and your involvement in the study will finish.

What are the benefits for me taking part in this study?

There will be no immediate direct benefit to you should you decide to participate in this study. However, there could be benefit to future patients that are investigated for prostate abnormalities or cancer.

What are the potential disadvantages or risks for me in taking part in this study?

There is no potential risk associated with taking part in this study above those already identified in the guidance you will have received from the hospital for routine samples

taken for the investigations of prostate disease; there are commonly risks of bleeding from the biopsy site and some discomfort afterwards. Having a blood sample can be a little uncomfortable for some people and can cause some bruising.

Will my taking part in the trial be kept confidential?

Yes. We will protect your confidentiality at all times. The following steps will ensure that your confidentiality is maintained when participating in the study.

Your consent to participate in the study with your details will be kept locked in a secure NHS location and separate from the study data which will be allocated a code number to protect your identity.

Your blood sample, tissue sample and data necessary for research purposes will be assigned a unique study number. Researchers working outside of Dartford & Gravesham NHS Trust and employed by the University of Exeter, who work with your blood samples, tissue samples and data, will not know your identity. Your data will be stored using a unique, anonymous study identification number for all research purposes to protect your confidentiality.

A single table linking your anonymous study identification number to your NHS number identity will be stored on a separate password protected document on an NHS computer. This will only be accessed by your direct care team.

The link will be used to retrieve only relevant health information from your medical and other health related records for the purpose of this study. The retrieved information will be anonymous.

All study data to be used for sample processing at the Biophysics lab (University of Exeter) will be stored in a restricted access, study database. The study data will be connected to your study identification number only and your personal details will never appear in this database. Access to the study database will be password protected, encrypted and will only be used by named researchers working on this study, under the direct supervision of the senior scientific investigator.

What will be stored on the research database at Darent Valley Hospital?

Information that will be stored on the research database at the NHS Trust (Darent Valley Hospital) will be anonymised.

When will this study end?

Your involvement in the study will end after your study samples have been collected. The study will end as soon as all the data collected are analysed by the research team, the results are presented, and recommendations are documented. The anonymised samples will be stored for up to 3 years at the University of Exeter following last participant recruitment. The samples may be used for future research which we will first ask your consent for; and if this occurs then a separate ethical approval will be applied for. Finally, tissues and data relating to this study will be securely destroyed.

How will I withdraw from the study if I want to do so?

You can decide to withdraw from this study at any time without giving any reason without it affecting the standard of care you receive or your legal rights.

You can withdraw from the study by telephoning us on **01322 428612**, Monday to Friday or by writing to the coordinating Centre (Please see bottom of the leaflet). This will allow us to determine the desired level of withdrawal from the following two options: **“No further contact”**, which means that the research team would not contact you directly anymore but will still have your permission to use your information, blood samples and tissue samples provided previously for this research study or future research.

“No further use”, which means that in addition to no further contact, all previous data collected would not be used any more for the purpose of this study or future research.

Who will be able to use my information, blood samples and tissue samples?

A copy of the results of your anonymous blood samples, tissue samples and data will be available only to researchers of this study, who have relevant research ethical approval from the Health Research Authority and scientific knowledge for the planned research. We will ask your permission in the consent form to store any unused samples for future research following ethical approval of a new study.

Anonymised results from this research will be written up as part of the researcher's PhD study and may be published for conferences and journals so that future patients

and researchers may benefit from its findings. Neither you nor the data you have provided will be able to be identified in any of the write up or publications to protect your confidentiality.

Will I be told the study specific results obtained from my blood samples or tissue samples?

Your Consultant will contact you with your routine results at the appropriate time after your standard care investigations and your standard care will progress in the normal manner. Any information discovered as a result of the research study will be made available in a brief report which you will be able to access via the clinic that you attended. No participant will be identified in the report findings. In the unlikely event that anything untoward is discovered in any of the samples that have been collected for research purposes, then the treating clinician at Dartford & Gravesham NHS Trust will be informed by the research team, using the unique study number and your clinician will contact you directly if required.

Who has approved the study?

All research in the NHS is looked at by an independent group of people called a research ethics committee to protect your interests. This study has been reviewed and given a favourable opinion by the London-Stanmore Research Ethics Committee and approval by the Health Research Authority. The Research & Development Department at Dartford & Gravesham NHS Trust have also approved the study.

What will happen if an invention is made using my blood samples and tissue samples?

You are freely giving your blood samples and tissue samples. This research is a non-commercial study without any profit from this study. However, for future research we may work together with commercial companies to develop inventions for the benefit of patients, and we hope that this will help the NHS to improve health care in future. If this happens a separate ethical approval will be obtained

Your sample may help researchers in the public and private sector to make an invention. If an invention results from this research undertaken with your blood or tissue samples, you will not receive any compensation or payment.

What happens if something goes wrong?

If you are not happy with any aspect of this research study, in the first instance please contact the research team directly. If you are not able to resolve your complaint, please then contact the Head of Research & Development at the hospital, or please contact the Academic Supervisor at the University of Exeter, who can contact the Sponsor Representative and Research Ethics and Governance Office. If you still do not feel the issue has been resolved, the NHS Complaints department should be contacted (Patient Advice and Liaison Service – PALS). Full details are found below under contact details.

Who is organising and funding the research?

This study is being organised and funded by University of Exeter and Darent Valley Hospital as part of the researcher's PhD study.

Contact numbers for the research team

Thank you for taking the time to read this leaflet.

If you have any further questions do not hesitate to ask. For further information please contact:

Chief Investigator: Basseyy Ndiyo (PhD student researcher)

Address: Department of Urology, Darent Valley Hospital

Tel: 01322 428100

Principal Investigator: Prof Sanjeev Madaan

Address: Department of Urology, Darent Valley Hospital

Tel: 01322 428612

Academic Supervisor: Prof Nicholas Stone

Address: Department of Physics & Astronomy,
University of Exeter,

Tel: 01392 726531

Contact for PALS: <http://www.dvh.nhs.uk/contact-or-visit-us/compliments-complaints/>

Please contact: Senior Governance and Patient Experience Manager at the following address;

Complaints Department, Dartford and Gravesham NHS Trust, Darent Valley Hospital, Darenth Wood Road, Dartford, Kent, DA2 8DA.

Telephone: 01322 428436

Email: dgn-tr.PALS@nhs.net

Appendix G -Curriculum Vitae

NDIYO, BASSEY

MSc Medical Imaging

HCPC: RA43610 UK Registered Diagnostic Radiographer

Clinical Research Fellow – Dartford & Gravesham NHS Trust

Home Address: 1 Allium Rise Dartford DA1 5TS UK

Telephone: 07403458902

Email: bassey.ndiyo@inhealthgroup.com bn235@exeter.ac.uk

PERSONAL STATEMENT

I have a strong track record of working at the interface between physics, engineering, and medicine. I have the ability to develop high-quality, cutting-edge research with little or no supervision. I am a dynamic, reliable, self-motivated, confident, and patient focused Medical Imaging Specialist with people management skills. I am able to prioritize my work effectively, pay close attention to details and maintain high standard of patient care. Furthermore, I possess the necessary skills to function effectively in research, academic and clinical environments.

EDUCATION AND QUALIFICATIONS

2015-2019

2018-2020

	University of Exeter	MPhil (2019)
2002-2007	HPCP	Full registration and licence
1995-1999	City University, London	MSc (Medical Imaging)
1985-1990	Federal School of Radiography, Lagos	DIR Diagnostic Radiography
	Duke Town Secondary School, Calabar	West African Senior School Certificate Examination

EMPLOYMENT HISTORY

2010-Till date

2011-2012

InHealth Group Limited

Senior Radiographer

2008- 2009

BMI Chiltern Hospital

CT Clinical Lead
Radiographer

2004-2008

InHealth Group Limited

CT Superintendent
Radiographer

2002-2004

Cromwell Hospital
London

Senior 1 Radiographer/
PACS Administrator

Locum Agency, UK

Locum Radiographer

2001-2002

Federal Medical Centre,
Azare, Bauchi

Radiographer

2000-2001

Specialist Hospital, Bauchi

Radiographer

AWARDS

Dartford & Gravesham NHS Trust - Research Competition Finalist -2019

TEACHING & PRESENTATION

- **2016 Ndiyo B**, Differentiating between aggressive and Indolent prostate cancer using Multiparametric MRI & Vibrational Spectroscopy, Annual Scientific Conference of NIRAD, London.
- **2017 Ndiyo B**, Beyond PSA: Raman liquid biopsy for identification of markers for Prostate cancer, Annual Scientific Conference of NIRAD, Birmingham.
- **2018 Ndiyo B**, Raman Spectroscopy: A real time molecular imaging can revolutionise Prostate cancer management, Urology study day with Urologist, Kent.
- **2019 Ndiyo B**, The Role of Raman Spectroscopy in diagnosis & Risk Stratification of Prostate cancer, Annual Research Competition, Dartford & Gravesham NHS Trust.

RESEARCH AND OTHER PROJECTS

- The Role of Raman spectroscopy in diagnosis and Risk stratification of Prostate Cancer

CERTIFIED COURSES

- 2008 Managing Safely – Institute of Occupational Safety and Health
- 2016 Radiographer led CT Colonography – Peterborough & Stamford Hospitals NHS Trust
- 2014 Cardiac CT Course Royal Brompton & Harefield NHS Trust
- Comprehensive list of courses available on request.

RESEARCH INTEREST

- To develop novel diagnostic approaches for clinical diagnosis of molecular diseases such as cancers. I am currently utilising a multidisciplinary approach of micro-spectroscopic imaging techniques and histopathology to interrogate biochemical fingerprints of tissues and biofluids for suspected prostate cancer patients (as part of My PhD Thesis).
- Translation of novel optical research tools into routine clinical practice from bench top to bedside.
- Clinical translation of vibrational spectroscopies and imaging for disease diagnosis and therapeutic guidance.

GOVERNING BOARD MEMBERSHIP – Holy Trinity Church of England, Primary School

- Chair- Standards, Ethos and Wellbeing Committee

- Responsible for raising school standards through three strategic functions by ensuring clarity of vision, ethos and strategic direction.
- Able to hold head teacher to account for the educational performance of the school and its pupils.
- Financial performance oversight of the school and ensuring that the money is well spent.
- I am an elected member of this governing body.

INTEREST:

- Exploring new areas
- Travelling
- Reading and writing
- Playing football

REFERENCES:

Prof. Nicholas Stone

Professor of Biomedical Imaging and Biosensing / NHS Consultant Clinical Scientist

(1st PhD Supervisor)

University Lead for Healthcare Technologies

Director of EPSRC RaNT Programme

Physics and Astronomy

College of Engineering, Mathematics and Physical Sciences

University of Exeter

EX4 4QL

Email:n.stone@exeter.ac.uk

Prof. Sanjeev Madaan PhD, FRCS(Urol), FEBU

(2nd PhD Supervisor)

Consultant Urological Surgeon & Lead Cancer Clinician | Darent Valley Hospital, Dartford

Visiting Professor | Canterbury Christ Church University

Speciality lead for Urology Cancer Research | CRN Kent, Surrey & Sussex

Tel: +44(0)1322 428612

Sanjeev.madaan@nhs.net

Appendix H: University's Letter of sponsorship



RESEARCH ETHICS AND
GOVERNANCE OFFICE

Lafrowda House
St Germans Road
Exeter
Devon
EX4 6TL

Telephone +44 (0)1392 723588
Web www.exeter.ac.uk

14th December 2017

Project title: 'An evaluation of RAMAN spectroscopy for the diagnosis and risk stratification of prostate cancer'

Sponsor's Reference: 1718/22

IRAS ID: 236129

Chief Investigator: Mr. Bassey Ndiyo, Department of Physics & Astronomy, College of Engineering, Mathematics & Physical Sciences, University of Exeter, EX4 4QL

Dear Bassey,

I confirm that the University of Exeter will act as lead sponsor for the above study, undertaking its responsibilities as outlined in Health Research Authority's 'UK policy framework for health and social care research' (v3.2, 10/10/2017). The University will ensure that the necessary insurance cover for professional indemnity and public liability are in place before the study commences.

Before participant recruitment commences, the appropriate HRA, ethics and NHS R&D approvals must be in place; please ensure that I have received copies of any correspondence or approval letters.

As Chief Investigator, you are responsible for the management and conduct of the study and are expected to deliver the project in accordance with the University's Code of Good Conduct in Research (<http://www.exeter.ac.uk/research/inspiring/about/goodpractice/>).

The primary responsibility for the following lies with the Chief Investigator:

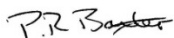
- Establishing and maintaining a Master File and Site Files as appropriate throughout the life of the study. Please find a suggested index attached for information.
- Ensuring that the researchers, students or others involved in conducting the project have the necessary training, experience, qualifications, support and supervision to carry out their tasks.
- Ensuring that all amendments to the study have received appropriate ethical review and R&D approvals. In cases where it is unclear if the amendment is minor or substantial, I will be responsible for making the judgement. Please contact me to discuss potential amendments at the earliest opportunity.
- Providing annual, progress or end of project reports to Research Ethics Committees, funders and others as required. Please ensure that I receive copies of all reports.
- Reporting adverse events or breaches of protocol or good practice, should they occur (a template adverse event report form is available at <http://www.hra.nhs.uk/resources/during-and-after-your-study/progress-and-safety-reporting/> . You must ensure that I am informed of adverse events or breaches as soon as possible after they occur and **always within 24 hours** of the incident. If required, I will take responsibility for ensuring that the event or breach is reported to the NHS REC, funder or other appropriate organisation within 15 days of the incident.
- Appropriate dissemination of the findings

- Satisfactory storage of any personal data and archiving of study material

Please note that announced or unannounced monitoring visits may be conducted either as part of the University's routine research governance audit process or in response to a specific concern or incident. The University reserves the right to withdraw sponsorship and take any action necessary to ensure the safety of participants if it believes that the Chief Investigator is not fulfilling their obligations.

Please do contact me at any time if you have queries or concerns, for additional support or to discuss any aspect of your project.

Yours sincerely,



Pam Baxter

Senior Research Ethics and Governance Officer

Direct line: 01392 72(3588)

Email: p.r.baxter2@exeter.ac.uk

I declare that as Chief Investigator for the above named study I, or my nominated delegate, will carry out my responsibilities as outlined above.

Signature of CI _____

Date _____

Appendix I: Material Transfer Agreement

Maidstone and  Tunbridge Wells

NHS Trust

MATERIAL TRANSFER AGREEMENT

This Agreement dated _____ is made

BETWEEN

- (1) Maidstone and Tunbridge Wells NHS Trust, Histopathology Department, The Maidstone Hospital, Hermitage Lane, Maidstone, Kent, ME16 9QQ, (“MTW”); and
- (2) University of Exeter, Northcote House, The Queens Drive, Exeter, EX44QJ (“UoE”)

RECITALS

UoE has agreed to provide MTW with prostate biopsy material taken for research purposes as further described in the Schedule (the “Materials”) and MTW has agreed to receive the Materials and perform the analysis outlined in this Agreement. In this Agreement, the Materials shall be accompanied with a copy of the signed consent form which is relevant to each sample received that UoE has agreed to provide MTW with under, or in connection with this Agreement.

IT IS AGREED as follows:

1. MTW confirms the Materials is being handled is outside standard protocol.
2. MTW will not accept any responsibility or liability in respect of the opinion MTW provides on the Materials. The opinion provided by MTW **must not be considered a diagnosis** in any way.
- s. MTW does not accept responsibility for transportation of the Materials. MTW do however have an expectation that samples (i.e. Materials) are sent safely packed according to UN3373 specifications. That means the sample container must be within a sealed, watertight bag, (a clear bag as coloured bags tend to indicate a disposal pathway) and that must be placed in an outer, rigid, watertight container that has been appropriately labelled as to contents and hazard. This container must also clearly state the address of the designation laboratory and provide the contact details of the sender in case of emergency. It is the responsibility of UoE to ensure the courier transport of the Materials understands the nature of what they are carrying and is H&S compliant. MTW reserves the right to terminate this arrangement if the Materials” are presented in any way that places its staff at risk (e.g. leaking sample containers).
4. MTW will not review the original diagnosis relating to any of the Materials received. Resolution of any discrepancy between the opinion provided by MTW in connection with the Materials and

any earlier diagnostic samples for the same patient resides entirely with Dartford and Gravesham NHS Trust, the organisation provided with the original diagnosis.

5. UoE warrants that where required the Material has been obtained from humans with the appropriate consent as required by the Human Tissue Act 2004 or the Human Tissue (Scotland) Act 2006 (as applicable) and with ethical approval and UoE shall be liable for any *claims arising due to the breach of this warranty. UoE further warrants that it has not provided any information, (and does not intend to provide any information) which has led or may lead to MTW being able to identify the person from whom the relevant material came. MTW requires copies of the consent forms to come with the samples comprising the Materials. MTW will not commence processing of samples unless there is clear consent provided. Consent forms will not be seen by the reporting pathologist. If the patient name needs to be redacted from the consent form to provide anonymity MTW will accept the Materials but MTW will expect the trials number to be on both the sample pot and the consent form so MTW can tie the samples together with the biopsy received.*
6. Samples must come in manageable batch sizes. First batch will be 10 cases. Once MTW have processed the samples received in the first batch, MTW will confirm if slightly bigger batches can be accommodated.
7. UoE must provide MTW with a sample of the spreadsheet that will be used to recording the findings for each biopsy received.
8. If the Materials prove to be problematic to interpret due to their having been handled in a non-standard way, MTW reserves the right to discontinue.
9. Opinions provided by MTW will be based upon a single H&E stained slide. No additional laboratory work will be performed so there will be no further tests.
10. The opinion provided by the consultant at MTW will only indicate presence of malignancy (or not). MTW may provide brief comments to indicate any limitations in interpretation.
11. All tissue blocks and slides will be returned to UoE once MTW have finished with them. UoE will be informed and expected to arrange prompt collection by the courier of their choice.
12. MTW will provide the formalin pots to place the samples in and UoE is required to arrange a courier to collect them. MTW will dispose of the empty formalin pots.
13. For the avoidance of doubt nothing in this Agreement will prevent UoE from using the opinion provided by MTW for the purposes of the Research Project.
14. This Agreement will commence on the date of final signature and will continue until the first anniversary of the commencement date.
15. MTW understands that the Materials may have hazardous properties, contain infectious agents or pose other health and safety risks. Except as set out in clause 5 UoE makes no representations and gives no warranties either express or implied in relation to it: for example (without limitation), no warranties are given about quality or fitness for a particular purpose, or freedom from infection. UoE will not be liable for any use made of the Materials by MTW. MTW will use the Materials in accordance with good laboratory practice standards, all due skill and care and with dignity, sensitivity and respect. MTW will comply with all applicable laws, approvals, rules, codes of practice

and regulations governing the transportation, storage, use and disposal of the Materials.

16. MTW undertakes to store the Material in accordance with all applicable laws and not to attempt to identify or contact the donor of the Materials or to compromise or otherwise infringe the confidentiality of information on the donors and their right to privacy.
17. UoE has the right to terminate this agreement forthwith at any time by means of written notice to MTW if the ethical approval is withdrawn or if MTW is in breach of this Agreement. In the case of any termination, MTW shall immediately discontinue all use of the Materials and, at UoE's discretion, promptly return or destroy all unused Material and provide written confirmation that this has been completed. If requested, MTW must certify that it has complied in full with any such requirement of UoE. Should an individual donor or their next of kin rescind their consent, UoE will require and MTW agrees to discontinue using the appropriately identified sample and return or destroy it in accordance with UoE's instructions.
18. The liability of either party for any breach of this Agreement or arising in any other way out of the subject matter of this Agreement, will not extend to loss of business or profit, or to any indirect or consequential damages or losses.
19. This Agreement constitutes the entire agreement between the parties and supersedes and extinguishes all previous agreements, promises, assurances, warranties, representations, and understandings between them, whether written or oral, relating to its subject matter. Any amendment(s) to this Agreement shall be in writing and must be signed by an authorised representative of each party.
20. This Agreement shall be governed and construed in accordance with the laws of England and Wales and the Parties agree to the exclusive jurisdiction of the English Courts.

AGREED by the parties through their authorised signatories:

SIGNED by

Date:

Hazel Everest, Research and Clinical Audit Manager

Maidstone and Tunbridge Wells NHS Trust

SIGNED by

Paul Denham, Histology Lead Biomedical Scientist Maidstone and Tunbridge Wells NHS Trust

SIGNED by

.....

University of Exeter

SIGNED by

.....

Date:

19/12/2019

Bassey Njoku, Student, University of Exeter

